Optical and Behavioural tools to investigate the Neural Correlates of Learning and Memory

Submitted in partial fulfilment of the requirementsof the degree of

Doctor of Philosophy

by

Meenakshi P

(SR No.03-09-00-10-11-15-1-12948)

(CSIR No. 09/079(2697)/2016-EMR-I)

Supervisor

Dr. Balaji Jayaprakash

Assistant Professor

Centre for Neuroscience

INDIAN INSTITUTE OF SCIENCE

(July 2021)

Declaration

I declare that the current written submission represents original research work towards my PhD degree. I have adequately cited and referenced the original sources when describing the ideas and works carried out by others. I also declare that I have adhered to all principles of academic honesty and integrity. All experiments involving animals were approved by the Institutional Animal Ethics Committee of the Indian Institute of Science.

(Meenakshi P.)

(SR No.:03-09-00-10-11-15-1-12948)

(CSIR No.: 09/079(2697)/2016-EMR-I)

Date: 12-07-2021

Place: IISc, Bangalore

Certification

This dissertation titled **Optical and Behavioural tools for investigating the Neural Correlates of Learning and Memory** by Ms. Meenakshi P. (IISc Sr No. 03-09-00- 10-11-15-1-12948, CSIR File No. 09/079(2697)/2016-EMR-I) is the result of original and independent work for the degree of Doctor of Philosophy in Neuroscience at the Indian Institute of Science, Bangalore, India.

Supervisor

Dr. Balaji Jayaprakash

Date: 12-07-2021

Place: IISc, Bangalore

Indian Institute of Science, Bengaluru, India

Certificate of Course Work

———————————————————

The details of the course work are given below:

SI No.	Course code	Course name	Credits
1	DB 201	Mathematics and Statistics for Biologists	2:0
2	NS 201	Introduction to Systems Neuroscience	3:0
3	NS 202	Introduction to Molecular and Cellular Neuroscience	3:0
4	NS 203	Optical Spectroscopy and Microscopy	3:0
5	NS 302	Topics in Molecular and Cellular Neuroscience	2:0
6	MB 209	Cellular Neurophysiology	3:1

Dedicated to

Mus musculus

As Allegra Goodman stated, “Here was the human body writ small”.

Thank you for your contributions to science.

To my parents,

Shivaja V and Prabod Kumar B

We finally did it!

Acknowledgements

First, I would like to thank my guide and mentor, Balaji Jayaprakash for his tireless support and belief in me. I am grateful for his patience in guiding me through the various phases of my PhD training. It has been a revelatory experience. It is no secret that I am terrified of mathematics and analytical derivations. In my opinion, our biggest accomplishment as a mentor and student working on solving problems related to learning and memory together was overcoming this aversion of mine. Thank you for giving me the tools to challenge my misconceptions about myself.

I thank Prof. James Chelliah, Prof. Varsha Singh, Prof. Rishikesh Narayanan of the Comprehensive Examination Committee for their technical inputs during the earlier stages of the research project as well as their unstinted support during this time. For the constructive criticism and feedback obtained during annual work presentations, my gratitude goes to the Thesis Advisory Committee, especially Prof. Aditya Murthy and Prof. Naren Ramanan. It was during these interactions that I learnt to see the ideal and practical sides to scientific inquiry, such as, one needs to be willing to explore different domains to address the ever-evolving research problem.

The course work involved in this research journey has been quite exhaustive. I learnt to appreciate the breadth and depth of neuroscience and cultivate the necessary skill of critical thinking. For this, I thank the faculty members, Prof. Vijaylakshmi Ravindranath, Prof. Shyamala Mani, Prof. Deepak Nair, Prof. SP Arun, Prof. Supratim Ray, Dr. Sridharan Devarajan, Dr. Sachin Deshmukh, , Dr. Mini Jose, Dr. Swananda Marathe, Dr. Srikanth Padmala, Prof. Kavitha Babu of the CNS department as well as Prof. Sujit Sikdar, Prof. Rishikesh Narayanan of MBU department.

I was fortunate to have worked in a supportive and intellectually stimulating lab environment, with fruitful discussions and exchange of ideas with the lab members. Ashish, Vikram, Aditya, Suraj, Shruti, Sankha, Richa, Thomas, Manish, Nirupam, Sharaj, Shireen, Aditi, Nruthyathi, Dhruv, Neha, Yagika, Shruthi, Vinayak et al. Thank you, each one of you for enriching my time in the lab.

Outside of the lab, the few people who experience the good and bad times that comes with pursuing a PhD are my batchmates: Prijesh, Vivek, Warsha, Deepjyoti, Sriram, Ilina, Varsha, Dhruv. Thank you for your solidarity in through this journey. The sentiment extends to the senior as well as the junior students at CNS who made every CNS seminar and events a joyful and stimulating activity. Anindo, Ruturaj, Monika, Sumitash, Prasanna Sricharan, Akash, Murthy, Indraja, Sidrat, Mahadev, Medha, Vishakh, Prabhaha, Garima, Soumen, Arnab et al Thank you.

Forming the solid base of our work, the backbone of research, is a team that silently performs the mundane, trivial tasks that are vital for ensuring the success of the experiments that are needed for our research, My heartfelt thanks go to the Animal House Facility team, specifically Prof. Ramachandran, Ms. Rosa ma'am and lab attenders Gangadhar, Annappa, Manjunath.

The assistance provided by the CNS administrative and support staff made it easier for me to focus on my research work and minimise the time spent on tedious but necessary paperwork. Ms. Vyjanthi, Ms. Lakshmi, Mr. Karthik, Mr. Karthik, Mr. Salman have supported me tirelessly. My sincere thanks to all of them.

For their continuous backing in terms of funding and finance, I would like to thank IISc Scholarship section, Finance and Accounts section. Ms. Mangalam ma'am, Mr. Manohar, Ms. Gyanakumari, Mr. Ganesh, thank you for patiently taking the time to help me with administrative tasks.

This PhD research work would not have been possible without funding from different agency. CSIR for providing me with a fellowship to carry out this dissertation. I thank the Government of India and the Indian Institute of Science provide a platform and encourage young people like me to pursue such specialised research. Lab grants provided by DBT, SERB, TATA, Pratiksha Trust, made it possible to work in a well-equipped lab with cutting edge tools.

For their staunch support and unflinching belief in me, I thank my parents Shivaja V and Prabod Kumar. I love you both very much and appreciate you supporting my dreams. The love of my family members kept me sane through all the bad days that are inevitable (PhD or not).

These acknowledgements would be incomplete without mentioning the efforts of my former teachers and mentors who saw my love for science and nurtured it. I specifically would like to thank Dr.Suma S for her excellent classes that sparked my love for molecular biology and engineering. I would also like to thank Prof. MRS Rao who provided me the opportunity to carry out my masters' research in his lab. It was my first experience in a research environment, and I am forever grateful for that experience.

Lastly, I would like to thank my friends for their love and support through my journey. They were always there to make me laugh and ensure that I took care of myself. Thank you for filling my life with so much joy and fun.

I would like to conclude my note on gratitude by stating that I am fortunate to have been selected for the PhD course in Neuroscience six years ago. Back then, I had a set idea of what my training and learning would entail. I looked forward to developing myself as a scientist. It has been a few tough years, and with the help of each person I interacted with during the time, I believe I have achieved that goal and more. Thank you, all.

Abstract

Events in our everyday life are encoded as memories that can be consciously recollected and remembered, although our ability to retrieve the specific details associated with these events diminish with time. Such losses present itself as an inability to distinguish between closely related events. Studying this phenomenon requires development of sensitive tools and methods that can measure and follow these changes at neuronal as well as behavioural scales. I have developed such tools as a part of my thesis. Specifically, it is of interest to know how multiple memories that share common content are organised in brain preserving their identity especially when two such events occur closer in time.

First, we sought out to obtain a general method which distinguishes neurons that took part in multiple temporally separated events by utilizing immediate early gene expression kinetics. Immediate early genes (IEGs) are widely used as a marker for neuronal plasticity. Here, we modelled the dynamics of IEG expression as a consecutive, irreversible first order reaction with a limiting substrate. We showed that such a model, together with two-photon in vivo imaging of an IEG-fluorophore expression, can be used to identify distinct neuronal subsets representing multiple memories. We imaged the retrosplenial cortex of cFOS-GFP transgenic mice to follow the dynamic cellular changes resulting from contextual fear conditioning (CFC) behaviour. The analytical expression allowed us to segregate the neurons based on their temporal response to one specific behavioural event, thereby improving the sensitivity of detecting plasticity related neurons. This enabled us to establish representation of context in retrosplenial cortex at the cellular scale following memory acquisition.

Secondly, we developed a sensitive measure to assess spatial memory retention during learning and recall in Morris wate maze behaviour paradigm. Conventional behavioural measures for testing hippocampal dependent memory in Morris water maze involves comparing the residence time of the mice across different quadrants. Such measures are inherently limited in their ability to extend the behavioural task to discern out subtle deficits in memory. Here we used the velocity vector field to describe the search pattern of the mice and develop quantitative measures that are intuitive as well as sensitive to measure the degree of impairment in the memory rather than just identifying if there is an impairment.

Lastly, we focused on developing a method to obtain fluorescence lifetime from steady state measurements utilizing a conventional custom built two photon imaging system. Fluorescence at optical saturation is a function of absorption cross section and excited state lifetime. Ultrashort pulses used in multi-photon microscopy/imaging/spectroscopy depletes the ground state population. This depletion can be modeled and measured through steady state fluorescence. We use this to establish a proof of principle application of measuring lifetime through steady state fluorescence.

Contents in brief

Contents

retrosplenial cortex.
Section 4.3 discusses the above findings.
Section 4.4 describes the methodology.
Section 4.5 contains the figures and figure legends corresponding to Chapter 4.
Section 4.6 contains the table and legends corresponding to Chapter 4.
Section 4.7 lists the references for Chapter 4.

Chapter 5 Vector field-based analysis to assess spatial memory in navigational tasks

Chapter 5 describes a new framework for analysing spatial memory in navigational tasks, specifically using Morris water maze as an example, using velocity-based vector fields and their properties.
Section 5.1 reviews existing measures utilized to assess spatial memory in Morris water maze, highlighting their strengths and weakness. It emphasizes the need for measures that are sensitive in detecting subtle memory deficits providing the context of the current work.
Section 5.2 provides a detailed formal description of how vector-based calculus principles reveal the behavioural responses that are a result of spatial memory alone.
Section 5.3 shows the application of the framework developed in Section 5.2 to detect search centres from a divergence heat map derived from swim trajectories in Morris water maze (MWM) task.
Section 5.4 discusses and compares the proposed method with existing methods, highlighting the differences and the advantages of the current method.
Section 5.5 describes the methodology.
Section 5.6 contains the figures and figure legends corresponding to Chapter 5.
Section 5.7 lists the references for Chapter 5.

Chapter 6 Comparative analysis of spatial memory in different mouse strains using Morris water maze task

Chapter 6 shows the application of the framework developed in Chapter 5. An analysis of spatial memory for platform location in Morris water maze (MWM) comparing different strains of mice is presented.
Section 6.1 briefly reviews the literature on comparative studies on the cognitive

ability of different strains of mice.

Section 6.2 presents the results of the nature of spatial memory for two albino strains of mice in the reference task of MWM, as well as two strains of mice that underwent goal reversal training in MWM.

Section 6.3 discusses the findings and their implications.

Section 6.4 describes the methodology.

Section 6.5 contains the figures and figure legends corresponding to Chapter 6.

Section 6.6 lists the references for Chapter 6.

Chapter 7 Analysis of subtle spatial memory differences in Noonan syndrome mouse models using Morris water maze task

Chapter 7 focuses on the analysis of spatial memory in Noonan syndrome (NS) mouse models, with the goal of dissecting subtle memory deficits.

Section 7.1 reviews NS and the mouse model used for the analysis.

Section 7.2 describes the nature of spatial memory in two NS mouse models.

Section 7.3 Discussion.

Section 7.4 describes the methodology.

Section 7.5 contains the figures and figure legends corresponding to Chapter 7.

Section 7.6 lists the references for Chapter 7.

Chapter 8 Development of optical measures to improve contrast in in vivo imaging

Chapter 8 describes a new optical method to measure the lifetime of a fluorophore using steady-state fluorescence measurements

Section 8.1 provides a brief introduction to the concept of fluorescence lifetime and time correlated single photon count (TCSPC), a widely method to estimate lifetime.

Section 8.2 describes the formally derived analytical expression to obtain lifetime as a function of delays between excitation pulse pairs.

Section 8.3 presents a proof-of-principle for the method by experimentally obtaining lifetime value for two fluorescent solutions.

Section 8.4 summarises Chapter 8.

Section 8.5 describes the methodology.

Section 8.6 contains the figures and figure legends corresponding to Chapter 8.

Section 8.7 lists the references for Chapter 8.

Chapter 9 Conclusion

Appendix A Two photon microscopy

Appendix A describes the custom built two-photon microscope in the Neurodynamics lab along with its characterizations and the settings used for in vivo imaging experiments mentioned in Chapters 3-4, 6.

Appendix B Generation of molecular probes to visualise neuronal structure and activity

Appendix B briefly described the design and cloning strategy, plasmid constructs, AAV virus packaging, and in vivo expression of molecular probes to visualise neuronal structure and activity in mouse brain.

Appendix C Software for data extraction and analysis

Appendix C details the development of hardware and software required to carry out the experiments described in this thesis.

Appendix D Data organization: Codebook

Appendix D details the organization of the raw data collected, data extracted, analysed, and stored in the experiments carried out in Chapters 3-6. It also provides the links to code used from data analysis.

List of Abbreviations and Symbols

CFC	Contextual Fear Conditioning
Ctxt	Context
DAC	Double Activation Cell
eGFP	enhanced Green Fluorescent protein
Hpc	Hippocampus
IEG	Immediate Early Genes
MWM	Morris Water Maze
PD	Probe day
RSc	Retrosplenial cortex
SAC	Single Activation Cell
shGFP	short half live Green Fluorescent protein
TG	Transgenic
WT	Wild type

List of Publications

Journal Papers

1. Meenakshi, P., and J. Balaji. 2017. Neural Circuits of Memory Consolidation and Generalisation. *J. Indian Inst. Sci.* 97:487–495. doi:10.1007/S41745-017-0042-4.
2. Meenakshi, P., S. Kumar, and J. Balaji. 2021. In vivo imaging of immediate early gene expression dynamics segregates neuronal ensemble of memories of dual events. *Mol. Brain*. 14:102. doi:10.1186/s13041-021-00798-3.

In review

1. P. Meenakshi, D. Mehrotra, N. Nruthyathi, D. Almeida-Filho, Y-S. Lee, A.J. Silva, J. Balaji. "Novel measures of Morris water maze performance that use vector field maps to assess accuracy, uncertainty, and intention of navigational searches." *(In review).*
(bioRxiv 2021.07.04.451032; doi: https://doi.org/10.1101/2021.07.04.451032)
2. Kumar S., P. Meenakshi, Kaushik Y., and J. Balaji. "Spatially correlated, NMDAR independent spine loss underlies integration of related information." *(In review).*
(bioRxiv 2020.12.17.423264; doi: https://doi.org/10.1101/2020.12.17.423264)

Conferences Papers

1. [P. Meenakshi, D. Mehrotra, N. Nruthyathi, Y.S. Lee and J. Balaji]. [Vector maps of flow is sensitive in determining the centre of intended search, uncertainty surrounding the search and the absolute error associated with the spatial memory in water maze]. 2019 Neuroscience Meeting Planner. Chicago, IL: Society for Neuroscience, 2019. Online. (As first and presenting author.)
2. [P. Meenakshi, S. Kumar, and J. Balaji]. [An In vivo approach to identify and segregate neuronal ensembles of multiple memories using temporal expression dynamics of a single immediate early gene]. Program No. 709.20. 2017 Neuroscience Meeting Planner. Washington, DC: Society for Neuroscience, 2017.

Online. (As first and presenting author.)

3. [S. Kumar, P. Meenakshi and J. Balaji]. [Beta imaging: Fluorescence Saturation dynamics-based parameter generates contrast within dendrites in vivo]. Program No. 709.23. 2017 Neuroscience Meeting Planner. Washington, DC: Society for Neuroscience, 2017. Online.

CHAPTERS

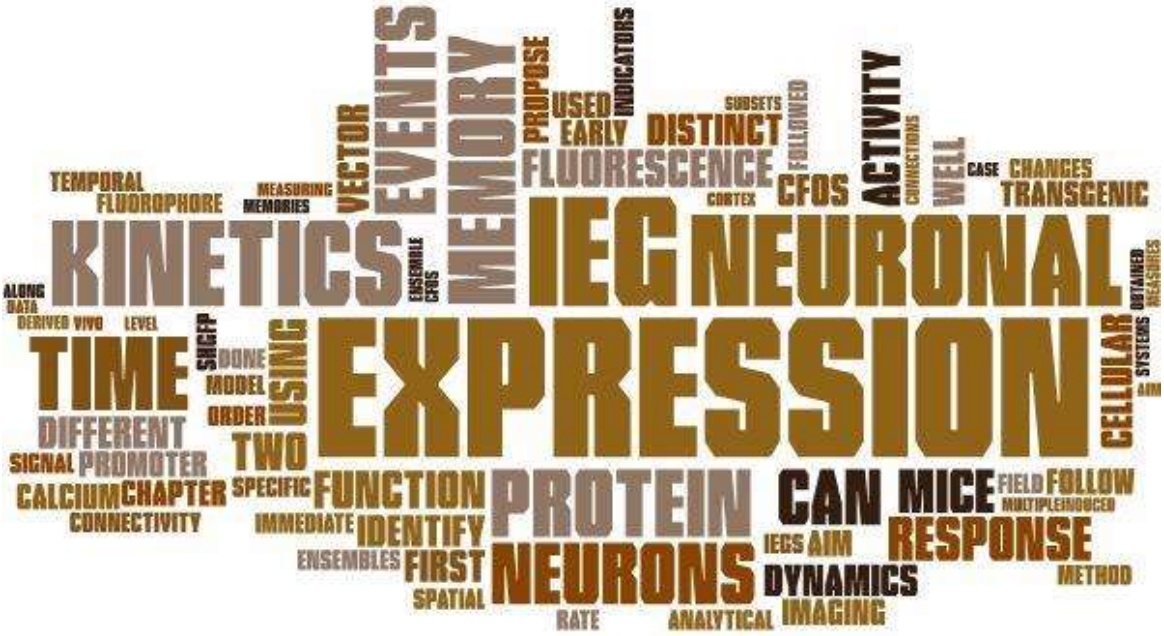
EXPRESSION
KINETICS
IEG
NEURONAL
MEMORY
EVENTS
TIME
PROTEIN
NEURONS
FUNCTION
CAN
MICE
RESPONSE
IDENTIFY
FIRST
DYNAMICS
IMAGING
ANALYTICAL
RATE
SPATIAL
IEGS
AIM
FOLLOW
FIELD
METHOD
TWO
USING
DIFFERENT
PROMOTER
CALCIUM
CHAPTER
CONNECTIVITY
SPECIFIC
IMMEDIATE
ENSEMBLES
DONE
MODEL
ORDER
SHGFP
VECTOR
TEMPORAL
FLUOROPHORE
MEASURING
MEMORIES
PROPOSE
USED
EARLY
INDICATORS
DISTINCT
SUBSETS
FOLLOWED
FLUORESCENCE
CFOS
CORTEX
ACTIVITY
CONNECTIONS
WELL
CASE
CHANGES
TRANSGENIC
CELLULAR
SYSTEMS
OBTAINED
MEASURES
ALONG
DATA
DERIVED
VIVO
LEVEL
ENSEMBLE
CFOS
AIM

CHAPTER 1

Introduction

Abstract

The phenomenon of memory is quintessential in shaping who we are through our experiences. Memory acquisition, storage and retrieval are vital cognitive functions that enable learning, adaptation, and survival. Years of research has developed our understanding of the various types of memory and the brain regions associated with its expression. As the research methods and techniques to study the mechanisms under lying memory formation and expression evolved, our understanding of memory phenomena improved. At the level of behaviour, development of simple as well as complex memory tasks along with improvements in assessing the behavioural readout, i.e. the quality or nature of the memory, allowed the investigation of finer, precise questions about processes such as memory generalisation and discrimination. Recently, the field of memory research has seen an unprecedented effort in deciphering the neural correlates of memory and learning using advanced molecular and optical techniques. The current chapter provides a brief primer of the progress made in the field of memory research.

1.1 Introduction

The phenomena of memory comprise a series of complex processes starting with encoding, followed by consolidation, and finally retrieval of information. Over the years, multiple memory systems have been identified based upon the involvement of different brain regions in supporting different types of memories.

1.2 Historical perspective

Scientists have been searching for the structures and regions of the brain responsible for learning and memory since the early 1800. The concept that memory is not a unitary phenomenon but can be classified into different types depending on certain criteria came about through various studies involving animal models and human patients.

A key event in memory research was the identification of the hippocampus as an indispensable brain region for making new memories of life-long events. The role of hippocampus in memory encoding came from studying patients who had undergone bilateral removal of medial temporal lobe. These patients who had their hippocampal and para-hippocampal regions removed showed a specific type of amnesia. They suffered from anterograde amnesia, i.e., the inability to form new memories, while also showing graded retrograde amnesia. However, the anterograde amnesia was specific to certain kinds of memory. While these patients could not learn the name of their doctor or the hospital they were in, they were able to learn new motor skills. That is, they lost the ability to learn any information that required them to declare their experiences such as names of people and places, whereas they retained the ability to learn procedural memories such as the ability to mirror drawing. Findings from studying such amnesic patients, along with other studies on animal models, led to the identification of different memory systems, as described below.

Classification of memory based on the brain region required for encoding categorises memory into declarative (explicit) and non-declarative (implicit) before introducing further sub classes (Cohen and Squire, 1980). Declarative memories are defined as the memories that can be consciously recalled. They are strongly dependent on the hippocampus both for its acquisition and retrieval. These memories have a strong component of “what, when and where” information, e.g., information involving events and facts, i.e., declarative memory is further classified

into episodic and semantic memory. Episodic memory or memory of an event is linked to the context and time associated with it during acquisition. Semantic memory is the memory of factual information. In many instances such a clear classification may not be possible, e.g., autobiographical memory contains components of both episodic and semantic memory.

On the other hand, non-declarative memory is unconscious memory that is expressed through performance and acquired through procedural learning of skills and habits. Apart from these procedural memories, memories associated with priming, perceptual learning, classical conditioning, and non-associative learning are thought to belong to this class. Figure 1.1 depicts the classification of memory based on memory encoding and retrieval.

Another classification of memory system focuses on the time scales at which you can disrupt the memory consolidation process. This is described in section 1.1.3.

1.3 Rodent models to study memory and learning

Although much of the evidence for memory classification came largely from human studies, hippocampal-dependent tasks and the structures associated for its behavioural expression were identified in rodents (Kim and Fanselow, 1992).

One such behaviour, the contextual fear conditioning (CFC) is a multimodal memory task (Fig. 1.2 (A-C)). During training, rodents are taught to associate a particular context (CS) with a footshock (US). Memory retention of this association is tested by placing the rodent back into the training context and measuring its freezing response (CR). The freezing response in rodents is an evolutionary response to stressful situation which can be defined as cessation of all movements except breathing.

Another commonly used behavioural paradigm to study hippocampal memory is the Morris water maze. It is multiple trial spatial memory task where rodents are trained to locate a hidden platform in a pool of water in relation to distal cues. During training, rodents are made to swim in a pool filled with opaque water till either the platform is found, or the trial duration ends (60-seconds). Over many training sessions, the latency, or time taken, to reach the platform reduces, indicating that the ability of rodent to locate the platform has improved (Fig. 1.2 (D-F)). However, spatial memory is tested during probe trials where the platform is removed from the pool. The rodent is made to search for the trial duration (60s),

and different measures are used to quantify the retention of spatial memory (See: Chapter 5, Section 5.1).

In both CFC and MWM, the context-dependent memory in rodents consist of representations derived from detailed somatosensory inputs, similar to the episodic memory in humans. Additionally, since these memories have been shown to be initially dependent on the hippocampus for its expression, they are deemed to be episodic-like memories (Rosenbaum et al., 2001). Similarly, other hippocampal-dependent memory tasks are used as a proxy for declarative memory in rodents, e.g., social transfer of food preference (STFP), Barnes Maze, Flavour-Place association task.

A major advantage of using rodents to study learning and memory is the opportunity to design experiments to investigate causal relationships of brain structures and behaviour manifestation. Vast improvement in molecular and optical methods allow the visualisation and manipulation of neuronal activity in different regions of the brain. For example, transgenic mice provide a valuable tool to study molecular, cellular and network level mechanisms in the brain, as well as molecular probes delivered through viral expression systems allow for relatively easy, precise spatial and temporal manipulation of neuronal activity.

1.4 Memory consolidation

Consolidation of memory takes place over different time scales, i.e. cellular level consolidation (6 - 24 hours) and systems level consolidation (months to years in humans, weeks to months in mice) (McGaugh, 2000).

1.4.1 Cellular consolidation

Cellular consolidation refers to a set of molecular changes that alter the synaptic strengths by remodelling existing synapses or by increasing synaptic contacts. The stabilization of memory immediately after learning takes place within hours. Evidence for the lability of the memory during initial stages came from studying the effect of protein synthesis inhibitors on memory retention. Goldfish were trained in a place aversion task using a tank with two arms for the goldfish to reside in, connected by a thin tube for travel. In one arm, the goldfish were trained to associate an aversive stimulus (Shock arm), whereas the alternate arm of the tank was safe for residence. Immediately after training, the goldfish were injected with puromycin intracranially to stop protein synthesis. During memory recall test, fish

administered with puromycin showed absence of place aversion memory compared to control groups who reduced the amount of time spent in the shock arm of the tank. Similar studies demonstrating the role of protein synthesis in cellular memory consolidation have been shown in rodents as well. Thus, the process of memory cellular consolidation of acquired memory is dependent on protein synthesis and is labile before consolidation during the initial period of a few hours.

1.4.2 Systems consolidation

Systems consolidation refers to memory taking representation and hence acquiring the ability to be retrieved independent of hippocampus over weeks to months, i.e., the memory becomes resistant to lesion/loss of hippocampus. Along with evidence from amnesic patients with damaged MTL (Scoviille and Milner, 1957), the graded nature by which the memory becomes independent of the hippocampus in animal models was shown by Kim and Faneslow (Kim and Fanselow, 1992). Rats underwent CFC training to associate a shock (US) with a context A(CS). Different groups had their hippocampus lesioned at different intervals of time from training day. It was observed that the time of hippocampal lesions influenced the extent of graded retrograde amnesia. Rats that underwent hippocampal lesions after 28 days showed memory retrieval comparable to the control animals, indicating that the memory recall had become independent of the hippocampus (Fig. 1.3).

Standard Consolidation Theory

The Standard Consolidation Model (Squire et al., 1984) states that memories acquire extra-hippocampal representations through repeated reactivation of the hippocampal-cortical connections, either through recall of cues or by reactivation of the memory during sleep. The reactivation leads to strengthening of connections between the distributed cortical networks which makes the memory independent of the hippocampus over time.

This is shown to be dependent on the hippocampus initially and becomes independent of hippocampus during memory retrieval. Over time, different brain regions are involved in the expression of the memory. It is thought to become less dependent on the hippocampus over time and supported by a broad network of cortical brain areas. This time dependent transfer of information from hippocampus to cortical regions is known as systems consolidation (Fig. 1.4).

Multiple Trace Theory

An alternate model is the Multiple Trace Theory (MTT). MTT hypothesize that the hippocampus plays a role in episodic, but not semantic, remote memory, i.e. contextual memory is always dependent on the hippocampus for details whereas semantic memories are independent of hippocampus after systems consolidation. Evidence for remote memory dependence on the hippocampus comes from optogenetics studies where inhibition of the hippocampus immediately before testing remote memory retrieval affects the memory (Goshen et al., 2011) and hippocampal inactivation impaired expression of specific but not generalized memories (Wiltgen et al., 2010). Another study (Lesburguères et al., 2011) showed that inhibition of the cortical circuit within 24 hours after memory acquisition affects the ability of the animal to retrieve the memory at a remote time point. This indicates the role of the hippocampal-cortical circuit, and not just the role of hippocampus, at the recent time point in formation/encoding of remote memories.

Multiple trace theory emphasizes the distinction between two types of declarative memory, episodic and semantic, proposing that detailed episodic memory always require the hippocampus for expression, whereas the standard theory maintains that detailed episodic memories can become independent of the hippocampus over time. The standard theory views memories as transferred from the hippocampus to a stabilized cortical representation over time, freeing up the hippocampus for encoding of new memories whereas the multiple trace theory emphasizes the dynamic nature of a consolidated memory as detailed hippocampal representations co-exist with generalized cortical representations. All these lines of evidence point to the fact that the nature of memories encoded by the distributed cortical trace or the hippocampal trace is different at a remote time point compared to recent time.

1.4.3 Implications in memory discrimination and generalisation

As described above, the process of memory consolidation is susceptible to change. Generalization of a memory refers to the loss of details of the memory over time. In rodents, animals trained to associate context A (CS) with a footshock (US) can clearly distinguish the training context A with a novel context B during memory retrieval 24 hours later. However, if the animal is tested for memory recall at a remote time point (30-days), they tend to show freezing in both the training context A as well as a novel context B, i.e. the fear memory gets generalised to both contexts over time.

Similar behaviour of memory generalisation is seen in Morris water maze task. In the study (Richards et al., 2014), mice were trained in a modified water maze paradigm where the platform was randomly placed around the mean of a spatial distribution, but never at the mean. During probe trial one day post training, the mice were able to recall where the platform was last placed during training (measured by time spent in the platform area). However, 30-days post training, the mice recalled a generalised memory of where the platform was placed. They spent majority of the time at the mean of the platform distribution indicating generalisation of platform locations utilised during training via pattern generalisation.

However, discrimination of contextual information is still possible at a remote time point. In a related study using discrimination training, the animals are trained to associate context A (CS) with a footshock (US) (shock context) as well as learn to associate context B with the absence of footshock is given (safety context). The sensory features of the context were modified such that the two contexts had some overlapping similar features. These animals that undergo discrimination training can clearly distinguish between context A as the shock context and context B as a safety context, even during memory retrieval at a remote time point even after hippocampal lesions. This suggests that cortical memory can retain specific information, i.e., possess a detailed memory, depending on the training parameters.

1.5 Neural correlates of memory

1.5.1 Engram

Memory Trace or Engram is an ensemble of neurons which might constitute the physical representation of a memory. This concept was proposed by Richard Semon in 1921 as the Engram Theory (Schacter et al., 1978). Learning induced activation of a small ensemble of neurons results in persistent changes on the neuron that stores the information. Reactivation of this ensemble by relevant recall cues results in retrieval of the specific memory. The advancement in molecular tools now allow us to label or tag the neurons that were activated during learning. One study showed that the same neurons that were activated by exposure to a novel context in the CA1 of the Hippocampus were reactivated when re-exposed to the same environment (Guzowski et al., 1999). Another study employed transgenic mice to enable differential tagging of distinct populations of activated

neurons. Mice trained in fear conditioning showed that the same neurons in the amygdala that were activated during learning also were activated during recall (Reijmers et al., 2007). Development of optogenetics tools which allow to manipulate the activity of neurons further verified that reactivation of tagged cells manifested in the expression of a specific memory. When hippocampal neurons activated during context fear conditioning were reactivated in a novel context, the animals showed freezing response to a context it was never exposed to before (Liu et al., 2012; Ramirez et al., 2013). Similar experiment was done in the retrosplenial cortex (RSc) where reactivation of the neuronal ensemble was sufficient to induce fear response (Cowansage et al., 2014).

1.6 Visualising neuronal activity and plasticity

1.6.1 Calcium or voltage activity

Imaging the changes in cellular calcium in individual neurons using a sensor is a popular method of visualising neural activity. These sensors need to have high sensitivity and respond rapidly to rise and decay in cellular calcium. A popular group of calcium sensors are the genetically encoded calcium sensors or GECIs. It confers the advantage of genetic manipulation within an organism to allow its spatio-temporal expression. GCaMP is one such GECI, (Nakai et al., 2001) a fusion protein of green fluorescent protein (GFP) and the calcium being domain of calmodulin. As a result of calcium binding to the calmodulin domain, a conformational change takes place in the protein which results in increase in the fluorescence of GFP. Improvements made possible through molecular engineering has led to the development of a range of GECIs that cover a wider excitation spectrum, improving depth resolution *in vivo* imaging.

1.6.2 Immediate Early Gene (IEG) expression

A different approach to investigating behaviourally relevant neuronal activity utilizes cellular changes resulting in plasticity. Synaptic signals received by the neuron need to be translated into long-term plasticity in the neuronal circuit. Immediate early genes or IEG are rapidly and transiently expressed following neuronal stimulation. Its expression is tightly correlated with synaptic plasticity. The function of IEGs ranges from acting as growth factors, structural proteins, signal transduction molecules to being transcription factors that affect gene expression. It has a supposed role in stabilizing recent changes in the synaptic efficacy

(Lanahan and Worley, 1998).

IEGs are used as activity markers for mapping neuronal circuits activated in a particular behaviour. It provides a tool to determine the involvement of various brain regions in encoding a behaviour. The specificity of the expression for a given memory becomes difficult as stress and arousal also lead to its expression. However, with the ability of in vivo imaging and by maintaining a controlled environment we can overcome this problem as it allows us to investigate the same animal at different time points.

Arc

Activity-regulated cytoskeleton-associated protein (Arc) is a structural protein that is localized to the dendrites. Disruption of Arc impairs the maintenance phase of LTP and consolidation of long-term spatial memory (Guzowski et al., 2000). The kinetics of Arc mRNA are such that a few minutes after activation it is localized in the nucleus as intense foci, while 30 minutes later it has accumulated in the cytoplasm and dendrites of the cell (Guzowski et al., 1999).

cFos

cFos was one of the first IEGs to be identified. It was previously identified as a proto oncogene which suggests its regulatory role in the cell cycle (Sheng and Greenberg, 1990). Characterization of cFos activation in neuronally differentiated P12 cells demonstrated that it is induced in response to depolarizing conditions mediated through voltage gated calcium channels (Morgan and Curran, 1986). The first demonstration of cFos expression in vivo was shown in response to pentylenetetrazol (PTZ), a gamma-Aminobutyric acid (GABA) antagonist that causes seizures in mice (Dragunow and Faull, 1989). Seizures produced widespread cFos expression throughout the hippocampus, basal forebrain and cortex with mRNA levels peaking 60 minutes and protein levels peaking 90 minutes following seizure induction (Morgan et al., 1987). Normal forms of cell stimulation such as visual sensory stimulus and whisker stimulation induced cFos expression in the suprachiasmatic nucleus (Aronin et al., 1990) and the somatosensory cortex (Mack and Mack, 1992) respectively. In mice, contextual fear conditioning induced peak levels of Fos protein in regions throughout the brain 60 to 90 minutes following learning (Strekalova et al., 2003). To study the role of cFOS in memory, a global cFOS knockout mouse was generated. The mice were viable, but their phenotype showed lack of tooth eruption, altered haematopoiesis and small size in

comparison with wild-type littermates (Wang et al., 1992). On training in spatial memory, these mice showed severe impairments in the hidden version of the water maze as well as the visible (nonhippocampal) version of the water maze. Thus, in the global knockout, the developmental deficits were too strong to delineate any specific effect on memory. To circumvent this, two conditional cFos knockout mice lines were generated that ensured the removal of cFOS gene in the brain and not the entire body. The first line was created by crossing a transgenic mouse with floxed cFos gene with a Tg mouse expressing Cre recombinase under CaMKII promoter (Tsien et al., 1996). In this cFos conditional knockout, the knockout effect was limited to the hippocampus. Only when the mice were trained using an intense protocol for water maze did they showed normal spatial memory. The second conditional knockout was generated by crossing a Tg mouse with floxed cFOS gene with a Tg mouse expressing Cre recombinase driven by the nestin promoter, thus both neurons and glia lacked cFos gene in this Tg mice. These mice showed spatial memory deficits using a less intense training protocol in the water maze (one trial per day for 11 days) and showed deficits in long term memory for contextual fear conditioning (Fleischmann et al., 2003). Disruption of cFos function using antisense oligonucleotides in the hippocampus also resulted in impaired spatial memory in the water maze. It had no effect on short-term spatial memory but did affect long term memory (Guzowski, 2002). The above suggests that cFos may play a general role in coupling stimulation to long-term changes in gene transcription required for plasticity changes in the neuron. Thus, activation of cFos could serve as a potential marker for identifying the neurons encoding the information.

1.7 Figures

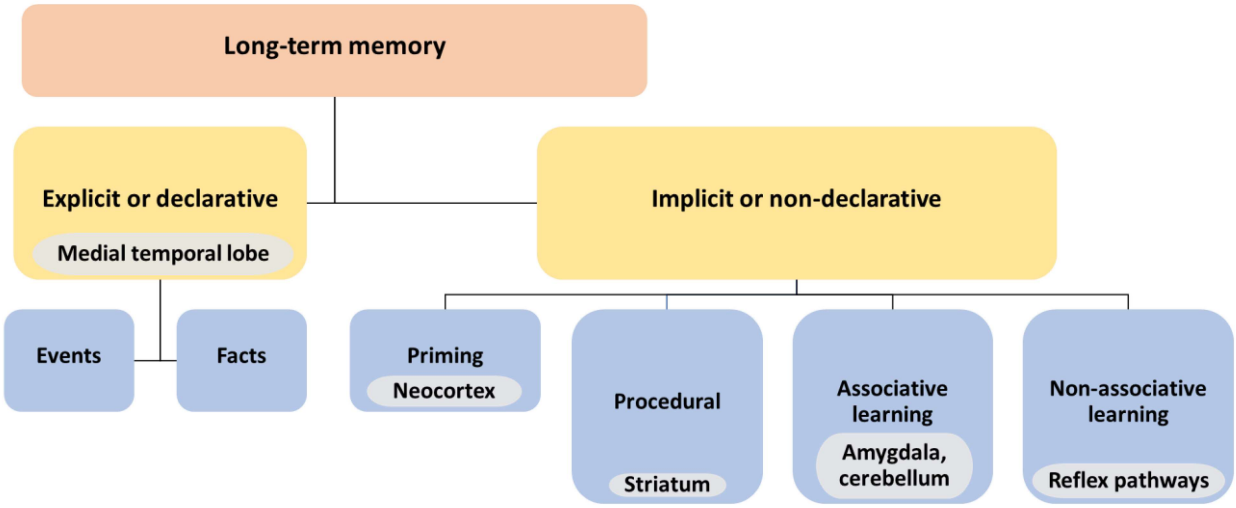

Figure 1.1: Classification of memory into different types based on brain region responsible for memory acquisition. Long-term memories are broadly classified into explicit or declarative and implicit or non-declarative memories. Declarative memories rely on the medial temporal lobe (hippocampal and para-hippocampal regions) for encoding information. Non-declarative memories are of different types as mentioned in the schematic (brain region responsible for encoding information is mentioned in grey box). Adapted from (Squire and Zola, 1996).

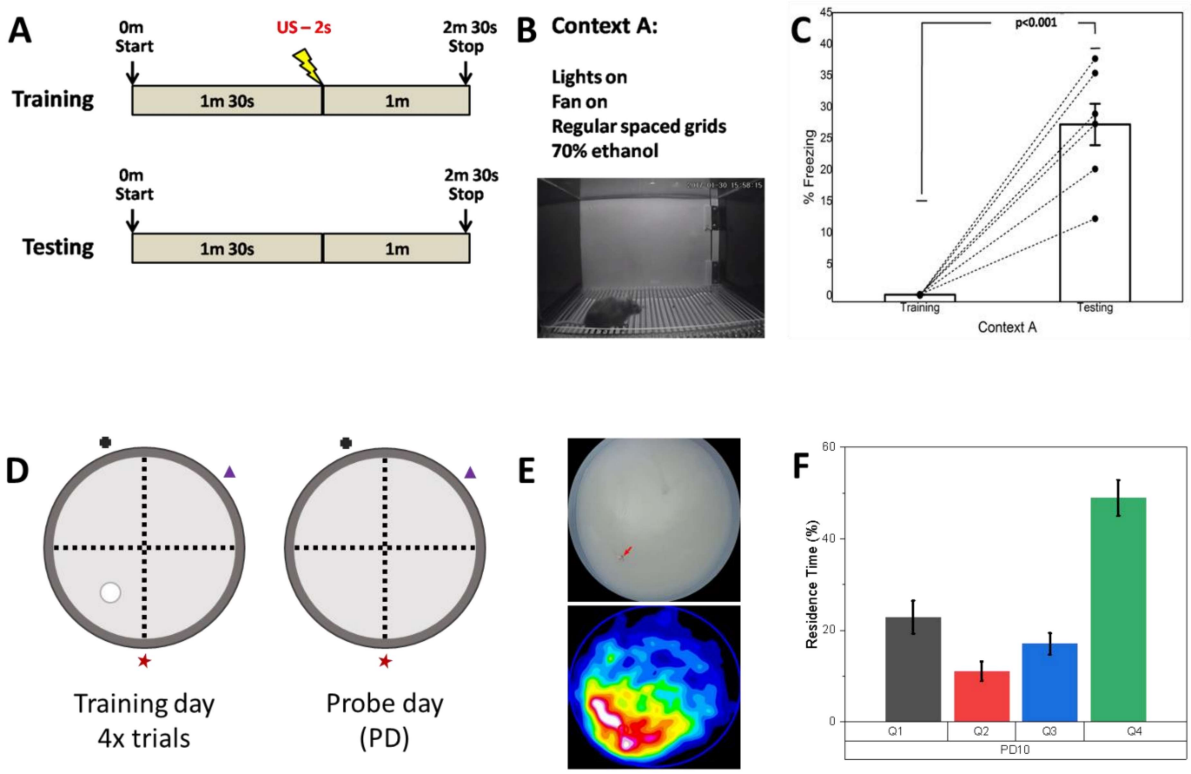

Figure 1.2: Behavioural tasks used to study hippocampal-dependent memory in rodents.

(A) Schematic describing the behaviour paradigm for contextual fear conditioning (CFC). Rodents are made to associate a particular context to a mild foot shock through exposure to a training context A (conditioned stimulus, CS) for 1min 30s, followed by a 0.7mA shock for 2 seconds (unconditioned stimulus, US) (Top). To assess memory retention, the rodents are placed into the training context A for a duration of 2min 30s without administering the US (Bottom). The amount of freezing is a proxy for memory retention as explained in (C).

(B) An example of a chamber used for contextual fear conditioning: context 'A' is defined by features such as light (visual), regularly spaced grids (tactile), and 70% ethanol (odour).

(C) Freezing is an evolutionary response to threat in absence of an escape route. It is defined as cessation of all movements except breathing. Quantifying freezing manually or through an automated software provides a measure of memory for the context.

(D) Schematic describing the behaviour paradigm for Morris water maze (MWM). Rodents are made to learn the location of a hidden platform (white circle in bottom left quadrant of the pool) in relation to distal cues (black circle, purple triangle, and red star). Usually, each training session or day consists of 4 trials. To test the presence of spatial memory for the platform, a probe test.

(E) A video frame from a training session shows the mouse on the platform located in a water maze pool. BALBc mice on the platform is indicated with a red arrow.

(F) Occupancy measured in each quadrant acts as a measure for spatial memory of the platform.

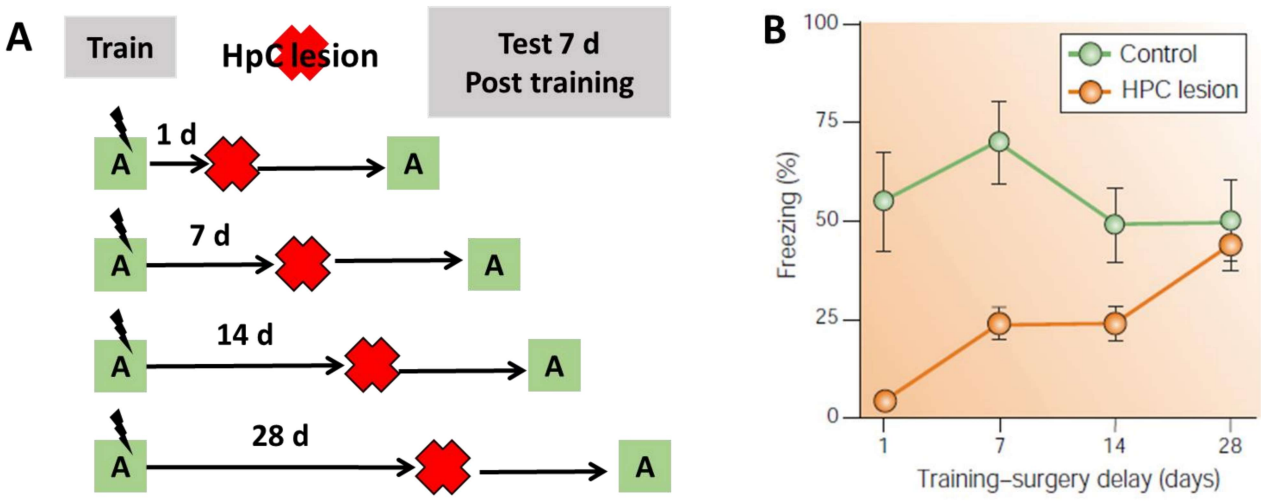

Figure 1.3: Evidence for systems consolidation in rodents.

(A) Schematic showing the experimental groups of rats used for behavioural paradigm.

(B) Hippocampus lesioned group of rats (Hpc lesion, orange) show graded memory retention as a function day of lesioning.

Adapted from (Kim and Fanselow, 1992; Frankland and Bontempi, 2005).

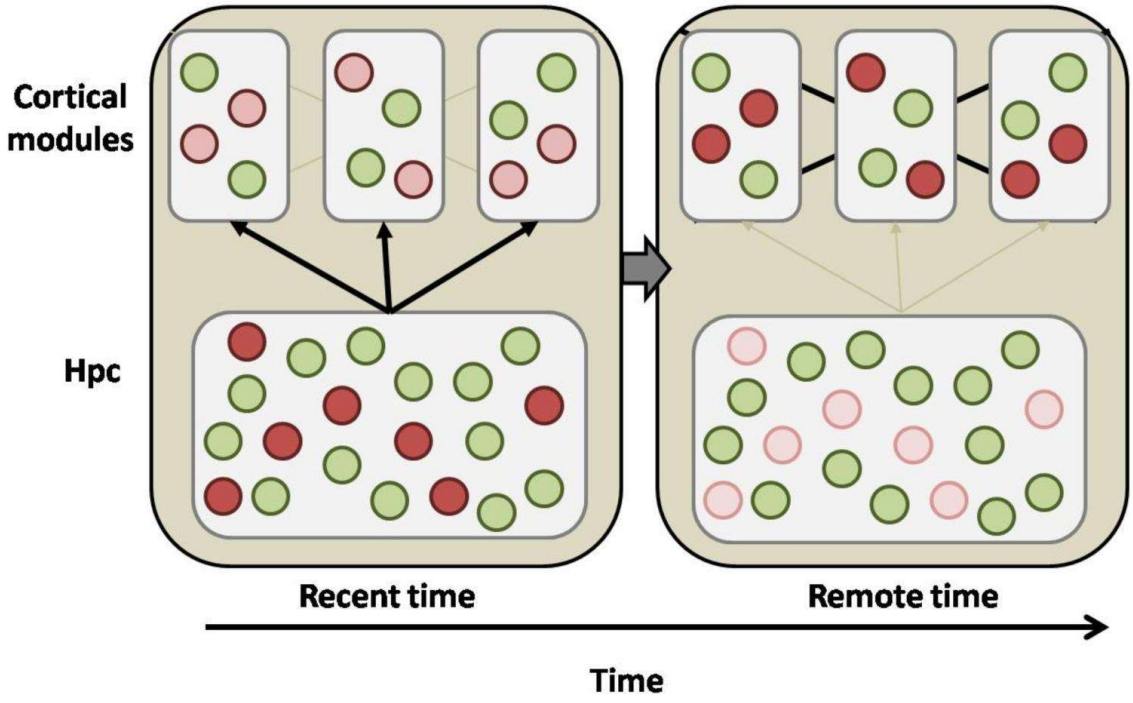

Figure 1.4: Standard model of systems consolidation. (Meenakshi and Balaji, 2017).

1.8 References

Aronin, N., S.M. Sagar, F.R. Sharp, and W.J. Schwartz. 1990. Light regulates expression of a Fos-related protein in rat suprachiasmatic nuclei. *Proc. Natl. Acad. Sci. U. S. A.* 87:5959–5962. doi:10.1073/pnas.87.15.5959.

Cohen, N.J., and L.R. Squire. 1980. Preserved learning and retention of pattern-analyzing skill in amnesia: Dissociation of knowing how and knowing that. *Science (80-.).* 210:207–210. doi:10.1126/science.7414331.

Cowansage, K.K., T. Shuman, B.C. Dillingham, A. Chang, P. Golshani, and M. Mayford. 2014. Direct Reactivation of a Coherent Neocortical Memory of Context. *Neuron*. 84:432–441. doi:10.1016/j.neuron.2014.09.022.

Dragunow, M., and R. Faull. 1989. The use of c-fos as a metabolic marker in neuronal pathway tracing. *J. Neurosci. Methods*. 29:261–265. doi:10.1016/0165-0270(89)90150-7.

Fleischmann, A., O. Hvalby, V. Jensen, T. Strekalova, C. Zacher, L.E. Layer, A. Kvello, M. Reschke, R. Spanagel, R. Sprengel, E.F. Wagner, and P. Gass. 2003. Impaired long-term memory and NR2A-type NMDA receptor-dependent synaptic plasticity in mice lacking c-fos in the CNS. *J. Neurosci.* 23:9116–9122. doi:10.1523/jneurosci.23-27-09116.2003.

Frankland, P.W., and B. Bontempi. 2005. The organization of recent and remote memories. *Nat. Rev. Neurosci.* 6:119–30. doi:10.1038/nrn1607.

Goshen, I., M. Brodsky, R. Prakash, J. Wallace, V. Gradinaru, C. Ramakrishnan, and K. Deisseroth. 2011. Dynamics of retrieval strategies for remote memories. *Cell*. 147:678–689. doi:10.1016/j.cell.2011.09.033.

Guzowski, J.F. 2002. Insights into immediate-early gene function in hippocampal memory consolidation using antisense oligonucleotide and fluorescent imaging approaches. *Hippocampus*. 12:86–104. doi:10.1002/hipo.10010.

Guzowski, J.F., G.L. Lyford, G.D. Stevenson, F.P. Houston, J.L. McGaugh, P.F. Worley, and C.A. Barnes. 2000. Inhibition of activity-dependent arc protein expression in the rat hippocampus impairs the maintenance of long-term potentiation and the consolidation of long-term memory. *J. Neurosci.* 20:3993–4001. doi:10.1523/jneurosci.20-11-03993.2000.

Guzowski, J.F., B.L. McNaughton, C.A. Barnes, and P.F. Worley. 1999. Environment-specific expression of the immediate-early gene Arc in

hippocampal neuronal ensembles. *Nat. Neurosci.* 2:1120–1124. doi:10.1038/16046.

Kim, J.J., and M.S. Fanselow. 1992. Modality-specific retrograde amnesia of fear. *Science (80-.).* 256:675–677. doi:10.1126/science.1585183.

Lanahan, A., and P. Worley. 1998. Immediate-early genes and synaptic function. *In* Neurobiology of Learning and Memory. Academic Press Inc. 37–43.

Lesburguères, E., O.L. Gobbo, S. Alaux-Cantin, A. Hambucken, P. Trifilieff, and B. Bontempi. 2011. Early tagging of cortical networks is required for the formation of enduring associative memory. *Science (80-.).* 331:924–928. doi:10.1126/science.1196164.

Liu, X., S. Ramirez, P.T. Pang, C.B. Puryear, A. Govindarajan, K. Deisseroth, and S. Tonegawa. 2012. Optogenetic stimulation of a hippocampal engram activates fear memory recall. *Nature*. 484:381–385. doi:10.1038/nature11028.

Mack, K.J., and P.A. Mack. 1992. Induction of transcription factors in somatosensory cortex after tactile stimulation. *Mol. Brain Res.* 12:141–147. doi:10.1016/0169-328X(92)90077-O.

McGaugh, J.L. 2000. Neuroscience - Memory - a century of consolidation. *Science (80-.).* 287:248–251. doi:10.1126/science.287.5451.248.

Meenakshi, P., and J. Balaji. 2017. Neural Circuits of Memory Consolidation and Generalisation. *J. Indian Inst. Sci.* 97:487–495. doi:10.1007/S41745-017-0042-4.

Morgan, J.I., D.R. Cohen, J.L. Hempstead, and T. Curran. 1987. Mapping patterns of c-fos expression in the central nervous system after seizure. *Science (80-.).* 237:192+.

Morgan, J.I., and T. Curran. 1986. Role of ion flux in the control of c-fos expression. *Nature*. 322:552–555. doi:10.1038/322552a0.

Nakai, J., M. Ohkura, and K. Imoto. 2001. A high signal-to-noise Ca 2+ probe composed of a single green fluorescent protein. *Nat. Biotechnol. 2001 192*. 19:137–141. doi:10.1038/84397.

Ramirez, S., X. Liu, P.A. Lin, J. Suh, M. Pignatelli, R.L. Redondo, T.J. Ryan, and S. Tonegawa. 2013. Creating a false memory in the hippocampus. *Science (80-.).* 341:387–391. doi:10.1126/science.1239073.

Reijmers, L.G., B.L. Perkins, N. Matsuo, and M. Mayford. 2007. Localization of a

stable neural correlate of associative memory. *Science*. 317:1230–3. doi:10.1126/science.1143839.

Richards, B.A., F. Xia, A. Santoro, J. Husse, M.A. Woodin, S.A. Josselyn, and P.W. Frankland. 2014. Patterns across multiple memories are identified over time. *Nat. Neurosci.* 17:981–6. doi:10.1038/nn.3736.

Rosenbaum, R.S., G. Winocur, and M. Moscovitch. 2001. New views on old memories: Re-evaluating the role of the hippocampal complex. *Behav. Brain Res.* 127:183–197. doi:10.1016/S0166-4328(01)00363-1.

Schacter, D.L., J.E. Eich, and E. Tulving. 1978. Richard Semon's theory of memory. *J. Verbal Learning Verbal Behav.* 17:721–743. doi:10.1016/S0022-5371(78)90443-7.

Scoviille, W.B., and B. Milner. 1957. LOSS OF RECENT MEMORY AFTER BILATERAL HIPPOCAMPAL LESIONS.

Sheng, M., and M.E. Greenberg. 1990. The regulation and function of c-fos and other immediate early genes in the nervous system. *Neuron*. 4:477–485. doi:10.1016/0896-6273(90)90106-P.

Squire, L.R., N.J. Cohen, and L. Nadel. 1984. The medial temporal region and memory consolidation: a new hypothesis. *In* Memory Consolidation: Psychobiology of Cognition. 185–210.

Squire, L.R., and S.M. Zola. 1996. Structure and function of declarative and nondeclarative memory systems. *Proc. Natl. Acad. Sci. U. S. A.* 93:13515–13522. doi:10.1073/pnas.93.24.13515.

Strekalova, T., B. Zörner, C. Zacher, G. Sadovska, T. Herdegen, and P. Gass. 2003. Memory retrieval after contextual fear conditioning induces c-Fos and JunB expression in CA1 hippocampus. *Genes, Brain Behav.* 2:3–10. doi:10.1034/j.1601-183X.2003.00001.x.

Tsien, J.Z., P.T. Huerta, and S. Tonegawa. 1996. The essential role of hippocampal CA1 NMDA receptor-dependent synaptic plasticity in spatial memory. *Cell*. 87:1327–1338. doi:10.1016/S0092-8674(00)81827-9.

Wang, Z.Q., C. Ovitt, A.E. Grigoriadis, U. Möhle-Steinlein, U. Rüther, and E.F. Wagner. 1992. Bone and haematopoietic defects in mice lacking c-fos. *Nature*. 360:741–745. doi:10.1038/360741a0.

Wiltgen, B.J., M. Zhou, Y. Cai, J. Balaji, M.G. Karlsson, S.N. Parivash, W. Li, and A.J. Silva. 2010. The hippocampus plays a selective role in the retrieval of

detailed contextual memories. *Curr. Biol.* 20:1336–1344. doi:10.1016/j.cub.2010.06.068.

CHAPTER 2

Aim and scope

Investigating the mechanisms operating at the scale of synapses, neuronal ensembles, and neural circuits is an area of intense focus in the field of learning and memory. The development of optical tools to investigate the changes at these cellular and sub-cellular scales enables us to ask finer, nuanced questions and obtain a deeper understanding of the underlying process. As discussed in the introduction, despite the work done to establish and understand systems consolidation, there is more to uncover regarding how and why memories change during this process. For example, are there changes at the ensemble level which result in the generalization of memory? Are the inputs received at the cortex sparse, or does the memory encoding in the cortex become sparse during systems consolidation?

In addressing such questions involving multiple memories, it is vital to identify and follow specific neuronal ensembles that might encode similar memories during systems consolidation longitudinally. One of the key objectives of the current project is developing such a method at the neuronal level.

2.1 Specific Aim 1: Optical tools

The working hypothesis of this aim is that the memory engram of multiple events can be identified using an immediate early gene's expression dynamics.

Here, we propose to follow the kinetics of an IEG expression in vivo to identify distinct neuronal subsets. The rationale is to use the kinetics of expression to estimate when the neuron's activity was induced. In the case of an IEG promoter tagged with a fluorophore, the kinetics can be followed by measuring the fluorescence as a function of time. Observing the fluorescence of individual neurons and describing its expression dynamics analytically, we can distinguish between neurons that took part in events that are separated in time.

Working towards this aim, we first derived the equation to describe the IEG expression kinetics. Next, we validated the model using fluorescence data obtained from cFOS-EGFP and cFOS-shGFP transgenic mice (Chapter 3). Lastly, we utilize the method to look at the contextual representation of dual context exposure in the retrosplenial cortex region of cFOS-shGFP transgenic mice (Chapter 4).

2.2 Specific Aim 2: Behavioural tools

We aim to develop sensitive measures to probe for spatial memory deficits in a navigational task such as the Morris Water Maze.

Here, we propose to utilize vector field properties as a proxy for spatial memory retention. We rationale that divergence and curl maps of a velocity vector field indicate the mouse's search centre and area.

Working towards this aim, we developed measures using velocity vector along an occupancy centre and its vector field properties to define spatial memory in terms of three components that are independent of each other: accuracy, uncertainty, and intensity of search (Chapter 5). We were able to establish and utilise the measures to compare the performance of different strains of mice (Chapter 6). Then we extend this to study spatial memory deficit in Noonan syndrome mice models (Chapter 7).

2.3 Specific Aim 3: Molecular probes

While Specific aim 1 addresses the information stored at a cellular resolution, a different approach is required to investigate the changes in the strength of connections between neurons in a network, i.e., the intra- and inter-connectivity. Intra-connectivity refers to the connections between neurons in an ensemble, whereas inter-connectivity refers to the connections between neurons across different ensembles.

To quantify the connectivity between neurons, we propose to modify the technique of simultaneous optogenetic activation of targeted cells and two-photon calcium

imaging. Simultaneous optogenetic activation and two-photon calcium imaging can be done by co-expressing a Channelrhodopsin (C1V1) and genetically encoded calcium indicators (GCaMP6f) under the CaMKII promoter. Channelrhodopsin allows for activation of the neuron, whereas calcium imaging acts as a readout for connection strength.

Towards this goal, a construct containing C1V1 along with GCaMP6f has been cloned into an AAV vector, as well as packaged into AAV virus (Appendix B).

Additionally, neuronal marker/filler probe, CaMKII-tdTomato was cloned into AAV vector and packed into AVV virus to visualize the complete neuronal structure.

CHAPTER 3

Novel method to identify and segregate different populations of neurons using expression dynamics of an immediate early gene

Abstract

Identifying neurons that are activated in response to memory acquisition and retrieval is vital to understand the molecular and cellular mechanisms of memory processes. Rapid and transient expression of Immediate Early Genes (IEGs) occur in response to persistent neuronal activity and hence IEGs are used as markers of plasticity. We propose to follow the kinetics of IEG expression *in vivo* to identify neuronal subsets, each corresponding to distinct events. First, we derived an analytical description for the expression dynamics of an IEG protein as a function of time. The resultant rate equation describing the concentration of protein as a function of time has an analytical form corresponding to the difference of two exponential terms. In case of a fluorophore expressed under an IEG promoter, the kinetics can be followed by measuring the fluorescence as a function of time. Next, we validated the model using data obtained from two transgenic mouse strains: cfos-eGFP and cfos-shGFP. We showed that cfos-GFP induced in response to seizure as well as behaviour (context retrieval) is well described by the analytical expression. Thus, we show the expression can be generalised to any IEG-fluorophore protein expression kinetics since the fluorescence signal as a function of time is well described by the derived analytical expression, irrespective of the transgenic mice used.

3.1 Introduction

Identifying and manipulating the neuronal ensembles of memory acquisition and retrieval as well as understanding the changes occurring in the circuits over time has been a major focus of memory research(Cajal, 1888; Josselyn et al., 2015; Josselyn & Tonegawa, 2020; Richards & Frankland, 2017). Immediate early genes are rapidly and transiently expressed in response to neuronal activity and hence used as a marker for plasticity. Generally, to identify the temporal coupling of IEG expression to different behaviours or events, it requires as many distinct molecular labels as the number of events that are being followed.

Cellular compartment analysis of temporal activity by fluorescent in situ hybridization (catFISH) (Guzowski, 2002; Guzowski et al., 1999; Guzowski & Worley, 2001) initially exploited the unique transport kinetics of Arc mRNA from the nucleus to the cytoplasm, and later improved to exploit the intronic regions of Arc that have faster kinetics along with other IEGs such as Homer (Wiltgen et al., 2010), to dissect the temporal engagement of neurons. Despite such improvements the method is limited to *in vitro* identification. Another technique uses a combination of IEG promoter-based expression and a modified Tet-OFF system to achieve the labelling of two distinct populations of neurons (Reijmers et al., 2007). In both cases, the visualisation of the signal is done post hoc *in vitro*, limiting the investigation of the neuronal population to a snapshot at any given time. Such methods cannot follow an ensemble of neurons and observe their evolution longitudinally.

Neuronal activity indicators such as genetically encoded calcium or voltage indicators (GECIs or GEVIs) are reporters of neuronal firing in sub-millisecond time scales (Knöpfel, 2012; Lin & Schnitzer, 2016). However, they do not necessarily report the plastic events that occur in response to these firings. Further, they require high-speed imaging with temporal resolution matching the indicators' response time, requiring the imaging be done on awake behaving mice. The slow kinetics of IEG expression enable following cellular plastic events in anesthetised mice after behavioural training(Attardo et al., 2018; Vania Y. Cao et al., 2013; Vania Yu Cao et al., 2015; Wang et al., 2006).

Here, we propose to follow the kinetics of IEG expression *in vivo* to identify distinct

neuronal subsets, each corresponding to distinct events. First, we analytically describe the IEG protein expression dynamics as a function of time. In case of a fluorophore expressed under an IEG promoter, the kinetics can be followed by measuring the fluorescence as a function of time. Among the various IEGs, cfos expression is a widely used marker for cellular activity (Dragunow & Faull, 1989). We validate our model using data obtained from cfos-eGFP (Barth et al., 2004) and cfos-shGFP (Reijmers et al., 2007) transgenic mice under two conditions: bicuculline-induced seizure and behavioural induction of IEG following contextual exposure. Following this, the kinetics of IEG-fluorescence expression is used to determine when the neuron was activated, enabling us to distinguish between neuronal populations that took part in different events that are separated in time. Thus, we hypothesize that the memory engram of multiple events can be identified using the expression dynamics of an immediate early gene and experimentally show that we can do so for two events.

3.2 Theory: Expression dynamics of an immediate early gene

3.2.1 Analytical description of IEG expression dynamics:

In order to model IEG expression kinetics in a neuron, we assumed that a pool of mRNA is present, that is translated to protein in response to behaviourally relevant neuronal activity or signal (Greenberg et al., 1986; Saha et al., 2011). In response to a signal, mRNA (A) is converted to protein (B) with a forward rate constant of protein formation (k_f). One of the marked features of IEG proteins is their auto degradation resulting in transient expression. As the protein forms, ubiquitination degrades the protein. We assumed such a reaction to be first order in protein formation with a degradation rate constant of (k_d). Thus, the IEG expression kinetics can be considered as consecutive first-order reactions (Fig. 3.1 (A)).

$$\mathrm{A} \xrightarrow{\mathrm{k_f}} \mathrm{B} \xrightarrow{\mathrm{k_d}} \mathrm{C}$$

where A is the concentration of the substrate for protein synthesis, B represents the number of protein molecules and C is that of the degraded products.

Given the first order nature of the reaction we proceeded to write the rate equations for A and B as follows,

$$\frac{d[A]}{dt} = -k_f[A]$$

$$\frac{d[B]}{dt} = k_f[A] - k_d[B]$$

We solved the above coupled differential equations to obtain the number of protein molecules ([B]) that is expressed transiently. We proceeded by solving for B in the Laplace space. Thus, using Laplace transform on the equations above we get,

$$\int_0^\infty \frac{dA(t)}{dt} e^{-st}\mathrm{dt} = -k_f\tilde{A}$$

$$\int_0^\infty \frac{dB(t)}{dt} e^{-st}dt = k_f\tilde{A} - k_d\tilde{B}$$

which can be reduced to the below equations,

$$-\mathrm{A}(0) + \mathrm{s}\widetilde{\mathrm{A}}(s) = -k_f \ \ldots\text{(i)}$$

$$-\mathrm{B}(0) + \mathrm{s}\widetilde{\mathrm{B}}(\mathrm{s}) = \mathrm{k_f}\widetilde{\mathrm{A}}(\mathrm{s}) - \mathrm{k_d}\widetilde{\mathrm{B}}(\mathrm{s}) \ \ldots\text{(ii)}$$

where A(0) is the maximum substrate concentration per signalling event. B(0) is the concentration of B at time t = 0, hence B(0)= B_0. Rearranging equation (i), we get the value of A(s)

$$\widetilde{\mathrm{A}}(\mathrm{s}) = \frac{\mathrm{A}(0)}{\mathrm{s} + \mathrm{k_f}}$$

Using this in equation(ii) and rearranging for ~B(s), we get,

$$\tilde{B}(s) = \frac{A(0)\mathrm{k_f}}{(s+k_f)(s+k_d)} + \frac{B(0)}{(s+k_d)} \ \ldots \text{(iii)}$$

At this stage we have several possibilities for B(0), each corresponding to a different and unique physical scenario as discussed in special cases.

Equation (iii) represents the number of IEG molecules in the Laplace space. Using partial fractions and obtaining the inverse Laplace transform, we have,

$$\mathrm{B}(t) = \frac{A_o k_f}{k_f - k_d}\left(e^{-k_d t} - e^{-k_f t}\right) + B(0)e^{-k_d t}$$

A fluorescence signal (F(t)) from a sample is proportional to the number of molecules (B(t)). Using the quantum efficiency (ϕ_f), the absorption cross-section of the fluorophore (ϵ_A) and the collection efficiency (C_f). we can write,

$$F(t) = B(t)\,\phi_f \epsilon_A\, C_f$$

For a given imaging system, the fluorescence signal (F(t)) is directly proportional to the number of molecules present at any given time (B(t)).

Thus, the equation can be rewritten as,

$$\mathrm{F}(t) = \left[\frac{A_o k_f}{k_f - k_d}\left(e^{-k_d t} - e^{-k_f t}\right) + B(0)e^{-k_d t}\right] \qquad \ldots\text{Eq. 3.1}$$

or $\mathrm{F}(t) = \left[\frac{A_o k_f}{k_f - k_d}\left(e^{-k_d t} - e^{-k_f t}\right)\right]$ $for\ B(0) is\ zero$

or $\mathrm{F}(t) = \left[\frac{A_o k_f}{k_f - k_d}\left(\alpha e^{-k_d t} - e^{-k_f t}\right)\right]$ for B(0) is a non-zero constant.

Using a similar approach, we generalised the equation for fluorescence expressed in a neurons in response to 'n' multiple activation events that are 't_d' time units apart, as follows:

$$F_{\mathrm{n}}(t) = \Sigma_{\mathrm{i}=1}^{\mathrm{n}} F_1(t - (\mathrm{i}-1)t_d)\mathcal{H}_{(\mathrm{i}-1)t_d}\begin{cases} 0, & t < t_d \\ 1, & t \geq t_d \end{cases}$$

In case of a double activation event, the equation simplifies to:

$$F_2(t) = F_1(t) + F_1(t - t_d)\mathcal{H}_{t_d}\begin{cases} 0, & t < t_d \\ 1, & t \geq t_d \end{cases} \ldots \text{Eq. 3.2}$$

where t_d is the time of the second activation event or signal.

3.2.2 Special cases:

We consider some special cases where the following physically relevant scenarios present as modifications to Eq. 3.1.

Case i) B(0) is constant :

There is a background, non- zero, steady-state expression of IEG-fluorophore protein fluorescence which is represented by B(0) = constant. We note that this case requires the frequency of the stochastic activity to be such that the protein production and decomposition lead to a quasi-steady state. The corresponding final expression for this case is given by,

$$\mathrm{F}(t) = \left[\frac{A_o k_f}{k_f - k_d}\left(\alpha e^{-k_d t} - e^{-k_f t}\right)\right]$$

where the co-efficient of the exponent representing the decay is modified but overall functional form largely remains unchanged.

Case ii) Stochastic activity:

First, we note that stochastic activity induced expression and decay is not any different from event induced expression when the frequency of activation is sparse. Case (i) represents a scenario where the frequency is high leading to a steady state expression. In these cases, the cell will fit to single or double activation profile with stochastic event response being one of the components.

Case (iii) Decay due to cellular decomposition/photobleaching:

Decomposition or photobleaching related responses do not have a formation component. Our analysis in terms of classifying the cells based on activation profile does not assume the nature of fluorescence decay. This could arise from cellular degradation or photobleaching or any other time dependent process. So, in principle our expression would cover any such decay as long as the defining parameters (such as incident intensity) are kept constant during the experiment. Thus, such a decay would reflect as modified value for k_d but not affect or alter the functional form of the resulting equation. Further, it has been shown that the time scales (Kumar et al., 2016) at which the photobleaching affects the fluorescence intensity (i.e., milliseconds) is longer than the pixel dwell time that we have used for imaging (4μs). Additionally, experimental evidence shows that photobleaching did not affect the fluorescence signal.

Thus, all the cases discussed above do not alter the final expression in terms of the functional form but do modify or alter the meaning of some of the parameters. Thus, a method that does not rely on the value of the kinetic parameters but utilises the functional form to test if the cellular response conforms to it (i.e., the fit) would be able to classify the cells relatively free of confounds.

3.3 Results

3.3.1 Consecutive first-order kinetics describes IEG protein expression following seizure induced by bicuculline administration.

We investigated whether the derived analytical expression (Section 3.2 and Fig. 3.1) describes IEG protein expression *in vivo* in cfos-eGFP transgenic mice. In these mice, eGFP is expressed under the cfos promoter where the level of fluorescence indicates the cfos protein concentration in the nucleus of the neuron. We used these mice to study the expression kinetics of cfos in response to seizures via bicuculline administration(Morgan et al., 1987). Immediately after the seizure, mice were subjected to *in vivo* imaging of the RSc as a function of time (Fig. 3.2 (A)). All throughout this time series image acquisition, we ensured that the imaging setup parameters, namely the incident power (30 mW), pulse width (~100 fs), excitation wavelength (900 nm), and gain of the detection system were kept constant. This resulted in a four-dimensional image stack consisting of three spatial and one temporal dimension. The image stack showed cfos-eGFP fluorescence as circular concentrated regions of higher intensities spread across the field of view. Figure 3.2 (B) shows a time series of cfos-eGFP fluorescence produced in response to seizure in the RSc.

Since we waited for the seizure to complete before anesthetising the mice and shifting it to the head-fixed stage for in vivo imaging, our first imaging time point was at 60 mins. We acquired images every 10 minutes for a total duration of 180 minutes from bicuculline administration. The fluorescence from these individual nuclei were identified as circular ROIs which decay to baseline values as a function of time.

The fluorescence values from these cells were extracted as explained in Methods (Fig. 3.3). For each imaging time point, the identified ROIs were loaded and recentred based on the centre of mass to correct any misalignment among images of different time points. Thus, the coordinates of the measurement ROIs are shifted rather than aligning the entire image (See Materials and Methods, Fig. 3.4). This enabled us to measure the fluorescence intensity using the directly observed raw intensity values without having to align the images using image registration

methods. These fluorescence values were then used to obtain the cellular responses/activity as a time series. These values were then fit to the Eq. 3.1. Fig. 3.2(C) shows the cellular activity profile of four representative cells and their fit to Eq. 3.1 in response to seizures with the fit parameters provided in Table 3.1.

3.3.2 Mice associate a mild footshock to a specific context when trained in contextual fear conditioning.

Transgenic mice were trained and tested along with wildtype littermates (n=6) as mentioned in methods section. Briefly, the animals were trained in context A and made to recall the context 24h later. The freezing measured during the pre-shock period on the training day served as a baseline response. Memory for the training context was assessed through freezing behaviour. We saw an increase in freezing response during retrieval 24 hours after training in context A (Fig. 3.5). Baseline freezing was near zero before training whereas during retrieval the mice showed a mean freezing of 27%.

3.3.3 Consecutive first-order kinetics describes IEG protein expression following a behavioural event.

Next, we investigated whether the derived analytical expression describes IEG protein expression *in vivo* in two strains of cfos-GFP transgenic mice in response to context exposure. Immediately after context exposure, mice were subjected to *in vivo* imaging of the RSc as a function of time (Fig. 3.6(A)). Our imaging time points ranged from 20 to 280 minutes. Typically, these images were ~10 minutes apart during the initial phase and later adjusted to capture the slower decline in fluorescence with minimal number of image acquisitions. We note that long periods of anaesthesia can alter the IEG expression. However, we limited the duration of each anaesthesia administration to 180 mins (except for one mouse where the administration lasted for 280 mins). Further we also note that IEG expression profile induced by constant presence of anaesthesia will have different time profile compared to a profile triggered by distinct behavioural event.

Similar to the images of cfos induced via seizure, the resulting images show cfos-eGFP fluorescence as circular concentrated regions of higher intensities spread across the field of view. Figures 3.6(B) and 3.7(A) show a representative snapshot

of cfos-eGFP and cfos-shGFP fluorescence image of RSc respectively.

The temporal profile is consistent in behaviourally induced cfos expression similar to seizure induced cfos expression. The fluorescence from these individual nuclei identified as circular ROIs increase initially, reaches a peak, and then decays to baseline values (Fig. 3.6(C)). The fluorescence response from few representative cells as a time series is presented in Figures3.6(C) and 3.7(B). The fluorescence values from these cells were extracted as described in the Section 3.3.1. We employed the above procedure in two different sets of mice: cfos-eGFP and cfos-shGFP. In both these cases, we extracted and used the fluorescence to obtain the cellular activity profiles and fit to equation 3.1. Figure 3.6(D) shows the cellular activity profile (open circles) and their fits (solid line) of four representative neurons of cfos-eGFP transgenic mice in response to context exposure. Similarly, Figure 3.7(C) shows the fit of fluorescence obtained from neurons of cfos-shGFP mice. The fit parameters are provided in Tables 3.2, 3.3 respectively.

3.3.4 Consecutive first-order kinetics can be generalized to protein expression kinetics of an IEG-fluorophore construct.

We saw a good agreement of our model with the observed data. Since adjusted R-square (Adj. R Sq) estimates the quality of a fit, we used this in our analysis to estimate the fraction of cells that fit with an Adj. R Sq. > 0.5. We saw that of the 2527 number of ROIs identified as cells from five mice, ~75 % of the cells shows a fit with an Adj. R Sq. greater than 0.5. A good agreement of the experimental data with our model in both these mice lines following seizure as well as the behavioural activation suggests that our method can identify the neuronal ensemble that represents activation, thus enabling us to use this as a criterion for identifying a cell that got activated. Further, the fluorescence signal as a function of time is well described by the analytical expression irrespective of the transgenic mice used. Thus, it supports the hypothesis that the analytical equation can be generalised to the protein expression kinetics of other IEGs (e.g., arc, zif).

3.3.5 Distribution of fit parameters demonstrates that the rise kinetics are identical for cfos-eGFP and cfos-shGFP expression.

The ROIs of successful fits and their fit parameters (describing the rate of

formation(k_f), decay(k_d) and extent of activation (A_0)) were used for data analysis. We obtained the histogram of these rate constants and fit to normal distribution to estimate the mean values of these rate constants as described in Figure 3.8. In case of decay constant k_d we see a bimodal distribution (verified through Akaike's Information Criteria (AIC)(Akaike, 1974)) and we report both the decay constants in Table 4.

From these values, we estimated the rise time and decay of the cfos-eGFP fluorescence following seizure or behaviour induced activation to be $1/k_f = 27 \pm 3$ mins and $1/k_d = 200 \pm 28$ mins (taking the faster component from Table 4), respectively. We used these rise and decay times to arrive at the sampling interval for further experiments. Similarly, cfos-shGFP expression following context exposure yields a rise and decay time of $1/k_f = 27$ mins and $1/k_d = 16$ mins (taking the faster component from Table 4), respectively. The faster component of decay constant is an indicator of how quickly the generated protein degrades. As expected, we see that the rise kinetics are identical for both these constructs considering the fluorophore is expressed under a cfos promoter.

During this process, we observed that some of the cells have an overlapping k_f and k_d values with high interdependency. We believe this is due to a difference in start time (when the cell got activated), resulting in a lower density of data points for a reliable estimate of the k_f, rather than the lack of fit. We included some of these cell responses (Please see footnote of Table 3).

Thus, we found the time to maximal activation estimated from Eq. 3.1 using the mean k_f and k_d values is different for cfos-eGFP (74.5 ± 0.7 mins) and -shGFP mice (41 ± 1 mins); in accordance with the genetic makeup of the mice and the properties of the transgene. In cfos -eGFP, the transgene is the fusion of eGFP and cfos protein, while in the cfos-shGFP just the GFP protein is expressed under cfos promoter. We note that these estimates of time to peak are different than what has been estimated from conventional studies. However, these estimates from conventional studies are not comparable to our estimates as further elaborated in the discussion section. Given a good fit of the cfos activation data, next we asked if we could use such a model to predict expression of cfos that occurs during memory formation, thereby enabling identification of neuronal ensemble that took

part in representation of memory.

3.4 Discussion

In summary, we derived an analytical equation to describe the expression profile of an IEG protein assuming irreversible, consecutive first-order reactions for protein formation and decay. We showed that the analytical expression can be extended to describe the expression profile in response to multiple activations of a neuron, e.g., double activation event. We validated the expression using two IEG-fluorophore transgenic strains of mice, i.e., cfos-eGFP and cfos-shGFP. Specifically, we showed that IEG protein expression profile, in response to seizure or context exposure behaviour, fits well to the analytical expression. In the process, we devised a method to classify neurons based on the number of times it was activated. Thus, we could follow the IEG protein expression dynamics to identify and segregate the activation of neurons into different groups based on the number of times a neuron was activated.

Since our method utilised the temporal profile of IEG expression, as opposed to intensity threshold, for identification, segregation, and classification of neurons, we could increase the specificity with which we identify behaviourally relevant neuronal ensembles, i.e., expression profiles that are temporally linked to behavioural start time.

Interestingly, we found cfos protein's maximum expression takes place around ~74 mins for fos-eGFP transgenic mice, and ~40 mins for fos-shGFP transgenic mice. These differences are consistent with shGFP having a shorter half-life. Previous studies report cfos expression peaks between 90-120 minutes for protein as detected by immunocytochemistry (IHC) analysis (Barth et al., 2004; Morgan et al., 1987). While we measured the cfos fluorescence in these mice and thus report the peak protein expression directly, other methods measure peak time to obtain maximum number of positive cell counts. In such cases, the time to peak represent the time at which maximum number of cells reach above threshold fluorescence. This is not necessarily the time at which cfos expression in each neuron reaches a maximum. Since the IHC is a single point measurement in time, it lacks the ability

to distinguish if the cell is in the rising or falling phase of the expression. Thus, a variation in the onset time, which is hard to control in IHC as the measurements are compared across different mice, can render cells in different phases with same fluorescence. Given the fact that the positive cells are identified using thresholds, the measurement yields an apparent peak for cell counts and the time at which this peak occurs is different from the time to peak expression of the protein itself. On the other hand, our method directly measures the rise and decay of the cfos expression from single cells through fluorescence for individual mice. Being a single cell measurement arising from the same mouse reduces, if not eliminates, the contribution of onset time variation. Thus, we argue that *in vivo* fluorescence signal is more sensitive and a direct measure of cfos-eGFP protein concentration level in a neuron in real time, compared to immunocytochemistry, leading to the discrepancy in reported time range of maximal cfos protein expression. Thus the other methods measure the time to get maximal cell fraction (Barth et al., 2004; Guzowski, 2002; Wen et al., 2013) rather than the maximal expression of protein in the cell.

Having established the method and such an estimate of time to peak or maximal expression of IEG, we next study the activation of RSc ensembles following dual context exposures, as described in Chapter 4.

3.5 Materials and Methods

3.5.1 Transgenic mice:

cfos-eGFP (B6.Cg-Tg(Fos/EGFP)1-3Brth/J Stock no: 014135) and fos-shGFP (B6.Cg-Tg(Fos-tTA,Fos-EGFP*)1Mmay/J Stock no: 018306) transgenic mice were obtained from Jackson Laboratory, USA and maintained at the Central Animal Facility, IISc. All protocols were approved by the Institute Animal Ethics Committee.

3.5.2 Craniotomy

Transgenic mice underwent a craniotomy to enable *in vivo* imaging (Trachtenberg et al., 2002). A sterile 6mm cover glass was positioned over the skull between the bregma and lambda, centred at retrosplenial cortex (RSc). The coordinates of the imaging area (RSc: 2mm from Bregma, 0.5mm laterally) were arrived at by visualising the blood vasculature. The mice were anesthetised using a solution of fentanyl (0.05 mg/kg), midazolam (5 mg/kg), and medetomidin (0.5 mg/kg) (FMM) dissolved in saline.

3.5.3 Artificially and behaviourally induced IEG expression:

Artificial IEG induction was produced by injecting mouse with 2mg/kg bicuculline intraperitonially to induce a seizure. Mild seizure symptoms were observed. On completion of the seizure, mouse was anesthetised with FMM to proceed to *in vivo* imaging.

For IEG induction in response to behaviour, mice were trained to associate a mild foot-shock (0.7mA, 2s) in context A (70% ethanol, spaced grill floor) on training day (Day 1, 2 minutes 30 seconds). To assess fear memory recall, these mice were placed in context A without shock for 2 mins 30 seconds after 24-48 h to measure their freezing level.

3.5.4 Imaging setup:

In vivo imaging was performed on a custom-built two-photon setup based on a Zeiss upright microscope (Axio Examiner Z1) equipped with a 25× water immersion objective (NA 1.05, WD 2 mm, Olympus XLPLN25XWMP2). Femtosecond pulses

from an ultrafast Ti:Sapphire laser (Newport, Tsunami) whose intensity was modulated using a half-wave plate (Thorlabs, AHWP05M) and a polarizer (Thorlabs, GL10-B) was used as as the excitation light source. The excitation beam was raster scanned using galvo scanning mirrors (Thorlabs, GVSM002) before entering the microscope body and was focussed on the imaging plane using the objective lens. The fluorescence that was collected by the objective lens in an epi-illumination geometry was then separated using a dichroic before being detected by photomultiplier module (H7422, Hamamatsu Corporation, Japan).A low noise current preamplifier (Stanford Research Systems, SR570) was used to amplify the photomultiplier tube photocurrent, which was further digitized using a data acquisition board (National Instruments, PCI-6110). ScanImage (r 3.8.1) software was used to interface instrument control and generation of galvometric scan command. Image acquisition was accomplished using a custom Matlab script interfaced with z-drive of the microscope. The digitized signal was analysed using Matlab, Origin and ImageJ for further analysis.

3.5.5 Estimation of fluorescence from neurons expressing cfos-GFP:

The *in vivo* images were analysed manually using a modified version of Time Series Analyzer plugin (Time Series Analyzer Plugin, Balaji 2014, https://imagej.nih.gov/ij/plugins/time-series.html) in Image J to quantify the fluorescence signal. The modified version of the plugin is publicly available as Java Repository in GitHub (GitHub link: https://github.com/TheNeurodynamicsLab/ImageJ_NDLPlugins). Fig. 3.3(A) describes the steps to extract the fluorescence signal from each neuron to obtain the fluorescence value of a neuron at a given time point. Briefly, for each individual neuron, the peak intensity at given time point was quantified by manually selecting the nucleus as the region of interest (ROI). The mean pixel intensity of the ROI through each z-stack was obtained and fit to a Gaussian function to estimate the activity of the ROI at a particular time point (Fig. 3.3(B)). We identified 2527 neuronal ROIs from 5 mice (3 cfos-shGFP, 2 cfos-eGFP).

3.5.6 Classification of SAC or DAC through curve fitting:

Curve fitting analysis of fluorescence as a function of time for each ROI was done

in Origin(v2020b) 's user-defined NLFit function using Levenberg-Marquardt algorithm.

The parameters were set as follows for data fitting to Eq. 3.1:

Parameter A was initialised to the maximum fluorescence of the ROI observed in the imaging session, while rate constants k_f and k_d were initialised to 0.01 and 0.001, respectively, at the start of the Levenberg-Marquardt algorithm for least squares minimisation.

For data fitting to equation 3.2, the additional parameter t_d was initialised with a value of 60 mins.

Post data fitting to Eq. 3.1 and 3.2, the preferred model (SAC or DAC) was selected based on Akaike Information Criterion (AIC). In brief, AIC measures the information loss incurred in choosing a fit model given the observed data and degrees of freedom. Thus, it considers the difference in number of parameters used in a fit as well as the goodness of the fit. A model with low AIC explains the observed data with minimal loss of information without over fitting, and hence is preferred. The goodness of fit was determined by an Adj. R Sq value and it was set to be greater than 0.5 to identify the selected ROI as an activated cell of the preferred model.

3.6 Figures

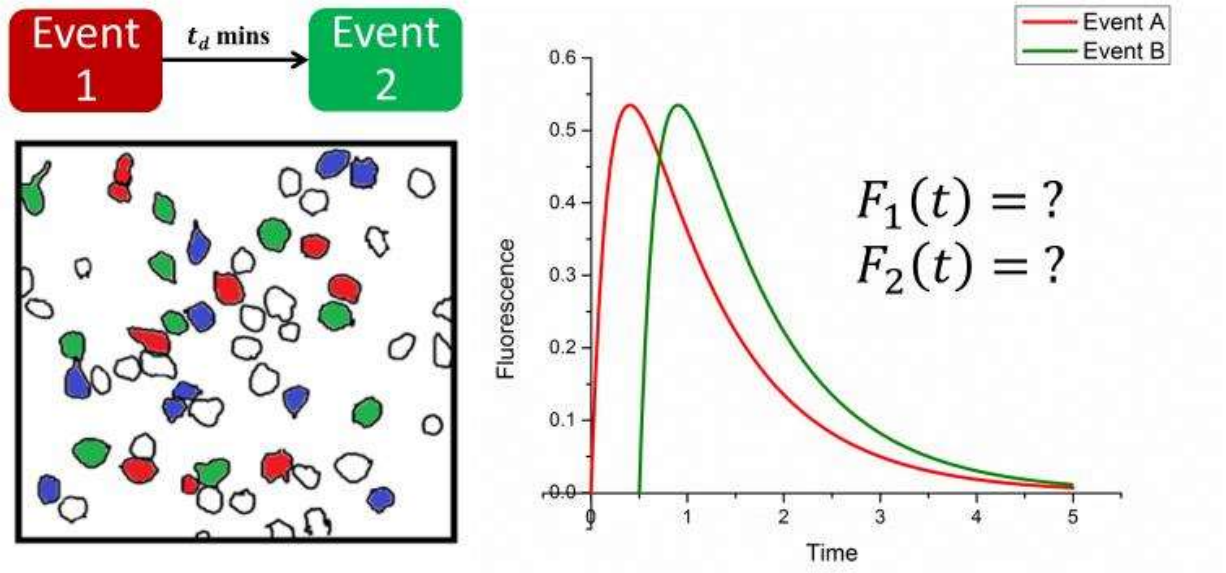

Figure 3.0: Graphical abstract

A

$$A \xrightarrow{k_f} B \xrightarrow{k_d} C$$

mRNA Protein Degraded Protein

B

$$F_1(t) = \frac{A_o k_f}{k_f - k_d}\left(exp(-k_d t) - exp(-k_f t)\right)$$

... Eq. (1)

C

$$F_2(t) = F_1(t) + F_1(t - t_d)\mathcal{H}_{t_d}\begin{cases} \&0, & t < t_d \\ \&1, & t \geq t_d \end{cases}$$

... Eq. (2)

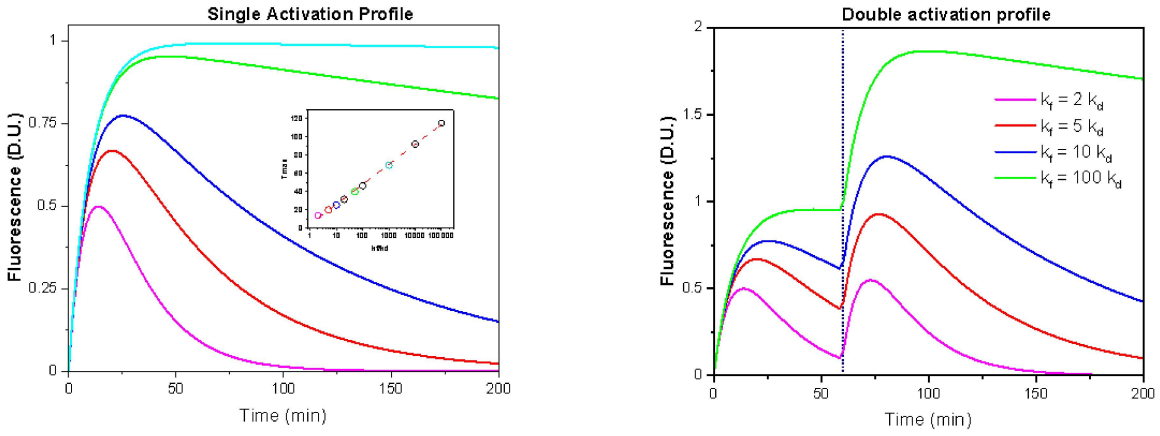

Figure 3.1: Analytical description of an IEG expression in response to plasticity related events.

(A) A simple consecutive reaction kinetics for the mRNA (A), protein (B) and degraded protein (C) describes the response to a plasticity signal. The reaction is

assumed to proceed with first order forward reaction rate constants k_f and k_d for the synthesis and degradation of proteins, respectively.

(B) Solving the coupled differential equations of the sequential chemical reaction described in (a), we get an expression (Eq. 1) for $F_1(t)$ that describes the fluorescence intensity corresponding to IEG coupled fluorophore at any given time 't' as a difference of two exponential terms with rate constants, k_f and k_d. The lines are the simulated response functions for five values of k_f/k_d ratios with parameter A and k_f set to 1D.U and 0.1min^{-1}. Time to maximal response, one of the key parameters necessary to time the neuronal tagging is plotted for these set of ratios as a scatter plot in the inset. The colour of the open circles corresponds to their respective solid lines. The red dashed line is a straight line fit of these scatter plot.

(C) Similarly, we describe Eq. 2 for a neuron that got activated twice where A, k_f, k_d are as previously described and t_d is the time of second activation event. Eq. 2 is simulated (solid lines) to show the response for four ratios of k_f/k_d with parameter A set to 1D.U., and the time gap between the two events (t_d) is set to 60 min as indicated by the black dotted line.

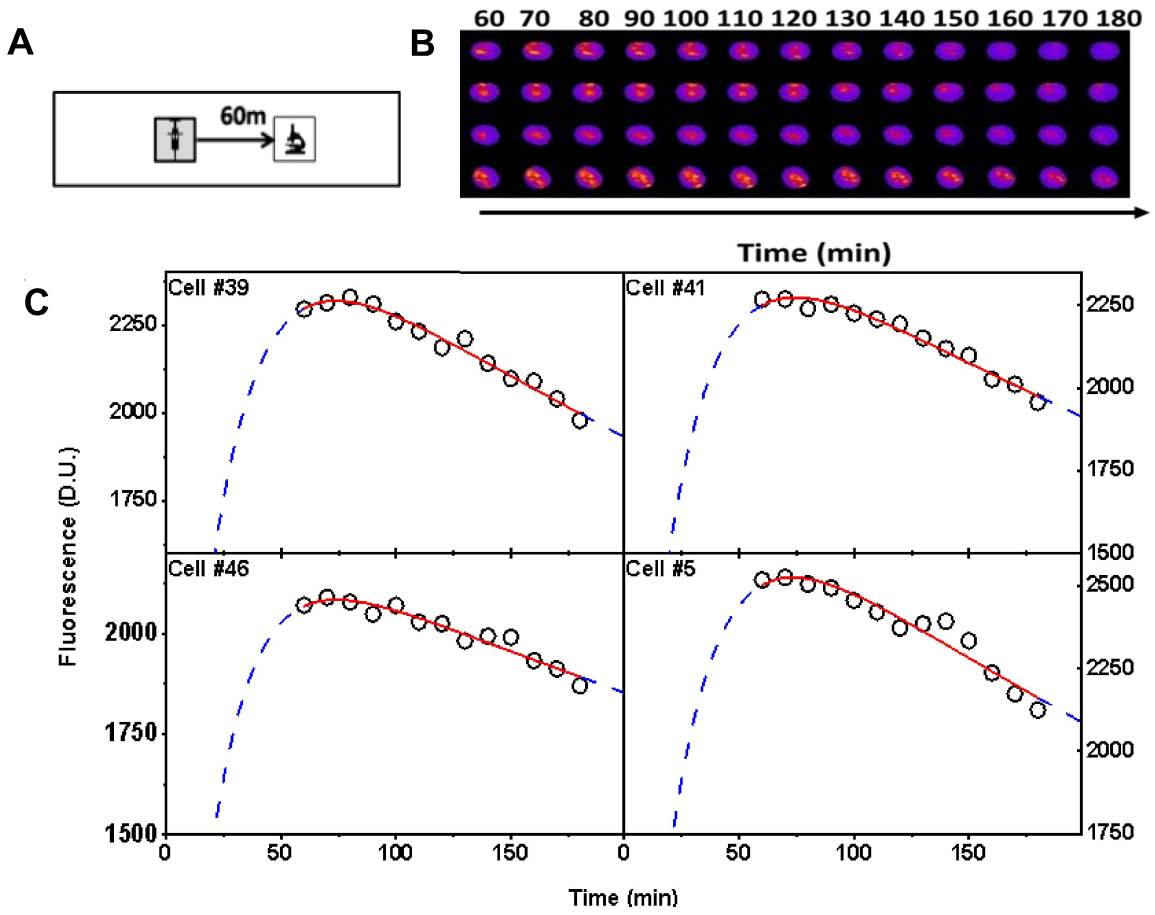

Figure 3.2: Seizure induced expression of IEG coupled fluorescence is described by first order consecutive kinetics:

(A) Schematic of IEG induction to bicuculline administration and following its dynamics in an anesthetised transgenic mouse through in-vivo imaging of the retrosplenial cortex (RSc).

(B) Select regions of interest centred around cells #39, #41, #46 and #5, are arranged as time series show the change in fluorescence across the entire cell nuclei.

(C) Quantitative measure of cellular response extracted from the time series images through custom built software for four representative cells are shown as open circles. The open circles are obtained using the workflow (SFig. 1) and represent the activity of a neuron at a given time. The red line is the fit of this activity to Eq. 1. Blue dotted line extends the solid red line to the activity of the cell outside of the imaging time frame as predicted by our model. See table 3 for fit parameter details.

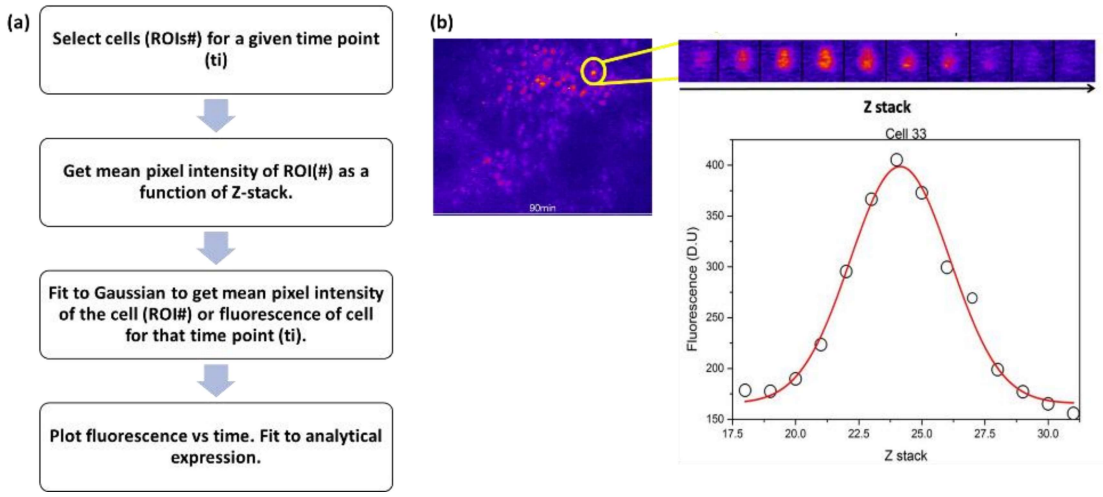

Figure 3.3: Workflow for data extraction from raw images.

(A) Workflow describing the steps for data extraction.

(B) Left: Snapshot of field of view at 90 mins. Yellow circle and inset top represent one neuron.

Top inset: Optical sections of the neuron at different Z positions in a stack.

Bottom: Gaussian fit to obtain mean pixel intensity or fluorescence of a neuron at a given time point. The open circles represent the mean pixel intensity of the neuron at a slice/Z position. The red line represents the Gaussian fitting of mean pixel intensity as a function of Z position.

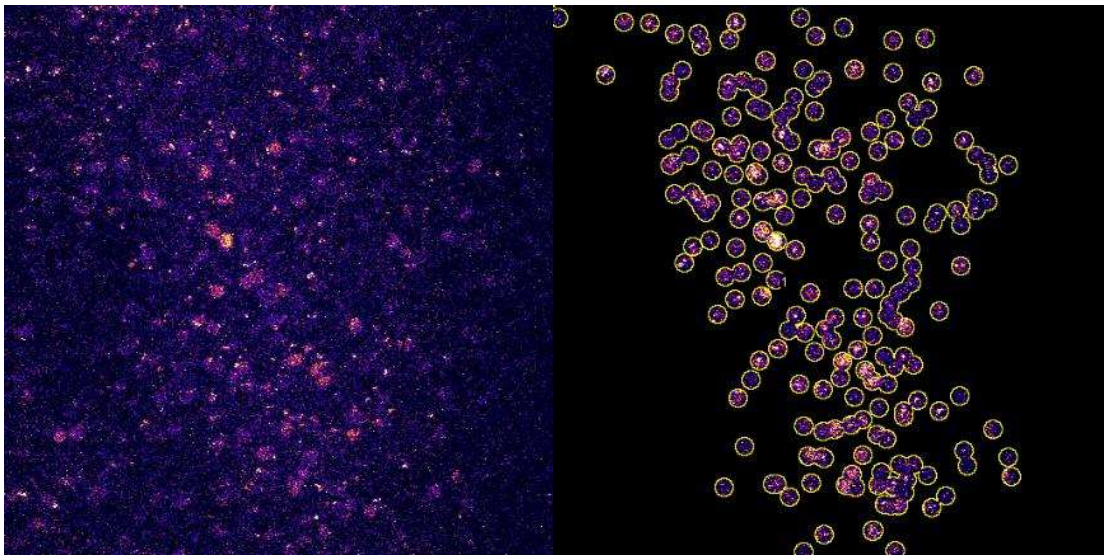

Figure 3.4: An optical section of neurons expressing cfos. Left image is an optical section of cfos-shGFP at 90 mins. Right image shows the ROIs that are identified, centred and their background cleared.

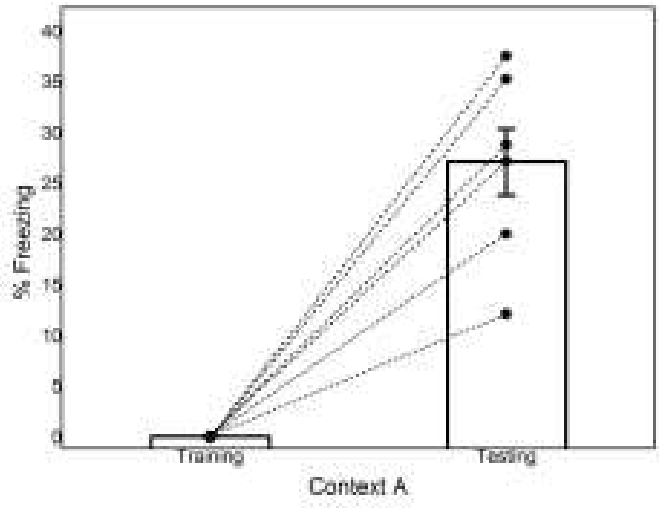

Figure 3.5: Freezing level of mice (n=6) on training in CtxtA and retrieval in CtxtA after 24 hours.

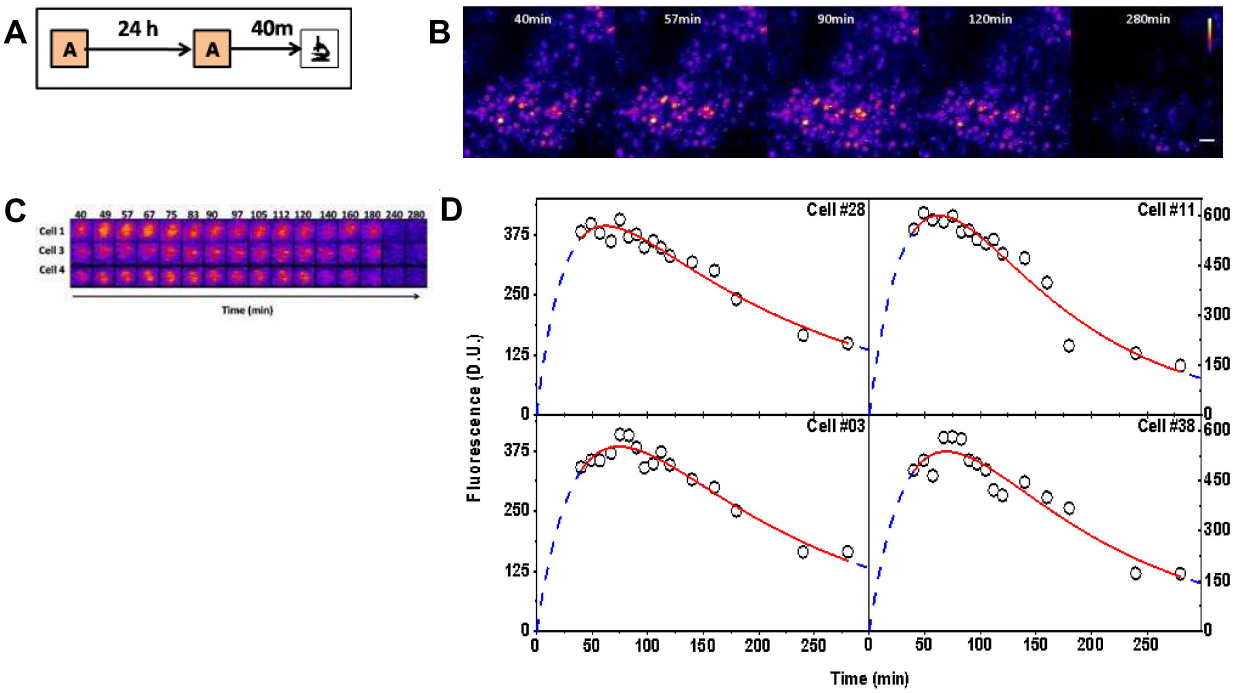

Figure 3.6: Quantification of behaviourally induced cfos-egfp protein expression fits well to derived equation.

(A) Behavioral schematic used for inducing cfos expression. Transgenic mice are trained in context A then made to recall the training context (Context A) after 24 hours. The resulting activation of IEGs is followed, through in-vivo imaging of the RSc in anesthetised mice.

(B) Maximum intensity projection of a stack of images corresponding to 200 x 200 x 200 μm region obtained at different time points. The cfos-EGFP signal is localised to the nucleus and hence the activated neurons appear as quasi circular regions of bright pixels with a diameter of ~20-pixel
units. Snapshots RSc area shown are that of time points 40, 57, 90,120 and 280 mins. The scale bar in the image is 20 microns.
(C) 3 representative image ROIs centred around cell “#01”, “#03”,” and #04” in cfos-EGFP transgenic mice across different time points are shown as image matrix.
(D) The quantitative measure of fluorescence and hence the cellular expression profile of four representative cells in (B) along with their fits to Eq. 1 are shown here. The open circles represent the amplitude of the cellular activity from a neuron at a given time. The red line is the fit of this data to Eq. 1. A good agreement of the fit to the observed data (Adj. R Sq > 0.92) indicates that our model is consistent with the observed cellular response. Blue dotted line extends the fits and spans the entire x-axis. See Table 4 for fit parameters.

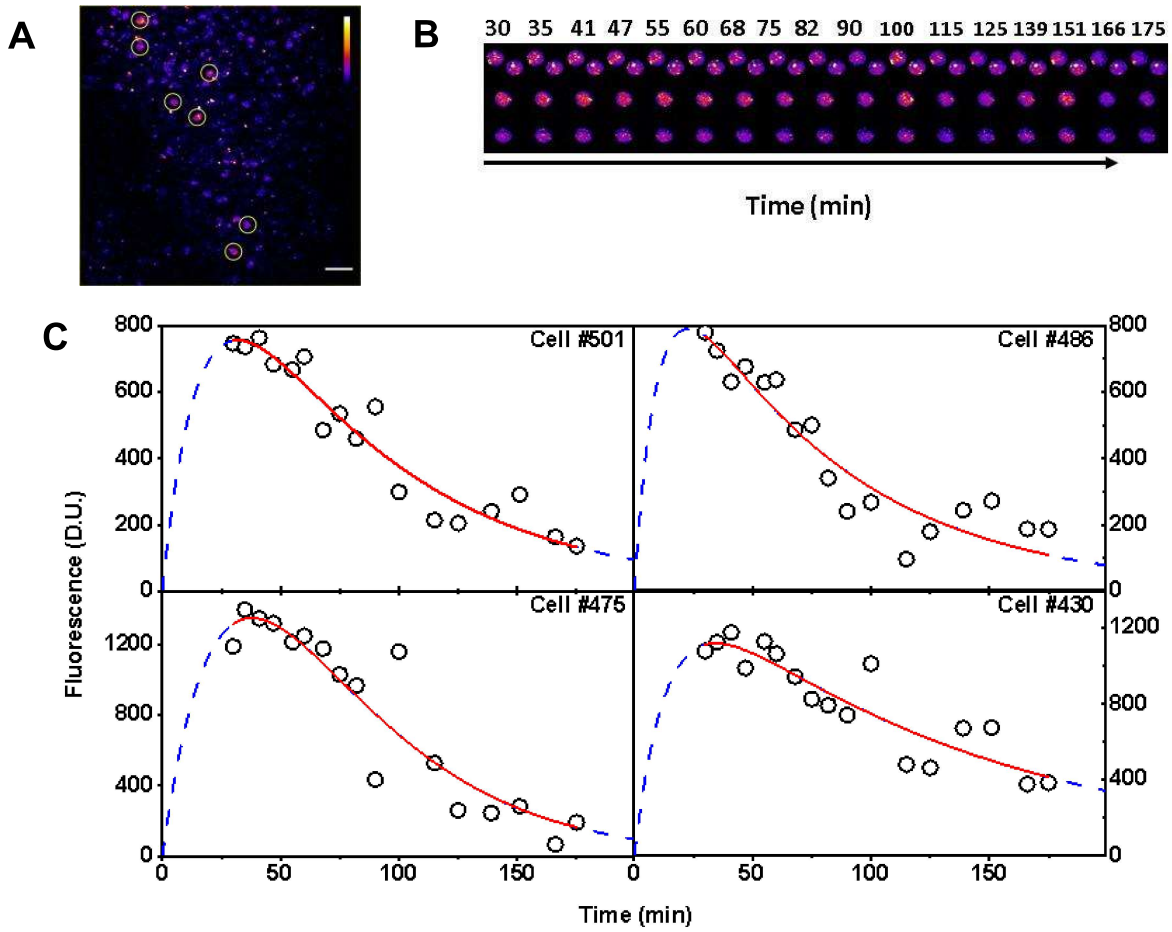

Figure 3.7: Quantification of behaviourally induced cfos-shgfp fluorescence describing the protein expression profile fits well to derived equation (Eq. 1). indicating that the analytical equation generalises to different fluorophore constructs.

(A) Images from the RSc region of the cfos-shgfp transgenic mice reveal the circular bright nuclei at 90 mins. The image is one of the 200 x 200 microns optical section. The scale bar represents 20 microns.

(B) 4 representative image ROIs centred around cells “#501”, “#486”, ”#475” and “#430” in cfos-shgfp transgenic mice across different time points respectively.

(C) are the corresponding quantitative measure of cellular expression profile of cells in (b) along with their fits to Eq. 1. The open circles represent the amplitude of the cellular activity from a neuron at a given time. The red line is the fit of this data to Eq. 1. A good agreement of the fit to the observed data (Adj. R Sq > 0.79) indicates that our model is consistent with the observed cellular response. Blue dotted line extends the fits and spans the entire x-axis as explained in Fig. 2. See

Table 5 for fit parameters.

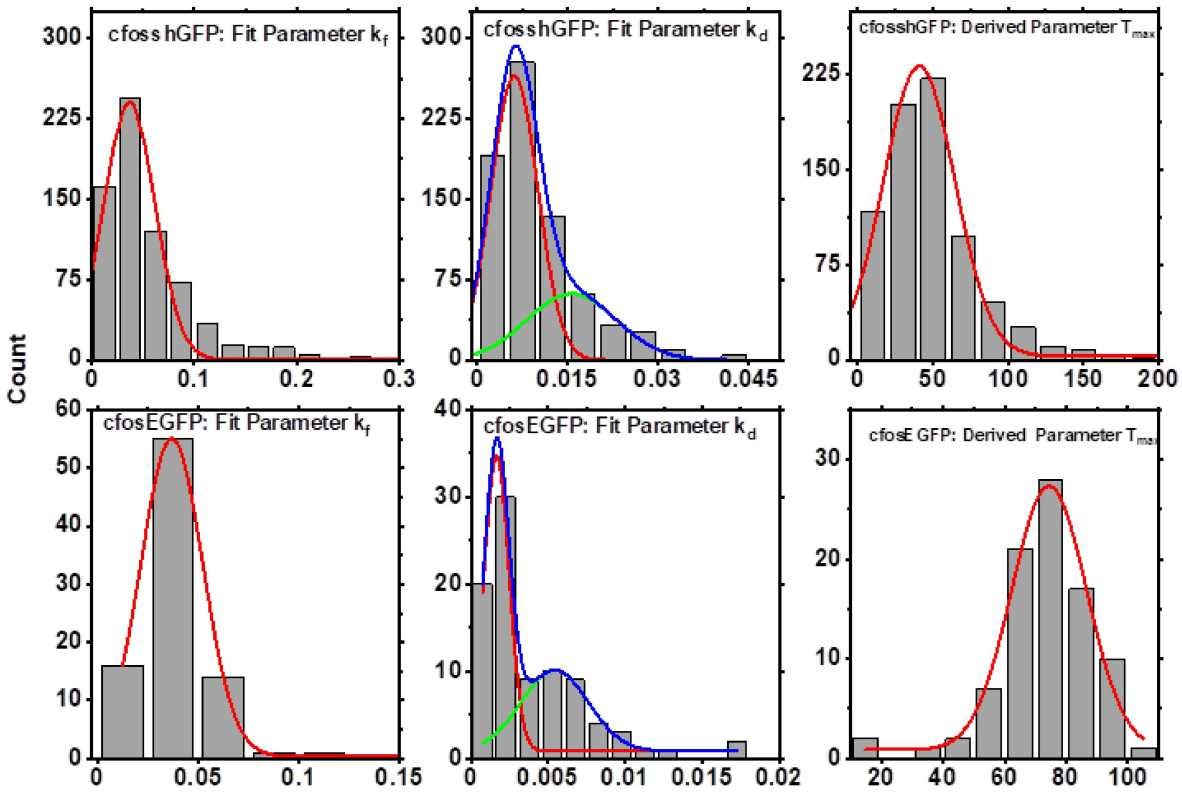

Figure 3.8: Frequency histogram of fit parameters: k_f, and k_d along with the derived parameter T_{max}.

(A) Histograms of the formation rate constant k_f fits (solid red line) to Gaussian distribution with a mean of 0.0369 min ^{1}.

(B) Top row shows parameter distribution plots for cfos-shGFP transgenic mice (n = ~700 cells). Bins with counts >10 were considered for fit. We see a bimodal distribution of k_d values in cfos-shGFP mice indicating populations of neurons with different decay kinetics. Bottom row shows the corresponding plots for cfos-EGFP transgenic mice (n = ~90 cells).

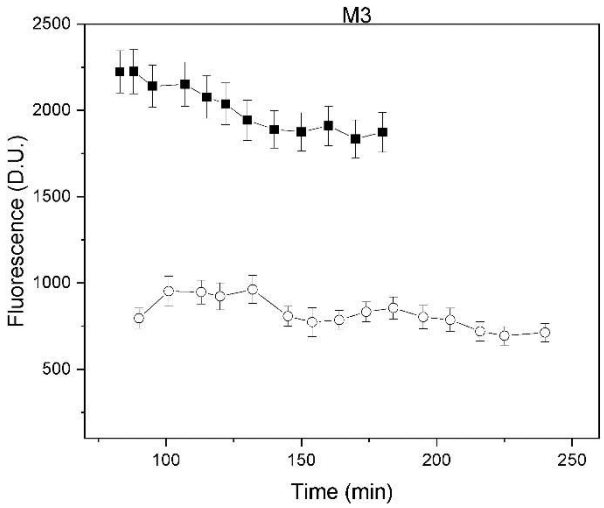

Figure 3.9: Fraction of IS1 SAC ROIs fit to equation 1 using fluorescence from imaging time points comparable to IS2 imaging time points (i.e. 80 min onwards from first context exposure) show that ~50% of data fit based on our criteria. The graph shows the average responses during IS2 of "non-fit" ROIs from one mouse represented as open circles as function of time. Black solid squares are the corresponding values for IS1. The change in fluorescence over ~15 imaging sessions over 160 mins show a moderate decrease of about 20 – 30 % as compared to cellular profiles that show an order of magnitude increase from the baseline (~0 for fit cells).

3.7 Tables

Fig No.	Cell No.	Amplitude (D.U.)	Error in Amplitude	k_f (min^{-1})	Error in k_f	K_d (min^{-1})	Error in k_d	Adj-R-sq	AIC
Fig 3.5	Cell #39	2640	39.68309	0.04605	0.00367	0.00176	1.41E-04	0.97354	85.43579
Fig 3.5	Cell #41	2576	37.18148	0.04616	0.00355	0.00168	1.34E-04	0.97265	83.87009
Fig 3.5	Cell #46	2262	32.49374	0.05358	0.00587	0.0011	1.30E-04	0.93118	84.81639
Fig 3.5	Cell # 05	2888	76.33026	0.04576	0.00633	0.00183	2.49E-04	0.92799	102.19985

Table 3.1: Summary of fit parameters of cfos-egfp expression in response to seizure data fit to equation 1.

Fig No.	Cell No.	Amplitude (D.U.)	Error in Amplitude	k_f (min^{-1})	Error in k_f	K_d (min^{-1})	Error in k_d	Adj-R-sq	AIC
Fig 3.6	Cell #28	541	26.39433	0.03675	0.00495	0.00514	5.31E-04	0.95524	97.85696
Fig 3.6	Cell #11	1050	148.97179	0.02585	0.00614	0.00895	0.00182	0.94341	123.23644
Fig 3.6	Cell #03	596	50.12666	0.02569	0.00406	0.00592	8.67E-04	0.93926	101.22503
Fig 3.6	Cell #38	461	27.40859	0.03473	0.0054	0.00487	6.20E-04	0.93042	98.06544

Table 3.2: Summary of fit parameters of cfos-egfp expression in response to single context exposure data fit to equation 1.

Fig No.	Cell No.	Amplitude (D.U.)	Error in Amplitude	k_f (min^{-1})	Error in k_f	K_d (min^{-1})	Error in k_d	Adj-R-sq	AIC
Fig 3.7	Cell #501	1183	148.68142	0.0593	0.02149	0.01404	0.00272	0.91592	150.73661
Fig 3.7	Cell #486	1089	104.53632	0.10002	0.07986	0.014	0.00265	0.86964	157.76146
Fig 3.7	Cell #475*	3663	416.218	0.02647	-	0.02647	0.0036	0.87058	184.62851
Fig 3.7	Cell #430	1471	157.13412	0.07198	0.03514	0.0079	0.00176	0.79118	172.29792

*The kf and kd values for these cells were shared.

Table 3.3: Summary of fit parameters of cfos-shgfp expression in response to single context exposure data fit to equation 1.

Transgenic mouse	Tmax (min)	k_f (min^{-1})	k_d (min^{-1})	
cfos-shGFP	41 ± 1	0.0369 ± 4 E-4	0.0062 ±1E-4	0.016 ± 0.002
cfos-EGFP	74.5 ± 0.75	0.0369 ± 2E-4	0.002±1E-4	0.005±7E-4

Table 3.4: Summary of the Tmax, kf and kd values from Gauss fit (in S2) to the respective distributions (Adj-R-Sq > 0.95).

3.8 References

Akaike, H. (1974). A New Look at the Statistical Model Identification. *IEEE Transactions on Automatic Control*, *19*(6), 716–723. https://doi.org/10.1109/TAC.1974.1100705

Attardo, A., Lu, J., Kawashima, T., Okuno, H., Fitzgerald, J. E., Bito, H., & Schnitzer, M. J. (2018). Long-Term Consolidation of Ensemble Neural Plasticity Patterns in Hippocampal Area CA1. *Cell Reports*, *25*(3), 640-650.e2. https://doi.org/10.1016/j.celrep.2018.09.064

Barth, A. L., Gerkin, R. C., & Dean, K. L. (2004). Alteration of neuronal firing properties after in vivo experience in a FosGFP transgenic mouse. *Journal of Neuroscience*, *24*(29), 6466–6475. https://doi.org/10.1523/JNEUROSCI.4737-03.2004

Cajal, S. R. y. (1888). Estructura de los centros nerviosos de las aves. *Revista Trimestral de Histología Normal y Patológica*, *1*(1), 1–10.

Cao, Vania Y., Ye, Y., Mastwal, S. S., Lovinger, D. M., Costa, R. M., & Wang, K. H. (2013). In vivo two-photon imaging of experience-dependent molecular changes in cortical neurons. *Journal of Visualized Experiments : JoVE*, *71*. https://doi.org/10.3791/50148

Cao, Vania Yu, Ye, Y., Mastwal, S., Ren, M., Coon, M., Liu, Q., Costa, R. M., & Wang, K. H. (2015). Motor Learning Consolidates Arc-Expressing Neuronal Ensembles in Secondary Motor Cortex. *Neuron*, *86*(6), 1385–1392. https://doi.org/10.1016/j.neuron.2015.05.022

Dragunow, M., & Faull, R. (1989). The use of c-fos as a metabolic marker in neuronal pathway tracing. *Journal of Neuroscience Methods*, *29*(3), 261–265. https://doi.org/10.1016/0165-0270(89)90150-7

Greenberg, M. E., Hermanowski, A. L., & Ziff, E. B. (1986). Effect of protein synthesis inhibitors on growth factor activation of c-fos, c-myc, and actin gene transcription. *Molecular and Cellular Biology*, *6*(4), 1050–1057.

https://doi.org/10.1128/mcb.6.4.1050

Guzowski, J. F. (2002). Insights into immediate-early gene function in hippocampal memory consolidation using antisense oligonucleotide and fluorescent imaging approaches. *Hippocampus*, *12*(1), 86–104. https://doi.org/10.1002/hipo.10010

Guzowski, J. F., McNaughton, B. L., Barnes, C. A., & Worley, P. F. (1999). Environment-specific expression of the immediate-early gene Arc in hippocampal neuronal ensembles. *Nature Neuroscience*, *2*(12), 1120–1124. https://doi.org/10.1038/16046

Guzowski, J. F., & Worley, P. F. (2001). Cellular Compartment Analysis of Temporal Activity by Fluorescence In Situ Hybridization (catFISH). *Current Protocols in Neuroscience*, *15*(1), 1.8.1-1.8.16. https://doi.org/10.1002/0471142301.ns0108s15

Josselyn, S. A., Köhler, S., & Frankland, P. W. (2015). Finding the engram. In *Nature Reviews Neuroscience* (Vol. 16, Issue 9, pp. 521–534). Nature Publishing Group. https://doi.org/10.1038/nrn4000

Josselyn, S. A., & Tonegawa, S. (2020). Memory engrams: Recalling the past and imagining the future. In *Science* (Vol. 367, Issue 6473). American Association for the Advancement of Science. https://doi.org/10.1126/science.aaw4325

Knöpfel, T. (2012). Genetically encoded optical indicators for the analysis of neuronal circuits. *Nature Reviews Neuroscience*, *13*(10), 687–700. https://doi.org/10.1038/nrn3293

Kumar, S., Singh, A., Singh, V. R., George, J. B., & Balaji, J. (2016). Saturation Dynamics Measures Absolute Cross Section and Generates Contrast within a Neuron. *Biophysical Journal*. https://doi.org/10.1016/j.bpj.2016.06.044

Lin, M. Z., & Schnitzer, M. J. (2016). Genetically encoded indicators of neuronal activity. In *Nature Neuroscience* (Vol. 19, Issue 9, pp. 1142–1153). Nature Publishing Group. https://doi.org/10.1038/nn.4359

Morgan, J. I., Cohen, D. R., Hempstead, J. L., & Curran, T. (1987). Mapping patterns of c-fos expression in the central nervous system after seizure. *Science*, *237*, 192+.

Reijmers, L. G., Perkins, B. L., Matsuo, N., & Mayford, M. (2007). Localization of a stable neural correlate of associative memory. *Science (New York, N.Y.)*, *317*(5842), 1230–1233. https://doi.org/10.1126/science.1143839

Richards, B. A., & Frankland, P. W. (2017). The Persistence and Transience of Memory. In *Neuron* (Vol. 94, Issue 6, pp. 1071–1084). Cell Press. https://doi.org/10.1016/j.neuron.2017.04.037

Saha, R. N., Wissink, E. M., Bailey, E. R., Zhao, M., Fargo, D. C., Hwang, J. Y., Daigle, K. R., Fenn, J. D., Adelman, K., & Dudek, S. M. (2011). Rapid activity-induced transcription of Arc and other IEGs relies on poised RNA polymerase II. *Nature Neuroscience*, *14*(7), 848–856. https://doi.org/10.1038/nn.2839

Trachtenberg, J. T., Chen, B. E., Knott, G. W., Feng, G., Sanes, J. R., Welker, E., & Svoboda, K. (2002). Long-term in vivo imaging of experience-dependent synaptic plasticity in adult cortex. *Nature*, *420*(6917), 788–794. https://doi.org/10.1038/nature01273

Wang, K. H., Majewska, A., Schummers, J., Farley, B., Hu, C., Sur, M., & Tonegawa, S. (2006). In Vivo Two-Photon Imaging Reveals a Role of Arc in Enhancing Orientation Specificity in Visual Cortex. *Cell*, *126*(2), 389–402. https://doi.org/10.1016/j.cell.2006.06.038

Wen, J. A., Deblois, M. C., & Barth, A. L. (2013). *Initiation , Labile , and Stabilization Phases of Experience-Dependent Plasticity at Neocortical Synapses*. *33*(19), 8483–8493. https://doi.org/10.1523/JNEUROSCI.3575-12.2013

Wiltgen, B. J., Zhou, M., Cai, Y., Balaji, J., Karlsson, M. G., Parivash, S. N., Li, W., & Silva, A. J. (2010). The hippocampus plays a selective role in the retrieval of detailed contextual memories. *Current Biology*, *20*(15).

https://doi.org/10.1016/j.cub.2010.06.068

CHAPTER 4

Memory representation of dual contexts in Retrosplenial cortex

Abstract

The retrosplenial cortex (RSc) has been shown to play an active role during the context-based behaviour though the nature of this role is still emerging. Since RSc might maintain contextual information in the form of independent representations and its interrelations, we sought to probe the cellular representations of different contexts in RSc. We have previously established an IEG based method (Chapter 3) for segregating the neurons based on their temporal response to a behavioural event, thereby improving the ability to detect neurons possibly undergoing plasticity. We used this method to distinguish between neuronal populations that took part in different events that are separated in time. Specifically, we investigated the cellular representations of two contexts that were retrieved close in time (60 minutes). We imaged the RSc of cfos-shGFP transgenic mice to follow the dynamics of cellular changes resulting from contextual fear conditioning behaviour, enabling us to establish a representation of the contexts at the cellular scale following memory acquisition. Our results indicate that cellular representation in RSc of contexts retrieved close in time are unique and independent, i.e., retrieval of two distinct memories close in time does not merge the neuronal ensembles of RSc when the memories are acquired 24 hours apart. Thus, we show evidence for our hypothesis that the memory engram of multiple events can be identified using the expression dynamics of an immediate early gene as well as study the independent representation of contexts retrieved close in time.

4.1 Introduction

Recent and emerging evidences suggest retrosplenial cortex (RSc) plays a vital role in encoding context-related information(Auger & Maguire, 2018; Auger et al., 2012, 2015; Miller et al., 2014; Mitchell et al., 2018). Clustered addition of spines is observed in RSc when contextual training is carried out across multiple sessions (Frank et al., 2018). Similarly, the inactivation of RSc prevents contextual retrieval in mice, both contextual fear conditioning and water maze post-training (Czajkowski et al., 2014; Opalka & Wang, 2020). Preferential activation of RSc during spatial navigation has also been reported (Cowansage et al., 2014). Interestingly, it is also shown that in schema-dependent encoding of related events, RSc is engaged only during the encoding of new learning related to prior information but not during encoding of completely novel information(Tse et al., 2011). More importantly, RSc lesion in rats abolishes their ability to resolve context-based conflicts (Nelson et al., 2014). Thus, all these studies suggest RSc plays an active role during the context-based behaviour, although the nature of this role is unclear. Given its function, we reasoned that RSc might maintain contextual information in the form of independent representations and its interrelations. If such contextual interrelations have cellular representations in RSc, we would be able to locate them using our method. This is possible as the method described in the previous chapter can identify, and longitudinally follow the activated cellular ensembles *in vivo*. Thus, in this study we simultaneously probe representation for a context, how it changes across time, and when a new context is introduced close in time.

4.2 Results

4.2.1 Identification and segregation of neuronal ensemble following dual context exposure.

In our efforts to identify and segregate the neurons that get activated in response to multiple events, we imaged the neuronal ensembles that emerge in response to contextual fear conditioning. We used the following behavioural paradigm to train and image the contextual representation in cfos-shGFP transgenic mice (Fig. 4.1). The mice were trained to associate a foot shock in context A (CtxtA) followed by safety training in context B (CtxtB) the next day. Imaging sessions were carried out following retrieval tests that were carried out 24 hours after safety training in context B.

In order to image the same region of brain and hence the cellular ensembles across the imaging sessions spanning days, we captured and utilised the vasculature of the brain as shown in figure 4.2 (top). This allowed us to image the same region within ~0.5 mm (our field of view). Next, we utilised the system of co-ordinates (and co-ordinate transform as required) to further refine our positioning within the field of view. We found that these measures were sufficient to provide a localisation accuracy to locate not just the cell body but the same spines (Fig. 4.2 bottom). We note that the positioning accuracy required for our purpose is at the cellular scale.

Our behavioural scheme consists of three context exposure sessions spread across two days. The mice were trained in CtxtA (shock context) and CtxtB (safe context). When tested for the fear memory they showed significant freezing compared to baseline (Fig. 4.3). Imaging was performed in two sessions during the retrieval days with first imaging session after exposure to CtxtA. 24 hours later, we imaged the mice following exposures to CtxtA followed by CtxtB. The exposures to contexts were 60 minutes apart. Thus, there are two imaging sessions: one following exposure to CtxtA (IS1) on the first day of retrieval, and another following exposure to CtxtB on the second day of retrieval (IS2). As described in the schematic (Fig. 4.1) the second day retrieval consists of exposures to two contexts, CtxtA and CtxtB, separated by 60 mins. In IS1, the imaging session ranged from

20-180 minutes whereas in IS2 the imaging points ranged from 90-300 minutes, at intervals of ~10 minutes, from the first context exposure. Since there were ~2500 ROIs to be processed, analysed, and classified, we developed a software-based workflow as described in Materials and Methods (Fig. 3.2).

In both these imaging sessions, we saw two kinds of cellular responses: (I) cells that were activated once (single activation cells, SAC) and (II) twice (double activation cells, DAC) in response to context exposure. Figures 4.4 and 4.5 show representative cfos expression of SAC and DAC fit to Eq. 3.1 and 3.2, respectively. The quality of the fit was assessed through the residuals displayed at the bottom panel of each response. Tables 4.1 and 4.2 summarises the fit parameters. Due to their difference in initial slope and curvature around the peak of DAC compared to SAC, DAC fit the double activation cell profile corresponding to Eq. 3.2 better as determined by our criteria (AIC and Adj. R Sq>=0.5). Figure 4.6 illustrates this behaviour using an example cell response. The cell responses from second imaging sessions were fit twice, once with a delay of 60 mins corresponding to time measurement starting from CtxtB exposure ("delayed IS2") and other with zero delay corresponding to time measurement starting from CtxtA exposure. The investigated ROIs had to fit either Eq. 3.1 or 3.2 on at least one of the imaging sessions (IS1 or IS2) for us to consider it as a neuron. We found that 71 + 6% of the investigated ROIs show a fluorescence response that fit at least in one of the imaging sessions.

Figure 4.7(A) shows the snapshot of the cellular activity at the RSc of cfos-shGFP transgenic mice. The green cells are the activated cells on imaging session 1 and the magenta are the activated cells on imaging session 2. The third panel overlays the cells that were activated on IS1 (green) and IS2 (magenta) to show the overlapping cells as white nuclei. Apart from these cells, the snapshot shows cells that were activated in IS1 or IS2 only. These images represent the fraction of overlapped cells across two context exposures and this fraction is not known so far in RSc. We estimate this number to be ~30% (Fig. 4.7 (B) white bar) and it is similar to what is observed in the other regions of the brain (Repa et al., 2001; Vazdarjanova & Guzowski, 2004).

4.2.2 Retrosplenial cortex ensembles in response to dual context exposure.

Next, we addressed whether there is a differential representation of a context when a new context is introduced. In the behavioural scheme (Fig. 4.1) used to train and image the contextual representation in cfos-shGFP transgenic mice, the mice were subjected to context exposure three times. We were interested in observing the neurons activated in response to these exposures or experiences. A neuron can get activated in response to any one or two or all these experiences. Hence, we used our method to segregate the activated neurons into different categories as described below.

Based on the temporal profile of expression, we interpreted the SAC that were identified following an exposure to a given context as representing that context or experience only, whereas the DAC as representing two events, e.g., representing two context exposures or context exposure followed by a spontaneous event or a spontaneous event followed by a context exposure. Next, we compared these groups with our behavioural scheme to reason and assign these different classes to the corresponding memory representations, e.g., since IS1 follows retrieval event in CtxtA and SAC IS1 responses are consistent with Eq 3.1 representing single events, we assign them to context A cellular ensemble. Similarly, these SAC and DAC were assigned to one of the eight categories as listed in Table 4.3. The Venn diagram in figure 4.8 represents the various categories of cells representing a context and their expected session wise fit result(s). We describe below the categories and their rationale.

Category 1) is the subset of cells that are activated in response to all three experiences, i.e., these cells show a profile that is consistent with SAC IS1 (CtxtA) and DAC IS2 (CtxtB).

Three categories describe the subsets of cells activated to a single experience only, namely categories 3) ,4), 5). These cells have expression profiles corresponding to one of the following: SAC in IS1 (CtxtA), SAC IS2 (CtxtA), SAC IS2 with 60 mins delay (CtxtB) respectively.

Three other categories (Categories 2, 6 and 7) represent the subset of cells that are reactivated. Category 2): These are cells that consistently respond only to context A i.e., SAC in IS1 (CtxtA) and SAC in IS2 (CtxtA). Category 6) are cells

activated in IS1 and fit a SAC or DAC profile and then reactivated in IS2 with a profile that can be classified to DAC or a SAC with 60 min delay. We interpret these cells as common between Ctxt A IS1 and Ctxt B. Similarly, category 7) are cells activated in response to CtxtA IS2 and CtxtB, i.e. DAC in IS2.

Finally, category 8) are the ROIs/cells that are not activated in response to any of the experiences as both IS1 and IS2 responses did not fit, i.e., the ROIs did not fit as a SAC or DAC.

Following this classification system, we estimated the fraction of neurons activated in response to single context exposure (CtxtA) during the first retrieval event as 44 ± 3% (Fig. 4.9, orange bar) and the fraction of cells that were activated in CtxtB, i.e., category 6, as ~42 ± 9% (Fig. 4.9, green bar). This allowed us to ask if the ensembles representing A and B are unique. We tested the uniqueness of these ensembles by estimating the fraction of the cells that were common between these two ensembles. We reasoned that an above chance overlap would indicate that the same population is getting activated in both the contexts, while an at chance overlap would indicate that the neurons recruited during the corresponding context retrieval are different and independent. We found the overlap fraction to be at chance (Fig. 4.9, yellow bar, 19±4%) suggesting that the population representation of these contexts is indeed unique and independent.

Next, we proceeded to investigate if it is possible to link two distinct memory representations by retrieving these memories close in time. It is interesting to note that if the memory formation were to happen within a time window, then their likelihood of overlapped neuronal representation in the hippocampus is high (Denise J. Cai et al., 2016; Silva et al., 2009). We asked if such overlap can be seen in RSc following temporally close context retrieval as opposed to acquisition. We estimated the chance of a neuron getting activated in CtxtA in IS1 (first exposure of context A) and chance of it getting activated in CtxtB (Fig. 4.9, pink bar, 42 ± 8%). We then compared it with the chance of a neuron getting activated in CtxtA in IS2 and CtxtB simultaneously (Fig. 4.9, brown bar, 55 ± 18%). Since CtxtA during IS2 and CtxtB occur closer in time (60-minute fraction) than CtxtA in IS1 (24-hour fraction), if such temporal linkage were to occur, we would see the 60-minute fraction being greater than 24-hour fraction. However, we found both

were comparable despite a trend of 60 min fraction being higher than the 24 h fraction (Fig. 4.9). Additionally, we found these ratios were comparable to that of reactivation probability estimated as fraction of neurons from IS2 CtxtA that got activated during CtxtA on IS2.

Next, we proceeded to test if our method can identify DAC even in this scenario. We estimated the fraction of DAC in CtxtA during IS2 population and compared it with DAC identified during IS1 or delayed IS2. Our comparison reveals that the fraction of DAC in CtxtA during IS2 is indeed significantly higher than DAC in IS1 or delayed IS2 (Fig. 4.10). We saw DAC of CtxtA followed by CtxtB (58.3 $\pm$16.3%) to be significantly different (t test: $p < 0.002$, one tailed) than DAC of either CtxtA or CtxtB (~13 $\pm$ 2%), thus, establishing the fact that following a protein expression kinetics allows one to segregate cells even when the mouse is exposed to two contexts close in time.

Since cfos is an IEG immediately downstream of CREB, we asked could the levels of cfos be predictive of reactivation probability during repeated retrieval. We estimated the reactivation probability by binning the neurons according to their amplitudes and estimating the fraction of fit neurons in each of these bins. The ratio between the number of fit or activated neurons to the total number of neurons represents the fraction of reactivated neurons in each intensity bin. We defined this ratio as the probability of reactivation in that bin. Figure 4.11 (A) shows this reactivation probability as a function of amplitude of cfos signal. We see a weak, but a significant correlation ($R > 0.6$) exists between the amplitude and the reactivation probability. In order to rule out the possibility that the difference in amplitude could bias the R.Sq of the cellular response fit and hence the reactivation probability, we also plotted the Adj. R.Sq of the fits as a function of amplitude in Figure 4.11 (B). We see that Adj. R Sq is invariant with respect to the amplitude of the cfos signal as indicated by a near zero slope of 3E-6 ± 4E-6.

4.3 Discussion

In summary, we followed the IEG protein expression dynamics to identify and segregate the activation of neurons into different groups as per the behavioural events. Conventionally, three probes are required to mark three retrieval events. However, our method requires one IEG-fluorophore to mark three retrieval events. Since our method utilises the temporal profile of IEG expression, as opposed to intensity threshold, for identification, segregation, and classification of neurons, we are able to increase the specificity with which we identify behaviourally relevant neuronal ensembles.

We found the level of cellular activation in RSc elicited by retrieval of CtxtA and CtxtB is nearly same and is similar to what has been found in other regions of the brain with dense encoding (Vazdarjanova & Guzowski, 2004). We saw responses of ~ 20% (data not shown) of neurons still show cellular response profile that enables them to be classified as active in CtxtA even though the exposure has occurred 90 mins prior to first imaging data point of imaging session 2. In order to arrive at an upper bound for fraction of cells that we could have missed we took the IS1 SAC data from 90 mins onwards and asked what fraction of those cells would still qualify as SAC (Fig. 4.12). We estimated that even after 90 mins we were able to fit ~50% of cells. Interestingly, many of the neurons activated in CtxtB show expression dynamics consistent with dual activation profile. We interpret this as a neuronal response to CtxtA as well as CtxtB exposure. Though the activated cellular fraction at RSc has not been reported before, our estimate is comparable to the ensemble size typically obtained in other regions through conventional studies (Guzowski & Worley, 2001).

Further we assigned the SAC from CtxtB exposure and DAC from CtxtA exposure of IS2 to CtxtB cellular representation. We note this fraction ~45% for CtxtB is similar to that of CtxtA cellular fraction. Thus, consistent with our hypothesis, these two contextual representations can be identified and assigned to different cell populations using cellular activation profiles.

One of the defining events of IS2 is the arrival of the CtxtB exposure after CtxtA. It is known that contextual exposure could be temporally linked through cellular

activation(D J Cai et al., 2016; Silva et al., 2009). This being the case, we expect a larger fraction of activated cells following CtxtA exposure in IS2 should be DACs. Thus, we compared the fraction of DAC seen in response to CtxtB following CtxtA exposure with that of DAC seen in response to a single context CtxtA or CtxtB. Such a piece of information is difficult to obtain through conventional molecular probing methods since the comparisons are made at a population level instead of a single cell.

One of confounding factors in conventional method is the difficulty in assigning the cell response to behavioural event. For example, DAC in response to single context exposure, either in CtxtA or CtxtB, would be falsely identified as representing two contexts in conventional methods. More importantly, majority of the ROIs that did not fit either single or double activation, would have been classified as representing one of the contexts when in fact they do not represent IEG activation intended through behavioural exposure. While it is possible the lack of fit could represent a different model of activation profile, we see a vast fraction of the non-fit ROIs to be invariant with respect to time. Since their fluorescence is measured to be above the baseline, these cells might add noise in the conventional estimates of cell fractions.

Further, we could identify the activated ensembles following different contextual memory retrieval in RSc as early as 24 hours. Taking advantage of these, we probed if distinct memories once formed could be linked through closely spaced retrieval events. As expected, we found that mere retrieval of two distinct memories close in time is not sufficient to link the RSc ensembles representing these memories if the memories themselves are acquired 24 hours apart.

4.4 Materials and Methods

4.4.1 Transgenic mice

fos-shGFP (B6.Cg-Tg(Fos-tTA,Fos-EGFP*)1Mmay/J Stock no: 018306) transgenic mice were obtained from Jackson Laboratory, USA and maintained at the Central Animal Facility, IISc. All protocols were approved by the Institute Animal Ethics Committee.

4.4.2 Craniotomy

Transgenic mice underwent a craniotomy to enable *in vivo* imaging as mentioned in section 3.5.2.

4.4.3 Dual exposure behaviour paradigm

Mice were trained to associate a mild foot-shock (0.7mA, 2s) in context A (70% ethanol, spaced grill floor) on training day (Day1, 2 minutes 30 seconds). The next day, these mice were placed in context B (20% ethyl acetate, smooth floor, triangle chamber feature) without shock for 2 mins 30 seconds (safety context training). After 24 hours (Day 3), mice were placed again in context A to test for memory recall. On Day 4, mice were placed in context A followed by context B separated by a time period of 60 minutes to test their ability to discriminate similar contexts at a recent time (24/48 hours). We used four cfos-shGFP mice for this experiment followed by imaging. Of the four one of the mice did not learn (no freezing in any of the retrievals).

4.4.4 Imaging setup:

In vivo imaging was performed as described in section 3.5.4.

4.4.5 Classification of SAC or DAC through curve fitting

Data analysis of fluorescence extraction and fit was carried out as previously described in section 3.5.5 and 3.5.6.

Additionally, for classifying cell responses to dual context exposure, fluorescence measured from selected ROIs as a function of time was fit to SAC or DAC profile

with t = 0 or t = 60 (IS2 delayed). Preferred model was chosen based on AIC score, and goodness of fit was assessed using Adj. R-sq.

4.5 Figures

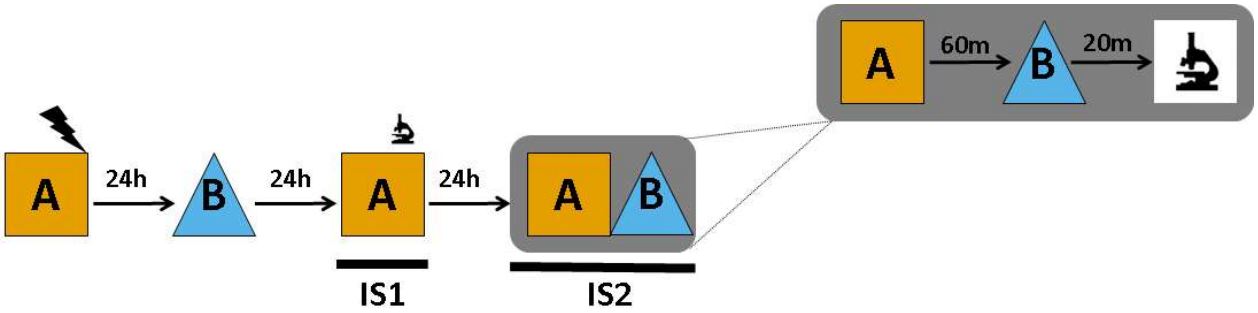

Figure 4.1: Outline the behavioural paradigm and imaging scheme. Mice were trained to associate a mild footshock in ctxt A (orange) on day 1 and trained for safety in ctxt B (blue) on day 2. On day 3, memory recall for ctxt A was tested followed by in vivo imaging of RSc (IS1). On day 4, mice underwent dual exposure contextual recall, i.e., mice were tested for memory for ctxt A followed by memory for ctxt B after 60 mins (grey box). Post ctxt B recall, RSc was imaged (IS2).

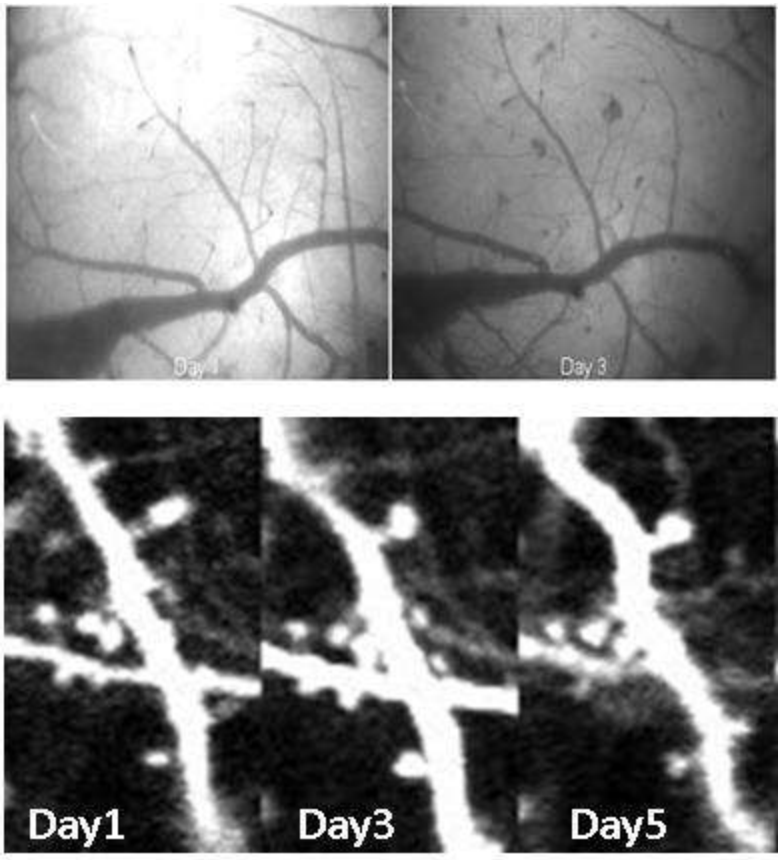

Figure 4.2: Longitudinal in vivo imaging of the same area across multiple days is achieved by using the unique blood vasculature of craniotomized mice. The representative images show the precision with which dendrites and their spines can be imaged across multiple days (1–5 days) in Thy1-YFP transgenic mice. The same method was followed for longitudinal in vivo imaging of cfos transgenic mice.

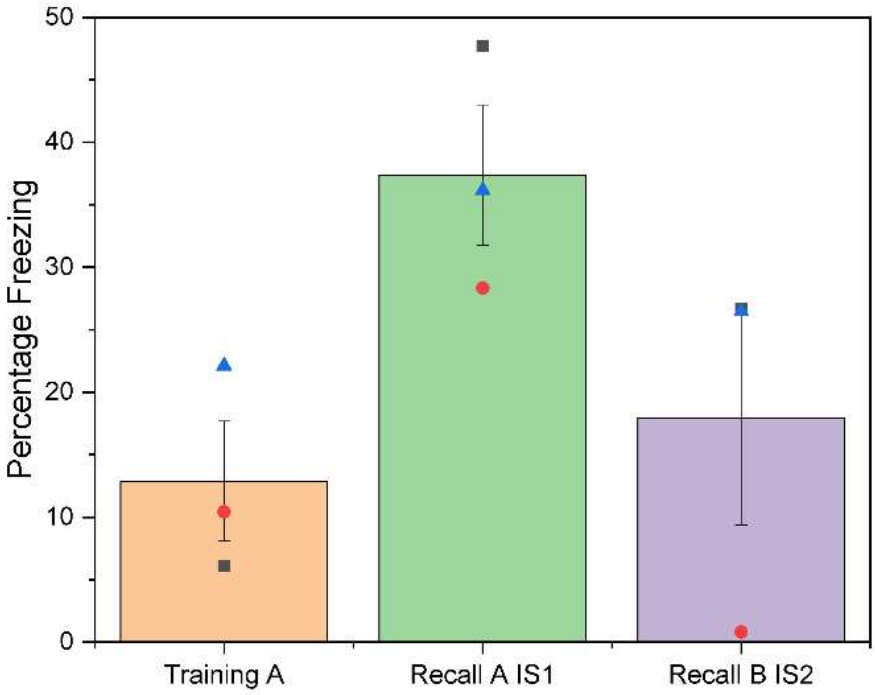

Figure 4.3: Freezing percentage of the mice used in dual exposure contextual recall paradigm. M1: Red circle, M2: Black square, M3: Blue triangle.

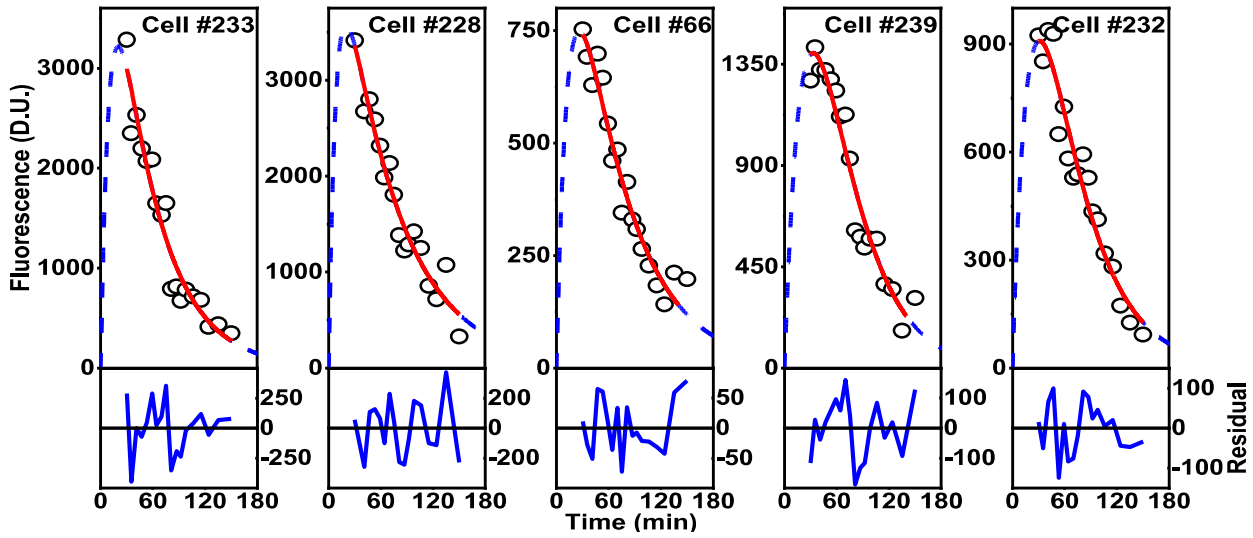

Figure 4.4: Representative plots of expression profile of single activation neurons.

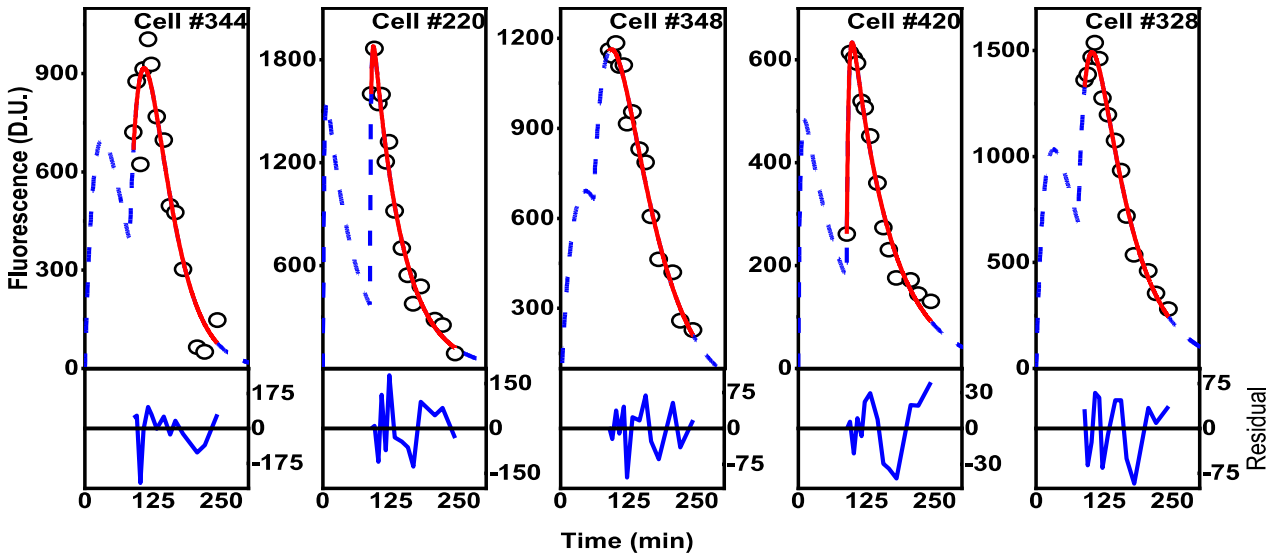

Figure 4.5: Representative plots of expression profile of double activation neurons. The response of the neurons(DAC) fit (red line) is explained better by DAC profile Eq. 3.2 rather than SAC profile Eq. 3.1. The dashed blue line shows the fit spanning the entire laboratory time frame of t = 0 min where the mouse was exposed to the first context A, followed by t = 60 min where the mouse was exposed to context B.

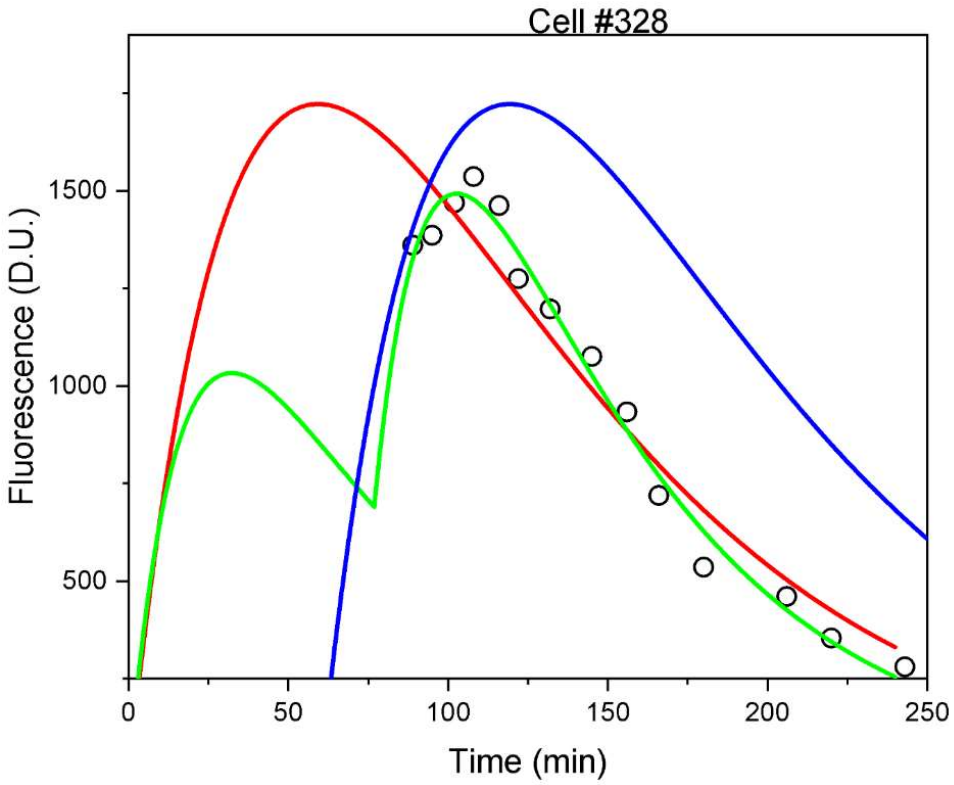

Figure 4.6: Comparison of a DAC fit to Eq 1 with (t = 60min, solid green line) and without (t = 0 min, solid red line) delay along fit to Eq 2(solid blue line).

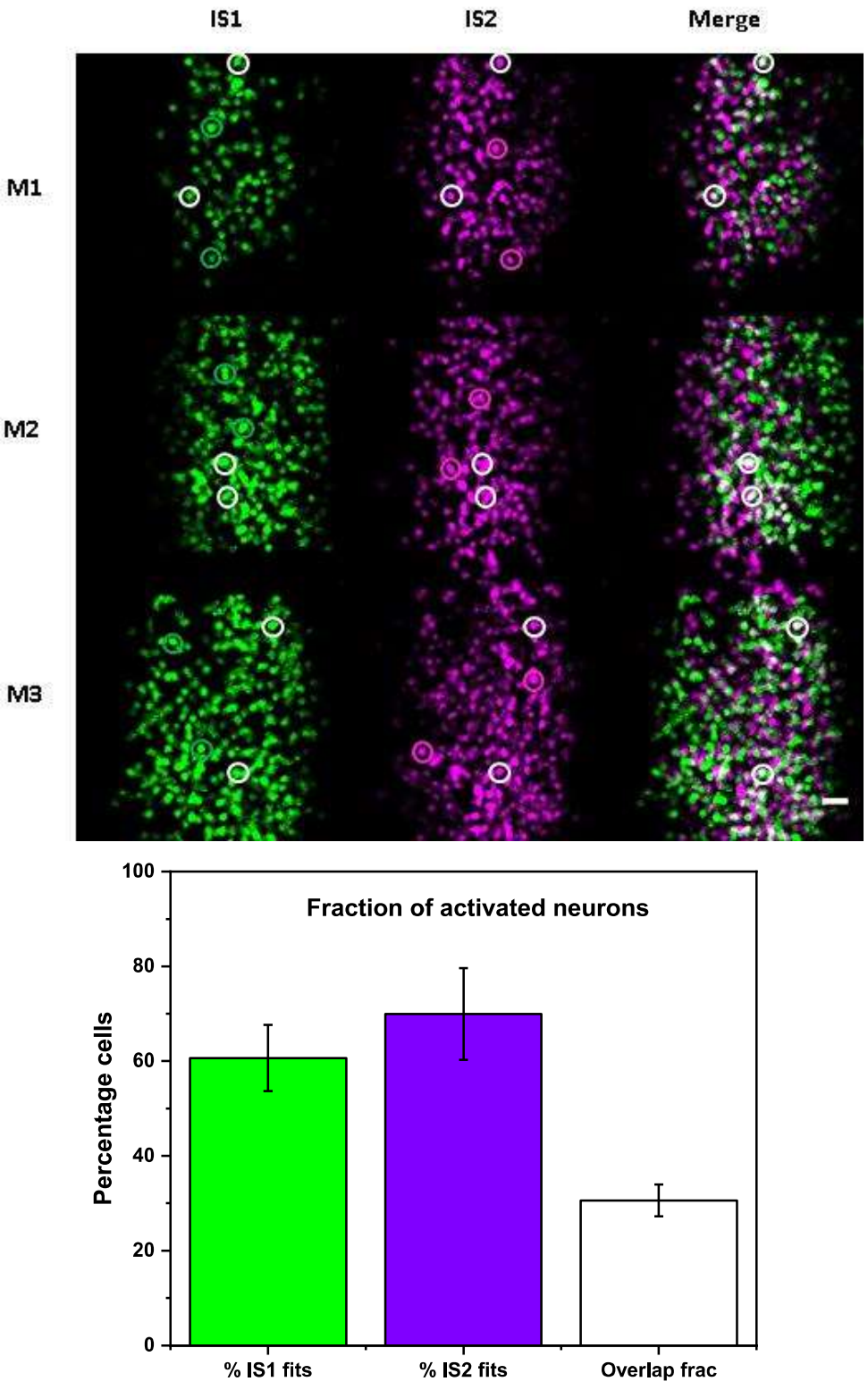

Figure 4.7: Representative snapshot of cfos neuronal ensembles.

(A) Representative snapshot of cfos neuronal ensembles at ~ 90 min on imaging sessions IS1 (green) and IS2 (magenta) with overlapping ensembles shown in white. We constructed these images from snapshots of the RSc at ~ 90 min after

the first context exposure of the imaging session. (B) Fraction of activated neurons on days IS1, IS2 and their overlap.

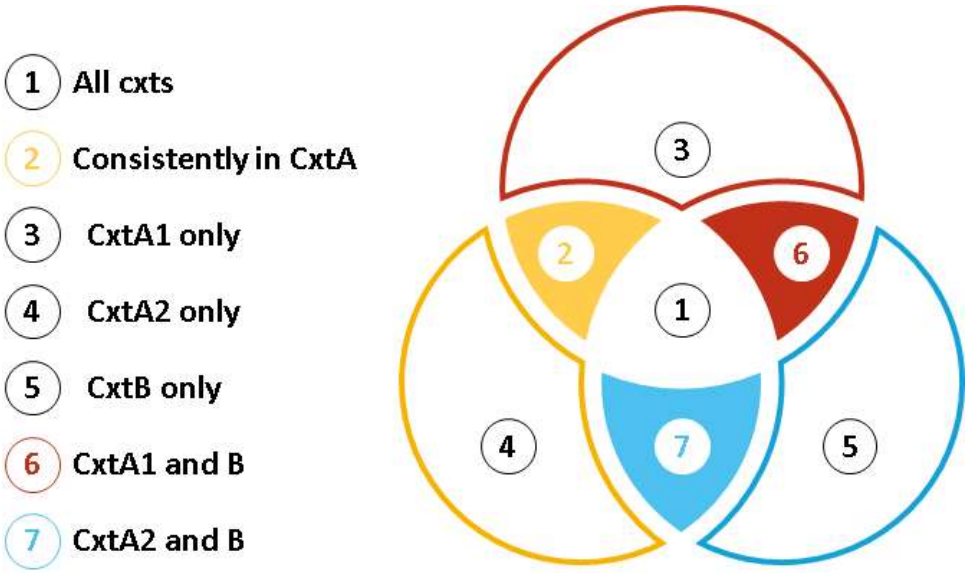

Figure 4.8: Visual schematic representing different categories of cells representing context information. The circles in the diagram represent the cellular ensemble that got activated in IS1(red), IS2(yellow) and delayed IS2 (blue).

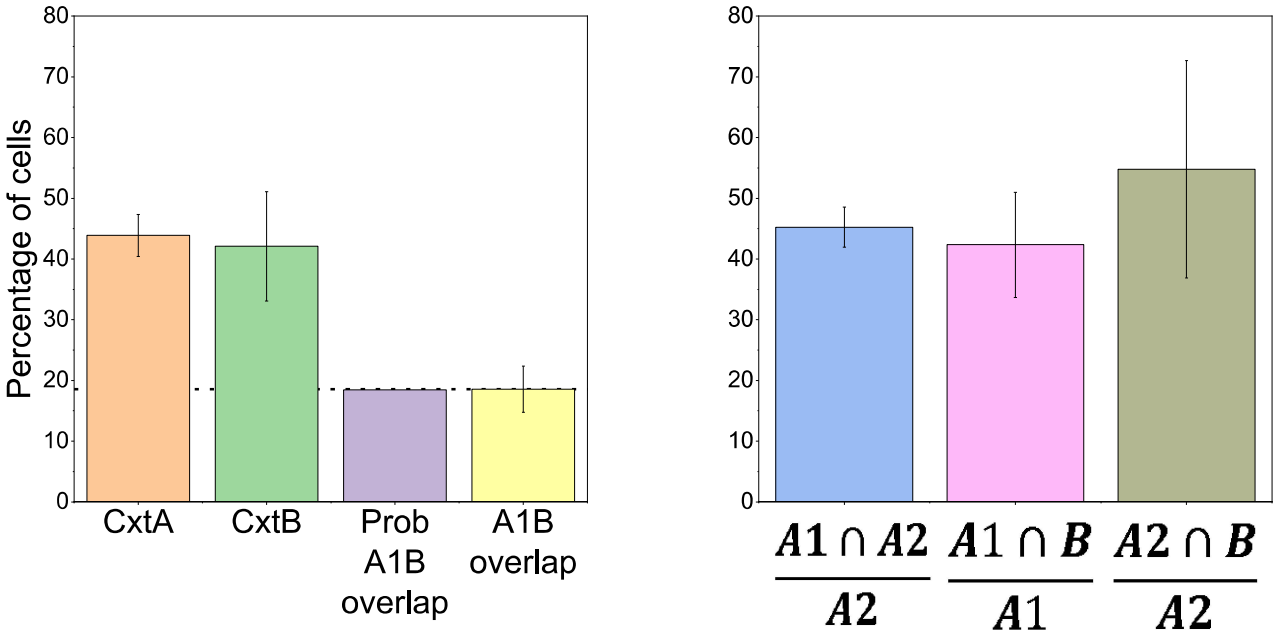

Figure 4.9: Fraction of activated neurons on different retrieval events. Different bars on the left represent activated neurons (SAC or DAC) in response to different ctxt exposure - Orange: Cxt A on IS1, Green: CxtB on IS2, Purple: chance factor determined as a product of CtxtA and CtxtB fractional activation , Yellow: observed overlap of CtxtA IS1 and CtxtB IS2 activation. The bars on the right side show the fractional activation to determine the overlap among/across the context with respect to CtxtA exposure in IS2. The blue bar represents the fraction of the cells that are part of Ctxt A IS2 and are also part of Ctxt A IS1. We estimate this fraction as this is independent of the activation across days. The pink bar represents the fraction of cells that are activated in Ctxt A IS1and Ctxt B IS2, while the grey bar represents the fraction of CtxtA IS2 cells that are active during Ctxt B IS2.

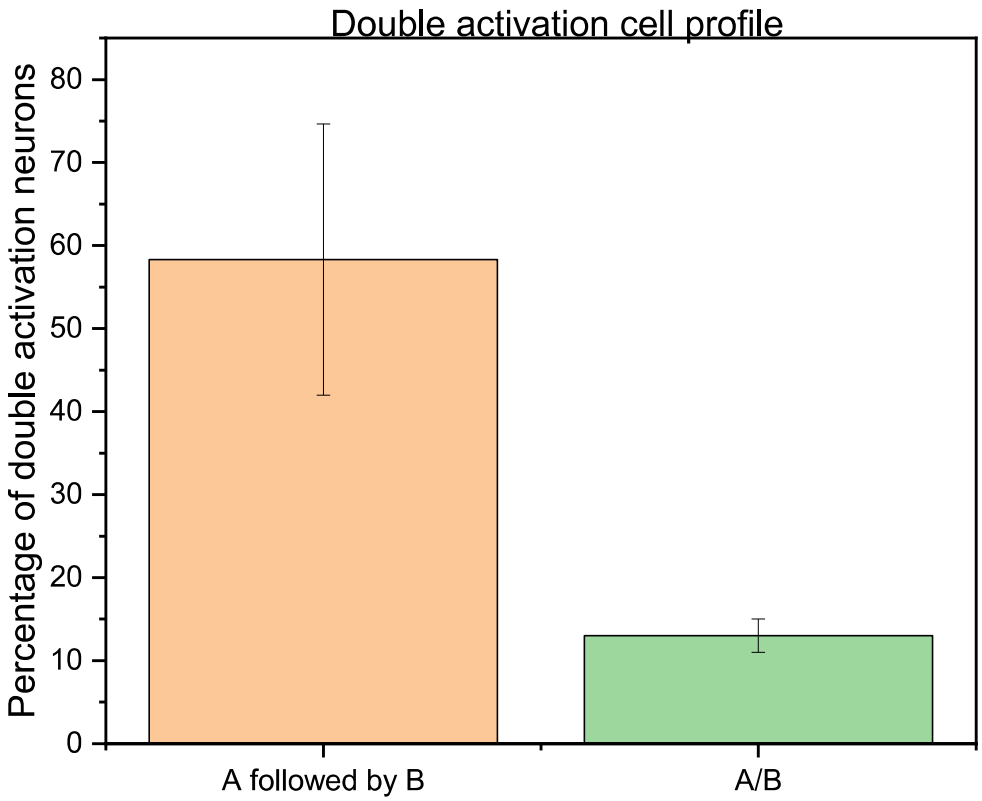

Figure 4.10: Fraction of DAC is significantly more in case of ctxt recalled close in time. The fraction of double activation cells in response to ctxt A followed by ctxt B on IS2 is significantly more than the fraction of double activation cells in response to single context exposure event

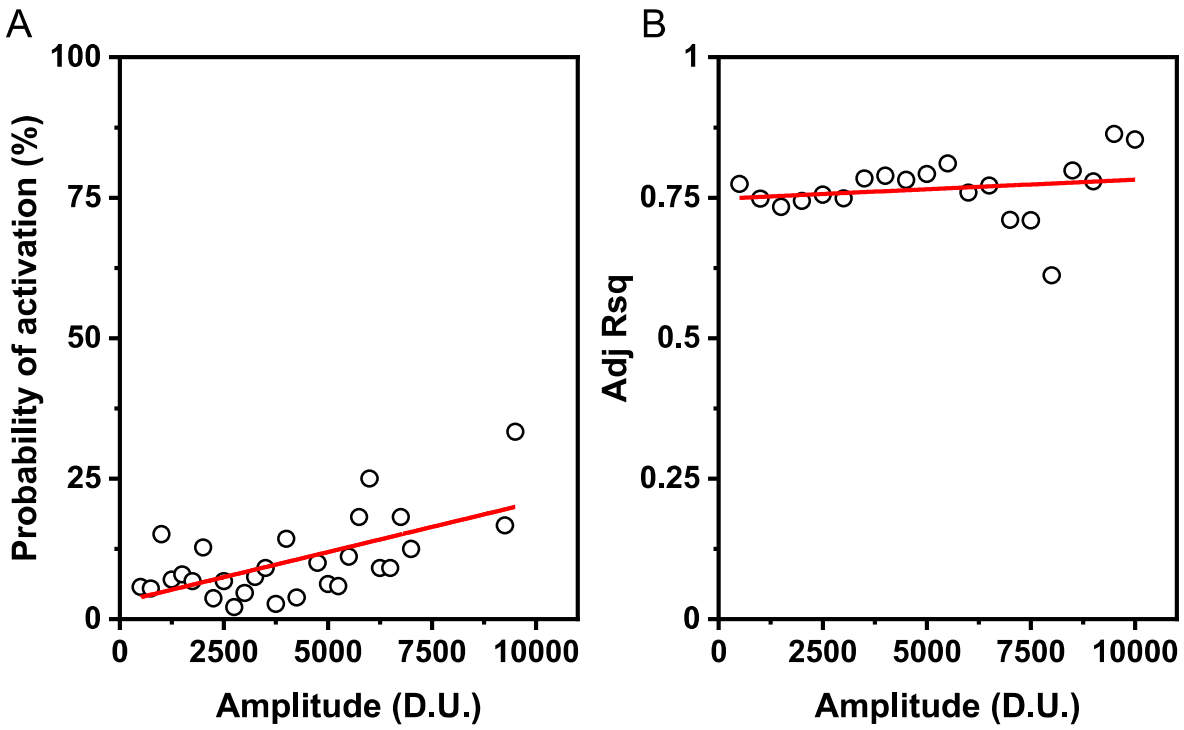

Figure 4.11: (A) Correlation between the amplitude of activated neurons in IS1 and the probability of reactivation of the same neurons in IS2. The probability of reactivation is calculated as N_{fit}/N_{bin} where N_{fit} is the fraction of neurons that fit with adj R-sq greater than 0.5, N_{bin} is the total number of cells within the amplitude bin I_{bin}. (Bin size = 500). (B) Correlation between the amplitude of fit neurons with the adj R-sq.

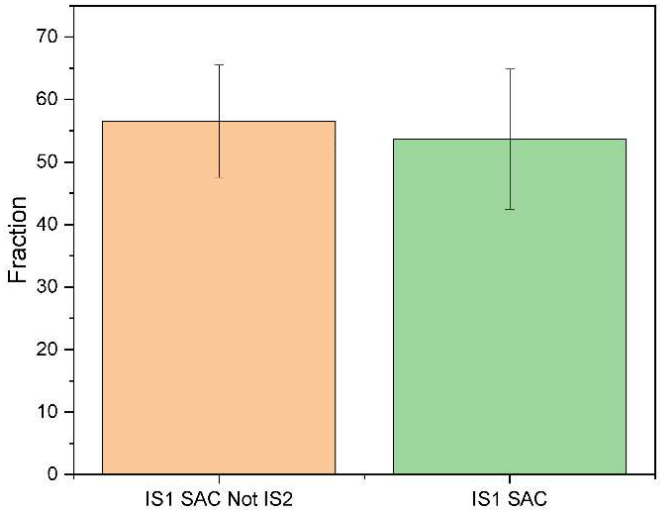

Figure 4.12: Fraction of IS1 SAC ROIs fit to equation 1 using fluorescence from imaging time points comparable to IS2 imaging time points (i.e. 80 min onwards from first context exposure) show that ~50% of data fit based on our criteria. The graph represents fraction of cells fit to equation 1 when the fit was performed with imaging time points comparable to IS2 imaging time points, i.e., ~80 min onwards. Orange bar is that fraction of fit ROIs of IS1 SAC but not IS2 SAC or DAC (mean of 3 mice, n = 32, 213, 162 ROIs) whereas green bar is the fraction fit ROIs of IS1 SAC (mean of 3 mice, n = 137, 327, 319 ROIs).

4.6 Tables

Fig No.	Cell No.	Amplitude (D.U.)	Error in Amplitude	k_f (min^{-1})	Error in k_f	K_d (min^{-1})	Error in k_d	Adj-R-sq	AIC
Fig 4.4	Cell #501	1183	148.68142	0.0593	0.02149	0.01404	0.00272	0.91592	150.73661
Fig 4.4	Cell #486	1089	104.53632	0.10002	0.07986	0.014	0.00265	0.86964	157.76146
Fig 4.4	Cell #475*	3663	416.218	0.02647	-	0.02647	0.0036	0.87058	184.62851
Fig 4.4	Cell #430	1471	157.13412	0.07198	0.03514	0.0079	0.00176	0.79118	172.29792

*The kf and kd values for these cells were shared.

Table 4.1: Summary of fit parameters of cfos-shgfp expression in response to single context exposure data fit to equation 1.

Fig No.	Cell No.	Amplitude (D.U.)	Error in Amplitude	k_f (min^{-1})	Error in k_f	K_d (min^{-1})	Error in k_d	Adj-R-sq	AIC
Fig 4.5	Cell #233	4894	420.98677	0.09777	0.05748	0.02089	0.00332	0.9343	202.68672
Fig 4.5	Cell #228	4856	282.65906	0.11699	0.07415	0.01537	0.00164	0.94395	187.96317
Fig 4.5c	Cell #66	1164	107.45433	0.07322	0.02521	0.017	0.00255	0.9444	146.82517
Fig 4.5	Cell #239*	3807	261.832	0.03036	-	0.03037	0.00229	0.94465	174.71616
Fig 4.5	Cell #232	1802	492.2815	0.04495	0.0202	0.02197	0.00738	0.9378	159.5796

*The kf and kd values for these cells were shared.

Table 4.2: Summary of fit parameters of cfos-shgfp expression in response to dual context exposure data fit to equation 1.

Venn Diagram section	IS1 (Cxt A1)	IS2 (Cxt A2)	IS2 (Cxt B)	Physiological meaning
1	1	1	1	Cell that is present in all contexts
2	1	1	0	Cell that is present in cxtA only
3	1	0	0	Cells present in IS1 cxtA only
4	0	1	0	Cells present in IS2 cxtA only
5	0	0	1	Cells present in B only
6	1	0	1	Cells present in IS1 cxtA and IS2 cxtB
7	0	1	1	Cells present in IS1 cxtA and IS2 cxtB
8	0	0	0	Cells not activated in all contexts

Table 4.3: Categories of behaviourally relevant neurons. Based on cellular response profile and fits as SAC or DAC in imaging sessions IS1 and IS2, the ROIs are classified into one of the eight categories as represented in the Venn Diagram (Fig. 4.8).

4.7 References

Auger, S. D., & Maguire, E. A. (2018). Retrosplenial cortex indexes stability beyond the spatial domain. *Journal of Neuroscience*, *38*(6), 1472–1481. https://doi.org/10.1523/JNEUROSCI.2602-17.2017

Auger, S. D., Mullally, S. L., & Maguire, E. A. (2012). Retrosplenial cortex codes for permanent landmarks. *PLoS ONE*, *7*(8). https://doi.org/10.1371/journal.pone.0043620

Auger, S. D., Zeidman, P., & Maguire, E. A. (2015). A central role for the retrosplenial cortex in de novo environmental learning. *ELife*, *4*(AUGUST2015). https://doi.org/10.7554/eLife.09031

Cai, D J, Aharoni, D., Shuman, T., Shobe, J., Biane, J., Song, W. L., Wei, B., Veshkini, M., La-Vu, M., Lou, J., Flores, S. E., Kim, I., Sano, Y., Zhou, M., Baumgaertel, K., Lavi, A., Kamata, M., Tuszynski, M., Mayford, M., … Silva, A. J. (2016). A shared neural ensemble links distinct contextual memories encoded close in time. *Nature*, *534*(7605), 115-+. https://doi.org/10.1038/nature17955

Cai, Denise J., Aharoni, D., Shuman, T., Shobe, J., Biane, J., Song, W., Wei, B., Veshkini, M., La-Vu, M., Lou, J., Flores, S. E., Kim, I., Sano, Y., Zhou, M., Baumgaertel, K., Lavi, A., Kamata, M., Tuszynski, M., Mayford, M., … Silva, A. J. (2016). A shared neural ensemble links distinct contextual memories encoded close in time. *Nature*, *534*(7605), 115–118. https://doi.org/10.1038/nature17955

Cowansage, K. K., Shuman, T., Dillingham, B. C., Chang, A., Golshani, P., & Mayford, M. (2014). Direct Reactivation of a Coherent Neocortical Memory of Context. *Neuron*, *84*(2), 432–441. https://doi.org/10.1016/j.neuron.2014.09.022

Czajkowski, R., Jayaprakash, B., Wiltgen, B., Rogerson, T., Guzman-Karlsson, M. C., Barth, A. L., Trachtenberg, J. T., & Silva, A. J. (2014). Encoding and storage of spatial information in the retrosplenial cortex. *Proceedings of the*

National Academy of Sciences of the United States of America, *111*(23), 8661–8666. https://doi.org/10.1073/pnas.1313222111

Frank, A. C., Huang, S., Zhou, M., Gdalyahu, A., Kastellakis, G., Silva, T. K., Lu, E., Wen, X., Poirazi, P., Trachtenberg, J. T., & Silva, A. J. (2018). Hotspots of dendritic spine turnover facilitate clustered spine addition and learning and memory. *Nature Communications*, *9*(1). https://doi.org/10.1038/s41467-017-02751-2

Guzowski, J. F., & Worley, P. F. (2001). Cellular Compartment Analysis of Temporal Activity by Fluorescence In Situ Hybridization (catFISH). *Current Protocols in Neuroscience*, *15*(1), 1.8.1-1.8.16. https://doi.org/10.1002/0471142301.ns0108s15

Miller, A. M. P., Vedder, L. C., Law, L. M., & Smith, D. M. (2014). Cues, context, and long-term memory: the role of the retrosplenial cortex in spatial cognition. *Frontiers in Human Neuroscience*, *8*(AUG), 586. https://doi.org/10.3389/fnhum.2014.00586

Mitchell, A. S., Czajkowski, R., Zhang, N., Jeffery, K., & Nelson, A. J. D. (2018). Retrosplenial cortex and its role in spatial cognition. *Brain and Neuroscience Advances*, *2*, 239821281875709. https://doi.org/10.1177/2398212818757098

Nelson, A. J. D., Hindley, E. L., Haddon, J. E., Nelson, A. J. D., Hindley, E. L., Haddon, J. E., Vann, S. D., & Aggleton, J. P. (2014). *A novel role for the rat retrosplenial cortex in cognitive control A novel role for the rat retrosplenial cortex in cognitive control*. 90–97. https://doi.org/10.1101/lm.032136.113

Opalka, A. N., & Wang, D. V. (2020). Hippocampal efferents to retrosplenial cortex and lateral septum are required for memory acquisition. *Learning and Memory*, *27*(8), 310–318. https://doi.org/10.1101/LM.051797.120

Repa, J. C., Muller, J., Apergis, J., Desrochers, T. M., Zhou, Y., & LeDoux, J. E. (2001). Two different lateral amygdala cell populations contribute to the initiation and storage of memory. *Nature Neuroscience*, *4*(7), 724–731. https://doi.org/10.1038/89512

Silva, A. J., Zhou, Y., Rogerson, T., Shobe, J., & Balaji, J. (2009). Molecular and cellular approaches to memory allocation in neural circuits. *Science*, *326*(5951). https://doi.org/10.1126/science.1174519

Tse, D., Takeuchi, T., Kakeyama, M., Kajii, Y., Okuno, H., Tohyama, C., Bito, H., & Morris, R. G. M. (2011). Schema-Dependent Gene Activation and Memory Encoding in Neocortex. *Science*, *333*(6044), 891–895. https://doi.org/10.1126/science.1205274

Vazdarjanova, A., & Guzowski, J. F. (2004). Differences in hippocampal neuronal population responses to modifications of an environmental context: Evidence for distinct, yet complementary, functions of CA3 and CA1 ensembles. *Journal of Neuroscience*, *24*(29), 6489–6496. https://doi.org/10.1523/JNEUROSCI.0350-04.2004

CHAPTER 5

Vector field-based analysis to assess spatial memory in navigational task

Abstract

Conventional behavioural measures for testing spatial memory in navigational tasks compare the residence time of the animals in different regions. Such measures are inherently simple and thereby are limited in their ability to extend the behavioural task to probe finer details about the nature of the memory. Here, we developed a vector field-based analysis framework to assess spatial memory in a navigational task. Specifically, we constructed velocity-based vector fields that describe the motion of animals or subjects as well as their search pattern in the Morris water maze (MWM) task. Next, we utilised the field properties to develop three metrics to quantify the nature of spatial memory: accuracy, uncertainty, and intensity of search. The proposed metrics resolve the information of spatial memory into measurable independent components and brings out the differences in the memory representation that are normally not possible to elucidate from conventional measures.

5.1 Introduction

Navigational tasks are widely used to address questions related to the neuroscience of spatial memory. One such task, the Morris water maze (MWM) and its modifications have been extensively used to study a variety of cognitive phenomena, especially related to hippocampal-dependent memory and spatial representations (Brandeis et al., 1989; D'Hooge & De Deyn, 2001; Redish & Touretzky, 1998). In the original or reference version of the MWM task, animals, over multiple trials, learn the spatial location of a hidden platform submerged in a pool of water using only the distal cues (R. Morris, 1984; R. G. M. Morris, 1981). Learning is assessed via performance during training trials whereas memory retention is investigated using a probe trial. During the probe trial, the platform is removed, and the animal is made to search for the platform in the pool typically for 60s. Thus, based on the animal's search behaviour during a probe trial, we assess its spatial memory. Many variations of the water maze exist to probe different questions, as listed below.

1. Marked platform task: The platform location is marked with a proximal cue, i.e. a flag. Thus, the task is independent of the hippocampus. It serves as a control to ensure proper motor/taxis as well as visual system of the animal.
2. Reference memory task: The traditional MWM task with a fixed platform location and distal cues.
3. Delayed match to place task: The platform location is changed every day. The animal is taught to associate a new platform location in the first training session of the day. This version of the MWM is used to probe for working memory.
4. Goal-reversal: The platform location is shifted, usually the place opposite the original training location. In such a case, the cues remail the same, but new spatial relations must be learnt by the animals.

There are several measures that have been proposed to estimate the extent of spatial memory retention. Traditionally, memory retention has been assessed by estimating and comparing the time spent by the animal in the quadrant of the pool where the platform was located during training (target quadrant) with the time spent in other three quadrants. The time spent in the target quadrant acts as a readout

for memory retention (Petrosini et al., 1998). Time spent in zones or areas of multiple sizes centred at the platform is also utilised as a parameter for measuring spatial memory as this provides a more localised readout for memory retention. Similarly, platform crossings, which describe the number of times the animal has crossed the platform location during a probe trial, is used as a metric for spatial memory. Additionally, path length is a metric that measures the total distance covered in search of the platform by the animal during a probe trial (Dalm et al., 2000). Other conventional measures report escape latency, the time taken to reach the platform location, thigmotaxis duration (Wolfer & Lipp, 1992), i.e., the time spent exhibiting wall-hugging behaviour, and average speed all as an indicator of functional swimming/motor skills. While these methods provide information on whether the animal can locate the platform, these measures are inherently simple and do not necessarily the capture the complexity associated with spatial memory and navigational performance.

Improvements over the classical measures have been proposed over the years (Pereira & Burwell, 2015). One such method is the proximity measure that calculates the average distance of the animal from the centre of platform location (Gallagher et al., 1993). This measure is effective in differentiating between two search strategies of equal path length: a focused search near the platform scores better than a diffused search around the platform. Incidentally, the proximity measure has been shown to be more sensitive than the quadrant, zonal and platform crossings in detecting spatial memory deficient in Morris water maze task (Maei, Zaslavsky, Teixeira, et al., 2009).

A different approach to quantify spatial memory uses increasingly complex methods that classify the swim trajectories into path strategies utilized by the animal. These approaches utilize methods and formulate strategies to describe the qualitative aspect of learning in the water maze task (Garthe et al., 2009; Gehring et al., 2015; Graziano et al., 2003). Such path strategy-based methods use semi-automated or machine learning algorithms to ensure feasibility of classifying the swim trajectory reliably. Interestingly, in certain cases, such methods detect multiple strategies within trials (Cooke et al., 2019; Overall et al., 2020; Vouros et al., 2018). These methods are dependent on a defined set of

possible strategies that have been previously identified in available datasets used to train the classifier. Thus, they are limited to the set of defined categories of search strategies, focus on the qualitative nature of learning, and provide a descriptive readout on the nature of spatial memory.

Maei *et al* proposed an entropy-based measure that uses the concept of entropy from information theory. This entropy-based measure H describes the extent of search at the platform location and the focus of this search (Maei, Zaslavsky, Wang, et al., 2009). This method utilizes the rationale that the animals improve their focus or "organize" their search efforts to locate the platform as a function of learning. Thus, its swim trajectories go from a highly disorganized state to a more organized state with training. Computing the entropy of the swim trajectories (summation of entropy in path variance (H_{path}) and entropy in error variance (H_{error})) provides a measure of greater sensitivity compared to the proximity measure. However, the extent of improved sensitivity of the entropy measure is dependent on the relative weighting of its components H_{path} and H_{error} in a given experimental setting, since one component maybe be more sensitive to particular search strategies that the other. Such estimates, despite being highly sensitive, do not provide a uniform scale of measurement that is intuitive and easy to compare due to their nonlinear nature. Additionally, this measure primarily estimates the disorderliness in the instantaneous behaviour, thus not utilizing or measuring the spatial variation of the navigational properties.

In this context, we propose new measures based on vector fields constructed from velocity components that are oriented towards a specific point in the water maze. Our proposition stems from the observation that the animals tend to slow down at and around the platform location during the probe trials with the expectation of landing on the platform. This behaviour gains prominence as they acquire the spatial memory for the location of platform. Such slowing down also occurs near the periphery when they are traveling towards the pool boundaries. In addition, they show similar behaviour when they overshoot the platform position and turn around. Thus, we believe, the measures developed to understand the properties of these vectors and their spatial distribution as a vector field could provide information regarding platform location as perceived by the animal. Therefore, in

summary, we develop a framework and derive measures to describe the navigation exhibited by the animals in the water maze.

The new framework and measures enable us to dissect subtle memory deficits in animals performing the Morris water maze task. We hypothesize that vector maps of two components, the velocity vector component along ($V_{\parallel t}$) and orthogonal ($V_{\perp t}$) to the occupancy centre, contain information on the intention of the animal's movement. Specifically, we reason that the velocity vector component along the occupancy centre ($V_{\parallel t}$) measures the animal's movement that contribute to its approach to the location and the velocity vector component orthogonal to the occupancy centre ($V_{\perp t}$) measures of the animal's movement that contributes to circular motion around the occupancy centre. Next, we calculate the vector field properties, namely, the divergence of $V_{\parallel t}$, to describe the rate of change of these measures in the 2D space. Specifically, we hypothesize that spatially localized negative divergence peaks of $V_{\parallel t}$ reveals convergence hotspots or the putative search centres (Pcs). Using the search centre, we quantify the spatial memory in terms of three independent metrics, namely accuracy, uncertainty, and intensity of search.

We argue that unlike the previously proposed measures, the three metrics based on divergence field property are sufficient to describe the nature of spatial memory irrespective of factors outside of memory-based phenomena, such as search strategy or differential motor skill ability.

5.2 Theory

5.2.1 Velocity-based vector fields for describing the intentional movement of animal swim trajectories:

i) Description of velocity vector fields

We first developed an analytical framework for describing the swim trajectories in terms of a velocity vector field. The position vector $(\overrightarrow{P_t})$ represents the point at which the animal is located at a given time ('t'- usually measured in video frames). The origin of the reference frame $O(0,0)$ is set to be the top left corner (Fig.5.1 (A)). Thus, from an image taken from the top, the pixel co-ordinates (P_x, P_y) can be used to write (P_t) as follows:

$$\overrightarrow{P_t} = P_x\hat{\imath} + P_y\hat{\jmath}$$

$\rightarrow$ P_x and P_y $are\ the\ distance\ in\ pixels\ from\ top\ left\ corner\ in\ the\ image$

…Eq.(i)

For convenience, we define a displacement vector $(\overrightarrow{D_t})$ that provides a relation of the animal's position with respect to a point of interest, e.g., the platform. This is calculated as the difference between the platform vector $\overrightarrow{P_L}$ and the instantaneous position vector ($\overrightarrow{P_t}$) defined above. (Fig. 5.1 (B)).

$$\overrightarrow{D_t} = \overrightarrow{P_L} - \overrightarrow{P_t}$$ …Eq.(ii)

The velocity vector $(\overrightarrow{V_t} = \frac{d}{dt}\overrightarrow{D_t})$ is a metric that describes the movement of the animal. Since we make these measurements from time lapse videos that are recorded at uniform frame rates, we can calculate the velocity vector as the difference between two consecutive displacement vectors. (Fig.5.1 (C)).

$$\overrightarrow{V_t} = \overrightarrow{D_{t+1}} - \overrightarrow{D_t}$$ … Eq.(iii)

ii) Definition of occupancy centre

Since we measure the component of velocity of the animal that is directed towards reaching the "goal", it is convenient to define the occupancy centre P_{oc} as the point where the likelihood of finding the animal is high given its trajectory. We calculate P_{oc} as the centre of mass obtained from the residence time map that is segmented using a maximum entropy threshold. Maximum entropy (ME) segmentation determines a threshold (T) that has the maximum entropy of the background (H_B) and foreground (H_F) in an image (Sahoo et al., 1988).

$$\mathrm{H_B} = -\sum_{\mathrm{i=1}}^{\mathrm{T}} p_i log_2(p_i)$$

$$\mathrm{H_F} = -\sum_{\mathrm{i=T+1}}^{n} p_i log_2(p_i)$$

where p_i is the number of pixels with value *i* divided by the total number of pixels in their respective segments (H_B and H_F), and *n* is the maximal possible intensity in the image. This enables us to segment out the regions with zero or low occupancy from regions of high occupancy without bias. The use of ME segmentation increases the fidelity and hence the confidence in our estimate of the occupancy centre as the most likely resided region based on a animal's swim trajectory. This is given by (Fig. 5.1(F))

$\mathrm{x_{cm}} = \frac{\sum_{\mathrm{i=1}}^{\mathrm{n}} \mathrm{x_i I_i}}{\sum_{\mathrm{i=1}}^{\mathrm{n}} \mathrm{I_i}}$ and $y_{cm} = \frac{\sum_{i=1}^{n} y_i I_i}{\sum_{i=1}^{n} I_i}$ where $I_i > T$

$$such\ that\ for\ the\ choosen\ T\ , the\ sum\ (H_B + H_F)\ is\ maximum$$

iii) Description of vector fields with respect to the occupancy centre

Using the occupancy centre, we computed two different measures to describe the animal's movement. First, the component of velocity vector along the occupancy centre, a spatial property that measures the contribution of the movement at that location towards the occupancy centre. This component is the vector projection or the velocity vector *V(t)* along the direction of the occupancy centre ($\widehat{d_{P_{OC}}}$), and is given by (Fig. 5.1(D))

$$\overrightarrow{V_{\|t}} = \left|\overrightarrow{V_t}\right| cos\,\theta_v\, \widehat{d_{P_{OC}}} \qquad \ldots \text{Eq.(iv)}$$

where $\left|\overrightarrow{V_t}\right|$ is the magnitude of the velocity vector and θ_v is the angle between the velocity vector $\overrightarrow{V_t}$ and a unit vector pointing towards the occupancy centre ($\widehat{d_{P_{OC}}}$) from the current position.

Second, the velocity vector component orthogonal to the occupancy centre is a spatial property that measures at that position, the contribution of the animal's movement to the circular motion about the occupancy centre. It is given by (Fig. 5.1(E))

$$V_{\perp t} = \left|\overrightarrow{V_t}\right| sin\,\theta_v\, \widehat{d_{P_{OC}}} \qquad \ldots \text{Eq.(v)}$$

where $\left|\overrightarrow{V_t}\right|$ is the magnitude of the velocity vector and θ_v is the angle between velocity vector $\overrightarrow{V_t}$ and the unit vector pointing towards the occupancy centre ($\widehat{d_{P_{OC}}}$). We note if ME segmentation yields multiple disconnected regions of comparable sizes then we need to consider multiple occupancy centres. In such cases we evaluate the velocity vector components towards each of them and take the weighted sum of their magnitudes. The weights are determined by the fractional area of the patch. In the current study we did not use such as approach.

Next, we resolved these vectors Eq.(iv) and Eq.(v) in a frame of reference defined with respect to the image of the pool. The origin is set at the top left corner of the image with right and down being the positive directions of its axis. Thus, the above vectors could be written as

$$V_{\|t} = V_{\|t} cos\theta_d \hat{\imath} + V_{\|t} sin\theta_d \hat{\jmath} \qquad \ldots \text{Eq.(vi)}$$

$$V_{\perp t} = V_{\perp t}\, cos\,\theta_d \hat{\imath} + V_{\perp t}\, sin\,\theta_d \hat{\jmath} \qquad \ldots \text{Eq. (vii)}$$

where θ_d is the angle, $\hat{\imath}$ and $\hat{\jmath}$ are the unit vectors along the height and width of the image frame.

5.2.2 Analytical expression of the putative search centres obtained from divergence in velocity-based vector fields.

i) Vector field properties

Divergence of a vector field indicates the difference or change in flux around an infinitesimal volume. We reason that given a vector field $V_{\|t}$, the point of convergence ("sink" in a vector field) could represent the point where the animal intends to reach. We hypothesize that if a animal intents to reach a specific location P_L' in the pool , then the velocity field would point inward from the region with progressively decreasing magnitude (as described in the introduction) around the point P_L' leading to a negative divergence value (i.e., indicating convergences) at P_L'. However, in general P_L' need not necessarily coincide with the platform location or occupancy centre, for they represent the centre of a region where the animal is most likely found, and not the actual platform location. We construct the vector field from vector projections (Eq. 1) to measure and represent the intention of the animal to move towards the occupancy centre as a function of its position in the pool. The heat map of the global minima of such a divergence would be indicative of the platform location as perceived by the animal. We calculate the divergence on the vector field describing the velocity along the occupancy centre in the image reference frame as

$$\mathrm{I}_{\mathrm{div}}(\mathrm{x},\mathrm{y}) = \nabla \cdot V_{\|t} = \frac{\partial}{\partial \mathrm{x}} V_{\|t} cos\theta_d + \frac{\partial}{\partial \mathrm{y}} V_{\|t} sin\theta_d \qquad \text{…Eq. (viii)}$$

Similarly, we reason that the curl of a vector field could indicate the tendency of rotation of an object placed at that location, and hence we propose that it could be used to extract the tendency of the animal to circle around any point in the pool. For completion, we describe the curl, but in subsequent analyses, we restricted our analyses to divergence.

Curl of a field is formally defined as the circulation density at each point of the field (i.e., the extent of rotation about a point). Thus, curl on $V_{\perp t}$ vector field would be informative of the extent of circular movement that the animal makes about the perceived platform location while searching for it. Using our notation, the curl can be written as:

$$\mathrm{I}_{\mathrm{curl}}(\mathrm{x},\mathrm{y}) = \nabla \times V_{\perp t} = \left(\frac{\partial}{\partial x} V_{\perp t} \sin\theta_d - \frac{\partial}{\partial y} V_{\perp t} \cos\theta_d\right) \hat{k} \quad \text{… Eq. (ix)}$$

ii) Description of the putative search centre (P_{cs})

Search centres can be obtained from the divergence calculated on the vector field of the velocity component pointing towards the occupancy centre. The convergence peaks in such a map are indicative of the search centres ($\overrightarrow{P_{cs}}$) or the platform locations as perceived by the animal.

We obtain the search centre or the convergence point by estimating the minima of the divergence on the velocity-based measure. For a two-dimensional surface, we obtain the critical point ((x_o, y_o)) by equating the first derivative to be zero and forcing the second derivative to be positive as follows:

$\overrightarrow{P_{cs}} = \sqrt{(\mathrm{x}_0^2 + \mathrm{y}_0^2)}$ for

i) $\nabla I_{div}(x_o, y_o) = 0$

ii) $H = I_{div_{xx}}(x_0, y_0) I_{div_{yy}}(x_0, y_0) + I_{div_{xy}}(x_0, y_0)^2$ where $H > 0$ and $I_{div_{xx}}(x_0, y_0) > 0$.

…Eq. (x)

5.2.3 Metrics to assess spatial memory:

We define and use three measures that are independent of each other to assess spatial memory in terms of various attributes of the search centre ($\overrightarrow{P_{cs}}$). The three independent measures namely, including accuracy of search, uncertainty about the search centre, and intensity at the search centre, are described next.

i) Accuracy of the search centre (α_{cs}) (Fig. 5.1(G))

Since the search centre is indicative of the animal's perceived platform location, the distance between the search centre and the platform location measures inaccuracy or error in the animal's ability to learn and remember the platform location. The difference in location measured in units of length can be difficult to compare across different laboratories, since the effective pool and platform sizes

can vary between laboratories. To address this problem, we developed a percentage measure that can be used for comparisons of animals' performances across laboratories. First, we realized that the maximum error in accuracy that the animal can make can be captured by the distance between the platform centre and the farthest pool boundary (*e*). Next, we defined the accuracy of search (α_{cs}) as 1 minus the fractional error, with fractional error being the ratio between the distance of the search centre from the platform and the maximum error. Thus, the accuracy of the search centre is given by

$$\alpha_{cs} = 100 * \frac{(e - d_{cs})}{e}$$

where $d_{cs} = \left|\overrightarrow{P_l} - \overrightarrow{P_{cs}}\right|$ … Eq. (xi)

Furthermore, to estimate the chance factor we consider the case of a naïve animal that does not have any knowledge of the platform location (e.g., an animal on its first day of training). At this point of training, animals usually exhibit wall-hugging behaviour (i.e., they swim in circles close to the wall). In such a scenario, the animal is moving about the pool centre as its navigational centre, and by virtue of symmetry the pool centre would reflect the search centre. We make use of this fact to define the chance accuracy as the accuracy when the search centre coincides with the pool centre and is given by

$\alpha_{chance_{Pc}} = 100 * \frac{r}{e}$, r -> is the radius of the pool

…Eq. (xii)

Thus, an accuracy value that is comparable to the chance factor (Eq. x) would reflect whether the animal is still exhibiting symmetric navigational behaviour. As the animal learns the rules of the water maze, this symmetry is broken. Comparisons of accuracy with the chance factor above yield a categorical measure of learning and memory in the maze.

ii) Uncertainty about the search centre (σ_{cs}) (Fig. 5.1(H))

Apart from the location of the search centre, the spread of the divergence values around the peak provide additional insights into the level of uncertainty in the internal representation of the platform position in the animal's performance. We calculated this by measuring Uncertainty about the search centre and defined it as the full width half maximum (FWHM) of the convergence peak representing the search centre. We assume that the convergence peak is a 2D Gaussian, and compute the FWHM by linearising the 2D Gaussian equation as previously described (*2D Gaussian fitting macro (Fiji/ImageJ) for multiple signals.* | *BIII*, n.d.). We express the uncertainty about the search centre in terms of the relative search diameter, defined as a ratio of the major axis of the Gaussian ellipse to the platform diameter.

$$d_{RS} = \frac{\sigma_{CS}}{d_{P_L}}$$

…Eq. (xiii)

iii) Intensity of search (I_{cs}) (Fig. 5.1(I))

The absolute search intensity (aI_{cs}), defined as the magnitude of convergence at the search centre, is a measure of the animal's searches in the search centre, i.e.,

$$aI_{cs} = -I_{div}(x_0, y_0)$$

… Eq. (xiv)

Additionally, we define the Relative search intensity (rI_{cs}) as the magnitude of convergence at the search centre normalised to the maximum convergence seen anywhere in the pool. We propose that this measure reflects the fractional effort of the animal's search at the search centre.

$rI_{cs} = \frac{I_{cs}}{I_{max}}$, I_{cs} -> I_{div} (x_0,y_0) and I_{max} -> is the maximum divergence inside the pool.

…Eq. (xv)

5.3 Results

5.3.1 Swim trajectories described as velocity vector fields reveal that the speed of intentional movement varies over the pool space as a function of training.

In an effort to assess the quality of spatial memory, we first seek to describe the movement of the mice using the most fundamental kinematic measure, namely, its velocity. For this, we use previously published water maze data (Lee et al., 2014) from Noonan syndrome(NS) mice and their littermate controls (Ptpn11 +/+). Using the time series of position data obtained from swim trajectories, we construct velocity vectors (Eq. iii, Fig. 5.1C). These vectors describe the distance covered per unit time as the mice search for the platform (Fig. 5.2 (A-D)). When we measure the magnitude of the velocity vector (speed) as a function radial distance from the platform, we note that it is invariant across space when the mice have no knowledge of the platform location (Fig. 5.3(A)). However, we see that, after training, the speed of the mice reduces closer to the platform during the probe trials (Red arrows in Fig.5.3 (B), (C), (D)). The speed of the mice also reduces when it is close to the pool boundary. We reason that studying the variation of speed across the spatial dimension will reveal the regions at which the mice slow-down in their effort to locate the platform. Specifically, we assert that the divergence on the velocity vector field will reveal the “sources” and “sinks” in that field, i.e., regions where the mice swim away from with high speed (divergence points) and regions where the mice swim into with low speed (convergence points). As a general case, we recognise at any given instant only a part of rodent’s movement and not necessarily the entire movement may be oriented along its intended direction. Given this scenario, we generate a vector field around the point in the pool where the mice are most likely to be found, i.e., the occupancy centre. We argue that the regions of low residence typically result from incidental occupancy of these locations merely by being on the navigational path of the mice rather than being the locations where the mice intend to go. We identify the high occupancy regions as the regions where the mice intend to stay. We use maximum entropy to demarcate these regions as the regions where the mice are more likely to sample. We calculate the centre of mass of these most likely occupied regions to get the

occupancy centre as shown in Fig 5.2 (E-H) for Ptpn11 +/+ mice on training day 1 as well as probe days 3, 5 and 7. Utilising this occupancy centre, we describe the swim trajectories in terms of velocity vector component along the occupancy centre (Eq. (vi)).

We reasoned if our assertion that a part and not necessarily the whole of the movement is utilised is true, then we might be able to see a change in this fraction as a function of training. In line with our assertion, we see that the mice show movements that are more aligned to the occupancy centre during the probe trials (Fig. 5.3 (F-H)) compared to the training (Fig. 5.3 (E)). Thus, we utilise the velocity vector component defined as in Eq. (vi) to construct vector fields and measure the divergence (Eq. (viii)). Fig. 5.3 (I) depicts the surface of divergence estimated using the wild type mice for the training day (D1) (Left panel) and probe day 7 (PD7) (right panel). We can clearly see the valley that emerges near the platform location as the mice acquires spatial memory.

5.3.2 Negative divergence in vector field of velocity component along the occupancy centre, rather than velocity itself, describes the putative search centres as convergence hotspots for a given swim pattern.

We construct a velocity vector field based on the movement of the mice during a probe trial to describe their swim pattern. Together with the velocity vector field, we construct a vector field of the velocity component along the occupancy centre (Eq.vi). We rationalise that the velocity component along the occupancy centre quantifies the effect of an intentional movement towards the occupancy centre. We determine convergence peaks on these vector fields. Given our assertion that for a given swim pattern, a convergence peak represents the point that the mice swim to, the convergence peak is a proxy for the perceived platform location as it represents the putative search centre of the mice. We generate such a convergence heat map for an individual mouse as well as a population of mice. A schematic of the workflow is presented in Fig. 5.4.

We show the velocity vector field maps for an individual Ptpn11+/+ mouse in Fig. 5.5 (A) as well as the velocity vector field for a population of Ptpn11+/+ mice (n =15) in Fig. 5.5 (C) for their trajectories on probe day 7. We see the divergence

map calculated on the vector field shows the presence of convergence peaks near the platform (Fig. 5.5 (F) and (H)). In comparison, the divergence map calculated on the velocity component shows a sharp, well-defined convergence peak near the platform for both individual and population trajectory (Fig. 5.5 (I), (J) and (L)). The spatial sampling of the pool during probe trial by an individual mouse is sufficient to detect convergence peaks, thus allowing us to identify putative search centres for each individual mouse. However, we use the trajectory from a group of mice to establish the method (presented in Chapter 6).

5.4 Discussion

In this chapter, we develop and present a new method to describe spatial memory in a navigational task based on timestamped xy trajectories. We hypothesize that using velocity-based vector fields and its properties allow us to pin-point putative search centres of the animal in the arena. On determining the search centre, the spatial memory can be described using three components or metrics: accuracy of search centre to the target location, uncertainty of the search or the spread in search area, and the intensity or the extent of effort in search.

We note that these three measures are independent of each other and are sufficient to quantify spatial learning and memory. To illustrate this, we consider a real-life navigational task of visiting a café located block “A” between intersections “I” and “II”. In this context if the person remembers and goes to block “B” then accuracy captures the difference between the true location of the café and the actual location person went to. On reaching the place and not finding the café the person back tracks and searches around the place. The extent of area within which the person searches reflect their own estimate of how erroneous their memory for the location is. In this example the person knows the café is between two intersections but does not remember the block. Uncertainty captures this effect in our measure. Finally, the intensity of the search at block “B” captures the probability and hence the intention of that the person to target the search for the café at that point.

Moreover, we reason that the metrics proposed here reflect the true nature of spatial memory. For example, whether animals use single or multiple search strategies in a trial, the combined effect of the search results in swimming toward a particular region or location. This effect of swimming toward the location will be detected as a convergence peak or hotspot, i.e., divergence field property is not preferentially sensitive or dependent on a particular search strategy. Additionally, since divergence measures the change in velocity in space, differences in absolute speed between strains of animal will not affect the measure, i.e. the divergence field property can dissociate a memory deficit and a motor deficit. Differences in swim speed affect many of the conventional measures as speed determines the occupancy and area coverage. We note that moderate differences in swim speed

does not affect training as the animal are left in the pool until they reach the platform. Both fast as well as slow swimmers reach platform during training. On learning the platform location, the animal reaches the platform in 1/10th of the maximum training duration thus only animal that are considerably slower (>10 times as slow) do not reach the platform by themselves affecting their learning. On the other hand, conventional measures such as quadrant, platform crossing and proximity being dependent on occupancy gets affected by changes in swim speed. However, divergence of vector field as set-up here measures how the vectors are changing in space rather than measuring the magnitude of the vectors thus minimizing if not eliminating the effects of difference in swim speed. Thus, the proposed metrics based on divergence of vector field improves the sensitivity of memory detection by uncoupling the effects of non-memory related processes from spatial memory.

Standardisation of behavioural tasks to minimise variability seen in experimental cohorts across different labs has been a difficult issue to solve in the field of behavioural neuroscience (Crabbe et al. 1999). In this context, we speculate that laboratory induced variation in mouse performance could be compared meaningfully since the proposed method quantifies memory using three measure that are independent of each other. While we have presented the description, derivation, and potential utility of both the divergence and curl vector field properties, we focused on developing and highlighting the power of the metrics derived from divergence vector field property for the current study.

5.5 Materials and Methods

5.5.1 Animal information

The data from fifteen male NS mice wild type littermate (Ptpn11 +/+) were used for the analysis presented in this chapter.

5.5.2 Description of water maze paradigm

The NS mice were trained as reported previously (Lee et al., 2014). Briefly, training sessions comprised 4 trials (2 blocks with 2 trials each) per day with 1-min inter-trial interval and 45-min inter-block interval. Mice were allowed to search the platform for 60 s or until reaching the platform. The probe tests were done immediately after the completion of training on days 3,5, 7.

5.5.3 Generation of velocity-based vector field via surface fit:

We describe the swim trajectories in terms of the velocity component along the occupancy centre for all pixels sampled by the mice. The value at each pixel is normalised to the number of times it has been sampled, i.e., the mean value at the pixel.

We perform a 5^{th} order polynomial surface fit (ImageJ Polynomial Surface Fit plugin) using an ROI of sampled pixels. The resultant surface is a continuous surface representing the velocity-based vector field. We require that the fit interpolates values for unsampled pixels within the sampled pixels ROI to compute the partial differential along the horizontal and vertical axis of the pool reference frame. Since the regions outside the ROI are not sampled, we do not consider it to be a part of vector field. We modified and used the Differentials Plugin (Unser, 1999) in ImageJ to obtain the components of divergence.

5.5.4 Estimation of error in generated velocity-based vector field:

The error in 5^{th} order polynomial surface fit is described by estimating the goodness of surface fit. The reduced chi-sq (χ_ν^2) describes the variance in the velocity-based measure among the population of mice as well as the variance in the estimate of fit values at each pixel.

$$\chi_v^2 = \frac{\chi^2}{v} = \frac{\sum_{i=1}^{n} \frac{\left(y_i - y(x_i)\right)^2}{\sigma_i^2}}{n - m}$$

where y_i is the actual value at the pixel *i*, $y(x_i)$ is the fit value at the pixel *i*, σ_i^2 is the variance in velocity-based measure value at the pixel *i*. *v* is the degree of freedom defined as the difference between the number of points sampled on the surface (*n*) minus the number of fitted parameters (*m*). In case of a 5th order polynomial equation, there are 14 coefficients or fitted parameters, hence the degree of freedom $v = n - 14$.

5.5.5 Estimation of error in field properties:

We represent the estimated error in the field properties as a percent error in residual of the surface fit.

$$\text{Residual sum sq} = \text{RSS} = \sum_{i=1}^{n} \left(y_i - y(x_i)\right)^2$$

$$\text{Weighted residual sum sq} = \text{wRSS} = \sum_{i=1}^{n} \frac{w_i \left(y_i - y(x_i)\right)^2}{\sum_{i=1}^{n} w_i}$$

where $w_i = \frac{1}{\sigma_i^2}$

$$\text{Percent error} = 100 \sum_{i=1}^{n} \frac{w_i \left(y_i - y(x_i)\right)^2}{y_i \sum_{i=1}^{n} w_i}$$

where y_i is the actual value at the pixel *i*, $y(x_i)$ is the fit value at the pixel *i*, σ_i^2 is the variance in velocity-based measure value at the pixel *i*.

Hence, we calculate the total error at each pixel of the field property as the sum of the fractional errors contributed by the x- and y-components with respect to the pool reference frame, given by,

$$\sigma_I = \sqrt{\sigma_x^2 + \sigma_y^2}$$

We utilize the mode of the distribution of error values to best represent the most

likely error estimate. We propagate this mode value of error when representing the derived parameters/metrics, i.e., accuracy of search, uncertainty of search and intensity of search

5.5.6 Identification of putative search centres:

We identify the putative search centre as the global minima of the divergence heat map. The obtained divergence heat map is separated into two images, each containing either only positive values (divergence values) or negative values (convergence values). The image with negative values is inverted to convert the minima to maxima for visual representation. Next, we normalize the intensity value to the maximum intensity value. We locate the maxima using the ImageJ's plugin Maximum Finder class. The algorithm is set such that a maximum is identified if and only if the point has a peak value difference that is more than 0.1% and that the point is not an edge.

5.5.8 Statistical analysis:

All statistical analysis was carried out in Origin (v2020b or 2021b). To perform two-way ANOVA on summarised statistics (i.e., ANOVA using mean and SEM), the raw data was recreated for 'n' individual mice by randomly sampling from a normal distribution using the population mean and SD of the metric being analysed. Based on ANOVA results, post hoc analysis was performed to carry out pair-wise comparisons. The data distribution was assumed to be normal. All data are represented as mean ± SEM.

5.6 Figures

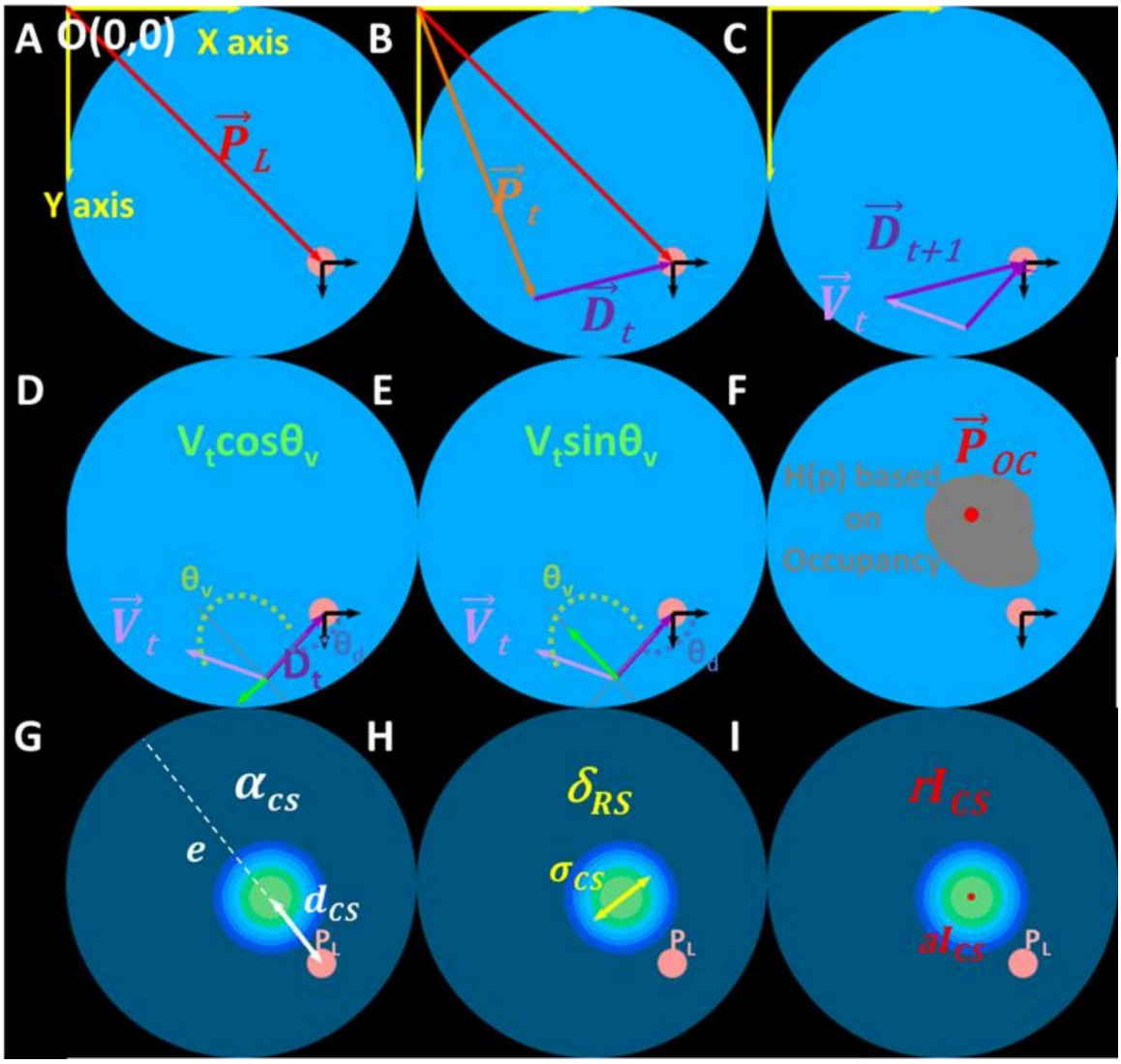

Figure 5.1: Schematic representation of the coordinate system used to describe the water maze pool and mouse trajectory as a velocity vector field. Three metrics derived from the velocity vector field that we define, and use, measure the quality of the spatial memory, namely accuracy, uncertainty, and intensity of search.

(A) The co-ordinate system and the reference frame that is used to represent the video frame data point acquired from a trial/session of a navigational behaviour. Origin of the coordinate system (O (0,0)) is located at the top left corner of the image. P_L (red arrow) is position vector of the platform (pink circle) centre.

(B) We define a position vector P_t (orange vector) as the point at which the mouse is located at a given time/video frame (*t*). Thus, the current position of the mouse to the platform location is given by the displacement vector D_t (purple vector).

(C) Velocity vector V_t (light purple vector) is calculated as the difference in displacement vectors obtained from consecutive video frames. The velocity vector describes the movement of the mouse. It is used as the base measure for developing three metrics for assessing spatial memory and its

retention.

(D) Resolving velocity vector into its components, a component along a vector pointing towards the platform from current position ($V_{\|P_L} = V_t \cos\theta v$, green vector) measures the mouse's movement that contributes toward or away from the platform. In this schematic the component is pointing away from the platform.

(E) Similarly, the velocity vector component orthogonal to the above component could represent the movement contributing to circular motion of the mice centred about the platform ($V_{\perp \mathrm{P_L}} = \mathrm{V_t} \sin\theta v$, green vector).

(F) However, to assess the quality of spatial memory, we resolve the velocity vector into its components with respect to the occupancy centre ($\vec{P}_{oc}$) given by the centre of mass (COM) of occupancy. COM calculated on a maximum entropy thresholded occupancy image and represents the most likely regions occupied by the mouse during probe trial. We create a vector field from these components to describe the mouse's intentional movement towards the occupancy centre as well as the extent of circling about that point. Analysing the field properties, namely divergence and curl, allows us to assess the spatial memory. The divergence heat map reveals convergence hotspots, the peak of which represents the putative search centres ($\vec{P}_{cs}$).

(G) We define accuracy in spatial memory (α_{cs}) as a measure that reflects the accuracy with which the mouse remembers the platform location. It is expressed as percentage of 1 minus the fractional error, where the error (d_{cs}) is the displacement between the search centre $\vec{P}_{cs}$ and the platform location P_L, and the maximum possible error (e) is the displacement of the farthest boundary/periphery of the pool from the platform.

(H) We define our second metric, uncertainty in search, as the spatial spread of the search (σ_{cs}), defined as the full width half maxima (FWHM) in x and y axis of the convergence peak. We describe the uncertainty in terms of relative search diameter (δ_{RS}), where the search diameter is normalised to platform diameter (d_{PL}).

(I) Lastly, intensity of search (I_{cs}) reveals the intensity or intent with which the mouse moves to the search centre. The absolute intensity of search (aI_{cs}) is represented by the convergence value at the search centre, whereas the relative intensity of search (rI_{cs}) is the convergence value normalised to the maximum convergence value in the pool space. Since the convergence value looks at the rate of change of the velocity vectors in a small area, the measure is not confounded by differences in swim speed among mice.

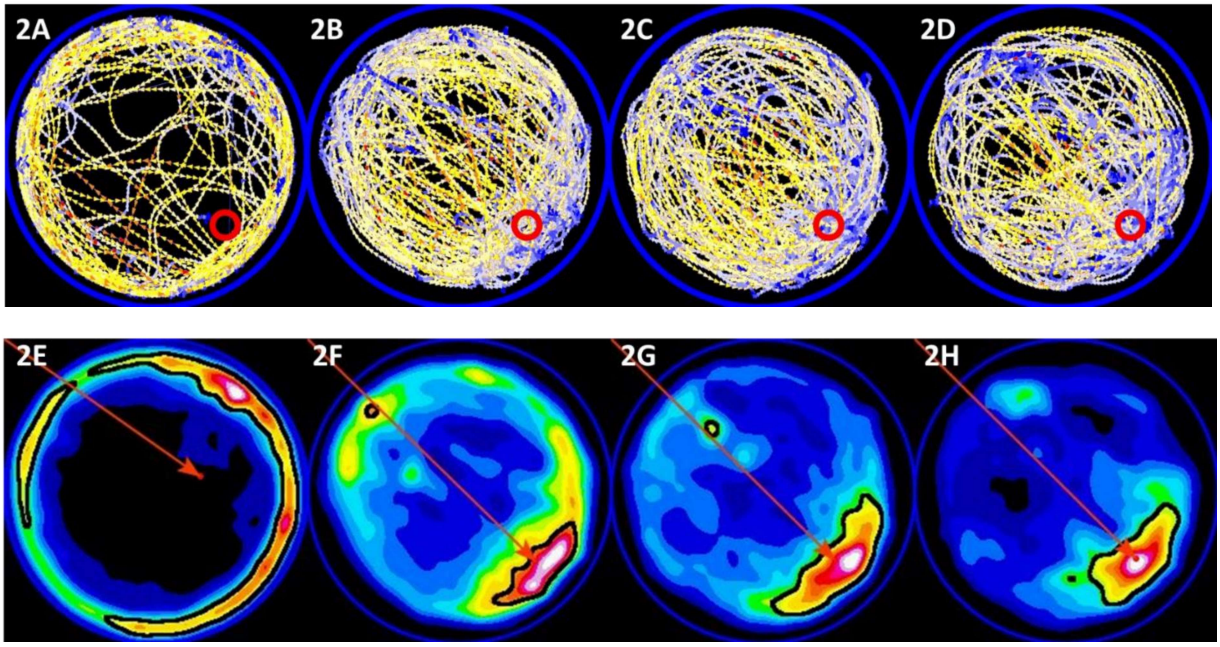

Figure 5.2: Velocity vector field, residence time heat map defines the occupancy centre.

The occupancy centre ($\vec{P}_{oc}$) is shown for the population data of *Ptpn11*+/+ wild type mice.

(A)-(D) show the velocity vector field on training day 1 (D1), probe day 3 (PD3), probe day 5 (PD5) and probe day 7 (PD7) respectively. LUT scale: 0 – 8 in pixels/frame.

(E)-(H) show the occupancy heat map on D1, PD3, PD5 and PD7 respectively. The region enclosed in black outline represents the most likely region of occupancy obtained using maximum entropy threshold (see Theory for details.) Based on the most likely region, the occupancy centre is calculated (shown as a red point). The position vector of this point in the image reference frame is shown as white arrows. See Supplementary Figures S1 and S2 for velocity vector field map, residence time heat map showing most likely occupied region, and occupancy centres for all strains/datasets used for analysis in this study. The images are Gaussian blurred (radius = 6) to approximate the point object to real world dimensions

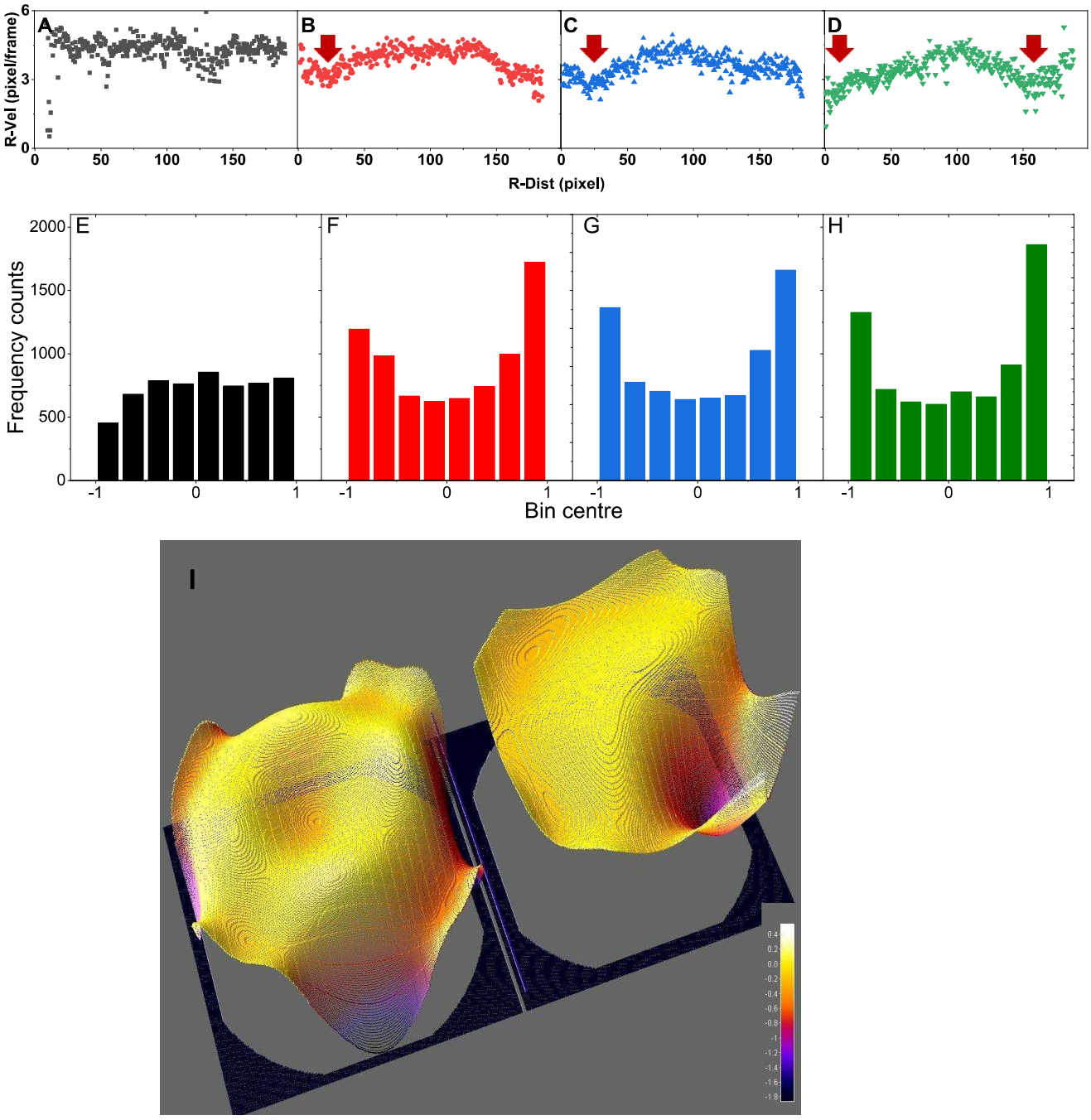

Figure 5.3: Divergence maps identify putative search centres or "sinks" as a result of differential distribution of velocity:

(A)-(D) The solid shapes (circles, squares, and triangles) are the magnitude of velocity (R-Vel) measured as a function of radial distance (R-Dist) on training and probe days (D1, PD3, PD5 and PD7 respectively). On D1 the speed of the mice is invariant across space as the scatter plot is almost parallel to the x axis representing the distance from the platform. With training, the speed of the mice is reduced near the platform and boundary ($r \rightarrow 0$ or $r \rightarrow 200$ pixels). R-Dist is in bins of 0.5 pixel and R-Vel represented as an average of all the times the animal traversed that bin.

(E)-(H) Histogram of efficiency of movement toward occupancy centre, given by $V_{||}/V_t$, in Ptpn11 +/+ mice on D1, PD3, PD5 and PD7 indicated as a function of training. The fraction of the

movements oriented along the occupancy centre increases as shown by the counts in bins -1 (aligned completely but away from occupancy centre) and 1 (aligned completely toward the occupancy centre).

(I) Surface plot of divergence measure that is developed in theory generated using dataset Ptpn11 +/+ mice on Day 1(left) and on PD7 (right) shows that spatially uniform progressive reduction in speed leading to convergence peaks (negative divergence seen as valleys). Such convergence peaks are analogous to sinks in electro/fluid dynamics. On Day 1 the divergence surface is largely invariant across the pool surface except for a mild depression at the centre and at periphery of the pool. On probe day 7, as the mice acquires the spatial memory for the platform location the surface changes its shape and has a clear valley centred around the platform location.

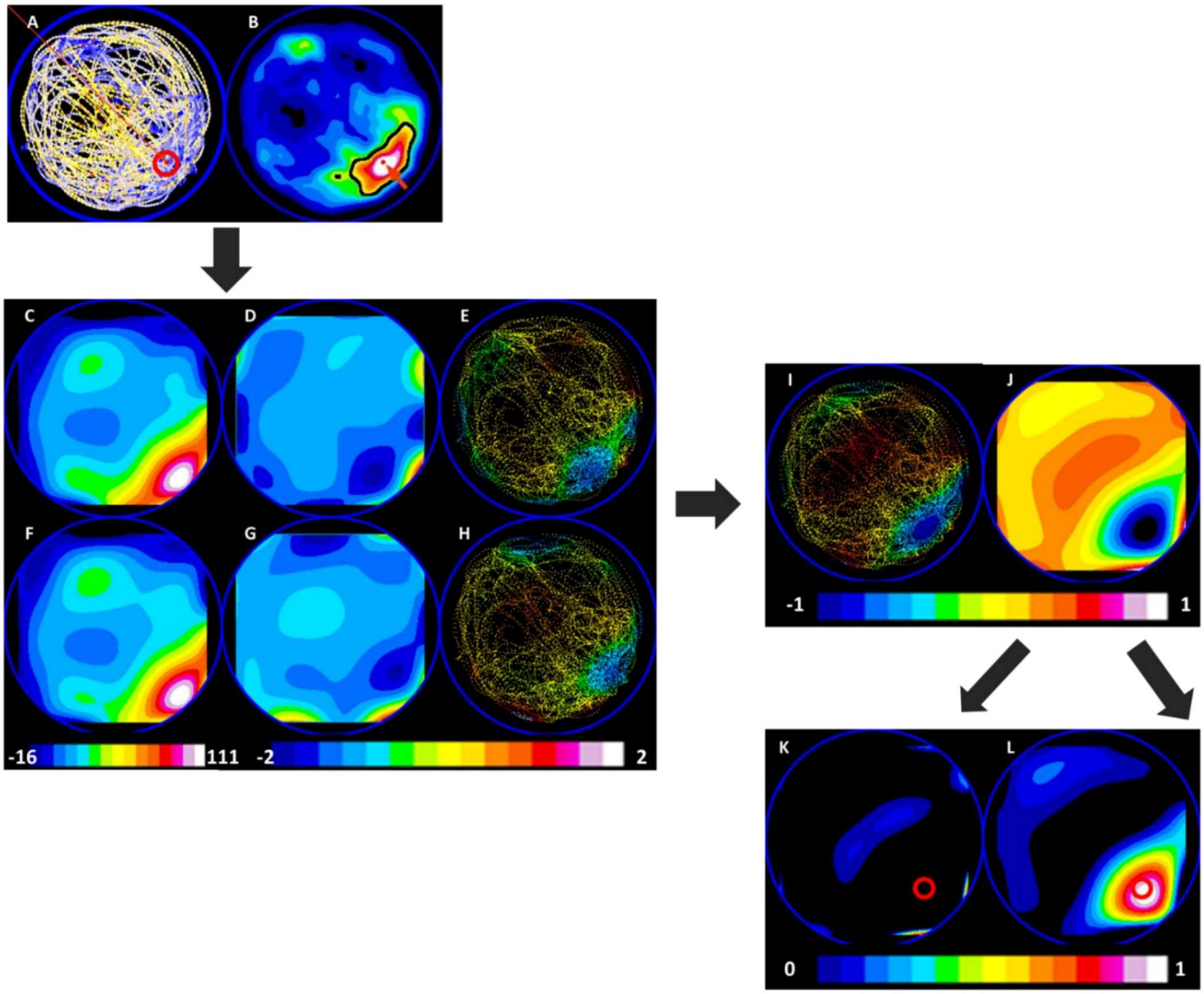

Figure 5.4: Workflow to generate divergence heat map revealing convergence hotspots.

(A) shows the population velocity vector field (n = 15 mice, data points = 8997 frames).

(B) shows the occupancy heat map. Using maximum entropy auto thresholding, the area for estimating COM of occupancy is determined (demarcated in black ROI). Occupancy centre is marked as a red dot. The red arrow indicates the position vector of the occupancy centre.

(C) and (F)Using the velocity vector field and the occupancy centre, velocity vector component along the P_{oc} ($V_{\parallel}$) was generated for spatially resolved components of the velocity vector, i.e. x-Image and y-Image. The x-Image (C) is the component along the horizontal axis, whereas the y-Image (F) is the component along the vertical axis.

An ROI encompassing the pixels that have been sampled is used to obtain an image that is a 5th order polynomial surface fit (D and G), thus obtaining a surface describing the velocity-based movement towards the occupancy centre. The change in measure along the horizontal or vertical axis is obtained by taking the differential with respect to x-axis or y-axis. We maintain the calculated values in the pixels that were sampled. (E)shows the differential with respect to x-axis for the x-Image, and (H)shows the differential with respect to y-axis for the y-Image, for the pixels sampled by the mice.

Adding the differential images (E) and (H) gives the divergence map as shown in (I). A smooth surface (J) representing the divergence values continuously in space is obtained after a 4th Order surface fit on (I). The divergence map (J) is split into an image with only positive values to represent the points of divergence (K), and only negative values to represent the convergence hotspots (L).

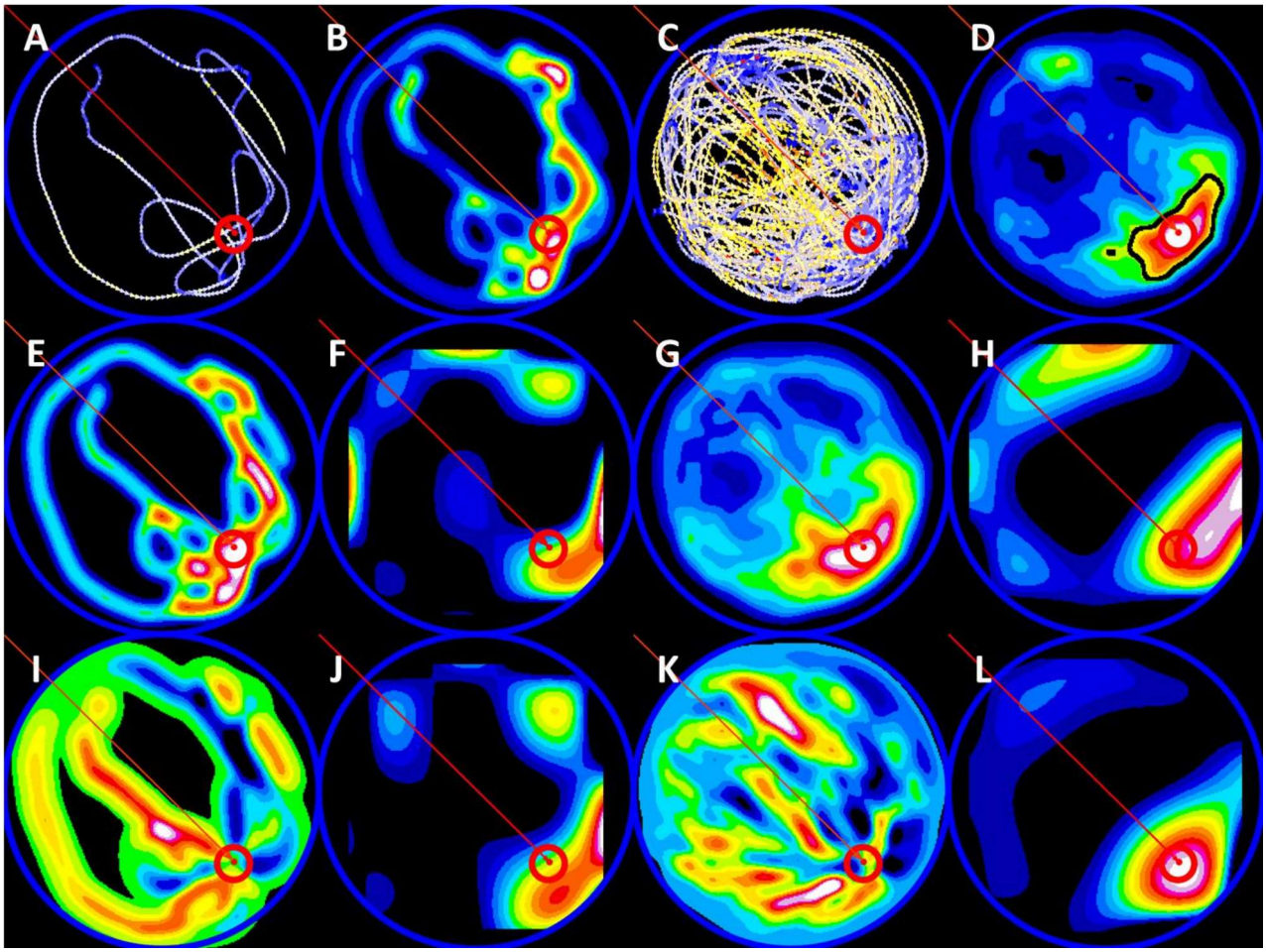

Figure 5.5: Component of the velocity along the occupancy centre and not the velocity is better at identifying putative search centre.

(A) and (C) show the velocity vector field maps for an individual *Ptpn11*+/+ mouse and a population of *Ptpn11*+/+ mice (n =15) on PD7 respectively.
(B) and (D) show the occupancy map for individual and population of mice. The most likely region is demarcated as a black outline in (D). This region is identified based on maximum entropy segmentation for the population representation. Subsequently, the occupancy centre is estimated and shown as a red arrow in both (B) and (D).
(E) and (G) are the velocity magnitude heat maps for the individual mouse and population respectively. Divergence calculated in Cartesian coordinates is used to generate a map and is placed inside the pool image. Bounding rectangle is used to orient and place the divergence map inside pool. The generated velocity vector fields reveal the search centres as convergence hotspots as shown in (F) and (H).
In comparison, (I) and (K) represent the heat map representing the magnitude of velocity vector component along the occupancy centre for individual mouse and population, respectively. The divergence calculated as above using these vector fields are placed in the pool image and resultant images show prominent and localised convergence hotspots identified by boundary in blue dashed lines. We term these convergence hotspots in velocity component maps as the putative search centres (P_{cs}). We use the vector field representing the population of mice during a session in subsequent analysis for identifying the search centre.
Blue ROI marks the pool perimeter and red ROI marks the platform. Vector field map (A and C) LUT scale: 0 – 8 pixel/frame.

5.7 References

2D Gaussian fitting macro (Fiji/ImageJ) for multiple signals. | *BIII*. (n.d.). Retrieved May 10, 2021, from https://biii.eu/2d-gaussian-fitting-macro-fijiimagej-multiple-signals

Brandeis, R., Brandys, Y., & Yehuda, S. (1989). The use of the Morris water maze in the study of memory and learning. *International Journal of Neuroscience*, *48*(1–2), 29–69. https://doi.org/10.3109/00207458909002151

Cooke, M. B., O'Leary, T. P., Harris, P., Brown, R. E., & Snyder, J. S. (2019). Pathfinder: Open source software for analyzing spatial navigation search strategies. *F1000Research*, *8*. https://doi.org/10.12688/f1000research.20352.1

D'Hooge, R., & De Deyn, P. P. (2001). Applications of the Morris water maze in the study of learning and memory. In *Brain Research Reviews* (Vol. 36, Issue 1, pp. 60–90). Elsevier. https://doi.org/10.1016/S0165-0173(01)00067-4

Dalm, S., Grootendorst, J., De Kloet, E. R., & Oitzl, M. S. (2000). Quantification of swim patterns in the Morris water maze. *Behavior Research Methods, Instruments, and Computers*, *32*(1), 134–139. https://doi.org/10.3758/BF03200795

Gallagher, M., Burwell, R., & Burchinal, M. R. (1993). Severity of spatial learning impairment in aging: Development of a learning index for performance in the Morris water maze. *Behavioral Neuroscience*, *107*(4), 618–626. https://doi.org/10.1037//0735-7044.107.4.618

Garthe, A., Behr, J., & Kempermann, G. (2009). Adult-generated hippocampal neurons allow the flexible use of spatially precise learning strategies. *PLoS ONE*, *4*(5). https://doi.org/10.1371/journal.pone.0005464

Gehring, T. V., Luksys, G., Sandi, C., & Vasilaki, E. (2015). Detailed classification of swimming paths in the Morris Water Maze: Multiple strategies within one trial. *Scientific Reports*, *5*(1), 14562. https://doi.org/10.1038/srep14562

Graziano, A., Petrosini, L., & Bartoletti, A. (2003). Automatic recognition of explorative strategies in the Morris water maze. *Journal of Neuroscience Methods*, *130*(1), 33–44. https://doi.org/10.1016/S0165-0270(03)00187-0

Lee, Y. S., Ehninger, D., Zhou, M., Oh, J. Y., Kang, M., Kwak, C., Ryu, H. H., Butz, D., Araki, T., Cai, Y., Balaji, J., Sano, Y., I Nam, C., Kim, H. K., Kaang, B. K., Burger, C., Neel, B. G., & Silva, A. J. (2014). Mechanism and treatment for learning and memory deficits in mouse models of Noonan syndrome. *Nature Neuroscience*, *17*(12), 1736–1743. https://doi.org/10.1038/nn.3863

Maei, H. R., Zaslavsky, K., Teixeira, C. M., & Frankland, P. W. (2009). What is the most sensitive measure of water maze probe test performance? *Frontiers in Integrative Neuroscience*, *3*(MAR). https://doi.org/10.3389/neuro.07.004.2009

Maei, H. R., Zaslavsky, K., Wang, A. H., Yiu, A. P., Teixeira, C. M., Josselyn, S. A., Frankland, P. W., & Maei, Hamid R., Zaslavsky, Kiriil, Wang, Afra H., Yiu, Adelaide P., Teixeira, Catia M., Josselyn, Sheena A., Frankland, P. W. (2009). Development and validation of a sensitive entropy-based measure for the water maze. *Frontiers in Integrative Neuroscience*, *3*(DEC). https://doi.org/10.3389/neuro.07.033.2009

Morris, R. (1984). Developments of a water-maze procedure for studying spatial learning in the rat. *Journal of Neuroscience Methods*, *11*(1), 47–60. https://doi.org/10.1016/0165-0270(84)90007-4

Morris, R. G. M. (1981). Spatial localization does not require the presence of local cues. *Learning and Motivation*, *12*(2), 239–260. https://doi.org/10.1016/0023-9690(81)90020-5

Overall, R. W., Zocher, S., Garthe, A., & Kempermann, G. (2020). Rtrack: A software package for reproducible automated water maze analysis. In *bioRxiv* (p. 2020.02.27.967372). bioRxiv. https://doi.org/10.1101/2020.02.27.967372

Pereira, I. T., & Burwell, R. D. (2015). Using the spatial learning index to evaluate performance on the water maze. *Behavioral Neuroscience*, *129*(4), 533–539. https://doi.org/10.1037/bne0000078

Petrosini, L., Leggio, M. G., & Molinari, M. (1998). The cerebellum in the spatial problem solving: A co-star or a guest star? *Progress in Neurobiology*, *56*(2), 191–210. https://doi.org/10.1016/S0301-0082(98)00036-7

Redish, A. D., & Touretzky, D. S. (1998). The Role of the Hippocampus in Solving the Morris Water Maze. *Neural Computation*, *10*(1), 73–111. https://doi.org/10.1162/089976698300017908

Sahoo, P. K., Soltani, S., & Wong, A. K. C. (1988). A survey of thresholding techniques. In *Computer Vision, Graphics and Image Processing* (Vol. 41, Issue 2, pp. 233–260). Academic Press. https://doi.org/10.1016/0734-189X(88)90022-9

Unser, M. (1999). Splines: A Perfect Fit for Signal and Image Processing. *IEEE Signal Processing Magazine*, *16*(6), 22–38. https://doi.org/10.1109/79.799930

Vouros, A., Gehring, T. V., Szydlowska, K., Janusz, A., Tu, Z., Croucher, M., Lukasiuk, K., Konopka, W., Sandi, C., & Vasilaki, E. (2018). A generalised framework for detailed classification of swimming paths inside the Morris Water Maze. *Scientific Reports*, *8*(1), 15089. https://doi.org/10.1038/s41598-018-33456-1

Wolfer, D. P., & Lipp, H. P. (1992). A new computer program for detailed off-line analysis of swimming navigation in the Morris water maze. *Journal of Neuroscience Methods*, *41*(1), 65–74. https://doi.org/10.1016/0165-0270(92)90124-V

CHAPTER 6

Comparative analysis of spatial memory in different mouse strains using Morris Water Maze task

Abstract

In the previous chapter, we developed a framework for describing the search pattern of animals in a navigational task using vector field and their properties. We characterised spatial memory using three metrics: accuracy, uncertainty, and intensity of search. Here, we use the framework to detect and distinguish spatial memory in different strains of mice. The first dataset compares the spatial memory in two albino strains of mice (BALB/cJ and SWR/J). We see that BALB/cJ and SWR/J mice learn the platform location at different rates in MWM paradigm. Next, we demonstrate a wider applicability of our method by analysing two strains of mice (C57Bl/6J and DBA/2J) trained in a goal reversal task. Our analysis clearly demonstrates that the accuracy of the search is high and is preserved for both old and new platform locations while the intention of search is higher for the new platform location. In summary, the proposed metrics resolves the information of spatial memory into measurable independent components, enabling us to differentiate memory representation that are normally not possible to elucidate from conventional measures.

Acknowledgments

I would like to thank Prof. Kempermann and Prof. Rupert Overall, CRTD, Dresden for allowing the use of the publicly shared C57Bl/6J and DBA/2J water maze data to assess the developed measures with respect to a goal reversal task.

6.1 Introduction

Animal models are widely used in neuroscience as it allows investigating the molecular, cellular and network level mechanisms of different cognitive tasks that cannot be carried out in human subjects (Rosenthal & Brown, 2007). There are multiple criteria that an animal model need to satisfy and one of them being that their endophenotype is equivalent of the human version of the illness (Bedell, Jenkins, et al., 1997; Bedell, Largaespada, et al., 1997; Justice & Dhillon, 2016). In these cases where the role of a specific gene or disease model is studied, the mice are inbred to maintain a homogenous genetic background such that an experimental design and its results and inferences are not influenced by other genetic factors. Typically, the genetic background and hence the mouse strain used for deriving the mouse model is dictated by practical considerations. Thus, it is vital to establish a baseline response of inbred mice strains using a battery of behavioural tasks.

Comparative studies between different strains of mice helps to establish the best strain that are suited for different behavioural tasks (Crawley et al., 1997; Upchurch & Wehner, 1988). For example, C57Bl/6J strain are suitable for hippocampal dependent tasks such as contextual fear conditioning or Morris water maze, however they are not the most suitable for auditory fear conditioning since their hearing decline with age. In contrast, DBA/2J have been shown to have poor performance in CFC and MWM, possibly due to functional differences in hippocampal formation, but are suitable for auditory fear conditioning (AFC) (Paylor et al., 1994).

Strain comparisons for MWM performance assessed via quadrant-based residence time shows that C57Bl/6J and DBA mice learn the WMW whereas BALB/cJ show poor performance (Brooks et al., 2005). The finding supports previous reports that C57Bl/6J are good learners (Stavnezer et al., 2002). However, the swim speeds vary among strains thereby making these comparisons difficult and ineffective. For example, in a study, BALB/cJ strain are the slowest to reach a marked platform, with DBA/2J strain swimming faster than BALB/cJ, and C57Bl/6J being the fastest swimmer (Brooks et al., 2005). The variation in speed could affect the quadrant-based residence time computed to assess memory for

platform in the hidden version of the MWM. Additionally, SWR/J strain of mice have been shown to have retinal degeneration, which affects their visual acuity (Wahlsten et al., 2005). Hence, we predict that these mice may perform poorly in MWM task.

A modified version of the MWM is the goal reversal task. Here, the platform is usually shifted to a different position in space that is sufficiently distinct. Thus, in the new configuration the new platform location is different while the spatial cues remain intact. The task tests for the flexibility of the animal in learning the new location and its ability to shift the search strategy from the old platform location to the new location, i.e., the ability to reverse the rules that have been learnt previously. Rule reversal learning has been adapted for other behavioural tasks involving forced 2-choice. For example, reports show that DBA strain perform better than C57Bl6 in rule reversal learning carried out in an odour discrimination (Mihalick et al., 2000) as well as a visual discrimination(Brooks et al., 2005).

In this context, we compare the spatial memory of two strains of albino mice in a reference version of the MWM. We assess the memory in terms of the metrics developed in Chapter 5 and contrast it with three measures used in the field: residence time, proximity, and entropy.

6.2 Results

6.2.1 Accuracy, uncertainty and intensity of search centres distinguish the nature of spatial memory between two albino strains of mice: BALB/cJ and SWR/J.

We analysed the WM swim trajectories of the BALB/cJ and SWR/J mouse strains. The divergence heat maps show a distinct convergence hotspot for both, BALB/cJ (n = 10) and SWR/J (n=9/10), groups of mice on all three probe days (i.e., PD3, PD7 and PD10 (Fig. 6.1 (A-D)). On calculating the accuracy in search for BALB/cJ mice, we observed as expected that the accuracy increases progressively and reaches an asymptote with additional training (Fig. 6.1 (E), Green solid bars, α_{cs} = 80 ± 2.2% (PD3), α_{cs} = 91 ± 1.3% (PD7), α_{cs} = 95 ± 1.5% (PD10)), reflecting accurate knowledge of the platform's location. Comparatively, SWR/J mice show an accuracy worse than chance levels (as defined in the theory section Eq. (xii)) on a probe trial at day 3 (PD3) and PD7, indicating that the mice are searching away from both the pool centre and the platform's location. Further training of SWR/J mice marginally improves the accuracy on PD10 (Fig. 6.1 (F), Blue solid bars, α_{cs} = 51 ± 0.66% (PD3), α_{cs} = 61 ± 1.15% (PD7), α_{cs} = 74 ± 1.41% (PD10)). The occupancy-based quadrant and platform measures show that SWR/J mice do not preferentially reside in the target quadrant (P4/Q4) on PD3, but with training, these mice preferentially reside in the training platform zone on PD10 (Fig. 6.2 (H), (J)). However, our analysis of swim trajectories shows that these mice focus their search away from both the platform location and the pool centre, indicating that they lack a specific, localised spatial memory of the platform's location. However, on PD10 these mice do show signs of having acquired a specific spatial memory for the platform's location.

Additionally, the relative search diameter increases as a function of probe trials for both BALB/cJ and SWR/J mice (Fig. 6.1 (G), BALB/cJ: Green diagonal bars, δ_{RS} = 7 ± 0.20(PD3), δ_{RS} = 9 ± 0.13 (PD7), δ_{RS} = 10 ± 0.17 (PD10) and Fig.6.1 (H), SWR/J: Blue diagonal bars, δ_{RS} = 3.17 ± 0.04 (PD3), δ_{RS} = 12.50 ± 0.24 (PD7), δ_{RS} = 5 ± 0.28 (PD10)). With training, their search strategies around the search centre

appear to shift from focussed and localised searches to more diffused and generalised searches.

For BALB/cJ mice, the search intensity is highest on the first probe trial (PD3; Fig. 6.5 (I), Green hatched bars, rI_{cs} = 61 ± 2%). Combined with the accuracy value, these two measures suggest that the mice have learned the platform location and concentrate their searches in the correct location. However, on PD7, there is a reduction in the intensity of the searches (rI_{cs} = 25 ± 0.4%). Since the accuracy of the search centre is high (>90%), the reduction in intensity could possibly be due to a memory of searching for the absent platform in PD3. The results suggest that the memory of the platform location is intact, but that the intention to locate it is reduced because there may be some acquired knowledge during PD3 that it may be absent from the pool. On PD10, the mice show an improvement in search intensity (rI_{cs} = 40 ± 0.6%), potentially reflecting the effect of continued extended training between PD3 and PD10.

In SWR/J mice, the intensity of search improves from PD3 to PD10 (Fig. 6.1 (J), Blue hatched bars, rI_{cs} = 6.6 ± 0.086% (PD3), rI_{cs} = 11.5 ± 0.22% (PD7), rI_{cs} = 59.3 ± 3.38% (PD10). The extent of this search intention is poor (<50%) for PD3 and PD7, reflecting poor spatial learning.

Thus, using convergence peaks as search centres, we can describe and compare the quality of spatial learning and memory across different probe trials for different strains of mice. From our comparisons, we find that the BALB/cJ mice perform better in the MWM than the SWR/J strain of mice.

6.2.2 Spatial memory of old platform location and new platform location is preserved in C57Bl/6J and DBA/2J mice trained in a goal reversal task.

Next, we analyse a publicly available dataset (Overall et al., 2020) containing two strains of mice (C57Bl/6J and DBA/2J) trained in a goal reversal task to highlight the power of the current vector field property-based measure in detecting search centres. We hypothesize that in such a task involving platform switching, the mice possess memories of both the old (conflict) and new (target) platform locations, and that due to recency effect, they bias their search to the new platform location.

Previously it has been found that DBA/2J mice perform differently in contextual memory tasks compared to other inbred strains due to functional differences in the hippocampal formation. In line with the above finding, we find that DBA/2J perform poorly in that, they do not show the presence of a specific search centre on PD3 (Fig. 6.3 (C)). In comparison, C57Bl/6J learn the platform with an accuracy of 86 ± 3 %, relative search diameter of 4.4 ± 0.15 and relative search intensity of 100 ± 3 (Fig. 6.3 (A), (E), (G), (I)).

As predicted, our method successfully reveals the presence of two convergence peaks or search centres on probe day 5 (PD5). The search centres correspond to the memory for the target location, i.e., the platform in north-east quadrant on training days 3 and 4, as well as memory for the conflict location, i.e., the platform in the south-west quadrant on training on days 1 and 2 (Fig. 6.3 (A-D)). Quantifying the search centres in terms of accuracy, uncertainty and intensity of search reveals the difference in nature/properties of the two memories.

We do not see a difference in accuracy of the search centres to their respective platform positions, i.e., search centre near the target location (Peak#1 new) and search centre near the conflict location (Peak#2 old). We conclude that since the mice recall the old as well as the new platform location with similar accuracy, the strength of memory for both the locations is high (Fig. 6.3 (E-F)).

In C57Bl/6J mice, we see that the relative intensity of search (rI_{cs}) at the search centre corresponding to the new platform location, Peak#1 new, is significantly higher than the relative intensity of search corresponding to the old platform location, Peak#2 old (Fig.6.3(I)). We infer that the recency effect of the new platform location biases the mice to search more intently in the target location. However, when it does not find the platform at the target location, it also investigates the conflict location, although it spends considerably less time in its search here. Similarly, we see the relative intensity of search (rI_{cs}) at the search centre corresponding to the new platform location, Peak#1 new, is slightly higher than the relative intensity of search corresponding to the new platform location, Peak#1 old in DBA/2J mice (Fig. 6.3 (J)). We infer that the mice search both platform locations, though it prefers to search at the new platform location slightly more intensely. Similar to C57Bl/6J, the DBA/2J mice search at the most recent

training location, although they never truly learnt the first platform location.

Since the purpose of this study was to determine whether training resulted in goal reversal, we defined a goal reversal efficiency measure (GRE) as rI_{cs} at the new location subtracted by the rI_{cs} at the old platform location divided by the sum of rI_{cs} at both the old and the new platform locations $\left(\mathrm{GRE} = \frac{rIcs_{new} - rIcs_{old}}{rIcs_{new} + rIcs_{old}}\right)$. A ratio of 1 in this measure would indicate goal reversal, while -1 would indicate no reversal, and 0 would mean no learning. We find the goal reversal efficiency for C57Bl/6J to be ~0.78 and DBA/2J to be~0.15, indicating that C57Bl/6J are more adapt at goal reversal than DBA/2J mice.

6.3 Discussion

We utilized the swim trajectories from different mice datasets performing Morris water maze task to illustrate the sensitivity and advantage of the newly proposed metrics. Analysing swim trajectories using the proposed metrics enabled us to detect memory deficits in different datasets of MWM task. We showed difference in strength of spatial memory for two different mice strains subjected to the same training paradigm (BALB/cJ and SWR/J). We also investigated whether the divergence field property on velocity-based measure could detect the presence of multiple search centres or spatial memories by analysing dataset of MWM goal reversal task. We see that the two strains of mice C57Bl/6J and DBA/2J, when trained in a reversal learning scheme involving two platforms, show the presence of two search centres, corresponding to the old/conflict as well as the new/target platform location. We are able to quantify the difference in strength or nature of these two spatial memories in terms of the extent of intention of search at their two locations or search centres, showing that both strains of mice prefer to search at the most recently trained platform location.

6.4 Materials and Methods

6.4.1 Animal and behaviour paradigm information

BALB/cJ (Stock no: 000651) and SWR/J (Stock no: 000689) inbred mice were obtained from Jackson Laboratory, USA and maintained at the Central Animal Facility, IISc. All protocols were approved by the Institute Animal Ethics Committee. 10 mice of each strain were trained in MWM task, and probed from spatial memory on days 3, 7 and 10.

5 ten-week-old female mice of C57Bl/6J (JAX Stock no: 000664) and DBA/2J (JAX Stock no: 000671) were trained in a goal reversal task as previously reported in (Overall et al., 2020). Briefly, Mice were trained for 6 trials per day for 3 days. For goal reverse task, mice were trained at the reversed goal location for 2 days. Days 3 and 5 were probe trials.

6.4.2 Generation divergence heat maps and estimated of search centre

Divergence heat maps and the putative search centres were calculated as developed in chapter 5 (Fig. 5.4, Section 5.5.3, Section 5.5.6).

6.4.3 Estimation of full width half maximum (FWHM) of convergence peak:

We estimate the FWHM of a convergence peak as previously described (*2D Gaussian fitting macro (Fiji/ImageJ) for multiple signals.* | *BIII*, n.d.). Briefly, the identified putative search centre is fit to a linearised 2D-gaussian function to obtain the FWHM in x- and y-axis. The size of the peak is initialised to 20 pixels before performing custom fit using ImageJ's Curve Fitter class implementing Simplex algorithm.

6.4.4 Statistical analysis:

All statistical analysis was carried out in Origin (v2020b or 2021b). To perform two-way ANOVA on summarised statistics (i.e., ANOVA using mean and SEM), the raw data was recreated for 'n' individual mice by randomly sampling from a normal distribution using the population mean and SD of the metric being analysed. Based on ANOVA results, post hoc analysis was performed to carry out pair-wise

comparisons. The data distribution was assumed to be normal. All data are represented as mean ± SEM.

6.5 Figures

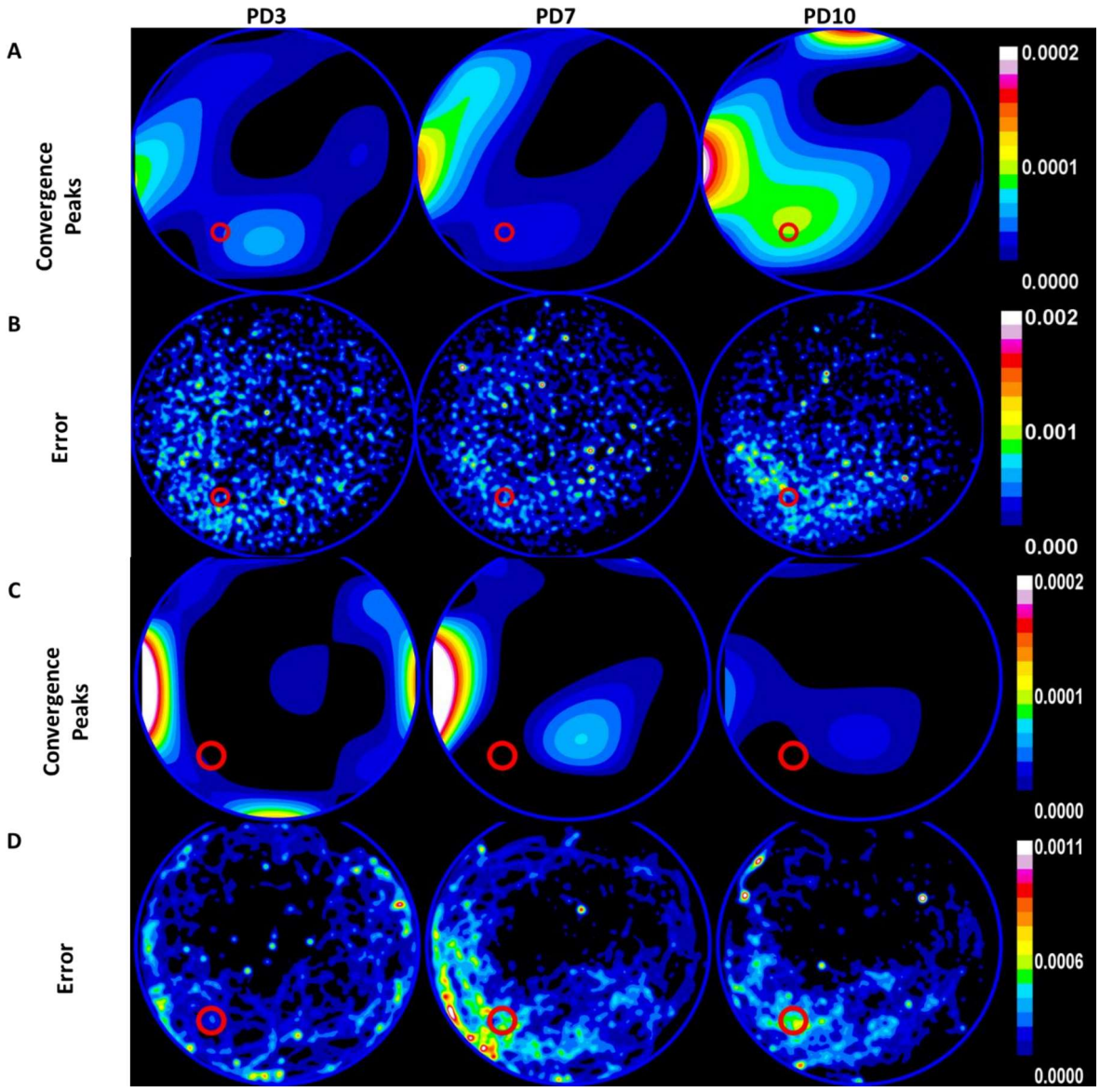
PD3
PD7
PD10
A
Convergence Peaks
0.0002
0.0001
0.0000
B
Error
0.002
0.001
0.000
C
Convergence Peaks
0.0002
0.0001
0.0000
D
Error
0.0011
0.0006
0.0000

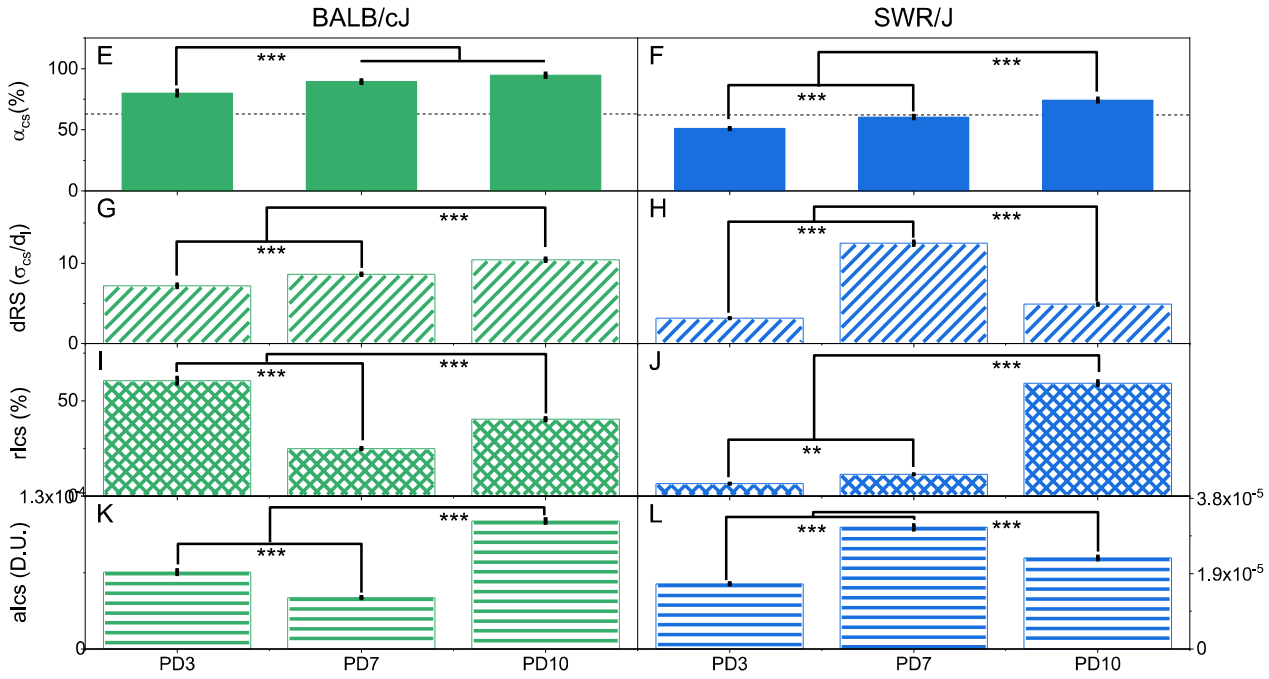

Figure 6.1: Description of spatial memory in BALB/cJ and SWR/J strain of mice using the three parameters: accuracy (α), uncertainty (δ_{RS}), and intensity of search (I_{cs}).

(A) and (C) are the divergence heat maps showing the convergence hotspots for the population of BALB/cJ (n=10, A) and SWR/J (n = 9-10, C) mice, respectively, on probe day 3 (PD3), probe day 7 (PD7) and probe day 10 (PD10).

(B) and (D) are the error heat maps of the calculated divergence within the population of mice of BALB/cJ (B) and SWR/J (D) mice. A 2D Gaussian smoothing of radius = 5 (BALB/cJ) or 10(SWR/J) is used for visual representation. Pool perimeter is shown as a blue circle and the platform location is shown as red circle.

(E) and (F) describe the accuracy of search centre for BALB/cJ (E) and SWR/J (F). The accuracy in search increases to maximum asymptotically across probe trials for BALB/cJ mice (Green solid bars, α = 80± 2.2 % (PD3), α = 91 ± 1.3 % (PD7), α = 95 ± 1.5 %(PD10)) as expected. Comparatively, SWR/J mice show poor accuracy for the platform below chance level (defined in theory) on PD3 and at chance on PD7 (One-sample t-test, PD3: $p < 0.001$, PD5: $p > 0.05$) whereas it shows an improvement in accuracy ($p < 0.001$) on PD10 (Blue solid bars, α = 51 ± 0.66 (PD3), α = 61 ± 1.15 (PD7), α = 74 ± 1.41 (PD10)). Dashed line shows the chance accuracy value (BALB/cJ: 63%, SWR/J: 62%). Two-way ANOVA with mice strain and training (measured across probe days) as factors revealed that accuracy is significantly different among the mice strain ($F_{1,52} = 467$, $p < 0.001$), and across training ($F_{2,52} = 82$, $p < 0.001$), however with a significant interaction between the mice strain and their training ($F_{2,52} = 5.66$, $p< 0.01$). Subsequent post hoc analysis indicated that BALB/cJ and SWR/J mice improved its accuracy over training. Based on the difference in accuracy, we conclude that BALB/cJ are better learners than SWR/J mice.

(G) and (H) describes the uncertainty in search centre as relative search diameter (δRS) for BALB/cJ and SWR/J mice respectively. The search strategy around the search centre appears

focused in nature on PD3 for BALB/cJ (Green diagonal bar, δRS = 7 ± 0.20). In case of the SWR/J mice, although the search centre is inaccurate, its search is focused (Blue diagonal bar, δRS = 3.17 ± 0.04). The relative search diameter increases on subsequent probe trials, indicating that both strains of mice use a more diffused search strategy in later probe trials (BALB/cJ: Green diagonal bars, δRS = 9 ± 0.13 (PD7), δRS = 10 ± 0.17 (PD10) and SWR/J: Blue diagonal bars, δRS = 12.50 ± 0.24 (PD7), δRS = 5 ± 0.28 (PD10)). Two-way ANOVA for uncertainty with mice strain and training showed that the means of the strains are significantly different ($F_{1,52} = 217$, $p < 0.001$), training had an effect ($F_{2,52} = 586$, $p < 0.001$) however the effect of training is different among the strains as there is an interaction (: $F_{2,52} = 504$, $p < 0.001$) between these factors. Post hoc analysis revealed that the search diameter shows a differential change as function of training.

(I) and (J) represents the relative search intensity (rIcs) for BALB/cJ and SWR/J mice. Since the relative intensity of search is obtained from normalising the absolute intensity at search centre with the maximum intensity observed during the session, we can compare the relative intensity across datasets that have been sampled at different frame rates. In BALB/cJ mice, the relative search intensity on the PD3 is the highest (Green hatched bars, rIcs = 61 ± 2%). However, on PD7, the intensity of search reduces (rIcs = 25 ± 0.4%) possibly due to effect of extinction but recovers and increases at PD10 (rIcs = 40 ± 0.6%). In SWR/J mice, the intensity of search improves with probe trials (Blue hatched bars, rIcs = 6.6 ± 0.086% (PD3), rIcs = 11.5 ± 0.22% (PD7), rIcs = 59.3 ± 3.38% (PD10)) though the overall extent of this search intention is poor (<50%). Two-way ANOVA for relative search intensity with strain and training as factors showed that the search intensity significantly differed both as function of strain ($F_{1,52} = 488$, $p < 0.001$) as well as training ($F_{2,52} = 608$, $p < 0.001$) with a strong interaction ($F_{2,52} = 835$, $p< 0.001$). Post hoc analysis substantiated our interpretation stated above.

(K) represents the absolute search intensity (aIcs) for BALB/cJ on PD3, PD7, and P10. In BALB/cJ mice, the intensity of search is given in green horizontal bars, aIcs = 6.5E-5 ± 1.8E-6 (PD3), aIcs = 4.4E-5 ± 6.6E-7 (PD7), aIcs = 1.1E-4 ± 1.7E-6 (PD10)). One-way ANOVA for absolute search intensity showed the means of the absolute search intensity are significantly different ($F_{2,27} = 488$, $p < 0.001$). Post hoc analysis established that the differences between the probe trail days are significant.

(L) represents the absolute search intensity (aIcs) for SWR/J mice on PD3, PD7, and P10. In SWR/J mice, the intensity of search improves with probe trials (Blue horizontal bars, aIcs = 1.64E-5 ± 2.13E-7 (PD3), aIcs = 3.07E-5 ± 1.749E-6 (PD7), aIcs = 2.29E-5 ± 4.36E-7 (PD10)). One-way ANOVA for absolute search intensity showed the means of the absolute search intensity are significantly different ($F_{2,25} = 286.7677$, $p < 0.001$). Post hoc analysis established that the progressive increase seen across the probe trial days is significant.

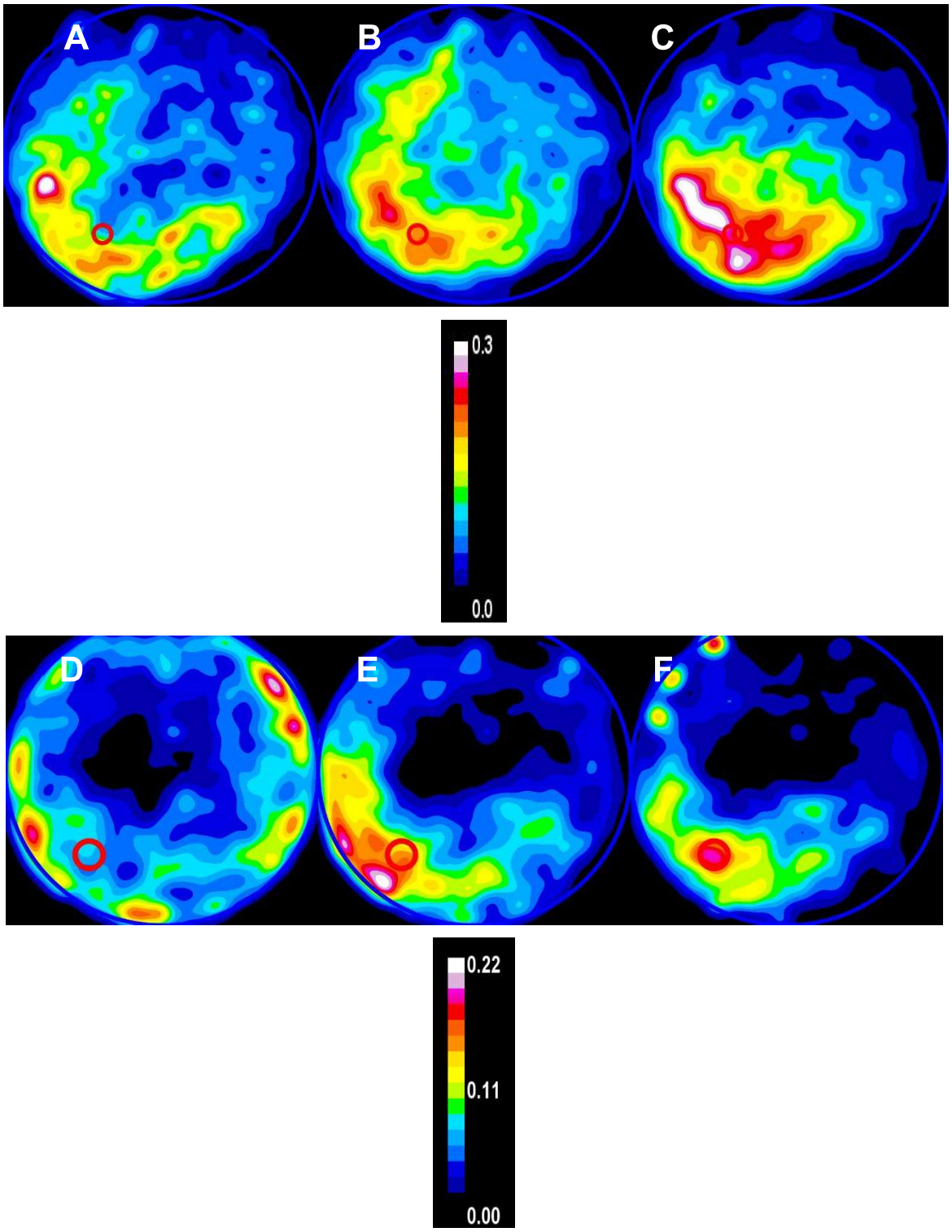
A
B
C
0.3
0.0
D
E
F
0.22
0.11
0.00

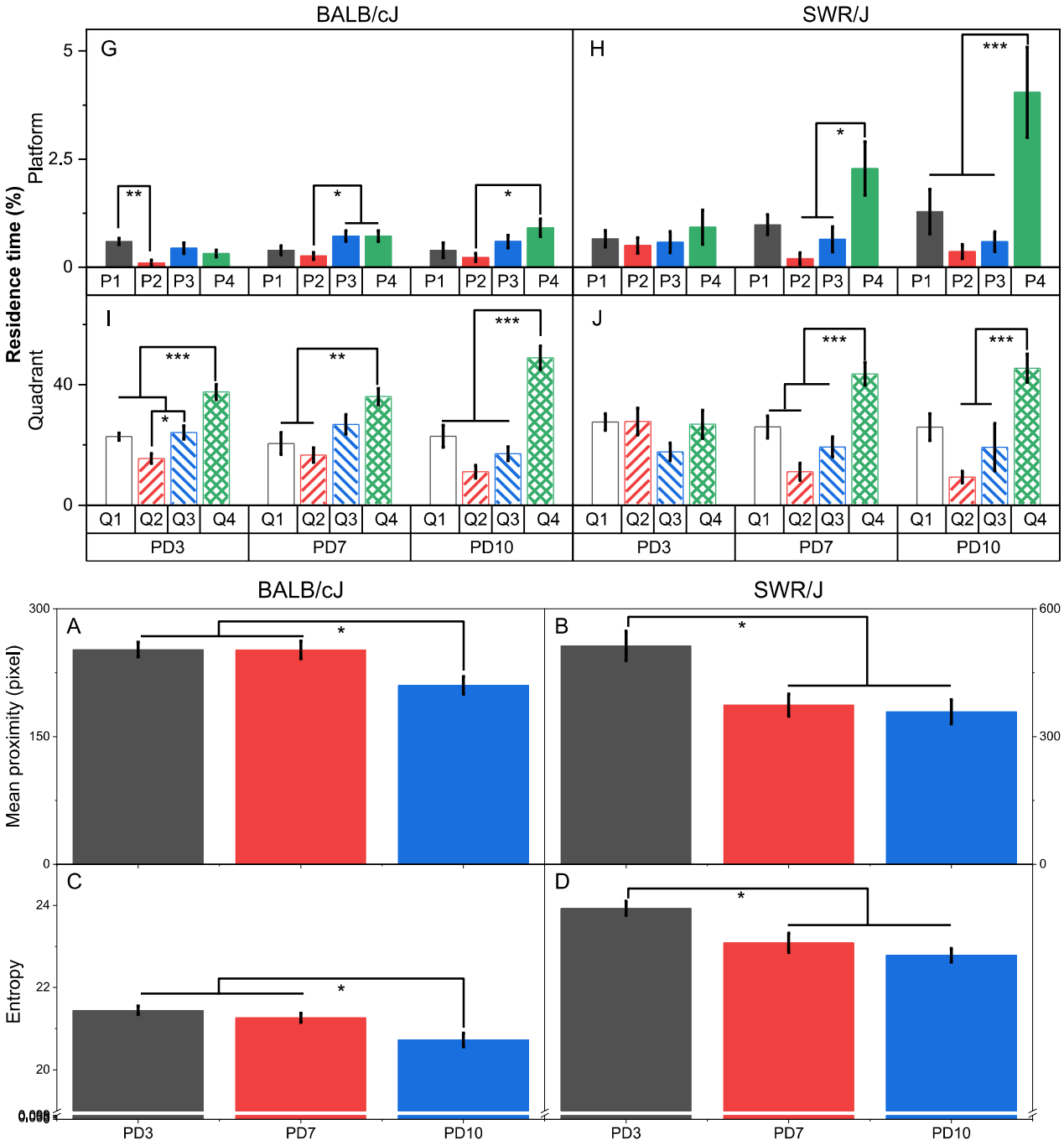

Figure 6.2: Other measures to assess spatial memory of BALB/cJ and SWR/J strains of mice.

(A-F) Residence time heat maps.

(G-J) bar graphs quantify the residence time. P4 and Q4 correspond to the target location.

(K-L) bar graphs represent the mean proximity value.

(M-N) bar graphs show the entropy measure.

The data is compared using one-way ANOVA and the means that are significantly different are indicated in the figure with asterisk (* >0.05, ** >0.01, *** >0.001).

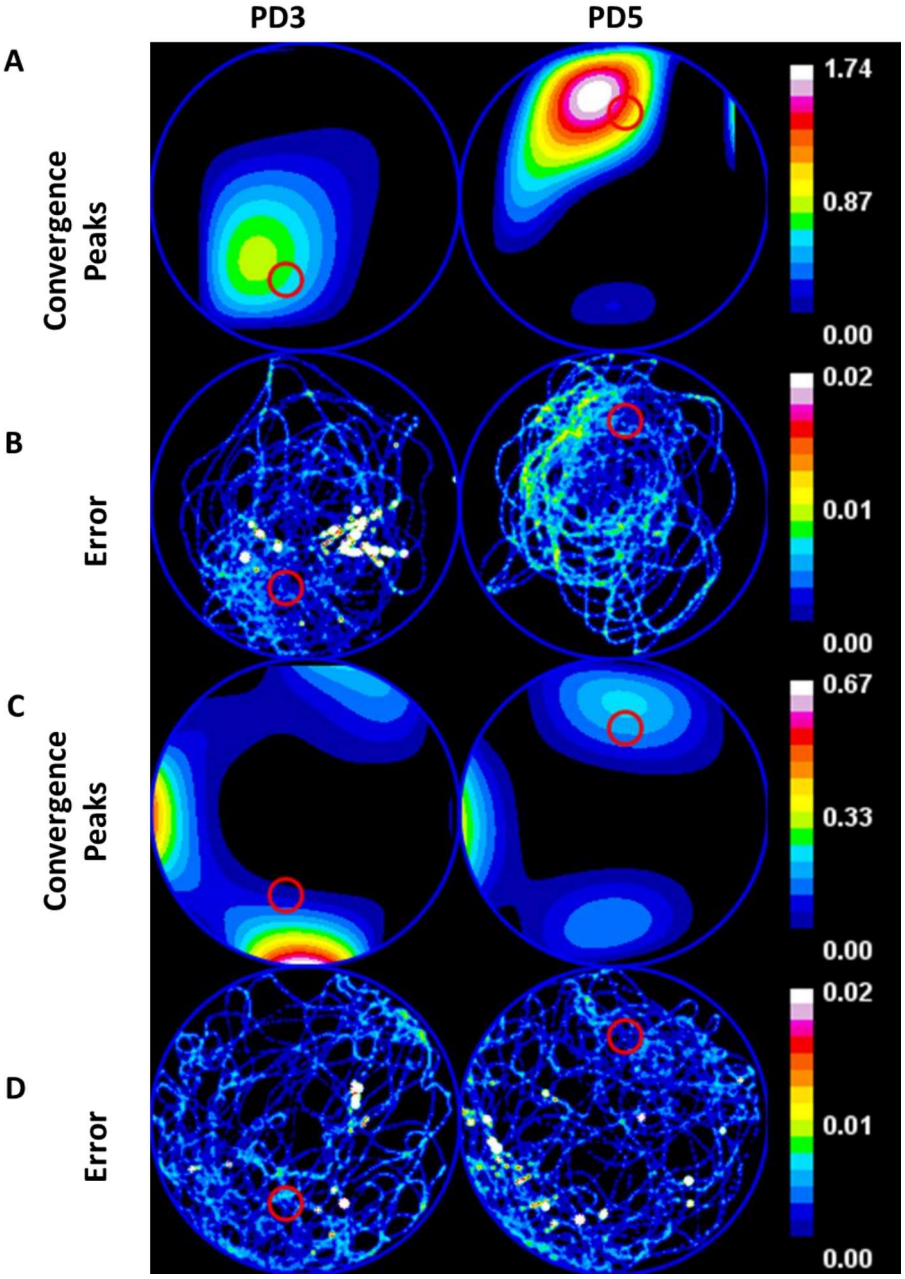
PD3
PD5
A
Convergence Peaks
1.74
0.87
0.00
B
Error
0.02
0.01
0.00
C
Convergence Peaks
0.67
0.33
0.00
D
Error
0.02
0.01
0.00

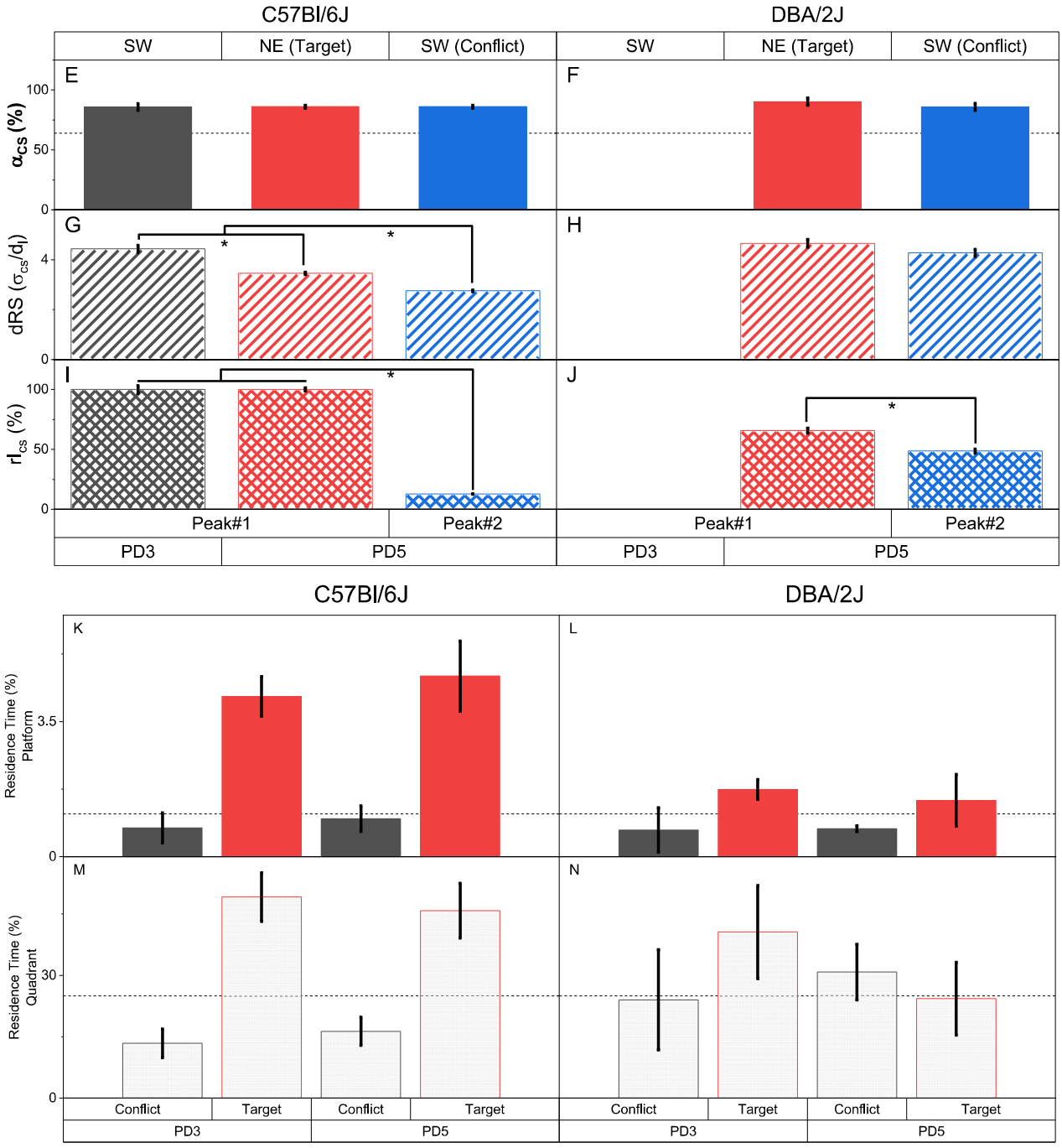

Figure 6.3: Convergence hotspots detects the memory for old as well as new platform location in goal reversal task. C57Bl/6J and DBA/2J strains of mice were trained with the platform in the south-west (SW) quadrant on probe day 3 (PD3), whereas the platform was shifted to the north-east (NE) quadrant on probe day 5 (PD5). Using accuracy (α), uncertainty (δ_{RS}), and intensity of search (I_{cs}), we show that C57Bl/6J and DBA/2J mice have memory for both platform locations, whereas the residence time measure shows that on PD5, C57Bl/6J mice do not search in old platform location above chance and that DBA/2J mice did not learn either of the platform location.

(A) and (C) shows the divergence heat map for the population of C57Bl/6J and DBA/2J mice (n = 5). C57Bl/6J mice show a distinct peak on PD3 and two peaks on PD5. In contrast, DBA/2J mice

do not show a convergence peak on PD3 but show two peaks on PD5. We consider both peaks on PD5 for further analysis and label the peak in NE quadrant/new platform location as Peak#1 and peak in SW quadrant/ old platform location as Peak#2.
(B) and (D) are the error in divergence contributed by variation within the population. A gaussian blur (radius = 4.75) was applied for visualising the sampled pixels.

(E) describes the accuracy of search centre for C57Bl/6J on PD3 and PD5. C57Bl/6J show a high degree of accuracy (Solid black bar, $\alpha = 86 \pm 2.8$) on PD3. On PD5, the accuracy of Peak#1 measured with respect to the target platform (NE quadrant) (Solid red bar: $\alpha_{cs} = 86 \pm 1\%$), as well as the accuracy of Peak#2 measured with respect to the conflict platform location (SW quadrant) (Solid blue bar: $\alpha_{cs} = 86 \pm 1\%$) is close to maximum. These results indicate that Bl6 mice have a highly accurate and precise spatial memory for both the platform locations, i.e. target location for PD5 and the conflict location on PD3. One- way ANOVA $F_{2,12} = 0.0034$, $p > 0.05$.

(F) describes the accuracy of search centre for DBA/2J mice on PD3 and PD5. The absence of a convergence peak on PD3 indicates that DBA/2J do not possess spatial memory for the PD3 platform location. However, on PD5, DBA/2J mice have two search centres as shown in the convergence heat map. The accuracy of Peak#1 measured with respect to the target platform (NE quadrant) (Solid red bar: $\alpha = 90 \pm 3\%$), as well as the accuracy of the Peak#2 measured with respect to the conflict platform location (SW quadrant) (Solid blue bar: $\alpha = 86 \pm 3\%$) is maximum. One- way ANOVA $F_{1,8} = 1.09$, $p > 0.05$. Thus, illustrating the ability of our method to detect and describe the aspect of spatial memory corresponding to two distinct platform locations. Dashed line shows the chance accuracy value (64%) in plots (E)-(F). Two-way ANOVA done for comparing the accuracy on PD5 with strain and peaks (platform locations) as factors showed that the means are not significantly different and there is no significant interaction (Strain $F_{1,16} = 0.78$, $p > 0.05$, peak: $F_{1,16} = 0.897$, $p > 0.05$, strain × peak interaction: $F_{1,16} = 0.973$, $p > 0.05$.

(G) describes the uncertainty in search for C57Bl/6J. On PD3, the relative search diameter is (Diagonal black bar) $\delta_{RS} = 4.43 \pm 0.15$. The relative search diameters of Peak#1 new PL (Diagonal red bar, $\delta_{RS} = 3.45 \pm 0.048$) and Peak#2 old PL (Diagonal blue bar, $\delta_{RS} = 2.75 \pm 0.039$) are not statistically different (One-way ANOVA $F_{2,12} = 85$, $p < 0.001$), thus, the uncertainty in search is similar for both the platform locations (SW and NE).

(H) describes the uncertainty in search for DBA/2J mice. The relative search diameters of Peak#1 new PL (Diagonal red bar, $\delta_{RS} = 4.66 \pm 0.16$) and Peak#2 old PL (Diagonal blue bar, $\delta_{RS} = 4.27 \pm 0.15$) are not statistically different (One-way ANOVA $F_{1,8} = 3.18$, $p > 0.05$), thus, the uncertainty in search is similar for both the platform locations (SW and NE).

Two-way ANOVA for mean uncertainty on PD5 with strain and peak as two factors showed that the uncertainty is different across the strain ($F_{1,16} = 148$, $p < 0.001$), and for location of the peaks ($F_{1,16} = 23$, $p < 0.001$) with no significant interaction($F_{1,16} = 1.993$, $p > 0.05$). From Post hoc analysis we see the search diameter is lesser for the older location then the new one reduces the uncertainty

in search area.

(I) Relative intensity of search shows C57Bl/6J mice maximally search at platform location on PD3 (Hatched black bar, 100 ± 3%) while on PD5 they search at both the new platform location (Hatched red bar, 100 ± 1%) as well as the old location (Hatched blue bar, 12.7 ± 0.2%). However, the intensity of search is higher for new location (One-way ANOVA $F_{2,12} = 592$, $p < 0.001$).

(J) Relative intensity of search of DBA/2J mice on PD5. The relative intensity of search for the platform at the target location (NE) (Hatched red bar, 66 ± 2 %) is significantly more than at the conflict location (SW) (Hatched blue bar, 49 ± 2%) (One-way ANOVA $F_{1,8} = 38$, $p < 0.001$). Thus, the mice search more intently in the target location, compared to the conflict location as a result of goal reversal training. We note that intensity of search for the old platform location in DBA/2J is considerably more compared to the C57Bl/6J.

Two-way ANOVA for relative search intensity with strain and peak as two factors show that difference in means across the strains is not significant :($F_{1,16} = 0.17$, $p > 0.05$) but mean intensity of search for the peaks are significantly different ($F_{1,16} = 1127$, $p < 0.001$)with a significant interaction($F_{1,16} = 510$, $p < 0.001$) between the factors. Post hoc analysis shows that goal reversal is complete for C57Bl/6J as indicated by lower search intensity for the old platform location while DBA/2J mice shows significantly more freezing at the old platform location. We estimate the efficiency of goal reversal training as $\left(\mathrm{GRE} = \frac{rIcs_{new} - rIcs_{old}}{rIcs_{new} + rIcs_{old}}\right)$. Thus, a value of 1 would indicate complete goal reversal while -1 would indicate no reversal with zero indicating that there is a conflict. Here we find this efficiency for C57Bl/6J to be ~0.78 and DBA/2J to ~0.15.

(K) and (M) The zone and quadrant residence time measure on PD5 for C57BL/6J mice. Both measures show that the mice spend significantly more time in the target location, whereas it resides in the conflict location at chance level. Thus, the residence time-based measures are unable to detect the presence of spatial memory for the older platform location. (L) and (N) The zone (solid bar) and quadrant (dotted bar) residence time measure PD5 for DBA/2J mice. DBA/2J mice occupy the target zone or quadrant at chance level. Thus, the measures are unable to detect the presence of spatial memory for both platform training locations.
Dashed line represents the chance value (1.11% and 25% respectively) in plots (K)-(N).

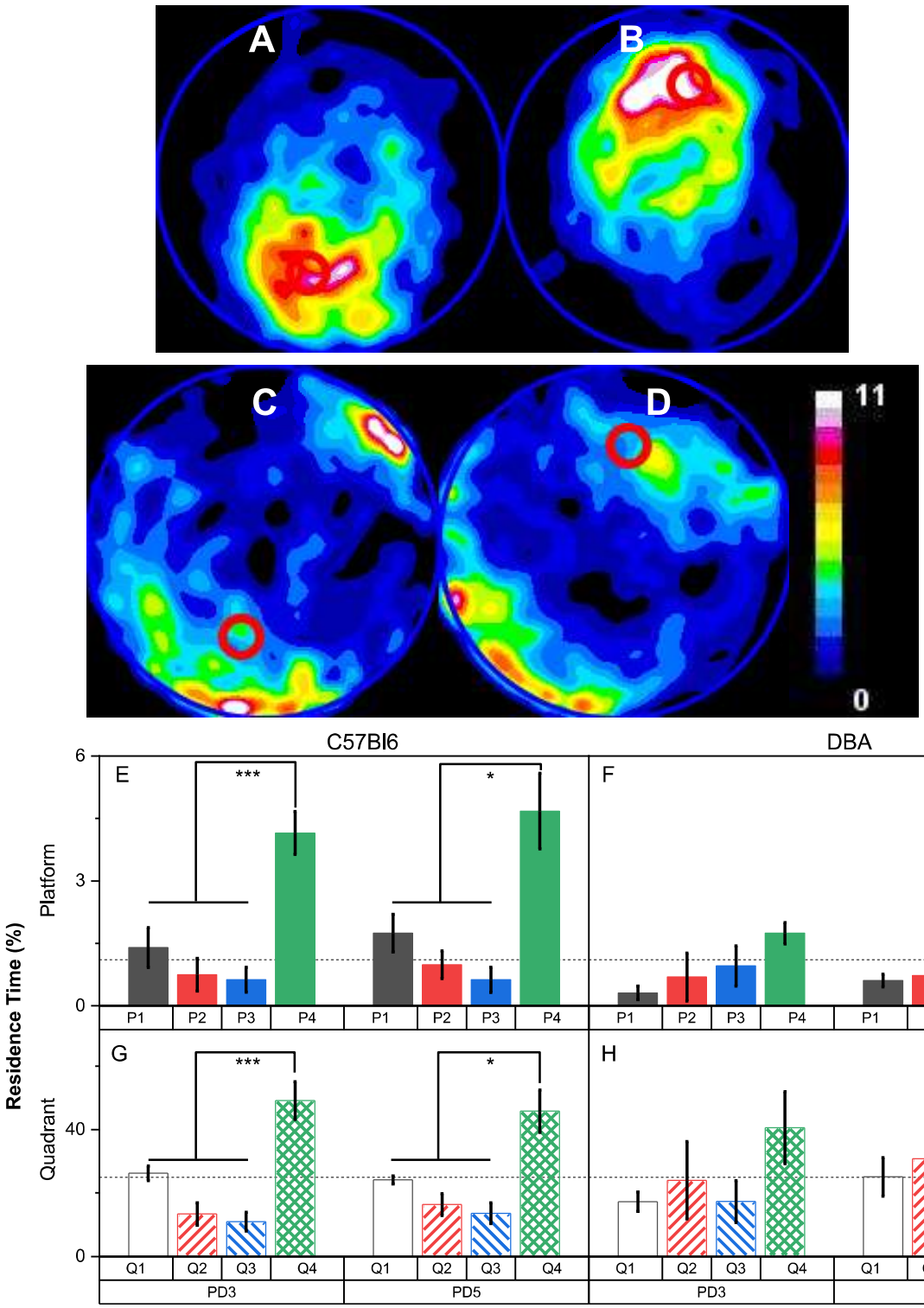
A
B
C
D
11
0
C57Bl6
DBA
E
F
G
H
Residence Time (%)
Platform
Quadrant
6
3
0
40
***
*
P1
P2
P3
P4
Q1
Q2
Q3
Q4
PD3
PD5

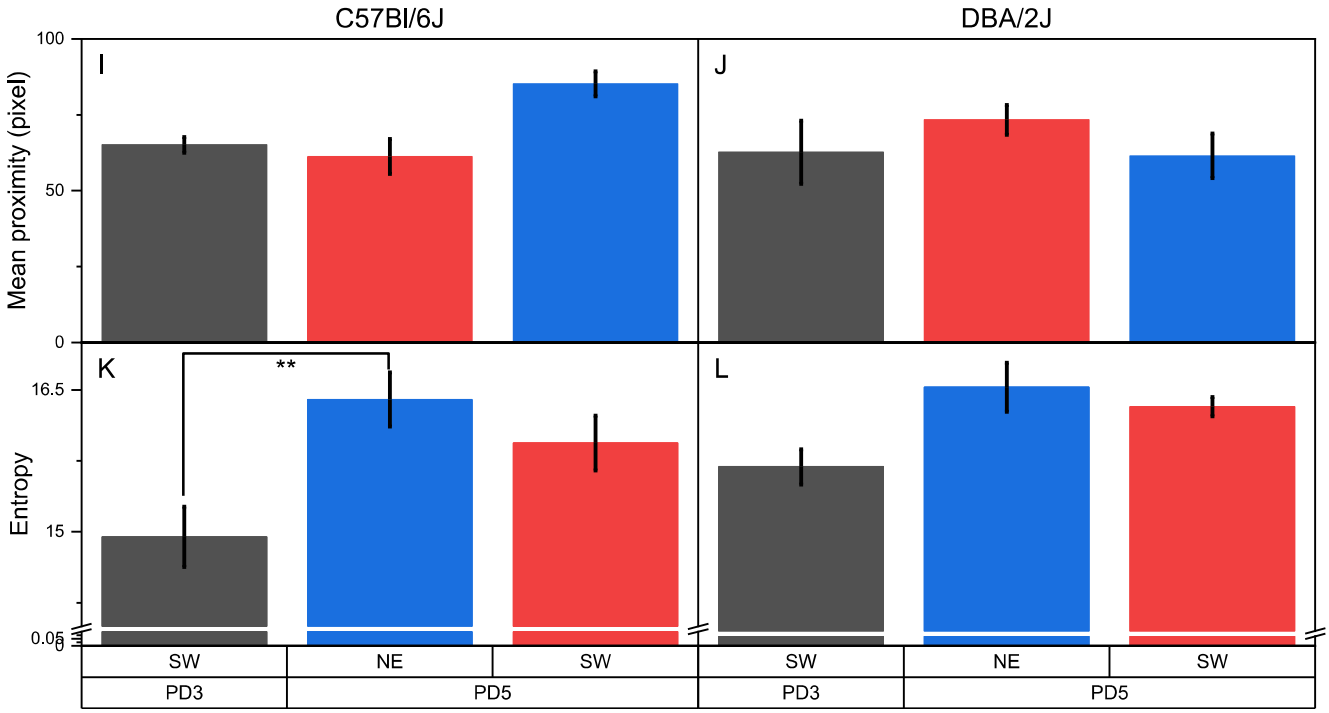

Figure 6.4: Other measures to assess spatial memory of C57Bl/6J and DBA/2J strains of mice trained in goal reversal task.

(A-D) Residence time heat maps.

(E-H) bar graphs quantify the residence time. P4 and Q4 correspond to the target location.

(I-J) bar graphs represent the mean proximity value. Two-way ANOVA for mean proximity with strain as between-subjects factor and peak as within-subjects factor shows that no significant difference between any factors with no interaction (strain $F_{1,24} = 3.61$, $p > 0.05$, peak $F_{2,24} = 0.749$, $p > 0.05$, interaction: $F_{2,24} = 3.27$, $p > 0.05$).

(K-L) bar graphs show the entropy measure. Two-way ANOVA for entropy with strain as between-subjects factor and peak as within-subjects factor indicate that the means are different across the , strains ($F_{2,24} = 4.441$, $p < 0.05$) but are different for the platform locations as indicated by the peaks ($F_{2,24} = 10.97$, $p < 0.001$) with no significant interaction: $F_{2,24} = 5.59$, $p > 0.05$.

The data is compared using one-way ANOVA and the means that are significantly different are indicated in the figure with asterisk (* >0.05, ** >0.01, *** >0.001).

6.6 References

2D Gaussian fitting macro (Fiji/ImageJ) for multiple signals. | *BIII*. (n.d.). Retrieved May 10, 2021, from https://biii.eu/2d-gaussian-fitting-macro-fijiimagej-multiple-signals

Bedell, M. A., Jenkins, N. A., & Copeland, N. G. (1997). Mouse models of human disease. Part I: Techniques and resources for genetic analysis in mice. In *Genes and Development* (Vol. 11, Issue 1, pp. 1–10). https://doi.org/10.1101/gad.11.1.1

Bedell, M. A., Largaespada, D. A., Jenkins, N. A., & Copeland, N. G. (1997). Mouse models of human disease. Part II: Recent progress and future directions. In *Genes and Development* (Vol. 11, Issue 1, pp. 11–43). https://doi.org/10.1101/gad.11.1.11

Brooks, S. P., Pask, T., Jones, L., & Dunnett, S. B. (2005). Behavioural profiles of inbred mouse strains used as transgenic backgrounds. II: Cognitive tests. *Genes, Brain and Behavior*, *4*(5), 307–317. https://doi.org/10.1111/j.1601-183X.2004.00109.x

Crawley, J. N., Belknap, J. K., Collins, A., Crabbe, J. C., Frankel, W., Henderson, N., Hitzemann, R. J., Maxson, S. C., Miner, L. L., Silva, A. J., Wehner, J. M., Wynshaw-Boris, A., & Paylor, R. (1997). Behavioral phenotypes of inbred mouse strains: Implications and recommendations for molecular studies. In *Psychopharmacology* (Vol. 132, Issue 2, pp. 107–124). Springer. https://doi.org/10.1007/s002130050327

Justice, M. J., & Dhillon, P. (2016). Using the mouse to model human disease: increasing validity and reproducibility. *Disease Models & Mechanisms*, *9*(2), 101. https://doi.org/10.1242/DMM.024547

Mihalick, S. M., Langlois, J. C., & Krienke, J. D. (2000). Strain and sex differences on olfactory discrimination learning in C57BL/6J and DBA/2J inbred mice (Mus musculus). *Journal of Comparative Psychology*, *114*(4), 365–370. https://doi.org/10.1037/0735-7036.114.4.365

Overall, R. W., Zocher, S., Garthe, A., & Kempermann, G. (2020). Rtrack: A software package for reproducible automated water maze analysis. In *bioRxiv* (p. 2020.02.27.967372). bioRxiv. https://doi.org/10.1101/2020.02.27.967372

Paylor, R., Tracy, R., Wehner, J., & Rudy, J. W. (1994). DBA/2 and C57BL/6 mice differ in contextual fear but not auditory fear conditioning. *Behavioral Neuroscience*, *108*(4), 810–817. https://doi.org/10.1037/0735-7044.108.4.810

Rosenthal, N., & Brown, S. (2007). The mouse ascending: Perspectives for human-disease models. *Nature Cell Biology*, *9*(9), 993–999. https://doi.org/10.1038/ncb437

Stavnezer, A. J., Hyde, L. A., Bimonte, H. A., Armstrong, C. M., & Denenberg, V. H. (2002). Differential learning strategies in spatial and nonspatial versions of the Morris water maze in the C57BL/6J inbred mouse strain. *Behavioural Brain Research*, *133*(2), 261–270. https://doi.org/10.1016/S0166-4328(02)00021-9

Upchurch, M., & Wehner, J. M. (1988). Differences between inbred strains of mice in Morris water maze performance. *Behavior Genetics*, *18*(1), 55–68. https://doi.org/10.1007/BF01067075

Wahlsten, D., Cooper, S. F., & Crabbe, J. C. (2005). Different rankings of inbred mouse strains on the Morris maze and a refined 4-arm water escape task. *Behavioural Brain Research*, *165*(1), 36–51. https://doi.org/10.1016/j.bbr.2005.06.047

CHAPTER 7

Analysis of subtle spatial memory differences in Noonan Syndrome mouse models using Morris Water Maze task

Abstract

Noonan syndrome (NS) is an autosomal-dominant genetic disorder caused by mutations in genes of the RAS/MAPK signalling pathway. One of the symptoms of NS is mild to severe cognitive impairment. Here, we investigate the spatial memory deficits in mouse models of Noonan syndrome (NS), namely: *Ptpn11* D61G/+ (severe manifestation of NS symptoms) and *Ptpn11* N308D/+ (mild manifestation of NS symptoms). Our analysis substantiates the reported differences between the *Ptpn11* D61G/+ Noonan syndrome mice and their wild type littermates in terms of accuracy and intensity of search. However, we observe that performance of the NS mutant mice on probe day 5 is similar to that of wildtype (WT) littermates on probe day 3 in terms of accuracy. Interestingly, while analysing the performance of mutant mice *Ptpn11* N308/+ (mild variant), our method significantly brings out the difference in memory between the mutant and the wild type littermates, which was previously undetected using the conventional methods. Thus, we could conduct rescue experiments and demonstrate the recovery of the spatial memory deficit using a mitogen activated protein kinase kinase (MEK) inhibitor SL327 in these mice.

Acknowledgments

I would like to specifically thank our collaborator, Prof. Y.S. Lee for sharing the water maze dataset carried out on NS mutant mice.

7.1 Introduction

Noonan syndrome (NS) is a congenital genetic disorder characterised caused by mutations in the genes of Ras/MAPK signalling pathway (Noonan, 1968; Romano et al., 2010). The severity of NS symptoms manifest over a wide range such that mild cases of the disorder are not detected (till the children of such individuals show the symptoms) as well as severe cases where the quality of life and life expectancy is affected. The moderate to severe cases of NS show symptoms such as impairment in growth and development. Mild cognitive impairment has also been reported. Majority of NS cases are a result of inherited mutated genes, however cases involving spontaneous mutations have also been reported. The mutated genes are part of the Ras/MAPK signalling pathway involving genes such as Ptpn11, SOS1, Ras, CBL. Mutation in Ptpn11 is the most common form of NS.

We focus our investigation on two mouse models of NS mice with a gain-of-function point mutation in non-receptor protein tyrosine phosphatase Ptpn11 gene: Ptpn11 D61G/+ and Ptpn11 N308D/+ (Araki et al., 2009, 2004). Ptpn11 D61G/+ mutant mice show severe cognitive deficits whereas Ptpn11 N308D/+ mutants show milder cognitive deficits. Spatial memory as assessed by MWM established that Ptpn11 D61G/+ mice do not learn the platform location after three training sessions (4 trials each) as indicated by quadrant occupancy and proximity measure on the first probe trial (PD3), whereas the training regime is sufficient for Ptpn11 +/+ mice to learn the platform location well (Lee et al., 2014). Additional training failed to improve spatial memory in Ptpn11 D61G/+ mice as reported by quadrant occupancy and proximity measure on PD7. The study also shows that while Ptpn11 N308D/+ perform similar to wild type littermates as measured by latency, during probe trial (PD3) these mice spend significantly lesser time in the target quadrant than wild type mice. Ptpn11 N308D/+ mice also search farther away from the platform as shown by proximity measure. However, with additional training (PD5), these mice show comparable spatial memory for the platform location as measured using quadrant and proximity measure. Lastly, the study showed that administration of SL327, a MEK inhibitor, is effective in reversing the memory deficits in Ptpn11 D61G/+ mice.

Here, we evaluate spatial memory of these two NS mouse models using the vector-

based analysis developed in Chapter 5 and used in Chapter 6.

7.2 Results

7.2.1 Ptpn11 D61G/+ mice learn platform location comparable to wild type littermates with additional training

We analyse the dataset of water maze performed on Noonan syndrome mice Ptpn11 D61G/+ and their wild-type littermates Ptpn11 +/+. Our method of analysis indicates that though Ptpn11 D61G/+ mice do not have a memory of the platform location on PD3, additional training does improve their spatial memory for the platform location. The divergence on velocity vector field along the occupancy centre reveals a search centre near the platform location on PD5 and PD7 (Fig. 7.1 (C)). Describing the convergence peak or search centre in terms of accuracy of search, uncertainty about search and intensity of search reveals the quality of the spatial memory in Ptpn11 D61G/+ during probe trials. The accuracy of the search centre to the platform location in Ptpn11 +/+ mice is not statistically different across the probe days (Fig. 7.1 (E), Black solid bars, $\alpha = 59 \pm 2.25$ (D1), $\alpha = 93 \pm 2.41$ (PD3), $\alpha = 93 \pm 2.60$ (PD5), $\alpha = 96 \pm 1.34$ (PD7)). Interestingly, we see that the accuracy of the search centre in Ptpn11 D61G/+ mice on PD5 is comparable to that of Ptpn11 +/+ mice on PD3 (Fig. 7.1 (F), Red solid bars, $\alpha = 60 \pm 2.10$ (D1), $\alpha = 62 \pm 1.91$ (PD3), $\alpha = 87 \pm 1.57$ (PD5), $\alpha = 92 \pm 2.12$ (PD7) ; Two-way ANOVA for accuracy with genotype as between-subjects factor and probe day within-subjects factor, genotype × probe day interaction: $F_{3,92} = 21$, $p < 0.001$; Bonferroni: Ptpn11 +/+ PD3 – Ptpn11 D61G/+ PD3: $p < 0.001$, Ptpn11 +/+ PD3 – Ptpn11 D61G/+ PD5: $p > 0.5$).

Additionally, the search intensity relative to the pool (rI_{cs}) increases as a function of training. Ptpn11D61G/+ mice increased their focused searches and their intention at search centre on PD7, and these are similar to their WT littermates in this probe trial (Fig. 7.1 (I-J)). However, there is a significant difference in the absolute intensity of search (aI_{cs}) between Ptpn11+/+ and Ptpn11D61G/+ mice (Fig. 7.1 (K-L)). Absolute intensity at a location in a divergence image measures the extent by which vector decreases over a unit distance. Given that in our case the video is uniformly sampled, this measure directly reflects a decrease observed over time, and hence the velocity. On the other hand, relative intensity measures

the fraction of slow down with respect to the steepest decline observed in the pool. Thus, the differences in search intensities (al_{cs}) could reflect either cognitive or motor deficits, while rl_{cs} differences reflect differences in spatial learning and memory. The difference we observe in search intensities (al_{cs}) in WT and mutants could be due to the differences in their swimming ability. In contrast, rl_{cs}, accuracy and uncertainty are sensitive to deficits in spatial learning and memory and are not directly affected by differences in motor performance.

7.2.2 Spatial memory deficit in MWM is rescued by SL327 drug in N308D/+ mice

Next, we analyse the dataset of water maze performed on Noonan syndrome mice Ptpn11 N308D/+ and their wild-type littermates Ptpn11 +/+. Noonan syndrome mice, specifically the swim trajectories of the above Ptpn11 N308D/+ and Ptpn11 +/+ mice on PD5. Additionally, we investigate whether administration of SL327, a MEK inhibitor, shown to reverse the memory deficits in Ptpn11 D61G/+ mice, could improve the accuracy and uncertainty in search of the platform location in PtpnN308D/+ mice. We find there are subtle differences in spatial memory.in terms of accuracy, uncertainty, and intensity of search between Ptpn11 N308D/+ and their wild type littermates. Ptpn11 N308D/+ show an accuracy of 80 ± 2% with an uncertainty of 5.5 ± 0.16 relative search diameter, whereas the WT mice show an accuracy of 94 ± 2 % with an uncertainty of 4.01 ± 0.092 relative search diameters. On treatment with SL327, Ptpn11 N308D/+ improves its accuracy to 95 ± 2% with a relative search diameter of 4.33 ± 0.074. Incidentally, treating WT mice with SL327 affects their accuracy and search area, i.e., α_{cs} = 88 ± 4 and δ_{RS} = 5.22 ± 0.235 ((Fig. 7.3 (C-E)), Two-way ANOVA for accuracy with genotype as between-subjects factor and treatment within-subjects factor, genotype × treatment: $F_{1,38}$ = 15, $p < 0.001$; Bonferroni: Ptpn11 N308D/+ Veh – Ptpn11 N308D/+ SL $p < 0.01$, Ptpn11 N308D/+ Veh – Ptpn11 +/+ Veh: $p < 0.01$).

7.3 Discussion

We utilized the swim trajectories from different mice datasets performing Morris

water maze task to illustrate the sensitivity and advantage of the newly proposed metrics. We show our method can detect subtle memory differences previously undetected using occupancy-based quadrant/platform, proximity, or entropy measures. Analysing swim trajectories using the proposed metrics enabled us to detect subtle memory deficits in NS mice performing MWM task. NS mutant mice Ptpn11 D61G/+ were previously shown not to possess spatial memory of the platform location even with additional training. However, our analysis reveals that these mice do learn the platform location with additional training, and that its accuracy and uncertainty in search area on PD5 is comparable to that of its wild type littermates on PD3. We also show similar results for a variant of NS mice Ptpn11 N308D/+ that has subtle memory deficit not detected by the conventional measure. We see that the administration of SL327 MEK inhibitor rescues memory deficits seen in Ptp11 N308D/+ mice.

7.4 Materials and Methods

7.4.1 Animal and behaviour paradigm information

10 male NS mice (Ptpn11 D61G/+) and 15 wild- type littermate (Ptpn11 +/+) were used for the analyses presented in fig. 7.1 and 7.2. 10 male NS mice (Ptpn11 N308D/+) and 11 wild- type littermate (Ptpn11 +/+) were used for the analyses presented in fig. 7.3 and 7.4. The NS mice were trained as reported previously (Lee et al., 2014). Briefly, training sessions comprised 4 trials (2 blocks with 2 trials each) per day with 1-min inter-trial interval and 45-min inter-block interval. Mice were allowed to search the platform for 60 s or until reaching the platform. The probe tests were done immediately after the completion of training on days 3,5, 7. For the experiments with MEK inhibitor, SL327 (32mg/kg, DMSO) was injected intraperitonially everyday 30 min before MWM training.

7.4.2 Generation divergence heat maps and estimated of search centre

Divergence heat maps and the putative search centres were calculated as developed in chapter 5 (Fig. 5.4, Section 5.5.3, Section 5.5.6).

7.4.3 Estimation of full width half maximum (FWHM) of convergence peak:

We estimate the FWHM of a convergence peak as previously described (*2D Gaussian fitting macro (Fiji/ImageJ) for multiple signals.* | *BIII*, n.d.). Briefly, the identified putative search centre is fit to a linearised 2D-gaussian function to obtain the FWHM in x- and y-axis. The size of the peak is initialised to 20 pixels before performing custom fit using ImageJ's Curve Fitter class implementing Simplex algorithm.

7.4.4 Statistical analysis:

All statistical analysis was carried out in Origin (v2020b or 2021b). To perform two-way ANOVA on summarised statistics (i.e., ANOVA using mean and SEM), the raw data was recreated for 'n' individual mice by randomly sampling from a normal distribution using the population mean and SD of the metric being analysed. Based on ANOVA results, post hoc analysis was performed to carry out pair-wise

comparisons. The data distribution was assumed to be normal. All data are represented as mean ± SEM.

7.5 Figures

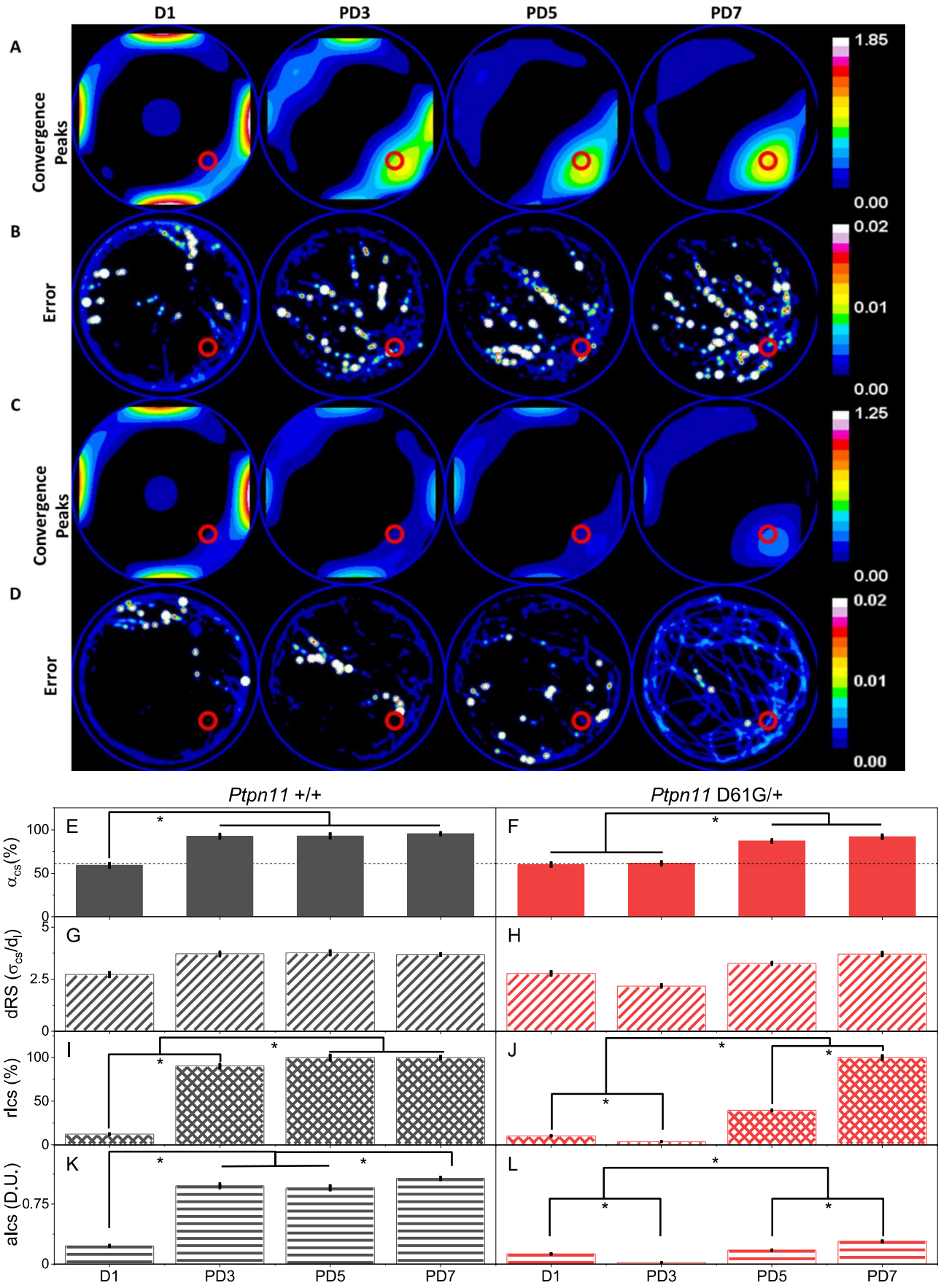
D1
PD3
PD5
PD7
A
Convergence Peaks
1.85
0.00
B
Error
0.02
0.01
0.00
C
Convergence Peaks
1.25
0.00
D
Error
0.02
0.01
0.00
Ptpn11 +/+
Ptpn11 D61G/+
E
F
G
H
I
J
K
L
αcs(%)
dRS (σcs/dI)
rIcs (%)
aIcs (D.U.)
100
50
0
5
2.5
0.75
D1
PD3
PD5
PD7

Figure 7.1: Description of MWM spatial memory in *Ptpn11* D61G/+ and wild type litters mates (*Ptpn11* +/+) using the three parameters accuracy (α), uncertainty (δ_{RS}), and intensity of search (I_{cs}) show that with additional training D61G/+ mice recall the platform location with accuracy and relative search intensity comparable to wild type littermates (PD3).

(A) and (C) are the divergence heat maps showing the convergence hotspots for the population of *Ptpn11* +/+ wild type (WT, n = 15) and *Ptpn11* D61G/+ transgenic (D61G, n = 10) mice, respectively, on training day 1 (D1), probe day 3 (PD3), probe day 5 (PD5) and probe day 7 (PD7). D1 heat map serves as a representation of the surface when the mouse has no knowledge of the platform location. After 3 training sessions of 4 trials each, WT mice show a convergence peak close to the platform location in the first probe trial on PD3, whereas the D61G/+ mice do not show any peak near the platform. With additional training, D61G show a convergence peak adjacent to the platform location on PD5 and PD7 indicating the presence of spatial memory.

(B) and (D) is a visual representation of the error estimates of calculated divergence within a population of mice for *Ptpn11*+/+ and *Ptpn11* D61G/+ mice respectively. A gaussian blur of radius 2 was applied for visual representation. Pool perimeter is shown as a blue circle and the platform location is shown as red circle.

(E) and (F) quantify the accuracy of search centre. In both wildtype and mutant mice, the accuracy of search centre starts at a chance level (61%, dashed line) on D1 (WT: α = 59 ± 2.25 (D1, black solid bars); one-sample t-test, $p > 0.05$ and D61G/+: α = 60 ± 2.10 (D1, red solid bar); one-sample t-test $p > 0.05$). In WT mice the accuracy reaches a maximum on PD3 itself (α = 93 ± 2.41 (PD3), α = 93 ± 2.60 (PD5), α = 96 ± 1.34 (PD7)). We see that D61G/+ mice perform at chance level when tested on PD3 (α = 62 ±1.91 (PD3, red solid bar); one-sample t-test, $p > 0.05$). However, with additional training, the accuracy of search centre improves on PD5 and PD7 (Red solid bars α = 87 ± 1.57 (PD5), α = 92 ± 2.12 (PD7); Two-way ANOVA for accuracy with genotype and training as factors showed that the means across the genotype ($F_{1,92} = 39$, $p < 0.001$), as well as across training day($F_{3,92} = 97$, $p<0.001$) are different with a significant interaction($F_{3,92} = 21$, $p< 0.001$). Post hoc analysis are consistent with our interpretation provided above. Interestingly, we see that the accuracy of TG mice on PD5 is comparable to that of WT mice on PD3 (Bonferroni: WT PD3 – D61G/+ PD3: $p < 0.001$, WT PD3 – D61G/+ PD5: $p > 0.5$) indicating that D61G/+ mice are able to learn the spatial memory task despite their cognitive deficits however with a slow rate of acquisition.

(G) and (H) quantifies the uncertainty in search centre in terms of relative search diameter (δ_{RS}) for WT and D61G/+ mice. In both WT (Black diagonal bars, δ_{RS} = 2.7 ± 0.103 (D1), δ_{RS} = 3.7 ± 0.097 (PD3), δ_{RS} = 3.7 ± 0.106 (PD5), δ_{RS} = 3.7 ± 0.052 (PD7)) and D61G/+ (Red diagonal bars, δ_{RS} = 2.7 ± 0.097 (D1), δ_{RS} = 2.18 ± 0.067 (PD3), δ_{RS} = 3.3 ± 0.059 (PD5), δ_{RS} = 3.7 ± 0.085 (PD7)) mice, the relative search diameter was found to be comparable across the three probe trials. Two-way ANOVA for uncertainty in search with genotype and training as factors showed that the difference in means across both, the genotype ($F_{1,92} = 1.78$, $p > 0.05$) and across training day ($F_{3,92} = 1.47$, $p > 0.05$), is not statistically significant. The interaction between the genotype and training day was also not statistically significant ($F_{3,92} = 0.996$, $p > 0.05$). This indicates that the search area or focus

does not change across probe trials.

(I) and (J) quantifies the relative intensity of search (rI_{cs}) for WT and D61G/+ mice. In case of WT mice, the relative intensity of search at the search centre (P_{cs}) is high on PD3 itself and reaches a maximum on PD5 and PD7 (Black hatched bars, rI_{cs} = 12 ± 1 (D1), rI_{cs} = 90 ± 9 (PD3), rI_{cs} = 100 ± 11 (PD5), rI_{cs} = 100 ± 5 (PD7)). In D61G/+ mice, the intensity of search at P_{cs} steadily improves from a low value on PD3 to a maximum on PD7 (Red hatched bars, rI_{cs} = 10 ± 1 (D1), rI_{cs} = 3.8 ± 0.26(PD3), rI_{cs} = 40 ± 2 (PD5), rI_{cs} = 100 ± 9 (PD7)). Two-way ANOVA for relative intensity with genotype and training as factors show that the means are significantly different both as a function of genotype ($F_{1,92}$ = 1.3E7, $p < 0.001$) and training day ($F_{3,92}$ = 31.3E7, $p < 0.001$ The interaction between the two factors was also statistically significant ($F_{3,92}$ = 4.5E6, $p< 0.001$). Post hoc analysis shows that the WT mice learned to search intently on PD3 (D1 < PD3) even though PD5 and PD7 search intensities are higher (PD3 < PD5, PD7) while the mutant mice progressively increased its search intensity from only after PD3 (D1 ~ PD3), that is intensity of search at PD3 < PD5 < PD7 as seen from post hoc analysis. The evidence further supports the notion that D61G/+ mutant mice learn the platform location and contribute its effort at the search centre after intense training.

(K) and (L) quantifies the absolute intensity of search (aI_{cs}) for WT and D61G/+ mice. The absolute intensity of search at P_{cs} is significantly different on probe days compared to training day in WT mice (Black horizontal bars, aI_{cs} = 0.229 ± 0.0087 (D1), aI_{cs} = 0.98 ± 0.02548 (PD3), aI_{cs} = 0.955 ± 0.02674 (PD5), aI_{cs} = 1.072 ± 0.01501 (PD7)). In D61G/+ mice, the absolute intensity of search at P_{cs} steadily improves with training (Red horizontal bars, aI_{cs} = 0.128 ± 0.00448 (D1), aI_{cs} = 0.019 ± 5.89E-4 (PD3), aI_{cs} = 0.175 ± 0.00315 (PD5), aI_{cs} = 0.285 ± 0.00656 (PD7). Both D61G as well as their littermates are trained and probed on the same experimental setup (with experimenter being blind to the genotype) as a result the absolute intensities can be compared across genotypes. Two-way ANOVA for comparing absolute intensity across genotypes and training as two factors indicate that absolute search intensities are significantly different between WT and D61G mice($F_{1,92}$ = 2677, $p < 0.001$) and as a function of training they increase ($F_{3,92}$ = 285, $p< 0.001$) their intention of search though at different rates (genotype × probe day interaction: $F_{3,92}$ = 224, $p< 0.001$). This we interpret as resulting from possible motor as well as cognitive deficits.

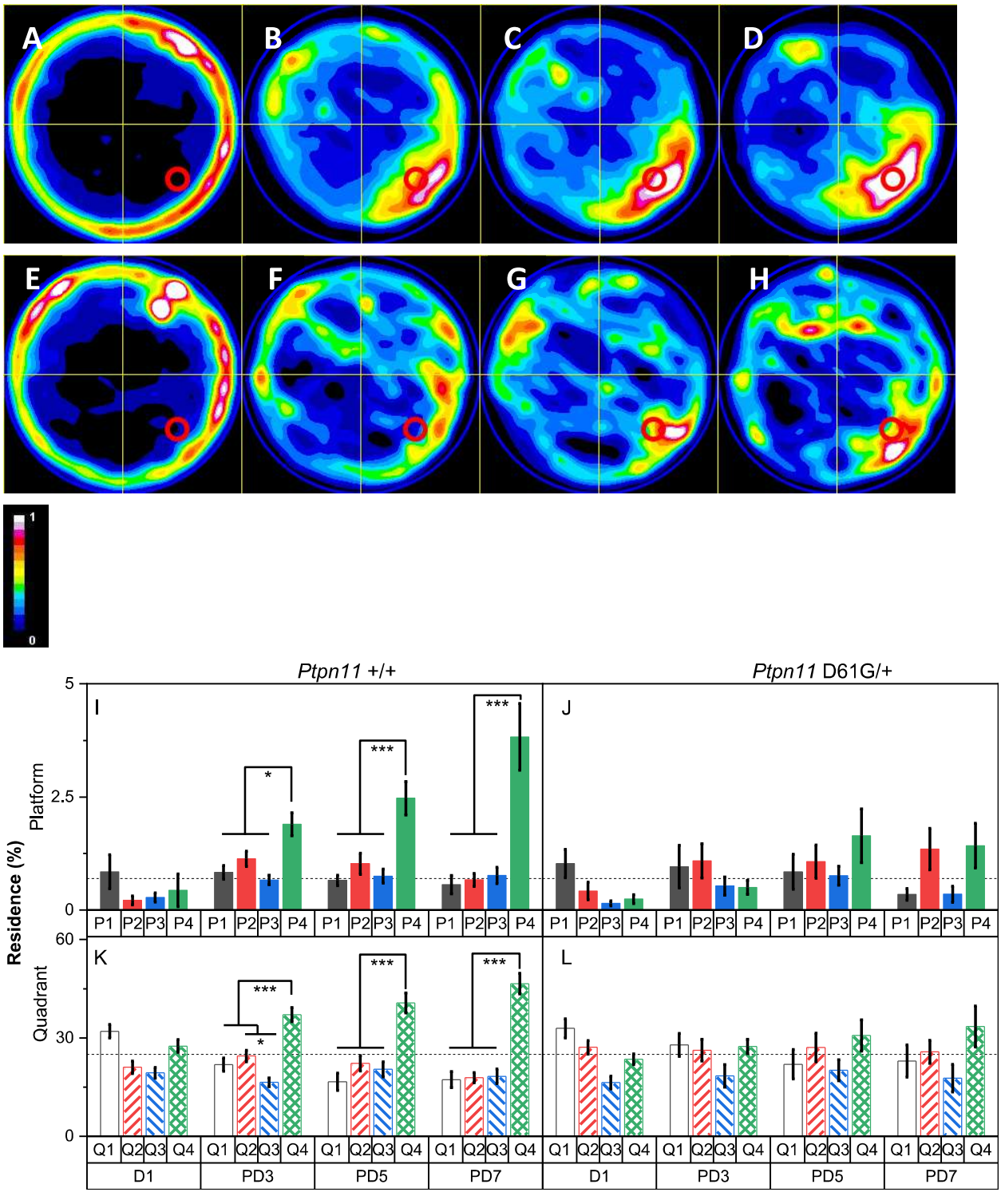
A
B
C
D
E
F
G
H
1
0
Ptpn11 +/+
Ptpn11 D61G/+
I
J
K
L
Residence (%)
Platform
Quadrant
5
2.5
0
60
30
0
*
***
P1 P2 P3 P4
Q1 Q2 Q3 Q4
D1
PD3
PD5
PD7

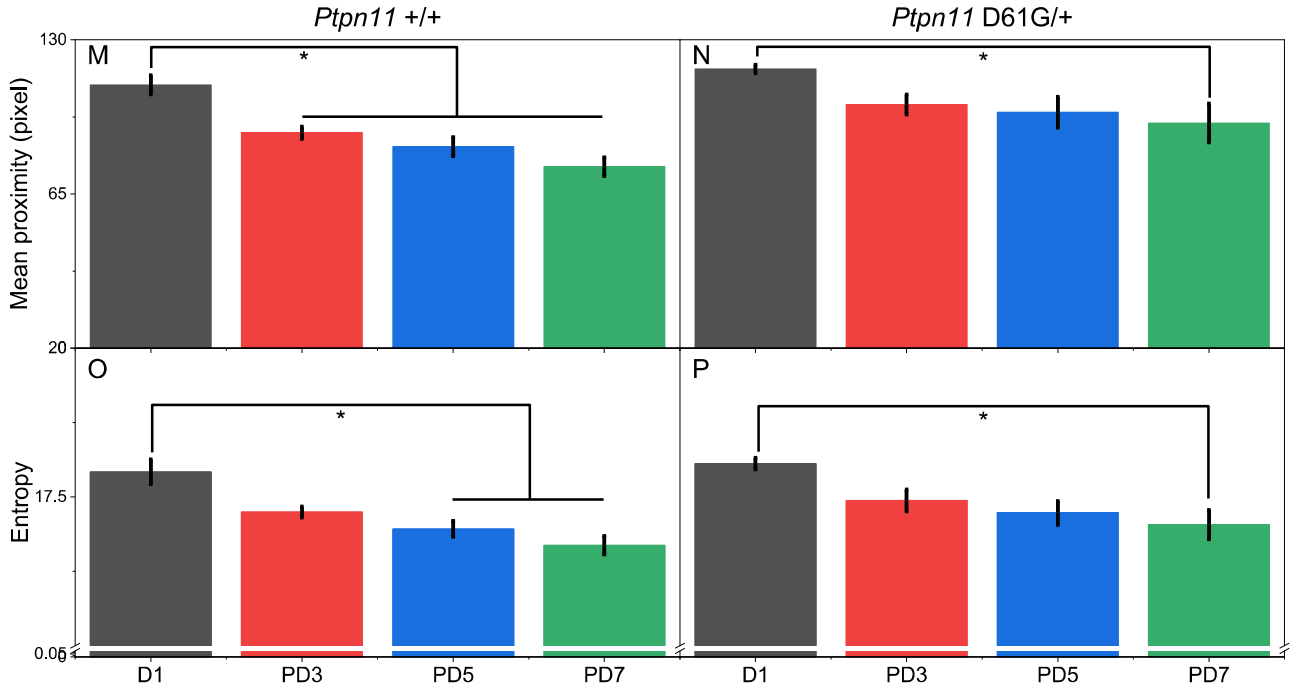

Figure 7.2: Other measures to assess spatial memory of *Ptpn11* +/+ and *Ptpn11* D61G/+ NS mice.

(A-H) Residence time heat maps.

(I-L) bar graphs quantify the residence time. P4 and Q4 correspond to the target location.

(M-N) bar graphs represent the mean proximity value.

Two-way ANOVA for mean proximity with genotype as between-subjects factor and training within-subjects factor indicate that differences across genotype: $F_{1,92} = 16$, $p < 0.001$ and training: $F_{3,92} = 15$, $p < 0.001$ are significant while , genotype × day interaction: $F_{3,92} = 0.576$, $p > 0.05$ is not significant.

(O-P) bar graphs show the entropy measure.

Two-way ANOVA for entropy with genotype as between-subjects factor and training as within-subjects factor indicate that differences across genotype: $F_{1,92} = 3.83$, $p > 0.05$, day: $F_{3,92} = 16$, $p < 0.001$, genotype × day interaction: $F_{3,92} = 0.14$, $p > 0.05$.

The differences in significance are indicated in the figure with asterisk (* >0.05, ** >0.01, *** >0.001).

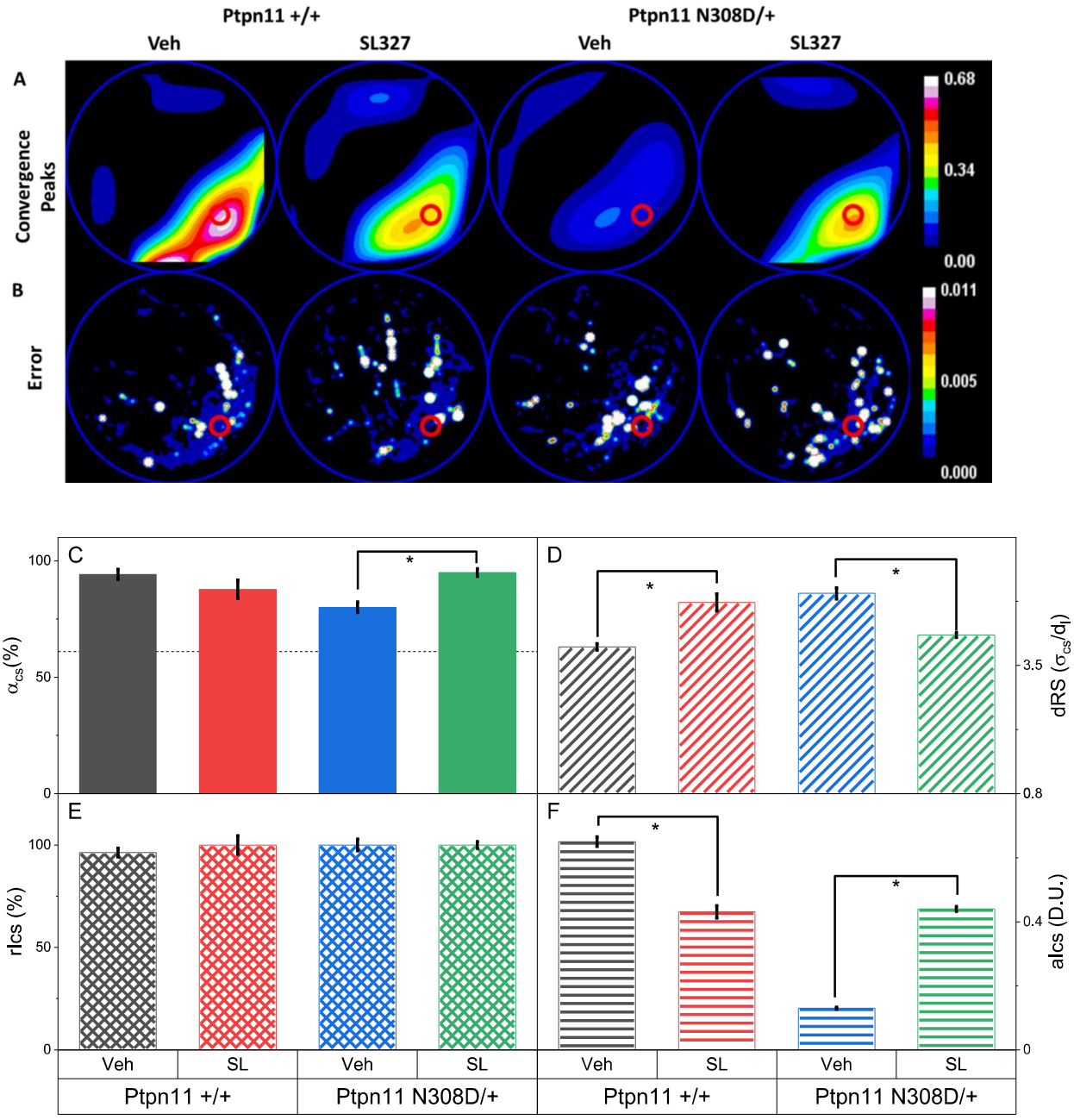

Figure 7.3: An MEK inhibitor SL327 rescues spatial memory deficits seen in *Ptpn11* N308D/+ mice.

(A) Divergence heat maps representing the convergence peaks for *Ptpn11*+/+ WT mice (n=11) and *Ptpn11* N308D/+ mutant mice (n=10) for saline (veh) and drug (SL327) treated conditions.

(B) Heat map of the error estimated on divergence values indicates the variation within the population of mice. A gaussian blur (radius = 6) was applied for visualising the error in the sampled pixels.

(C) Accuracy of search centre reveals that *Ptpn11* +/+ and *Ptpn11* N30D/+ show subtle difference in spatial memory (Solid bars: *Ptpn11* +/+ Veh α_{cs} = 94 ± 2 % (black), *Ptpn11* N308D/+ Veh α_{cs} =

80 ± 2% (red)). Treatment with MEK inhibitor SL327 rescues the deficit and brings the performance of N308D/+ mutant to the level of WT (*Ptpn11* +/+ SL327 α_{cs} = 88 ± 4 (blue), *Ptpn11* N308D/+ SL327 α_{cs} = 95 ± 2% (green); Bonferroni: *Ptpn11* N308D/+ Veh – *Ptpn11* N308D/+ SL $p < 0.01$, *Ptpn11* N308D/+ Veh – *Ptpn11* +/+ Veh: $p < 0.01$.). Two-way ANOVA for accuracy with genotype and treatment as two factors established that although there is no difference in the means of genotype ($F_{1,38} = 1.6$, $p > 0.05$) and the treatment ($F_{1,38} = 2.4$, $p > 0.05$) however there was significant interaction ($F_{1,38} = 15$, $p< 0.001$) indicating that the means of these factors are changing in opposite directions as revealed by the post hoc analysis with the rescue due to SL327 is significantly higher than the decrement in accuracy seen in the wild type following the administration of SL327. Dashed line shows the chance accuracy value (61%).

(D) Uncertainty in spatial memory is statistically different between N308D/+ mutant and WT littermates (Diagonal bars: *Ptpn11* +/+ Veh δ_{RS} = 4.01 ±0.092 (black), *Ptpn11* N308D/+ Veh δ_{RS} = 5.47 ± 0.159 (red); Bonferroni: *Ptpn11* N308D/+ Veh – *Ptpn11* +/+ Veh: $p < 0.001$). Administration of SL327 makes the search focussed for the mutant *(Ptpn11* N308D/+ SL327 δ_{RS} = 4.33 ± 0.074 (green)), however it also increases the search diameter in the wild type llittermates. (*Ptpn11* +/+ SL327 δ_{RS} = 5.22 ± 0.235 (blue),). N308D/+ mutant mice improve their performance (Bonferroni: *Ptpn11* N308D/+ Veh – *Ptpn11* N308D/+ SL $p < 0.001$), whereas the search area of their wildtype littermates becomes more diffused. Two-way ANOVA for uncertainty performed with genotype and treatment showed significant interaction (genotype × treatment interaction: $F_{1,38} = 56$, $p< 0.001$), without any main effect (genotype: $F_{1,38} = 3.3$, $p > 0.05$, treatment: $F_{1,38} = 0.068$, $p < 0.05$).

(E) The relative search intensities at the search centre are similar in both strains of mice (Hatched bars: *Ptpn11* +/+ Veh rI_{cs} = 96 ± 2 (black), *Ptpn11* N308D/+ Veh rI_{cs} = 100 ± 3 (red)). Treatment of SL327 did not alter the relative intensity contributed to the search centre in case of both strains of mice (*Ptpn11* +/+ SL327 rI_{cs} = 100 ± 5 (blue), *Ptpn11* N308D/+ SL327 rI_{cs} = 100 ± 2 (green)). Two-way ANOVA for relative search intensity with genotype and treatment as two factors found no significant difference among the means nor any significant interaction between the factors. (genotype: $F_{1,38} = 0.36$, $p > 0.05$, treatment: $F_{1,38} = 0.36$, $p > 0.05$, genotype × treatment interaction: $F_{1,38} = 0.36$, $p > 0.05$).

(F) The absolute intensities measured from these two groups of mice share the same units as they are carried out on the same setup at the same frame rate. The intensity of search differs in case of *Ptpn11* N308D and its WT littermates (Horizontal bars: *Ptpn11* +/+ Veh aI_{cs} = 0.65 ± 0.015 (black), *Ptpn11* N308D/+ Veh aI_{cs} = 0.13 ± 0.004 (red)).. Treatment of SL327 rescues the deficit seen in N308D mice such that the treated mice search more intently than that of the vehicle treated mutant mice. Although SL327 affects the performance of the WT type mice but the direction of change is opposite to that of the N308D mutant. (*Ptpn11* +/+ SL327 aI_{cs} = 0.43 ± 0.019 (blue), *Ptpn11* N308D/+ SL327 aI_{cs} = 0.44 ± 0.007 (green); Bonferroni: *Ptpn11* N308D/+ SL – *Ptpn11* +/+ SL $p >$ 0.5.) Two-way ANOVA done on the absolute search intensity with genotype and treatment as two factors showed that means of both the factors(genotype: $F_{1,38} = 1749$, $p < 0.001$, day: $F_{1,38} = 55$,

$p < 0.001$), as well as interaction is significantly different ($F_{1,38} = 1217$, $p < 0.001$) Post hoc analysis confirms our earlier interpretation that SL327 rescues the spatial memory deficit seen in N308D mice although the treated group search intention is still significantly lesser than the wild type vehicle. We also note that administration of SL327 significantly lowers the search intention in the wild type animals.

.

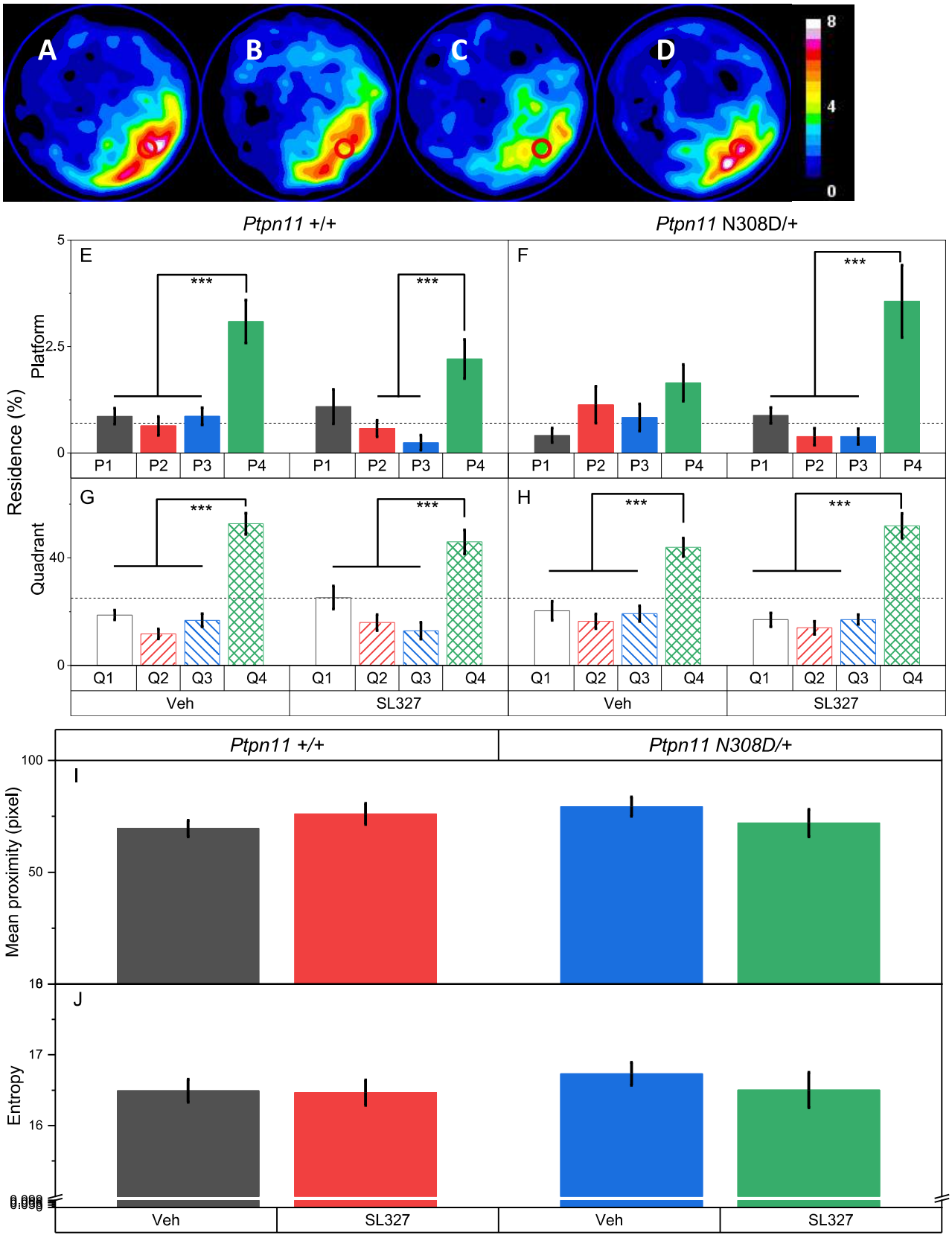

Figure 7.4: Other measures to assess spatial memory of *Ptpn11* +/+ and *Ptpn11* N308D/+ NS mice.

(A-D) Residence time heat maps.

(E-H) bar graphs quantify the residence time. P4 and Q4 correspond to the target location.

(I) bar graphs represent the mean proximity value. Two-way ANOVA with genotype as between-subjects factor indicated that mean proximity measure is not statistically different between *Ptpn11* +/+ and *Ptpn11* N308D/+ strains (genotype: $F_{1,38} = 0.354$, $p > 0.05$), nor across the within-subjects factor treatment between saline (Veh) and SL327 (drug) groups (treatment: $F_{1,38} = 0.00757$, $p > 0.05$). The ANOVA Main effect for interaction between genotype and treatment is also not (genotype × treatment interaction: $F_{1,38} = 2.13$, $p > 0.05$).

(J) bar graphs show the entropy measure. Similarly, the two-way ANOVA with genotype as between-subjects factor and treatment as within-subjects factor, show that the entropy measure was not statistically different between *Ptpn11* +/+ and *Ptpn11* N308D/+ as well as saline and SL327 (genotype: $F_{1,38} = 0.53$, $p > 0.05$, treatment: $F_{1,38} = 0.45$, $p > 0.05$). The interaction between genotype and treatment is also not statistically significant (genotype × treatment interaction: $F_{1,38} = 0.277$, $p > 0.05$).

The data is compared using one-way ANOVA and the means that are significantly different are indicated in the figure with asterisk (* >0.05, ** >0.01, *** >0.001).

Thus, mean proximity and entropy measures are unable to detect the subtle memory deficit, and its rescue by SL327, in *Ptpn11* N308D/+ mutant mice.

7.6 References

2D Gaussian fitting macro (Fiji/ImageJ) for multiple signals. | *BIII*. (n.d.). Retrieved May 10, 2021, from https://biii.eu/2d-gaussian-fitting-macro-fijiimagej-multiple-signals

Araki, T., Chan, G., Newbigging, S., Morikawa, L., Bronson, R., & Neel, B. G. (2009). Noonan syndrome cardiac defects are caused by PTPN11 acting in endocardium to enhance endocardial-mesenchymal transformation. *Proceedings of the National Academy of Sciences of the United States of America*, *106*(12), 4736–4741. https://doi.org/10.1073/pnas.0810053106

Araki, T., Mohi, M. G., Ismat, F. A., Bronson, R. T., Williams, I. R., Kutok, J. L., Yang, W., Pao, L. I., Gilliland, D. G., Epstein, J. A., & Neel, B. G. (2004). Mouse model of Noonan syndrome reveals cell type- and gene dosage-dependent effects of Ptpn11 mutation. *Nature Medicine*, *10*(8), 849–857. https://doi.org/10.1038/nm1084

Lee, Y. S., Ehninger, D., Zhou, M., Oh, J. Y., Kang, M., Kwak, C., Ryu, H. H., Butz, D., Araki, T., Cai, Y., Balaji, J., Sano, Y., I Nam, C., Kim, H. K., Kaang, B. K., Burger, C., Neel, B. G., & Silva, A. J. (2014). Mechanism and treatment for learning and memory deficits in mouse models of Noonan syndrome. *Nature Neuroscience*, *17*(12), 1736–1743. https://doi.org/10.1038/nn.3863

Noonan, J. A. (1968). Hypertelorism With Turner Phenotype: A New Syndrome With Associated Congenital Heart Disease. *American Journal of Diseases of Children*, *116*(4), 373–380. https://doi.org/10.1001/ARCHPEDI.1968.02100020377005

Romano, A. A., Allanson, J. E., Dahlgren, J., Gelb, B. D., Hall, B., Pierpont, M. E., Roberts, A. E., Robinson, W., Takemoto, C. M., & Noonan, J. A. (2010). Noonan syndrome: Clinical features, diagnosis, and management guidelines. In *Pediatrics* (Vol. 126, Issue 4, pp. 746–759). Pediatrics. https://doi.org/10.1542/peds.2009-3207

CHAPTER 8

Development of optical measures to improve contrast in *in vivo* imaging

Abstract

Fluorescence at optical saturation is a function of absorption cross section and excited state lifetime. Ultrashort pulses used in multi-photon spectroscopy depletes the ground state population. We reason that the depletion can be modelled and measured through steady state fluorescence. We developed a method to obtain fluorescence lifetime from steady state measurements utilizing a conventional custom built two photon imaging system and established a proof of principle application of by estimating the lifetime of rhodamine.

8.1 Introduction

8.1.1 Fluorescence intensity

Fluorescence is the type of emission of light from a substance after light matter interaction (Lichtman and Conchello, 2005; Lakowicz, 1999). When photons corresponding to the energy gap between the ground and excited state falls on the substance, the electrons get excited from the ground state to the excited state such that the electron in the excited state is paired to the electron in the ground state. The excited state electron undergoes vibrational relaxation and returns to the ground state by emitting a photon of lower energy. This is represented in a Jablonksi diagram (Fig. 8.1).

Fluorescence emissions generally have the following characteristics:

(i) Typically, the emitted fluorescence is of a higher wavelength compared to the excitation wavelength, a phenomenon known as Stokes shift, allowing for the spectral wavelength separation of excitation and emission light for a given fluorophore.

(ii) Kasha's rule states that the emission spectrum is independent of excitation wavelength. If an electron is excited to higher electronic or vibrational level, due to the strong overlap of states with similar energy levels, the electron dissipates the excess energy to rest in the lowest vibrational level of S1.

(iii) Fluorescence lifetime is the time the electron spends in the excited state before returning to the ground state.

(iv) The ratio of the emitted photon to the absorbed photon gives the quantum yield of a fluorophore. The higher the quantum yield, the brighter is the emitted fluorescence.

Both quantum yield and fluorescence lifetime can be influenced by certain factors (fluorophore quenchers, temperature, polarity, etc), thus these traits can provide information about the environment of the fluorophore.

Fluorescence intensity measurements can be made using detectors (e.g.

Photomultiplier tubes (PMT), scientific Complementary metal–oxide–semiconductor (scMOS)) to generate a contrast enhanced image of a sample containing fluorophores. However, time resolved measurements can be made to generate fluorescence lifetime images of a sample that provide information beyond intensity value or concentration of a fluorophore as discussed in the next section.

8.1.2 Fluorescence lifetime

As mentioned above, when a molecule is excited by a photon of appropriate energy, it undergoes a chain of photophysical events before returning to the ground state and emitting a photon of longer wavelength. The fluorescence lifetime of a molecule is the amount of time it spends in the excited state before returning to ground state. Since the different photophysical processes are associated with a certain probability defined by their rate constants, lifetime (τ) is calculated as

$$\tau = \frac{1}{T + k_{nr}}$$

where T is the decay rate constant, k_{nr} is the decay rate constant of all non-radiative processes. Thus, lifetime of a fluorophore indicates that 63% of the molecules have returned to ground state before τ time point.

Fluorescence lifetime is an intrinsic property of a fluorophore as it is dependent on the decay rate constants of different photophysical processes leading to fluorescence emission. Thus, the measured fluorescence lifetime is independent of different factors such as the excitation wavelength, duration of excitation, mode of excitation i.e. one-photon or two photons. Lifetime is also independent of the concentration of fluorophore. Measured lifetime is not affected by photobleaching. Since lifetime is an intrinsic property of the fluorophore, it is dependent on the fluorophore structure. Lifetime is also sensitive to the temperature, polarity and fluorescence quenchers present in its environment. These traits make fluorescence lifetime an excellent parameter to provide additional information on the environment of a sample, along with contrast enhancement of a sample.

Fluorescence lifetime requires time-resolved fluorescence measurements which can be obtained using either time-domain or frequency-domain methods. One of

the most common methods to measure time-domain measurements uses time-correlated single-photon counting (TCSPC).

8.1.3 Time Correlated Single Photon Counting

TCSPC works by generating a histogram of the different amounts of time taken between excitation and emission of a single photon when a sample is excited. Estimating the exponential decay of the histogram representing the range of lifetime of the sample provides the average lifetime of the fluorophore. TCSPC achieves this be detecting the start and stop time of the excitation pulse and the emitted photon respectively. In principle, a signal is sent to an electronics “clock”, i.e., constant function discriminator (CFD) which accurately times when the excitation pulse excites the fluorophore sample. The signal is used to generate a linear voltage ramp using a time-to-amplitude converter (TAC). Concurrently, the emitted fluorescence captured by a detector, setup such that a single photon is detected, signals the CFD which in turn signals the TAC to stop the linear voltage ramp. The voltage generated is digitized using an analog to digital converter (ADC) and a value is assigned representing the time taken between excitation and emission for a single photon by the fluorophore. Thus, by making repeated measurements, a histogram of decay can be obtained to elucidate the lifetime of a fluorophore. A schematic of the process is depicted in fig. 8.2.

It is vital that the detector counts single photons during each measurement since the histogram obtained from single photon counting accurately represents the decay waveform of a fluorophore. Additionally, modern TCSPC detectors and electronics require a dead time ranging from a few nanoseconds to microseconds, which is larger than the lifetime of commonly used fluorophores. Thus, detecting multiple photons would bias the decay curve to shorter time decay values.

8.2 Theory

8.2.1 Fluorescence described as a function of pulse in case of a train of pulses

8.1 Fluorescence as a function of pulses in case of a single pulse train

Initially, all the molecules are in the ground state ($n_g = N_T$). In response to an incident or excitation pulse, the molecules get excited from the ground state ($|e_g\rangle$) to the excited state ($|e_e\rangle$). The fraction of molecules excited from ground state to excited state in response to a pulse of a particular intensity (I) is given by

$$\alpha = \frac{N_T - n_g}{N_T} = \frac{1}{2 + \frac{k_f + k_b}{k1}} \qquad \text{…Eq.8.1}$$

We require an expression to describe the number of molecules in the ground state (n_g) as a function of pulse number (P_n) in a pulse train with inter-pulse separation of τ_{sep}. Depending on the relative magnitude of τ_{sep} and τ_f there will be a progressive depletion of ground state molecules as function of pulse number. This can be represented as a photophysical reaction. In such case the relationship between the ground state molecules between two consecutive pulses P_n and P_{n+1} can be summarised as below (Eq. 8.2).

$$n_g\,(P_n) \xrightarrow{K} n_g\,(P_{n+1}) \qquad \text{…Eq. 8.2}$$

The rate equation for the Eq. 8.2 is given by

$$\frac{d}{dP_n} n_g(P_n) = -K n_g(P_n) \qquad \text{…Eq. 8.3}$$

Integrating Eq. 8.3 with respect to P_n we obtain

$$n_g(P_n) = N_T \, exp\big(-K(P_n)\big) \qquad \text{…Eq. 8.4}$$

To determine K in Eq. 8.4, we consider the case of ground state molecules at pulse P_1 and P_2, where P_1 is the first incident pulse, and P_2 is the subsequent pulse. Thus, the difference of ground state molecules is given by

$$n_g(P_n) - n_g(P_{n+1}) = n_g(P_n)\,\alpha\, exp\left(-k_f \tau_{sep}\right) \quad \text{...Eq. 8.5}$$

Thus, K in Eq. 8.4 is given by

$$K = \alpha\, exp\left(-k_f \tau_{sep}\right) \quad \text{...Eq. 8.6}$$

The fluorescence emitted by the molecules between pulses P_n and P_{n+1}, i.e., during time interval τ_{sep} is a result of decay to ground state by the molecule present in the excited state before the arrival of P_n pulse as well as the molecules getting excited as a result of P_n pulse. Mathematically, we represent this as

$$F(P_n) = \int_0^{\tau_{sep}} \left[\underbrace{\left(N_T - n_g(P_n)\right)}_{Molecules\ in\ excited\ state\ before\ P_n} + \overbrace{\left(n_g(P_n)\alpha\right)}^{Molecules\ excited\ by\ P_n} \right] exp\left(-k_f t\right)$$

...Eq. 8.7

$$\mathrm{F}(P_n) = \left(N_T - n_g(P_n)[1-\alpha]\right)\left(1 - exp\left(-k_f t\right)\right) \quad \text{...Eq. 8.8}$$

Using Eq. 8.4 and Eq. 8.6 in Eq. 8.8, we get

$$F(P_n) = A(1 - B\, exp(-CP_n)) \quad \text{...Eq. 8.9}$$

where

$$A = N_T\left(\frac{1 - exp\left(-k_f \tau sep\right)}{k_f}\right)$$

$$B = 1 - \alpha$$

$$C = \alpha\, exp\left(-k_f \tau_{sep}\right)$$

Now we can integrate Eq. 8.9 between our time interval where we observed the emitted fluorescence, i.e., 0 to τ_{obs}.for $\tau_{obs} >> \tau_{sep}$

$$F_{obs} = \int_0^{\tau_{obs}} F(P_n) dP_n$$

$$F_{obs} = A\left[\tau_{obs} - \frac{B}{C}(1 - exp(C\,\tau_{obs}))\right]$$

8.2 Fluorescence as a function of pulses in case of two pulse trains with an onset delay of time $\tau 1$

Consider two pulse trains with pulses P_n^1 and P_n^2 with a time delay of τ_1. As derived in the previous section, the number of molecules in the ground state between two pulses is given by,

$$n_g(P_n^1) - ng(P_n^2) = n_g(P_n^1)\alpha_1\, exp(-k_f\tau_R) + \overbrace{\left(n_g(P_n 1) - n_g(P_n^1)\alpha_1\, exp(-k_f\tau_1)\right)\alpha_2\, exp(-k_f\tau_2)}^{Term\ \#1:\ no.of\ molecules\ available\ for\ Pn2} + \overbrace{\sum_{\gamma=1}^{n} dn_g\, P_\gamma^\gamma\, exp(-k_f(n-\gamma)\tau_R)}^{Term\ \#2}$$

Term #2 captures the decay of the population of ground state molecules that got accumulated before the P_n^1 pulse. However, for a typical use,

$$\tau_R = \frac{1}{80\cdot 10^6}\,\mathrm{s} = 12.5\mathrm{ns} \gg \tau_f = 4.5\mathrm{ns}$$

Thus, after two repetition rate duration, we can neglect term #2. Considering the effects due to one τ_R duration before τ_{obs},

$$n_g(P_n^1) - n_g(P_n^2) = n_g(P_n^1)\left[\alpha_1\, exp(-k_f\tau_R) + \left(1-\alpha_1\, exp(-k_f\tau_1)\right)\alpha_2\, exp(-k_f\tau_2)\right]$$

…Eq. 8.10)

We rewrite Eq. 8.10 as,

$$n_g(P_n^1) - n_g(P_n^2) = n_g(P_n^1)\cdot K \quad \text{where} \quad K = \alpha_1(1-\alpha_2)\, exp(-k_f\tau_R) + \alpha_2\, exp(-k_f\tau_2)$$

… Eq. 8.11

Rearranging Eq. 8.10 and using Eq. 8.11, we get the difference in ground state molecules as

$$\partial \mathrm{n_g}(\mathrm{P_n^1}) = n_g(P_1^{n+1}) - n_g(P_1^n)$$

$$\partial \mathrm{n_g}(\mathrm{P_n^1}) = -K n_g(P_n^1) \qquad \text{…Eq.8.12}$$

Solving the differential equation Eq.8.12, we get

$n_g(P_n^1) = N_T\, exp(-KP_n)$ …Eq. 8.13

The fluorescence emitted by a fluorophore on excitation is directly proportional to the molecules de-exciting from the excited state to the ground state. Thus, the fluorescence in the interval P_n^1 and P_{n+1}^1 is given by,

$F = \left[N_T - n_g(P_n^1)\right]\left(1 - exp\left(-k_f\tau_R\right)\right) + n_g(P_n^1)\alpha_1\left(1 - exp\left(-k_f\tau_R\right)\right) + n_g(P_n^1)\alpha_2\left(1 - exp\left(-k_f\tau_2\right)\right)\left(1 - \alpha_1\, exp\left(-k_f\tau_1\right)\right)$ …Eq.8.14

Rearranging Eq.8.14 and replacing $\tau_2 = \tau_R - \tau_1$, we get the fluorescence from P_n^1 and P_{n+1}^1 as,

$F = N_T[1 - (1 - \alpha_1)\exp(-KP_n^1)]\left(1 - \exp\left(-k_f\tau_R\right)\right) + N_T\exp(-KP_n^1)\left(1 - \alpha_1\exp\left(-k_f\tau_1\right)\right)\alpha_2\left(1 - \exp\left(-k_f(\tau_R - \tau_1)\right)\right)$ … Eq. 8.15

Thus, integrating the total fluorescence emitted in the interval t = 0 and t = $P_{obs} = \frac{\tau_{obs}}{\tau_R}$, the time of arrival of the n^{th} pulse P^n, we get

$\int_0^{P_{obs}} F(P_n^1)\,\partial(P_n^1) = N_T\left[\frac{\tau_{obs}}{\tau_R} - \frac{(1-\alpha_1)}{K}\left(1 - exp\left(-K\frac{\tau_{obs}}{\tau_R}\right)\right)\right]\left(1 - exp\left(-k_f\tau_R\right)\right) + \frac{N_T\alpha_2}{K}\left(1 - exp\left(\frac{-K\tau_{obs}}{\tau_R}\right)\right)\left(1 - \alpha_1\, exp\left(-k_f\tau_1\right)\right)\left(1 - exp\left(k_f\tau_1\right)exp\left(-k_f\tau_R\right)\right)$ …Eq.8.16

Here, $\frac{K\tau_{obs}}{\tau_R}$ represents the accumulated fraction of molecules after 'n' pulses. Thus, $\frac{K\tau_{obs}}{\tau_R} < 1$ would represent the state before ground state molecules are depleted.

Thus, Eq. 8.16 can be approximated to

$F = N_T\left\{\alpha_1\frac{\tau_{obs}}{\tau_R}\left[1 - \alpha_2\, exp\left(-k_f\tau_1\right) - (1 - \alpha_2)\, exp\, -k_f\tau_R + \frac{\alpha_1}{\alpha_2}\left(1 - exp\left(-k_f\tau_2\right)\right)\right]\right\}$ …Eq. 8.17

When $\frac{\alpha_2}{\alpha_1} < 1$, then

$F_{total} = N_T\left\{\alpha_1\frac{\tau_{obs}}{\tau_R}\left[1 - \alpha_2\, exp\left(-k_f\tau_1\right) - (1 - \alpha_2)\, exp\, -k_f\tau_R\right]\right\}$ …Eq.8.18

8.3 Results and discussion

8.3.1 Fluorescein lifetime

We measured the steady state fluorescence at different pulse delay time points ranging from 0 – 2000ps using 1000nm fluorescein solution in 1x PBS (pH7.4). In figure 8.4, the mean fluorescence of the ROI is represented as open circles. The red solid line is the fit to Eq. 8.18. The goodness of fit was assessed using Adj R-sq (Adj R-sq > 0.9). Thus, lifetime τ was found to be 2.186 ± 1.334 ns.

8.3.2 Rhodamine B lifetime

Similarly, we estimated the lifetime value for Rhodamine B solution. The steady state fluorescence measurements were obtained for different pulse delay time points ranging from 0 – 3200ps using rhodamine solution details. In figure 8.5, the mean fluorescence of 10 images taken for the different pulse-pair delays are represented as open circles. The red solid line is the fit to Eq. 8.18. The goodness of fit was assessed using Adj R-sq (Adj R-sq > 0.9). Thus, lifetime τ was found to be 2.1 ± 0.2ns.

8.4 Discussion

We derived an analytical expression to model fluorescence decay on excitation by using steady state fluorescence measurements at different dual pulse train delays. We developed the optical hardware and software setup to obtain the lifetime values of solutions. We showed a proof of principle of the method using fluorescein and rhodamine solution.

Fluorescence lifetime imaging (FLIM) is used extensively to address questions in biology as well as in neuroscience (Yasuda, 2012). Specially designed fluorescence resonance energy transfer (FRET) pair combinations of acceptor and donor molecules allow scientists to investigate a variety of molecular and cellular mechanisms in response to stimuli in cell lines and brain slices as well as in freely moving and behaving rodents. For example, quantifying FRET fluorescence using FLIM has been used to understand specific molecular interactions, activation of kinases in response to dendritic activity, as well as monitoring the levels of neurotransmitters such as dopamine in reinforcement learning task (Lee et al., 2021).

However, even with the latest technology to estimate lifetime of a molecule achieving a high spatial resolution along with a high temporal resolution is not possible. Studies achieving high temporal resolution capture the overall change in fluorescence in a region to estimate the lifetime. Such a method loses out on spatial resolution of the changes happening at the level of individual neurons and even within neurons. For example, FLIM using optical fibres allow estimation of lifetime in 1s time windows that can be coupled with the animal performing a behaviour.

On the other hand, studies achieving a high spatial resolution lose out on temporal resolution. The proof of principle presented in chapter 8 provides a method that can potentially bridge the compromise between spatial and temporal resolution when using two-photon FLIM.

8.5 Materials and Methods

8.5.1 Fluorophores:

The chemicals fluorescein and rhodamine B were obtained from Sigma-Aldrich. 50 nM of Rhodamine B was prepared in ethanol.

8.5.2 Optical setup:

A description of the custom-built optical setup for data collection is presented in Appendix C3 (Schematic shown in fig. C3). Briefly, a femtosecond pulsed laser (Tsunami, SpectraPhysics) tuned to the appropriate wavelength (Fluorescein: 760nm, Rhodamine B: 800nm, bandwidth = 15nm) was split into two parts using a 50-50 beamsplitter (ThorLabs: BSW29R). Two retroreflecting prism mirrors, one fixed on the optomechanical table and the other on the delay line stage placed on a linear actuator, were used to align the split beams into a collinear path centred to the microscope objective (Olympus 40xW Cat. no. LUMPLFLN). The delay line stage allowed varying the inter-pulse interval.

Fluorescence was captured using a monochrome sCMOS camera (Thorlabs DCC1240M). Appropriate emission filters (Fluorescein: FF01-520/70 along with an aqueous solution of copper sulphate (IR absorption), Rhodamine B: 2x FF01-612/69) were placed in front of the detector to improve the signal to noise ratio.

8.5.3 Data analysis:

Ten image replicates were obtained to calculate the average fluorescence emitted for each data point (i.e. each delay time point). The mean of the ten images was used to as the steady state fluorescence value for a given pulse-pair delay.

Curve fitting analysis of steady state fluorescence as a function of excitation time delays for a selected ROI was carried out in Origin(v2020b)'s user-defined NLFit function using Levenberg-Marquardt algorithm. The parameters were set as follows for data fitting at the start of the Levenberg-Marquardt algorithm for least squares minimisation: Parameter A was set to the fluorescence value at the shortest time delay or first data point, parameter B was set to the reciprocal or rate

constant equivalent of the reported lifetime of the fluorophore (in ps), and the parameter C was set to 0.5. The goodness of fit was determined by the Adj. R-sq. value.

A custom software written in Java utilizes ImageJ's (v52) Curve Fitter class using Simplex algorithm to generate a lifetime image for a series of input images of steady-state fluorescence. The software takes a series fluorescence intensity image at different excitation time delays and performs the fit to Eq. 8.18 for each pixel. Parameters are initialised as described above before fitting for each pixel, and obtained lifetime is assessed for goodness of fit based on Adj. R-sq. On completing the fits, the software outputs a lifetime image of the sample.

8. 6 Figures

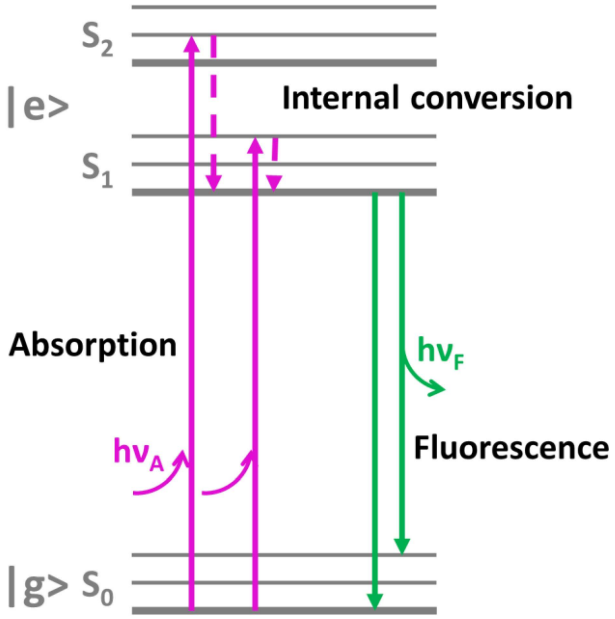

Figure 8.1: Jablonski diagram.

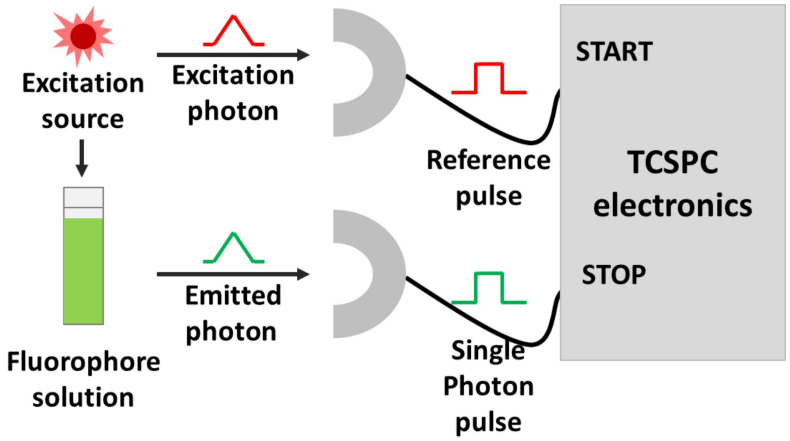

Figure 8.2: TCSPC (Time Correlated Single Photon Counting) schematic.

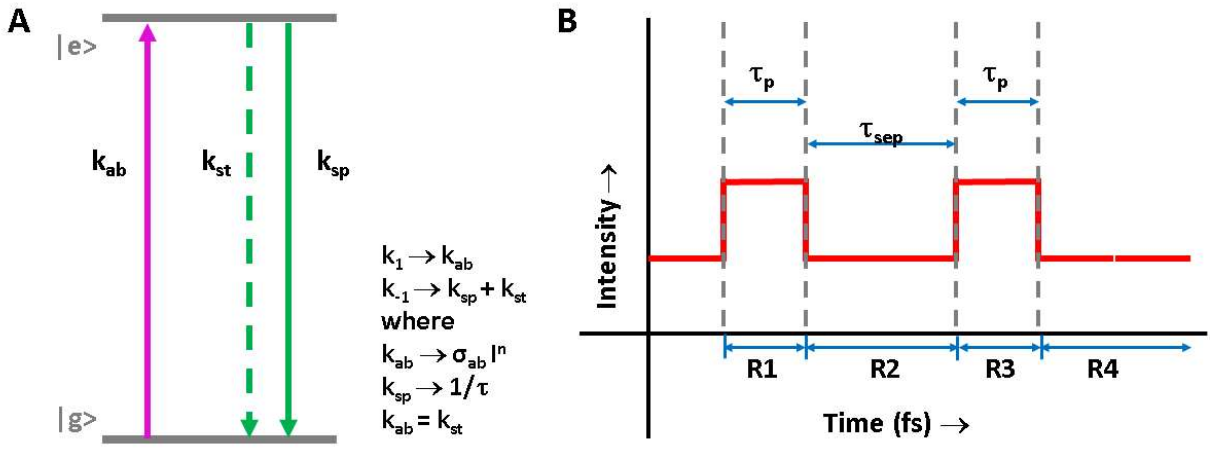

Figure 8.3: Schematic representation of a pulse pair used for excitation of fluorophore.

(A) Jablonski diagram showing excitation of the molecule from ground state |g> to excited state |e> with a rate constant k_{ab} (pink solid line). The molecule returns from excited state to ground state either by spontaneous emission (green solid line) with rate constant k_{sp} or stimulated emission (green dashed line) with rate constant k_{st}. Lifetime (t) is the reciprocal k_{sp}.

(B) A pulse pair comprising of two square pulses (red solid line) of width (t_p) and intensity (I_{pk}) separated by an inter-pulse duration t_{sep} is used to excite a fluorophore. The excitation pulse pair is divided into four regions (demarcated by grey dashes): R1, R2, R3 and R4, during which we model the population kinetics of the fluorophore molecules.

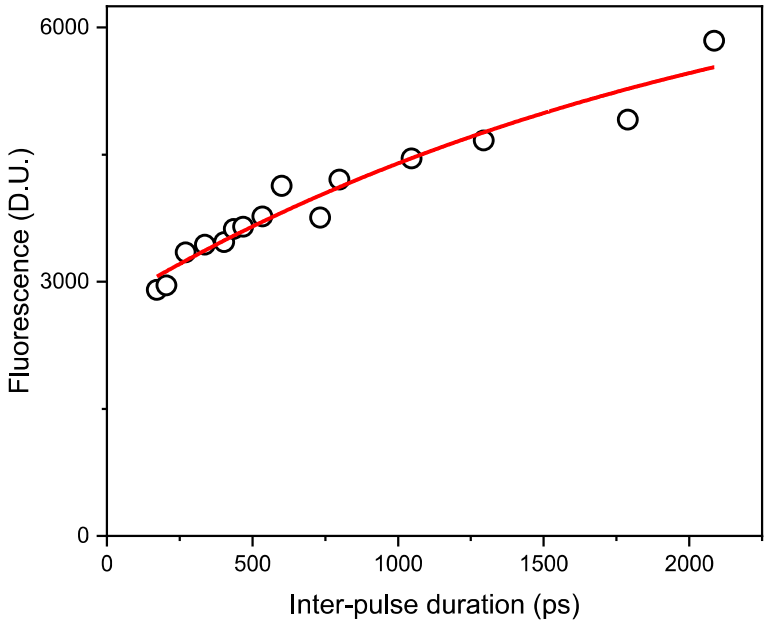

Figure 8.4: Lifetime measurement fluorescein. The mean fluorescence value of an ROI is represented as open circles. The red solid line is the fit to Eq. 8.18.

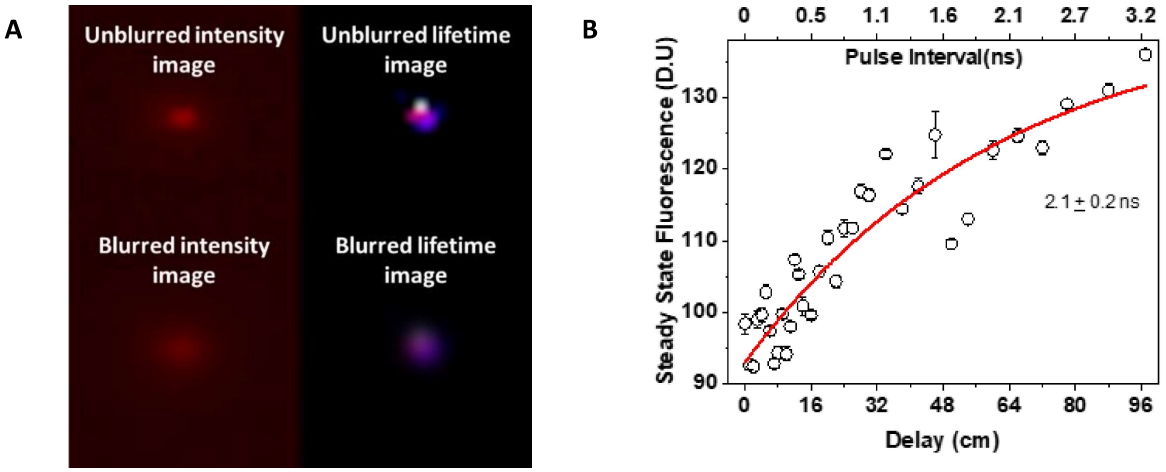

Figure 8.5: Lifetime measurement Rhodamine B. (A)Left: Intensity image of fluorescence emitted by Rhodamine B solution. Right: Lifetime image obtained by calculating the lifetime in each pixel. (B) The mean fluorescence value of an ROI obtained from 10 images is represented as open circles with error bars representing SEM. The red solid line is the fit to Eq. 8.18.

8.7 References

Lakowicz, J.R. 1999. Introduction to Fluorescence. *In* Principles of Fluorescence Spectroscopy. Springer, Boston, MA. 1–23.

Lee, Suk Joon, et al. "Cell-type-specific asynchronous modulation of PKA by dopamine in learning." *Nature* 590.7846 (2021): 451-456.

Lichtman, J.W., and J.-A. Conchello. 2005. Fluorescence microscopy. *Nat. Methods 2005 212*. 2:910–919. doi:10.1038/nmeth817.

Yasuda, Ryohei. "Imaging intracellular signaling using two-photon fluorescent lifetime imaging microscopy." *Cold Spring Harbor Protocols* 2012.11 (2012): pdb-top072090.

CHAPTER 9

Conclusion

In conclusion, we developed various molecular, optical, and behavioural tools to address questions related to learning and memory.

Specifically, we developed a novel method to identify, segregate and classify neurons in response to a behaviour based on their IEG expression profile. We utilised the method to investigate the contextual representation of two context retrievals linked in time in the retrosplenial cortex region. (Fig. 9.1 (A))

Next, we developed sensitive measures using velocity vector and its vector field properties to explain the nature of spatial memory in a navigational task. We utilised the method to compare performance in MWM of different strains of mice as well as assess spatial memory deficits in Noonan syndrome mice models. (Fig. 9.1(B))

Lastly, we developed an optical method to measure fluorescence lifetime using steady state measurements and provided the proof of principle of the method.

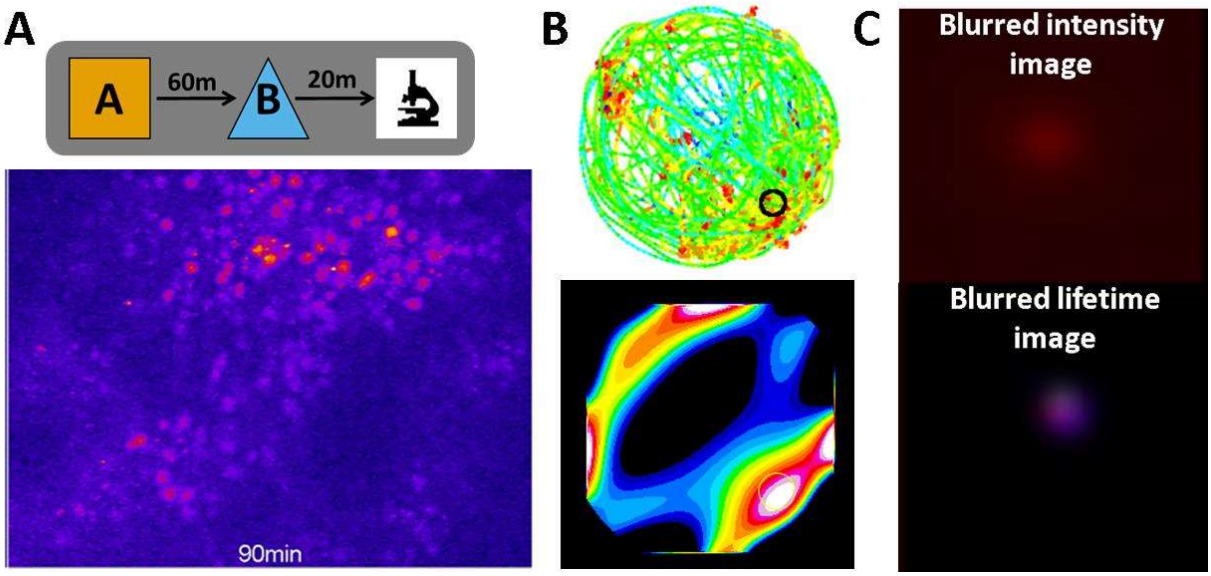

Figure 9.1: Conclusion

APPENDICIES

Appendix A

Two-photon microscopy

A.1 Introduction

Microscopy is routinely and widely used in biology to study molecular interactions, physiological mechanisms, structural and functional processes. As described in Chapter 8, fluorescence microscopy is an invaluable method to enhance image contrast of fluorescently labelled biological samples. However, fluorescence microscopy is suitable for certain biological samples, i.e., fixed cells, or thin tissue sections, where the penetration depth of the excitation light into the sample is small. With thicker samples, there is larger scattering of incident light and emitted fluorescence as the light travels through a heterogenous sample with mismatched refractive indices. Imaging thick tissue sections or live samples would require a setup such as confocal microscopy where a mechanical pinhole prevent out-of-focus light from being detected, thus creating optical sections of the sample. The optically sectioned sample can be reconstructed to give a sharp image of the sample. Even so, deep tissue imaging, such as cortical layers of the brain, require the use of non-linear optics to achieve the optimal parameters required for imaging, i.e., penetration depth, spatial resolution, temporal precision, and excitation and emission spectra of fluorophore tag.

Non-linear optics or multiphoton microscopy

Multiphoton microscopy refers to fluorophore excitation by more than one photon of the required wavelength of light. In one photon excitation, the fluorophore absorbs photon wavelength λ with the required energy for the molecule to go from ground state to excited state. However, in principle, a fluorophore can absorb n such photons of λ/n wavelength, a phenomenon first described by Maria Goeppert-Mayer in 1931. Such n-photon excitations follow non-linear kinetics, hence is also known as non-linear optics. In two-photon excitation, the fluorophore can absorb two photons of half the wavelength, λ/2, to excite the molecule. Due to the nature

of excitation, the focal volume in two-photon excitation is much smaller than one photon excitation. Thus, there is an inherent optical sectioning effect, which improves the contrast by reducing out of focus fluorescence light. Additionally, the use of longer wavelength improves the penetration depth of the excitation light in thick samples.

A.2 Components of a two-photon microscope

A.2.1 Excitation source: Femtosecond laser

We use the Tsunami laser by Spectra-Physics for the purpose of building a two-photon microscope. Tsunami is an ultrafast laser femtosecond laser that produces optical pulses in the range of femtoseconds (fs), i.e., 10-15s. The Tsunami laser contains a Ti:sapphire rod along with optical elements required for spectral wavelength amplification in the resonator cavity. A continuous wave (CW) laser, Millenia Pro, functions as a pump laser to excite and lase the active medium Ti-Sapphire crystal of the Tsunami laser.

The core of the Tsunami laser is the Ti-Sapphire crystal which is an aluminium oxide material doped with titanium oxide. On excitation with a pump laser, the Ti3+ ions undergo absorption transitions over the range of 400-600nm, and fluorescence transitions over the range of 600-1000nm. Thus, optimal lasing action can be obtained in the tuning range of 670nm – 1000nm wavelength.

Pumping optimization is achieved by longitudinal pumping using a narrow beam where the Ti-Sapphire rod is aligned colinearly with the laser mode to achieve overlap within the same volume within the crystal. This alignment ensures that the gain of the spectral profile is greater than the loss (via mirror surfaces, reflectors, dispersion control elements, etc) incurred during the roundtrip within the resonator cavity.

The laser cavity has a folded, ten-mirror configuration to allow a laser path length to achieve a repetition frequency near 80MHz. While the folded cavity configuration optimizes for space, the laser beam incident on mirrors at angles other rectilinear geometry. Thus, concave focusing mirrors are used which introduce astigmatism in the pump beam which matches the Tsunami cavity mode, ensuring a good beam

quality.

The required excitation wavelength is selected with the help of a prism pair and mechanical slit. The laser beam is spatially distributed between two prisms. This dispersed beam is filtered using a slit to change the wavelength and bandwidth of the output pulse.

A.2.2 Galvo Scanner

A Galvometer is a precision motor system that rotates a mirror mount in response to applied current. A galvo scanner system with two motors and two mirrors is utilised to achieve a point scanning behaviour of an area, i.e. raster scan. In raster scanning, the first mirror, i.e. fast scanner, moves the beam in the X-axis, and the second mirror, i.e. slow scanner, moves the beam in the Y-axis, to create a lateral movement of a 2-D area at the desired focal spot.

A.2.3 Scan lens and tube lens

When creating the focal spot of excitation, the beam must be focussed in two domains: one with respect to space and another with respect to time. We utilized the galvanometric mirrors, the scan, and the tube lenses to obtain a stationary beam in both space and time domain at the back of the objective (Fig. A1).

A.2.4 Multiphoton objectives

The objective lens of a microscope focuses the excitation beam to the focal spot. Thus, it is vital the objective creates a tight focal spot increase the probability of two-photon excitation. In case of two-photon microscopy, the excitation and emission spectra range infrared and visible wavelengths of light, hence the objective should have a good transmission efficiency for these wavelengths. Additionally, in vivo imaging of samples requires objectives with long working distance and high numerical aperture. High numerical aperture improves the collection efficiency of emitted fluorescence. The numerical aperture also determines the optical resolution of the image (Section A3.4). Commercially available multiphoton objectives optimize for these criteria to maximize for efficiency in two-photon microscopy.

A.2.5 Detectors

Photon detectors are instruments that detect photons and convert them to electrical signal via the photoelectric effect. A few types of detectors are briefly described below:

Array based detectors:

Charge-couple device (CCD) and complementary metal oxide semiconductor (CMOS) detectors are solid state, integrated circuits consisting of an array of capacitors. The electronic processing of the light intensity signal at each pixel, i.e. analog-to-digital conversion, and noise reduction, is carried out on the sensor chip itself. This results in low noise levels and sensitivity. The use of ICs provides CCDs/CMOSs high resolution and durability.

Photomultiplier tubes (PMTs)

Photomultipler tubes (PMT) are sensitive light detectors consisting of a vacuum tube with a photocathode that converts photons to current by virtue of the photoelectric effect.

A.2.6 Preamplifier

Current amplifiers strength weak electrical signals to ensure a sturdy and reliable signal transmission that is resistant to noise.

The SR570 (Stanford Research System) is a low-noise current preamplifier, providing a voltage output proportional to the input current. The operational bandwidth (which determines the galvoscanner speed) limits the sensitivity of the preamplifier.

A.2.6 Digital to Analog Conversion and Data acquisition

A software that generates the analog voltage waveforms to drive the scan mirrors, acquires the raw data from the photomultiplier tubes (PMTs), and processes these signals to produce images. We used ScanImage software (v3.8, Virdo Technologies) send the signal to generate the analog voltage waveform to the

galvo scanner and Ni-DAQ for converting photon signal to an image.

A.3 Description of the custom built two-photon microscope

A.3.1 Overview

The operation of the two-photon microscope carried out for the experiments carried out in the thesis generally followed the following steps. Tsunami (Spectra-Physics) femtosecond laser is tuned to the desired wavelength (760-1000nm) with an output power of 1.2-1.5W. The beam is directed to an inverted microscope (Axio Examiner.Z1, ZEISS). A dual-axis motor/mirror assembly with gold mirrors galvo scanner (GVS 102, ThorLabs) is employed for raster scanning of the sample. Raster scan is achieved by using a saw tooth voltage command waveform generated by Data Acquisition System (PCI 6110, National Instrument) and controlled via ScanImage software (v3.8, Virdri Technologies) on the galvo scanner. With the use of a scan and tube lens, the laser beam directed to a long working distance, high NA, water immersion, multiphoton 25x objective (XLPLN25XWMP2, Olympus). The beam size is adjusted to under fill the back focal plan of the objective (<16mm). A dichroic (FF705-Di01, Semrock) reflects the emitted fluorescence (<700nm) to the PMTs (PMT H7422-40, Hamamatsu). PMT is mounted with copper sulphate solution to eliminate infrared spectrum of the excitation light, and emission filters appropriate for the fluorophore being images was used to improve signal to noise ratio of detected photons.

Signal from the PMT is amplified using a preamplifier (SR570, Stanford Research Systems) before using an analog to digital converted (Ni-DAQ, PCI 6110, National Instruments) to generate an image.

A.3.2 Pulse width calculation

Pulse width calculation:

$$\Delta E \Delta t \geq \frac{h}{4\pi}$$

Replacing $E = h\nu$ and $c = \nu\lambda$, we get

$$h\Delta\frac{1}{\lambda}\Delta t \geq \frac{h}{4\pi}$$

Simplify to get

$$\Delta t \geq \frac{\Delta\lambda}{4\pi c\lambda_c}$$

where $\Delta\lambda = \lambda_2 - \lambda_1$ is the bandwidth and $\lambda_c$is the central wavelength of the bandwidth.

A.3.3 Dwell time calculation

For image acquisition of resolution 1024 x 1024, with a frame rate of 0.2 Hz, the dwell time on each pixel is calculated below.

Given:

Number of pixels per line = 1024

Number of lines per frame = 1024

Frame rate (Hz) = 0.2

4 ms per line

i.e. 4ms per 1024 pixels

Hence, time spent on one pixel is

4ms/1024 pixels = 0.00390625ms

i.e. 3.9 microseconds for 1 pixel.

Thus, the dwell time is ~4microseconds.

A.3.4 Optical resolution calculation

Olympus 25x multiphoton objective (XLPLN25XWMP2) has the following features:
Magnification: 25x

Immersion medium: Water
Numerical Aperture (NA): 1.05
Working distance: 2mm
Objective Field Number:18mm
Refractive index of water (n): 1.33

The Rayleigh criterion specifies the minimum separation between two light sources that may be resolved into distinct objects. Lateral resolution (l) and axial or depth resolution (d) are given by

$l \approx \frac{0.61\lambda}{NA}$ and $d = \frac{2n\lambda}{NA^2}$

respectively where NA is the numerical aperture, n is the refractive index, λ is the wavelength. Table A1 shows the theoretical values of lateral and axial resolution for wavelengths of light routinely encountered in the imaging experiments in the lab.

A.4 Characterisation of the two-photon microscope

A.4.1 Quality of acquired image

After acquiring the image for a given set of imaging parameters, its quality was assessed for the following. The spatial uniformity of signal detection was carried out using a homogenous solution. Fig. A2 (A) shows the image acquired for uniformly illuminated fluorescein solution. A line profile of fluorescence along the horizontal and vertical axis captures any anomalous variation of fluorescence as a function of time. For example, non-uniform illumination of sample or detection of emitted fluorescence will result in a gradation of fluorescence of a homogenous sample. Similarly, the presence of systematic noise would be indicated as periodic fluctuations in the profile plots. Such a plot profile can provide information on which imaging parameter may have to be optimised for improving the quality of the image. A brief table listing troubleshooting tips is presented in Table A2. In fig. A2 (B) and (C), the fluorescence detected in the different points in space show uniform fluorescence.

A.4.2 Point spread function

Due to the diffraction limit of light, a point object imaged through a microscope appears as a blur, i.e., the fluorescence signal is spread over several pixels instead of being localised to one pixel or a point. A point spread function describes the spatial distribution of the fluorescence of a point object as imposed by the diffraction limit.

The theoretical PSF, calculated as the lateral and axial resolution, estimates the resolving power of imaging system (i.e., combination of excitation wavelength, numerical aperture of objective, refractive index of medium) as shown in SectionA3.4. However, it is important to calculate the experimental PSF to estimate the resolving power of an imaging system as it determines, apparent size, brightness, the quality and resolution of the imaged sample.

A.4.3 Characterisation of two-photon excitation

The following graphs were obtained to characterise the two-photon microscope built in the lab.

1) Concentration of fluorophore versus fluorescence signal (Fig. A4).

2) Power of excitation beam versus fluorescence signal (Fig. A5).

3) PMT gain versus fluorescence signal (Fig. A6).

A.4.4 Imaging section and ex-vivo mammalian brain

Representative images of samples imaged through two-photon excitation is shown in figures A7-A9. The two-photon microscope is able to image samples that are brain sections, as well as ex-vivo and in vivo whole brains. The image resolution is sufficient to see the spines present on the dendrite of the neurons.

A.5 Materials and Methods

<u>Chemicals and fluorophores:</u>

200nm yellow-green and 400nm red fluorescent beads (F-8848 Invitrogen) were used for characterizing the image and data collected on the custom built two-photon microscope. The sample was prepared by vortexing the vials, mixing beads with 2% agarose in water, maintaining a 1000 times dilution of the 2% stock solution. The beads were excited using 750-800nm wavelength.

Fluorescein solution was prepared at the required concentrations (10-1000nM) in 1x phosphate buffered saline (PBS) at pH 7.4.

Brain sample:

Transgenic mice Thy1-GFP (JAX#) or C57BL6 (JAX#) mice infused with tdTomato virus were used for the experiments described in this section. Mice brains were extracted via transcardial perfusion. Extracted brains were placed in a solution of 4% formaldehyde for 5 days to crosslink fluorophore. Brains for sectioning were placed in sucrose solution. 50micron sections were made using a cryostat and mounted on slides.

Data analysis:

Digitized images stored as TIFF files were analysed using ImageJ (v52) software to extract mean fluorescence intensity in digital units (D.U.). Linear and non-linear curve fitting were carried out in Origin(v2020b) using Levenberg-Marquardt algorithm for minimizing least squares. Plots and graphs were generated in Origin(v2020b) for presentation.

A.6 Figures

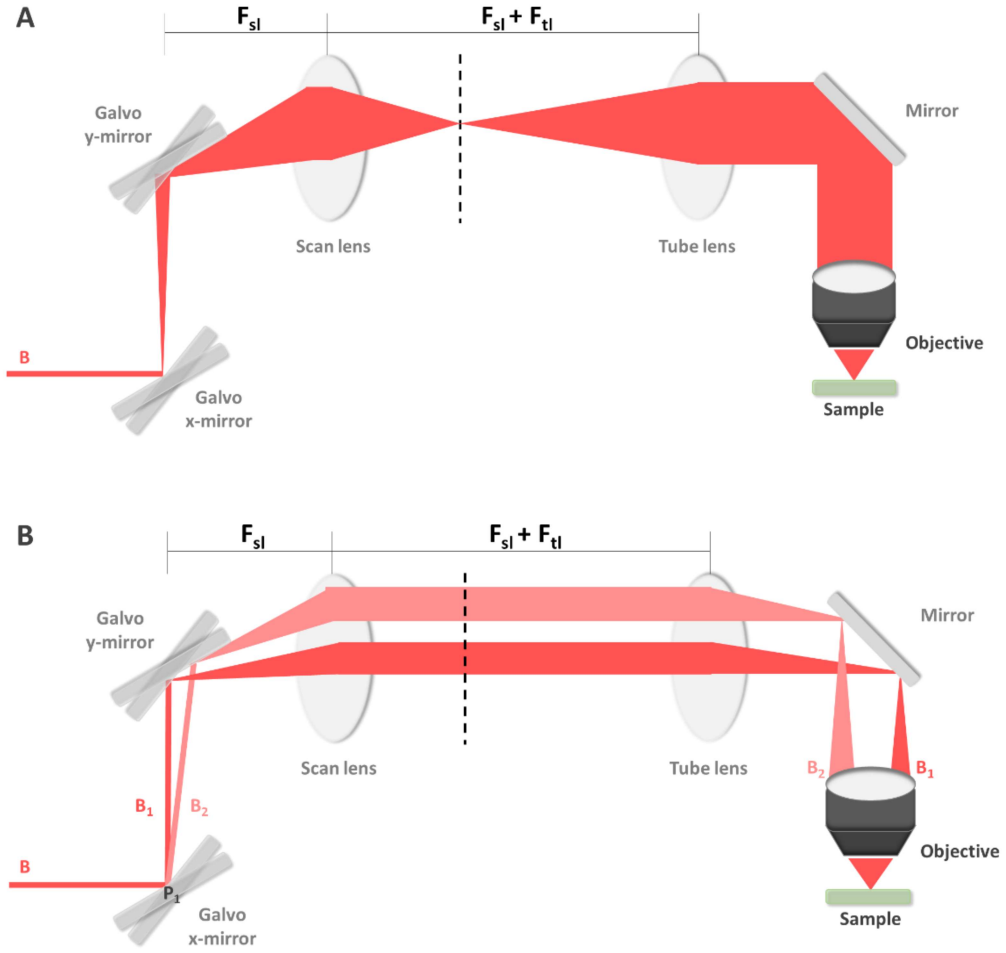

Figure A1: Schematic describing hinge point.

(A) Collimation of excitation in space domain at the hinge point ensures that the beam is collimated in space and stationary at the objective backfocal plane. The collimated laser input beam is reflected to scan lens via galvometric mirrors. The scan lens focuses the beam at its focal point (F_{sl}). The tube lens is placed at a distance of the sum of focal lengths of scan lens and tube lens ($F_{sl} + F_{tl}$) from the scan lens so that beam exiting the tube lens is collimated. The distance between scan lens and tube lens ensures that the input beam from the galvometric mirrors is collimated in the space domain at the objective backfocal plane.

(B) Collimation of excitation in time domain at the hinge point ensures that the beam is stationary at the objective backfocal plane. A stationary collimated beam (B) incident on the galvo mirror results in different reflected beams (B_1, B_2) with respect to time t_1, t_2 due to the galvo mirror position. Since these input beams B_1, B_2 appear to originate from the same incident point (P_1), the point appears as a

point source. The point source in time P_1 at a focal distance F_{sl} from scan lens ensures that the collimated beams B_1, B_2 focus to form a collimated focal plane in the time domain at the scan lens. The collimated beam in the time domain consists of the different reflected beams travels to the tube lens. As it goes through to the tube lens, the reflected beams (B_1, B_2) get focused at the focal point of the tube lens (F_{tl}). The objective backfocal plane coincides with F_{tl} such that each reflected beam B_1, B_2 form a focused spot on the plane. Thus, the beam appears stationary.

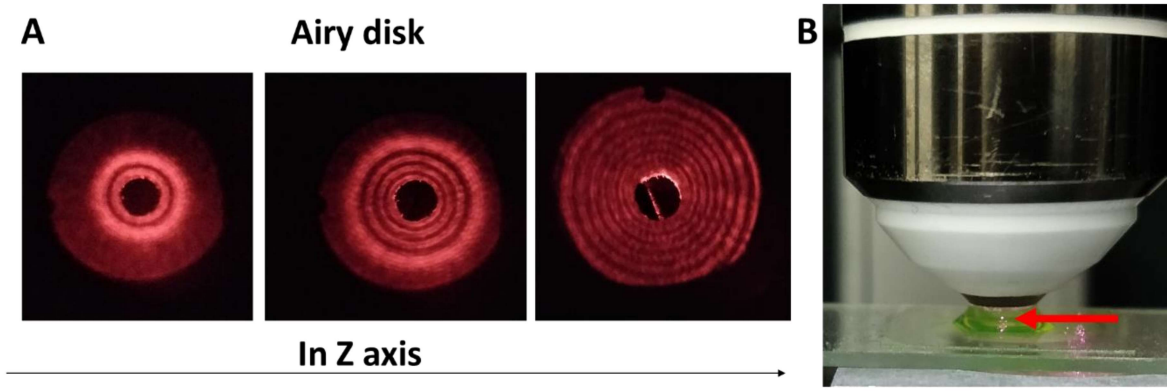

Figure A2: Assessment of laser beam alignment for two-photon excitation.
(A) Images of the airy disk at three different z-axis depths. The sharp concentric rings of the airy disk show the point spread function (PSF) of the image formed at the focal plane of the objective (using the excitation beam reflected from a glass slide).
(B) Two photon fluorescence of fluorescein solution seen as a precise focal volume (indicated by the red arrow).

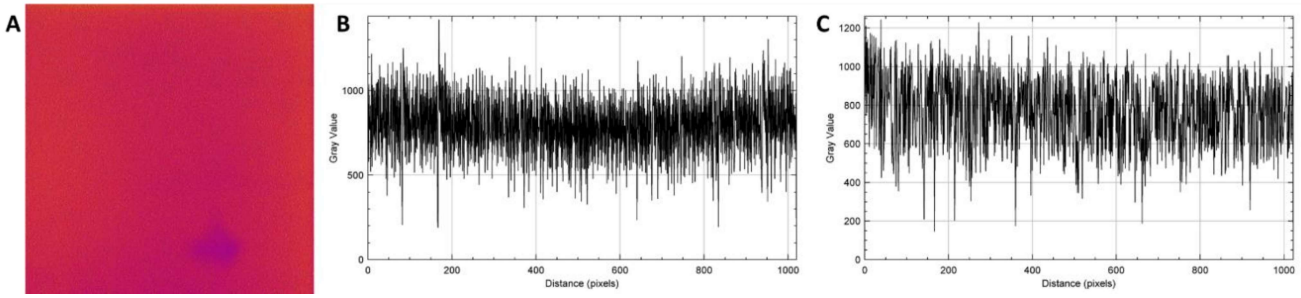

Figure A3: The excitation beam uniformly illuminates the solution in the imaging plane.
(A) Image of fluorescein solution in which the fluorescence was captured via photomultiplier tube (PMT) detector and digitized using NiDAQ and ScanImage.

(B) and (C) show the line profile plots of fluorescence (in D.U.) from fluorescein solution as a function of position (in pixel) in horizontal and vertical axis respectively. The line profile plots of the solution indicate that the area is uniformly illuminated or excited.

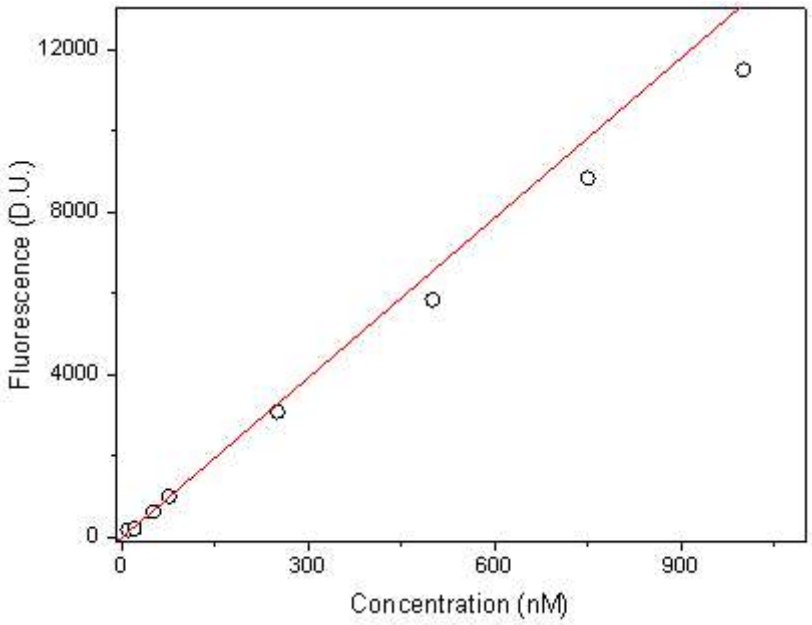

Figure A4: PMT signal as a function of concentration. Signal increases linearly as a function of fluorophore concentration. The deviation of fluorescence from linearity at higher concentrations (>500nM) of fluorescein is due to inter molecular absorption of emitted fluorescence.

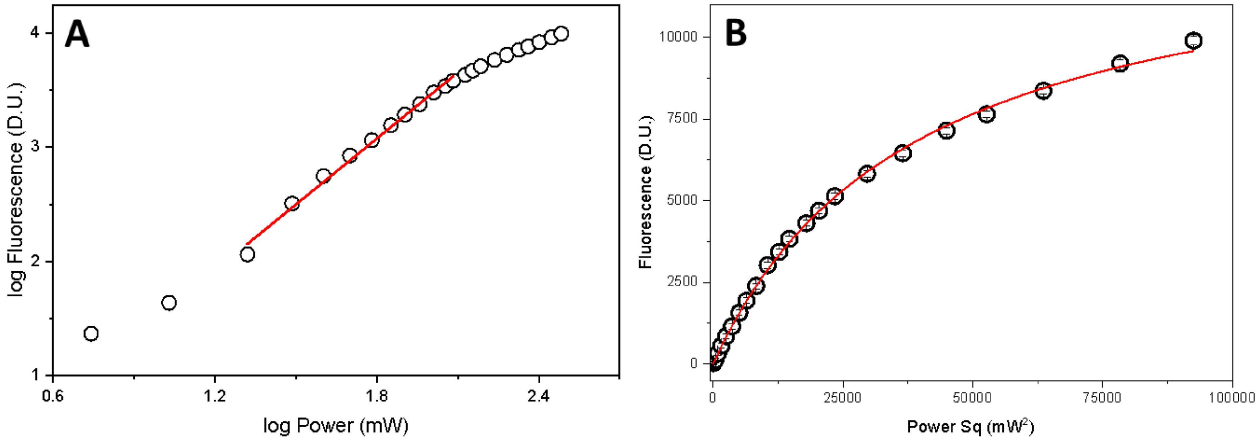

Figure A5: PMT signal as a function of incident power.

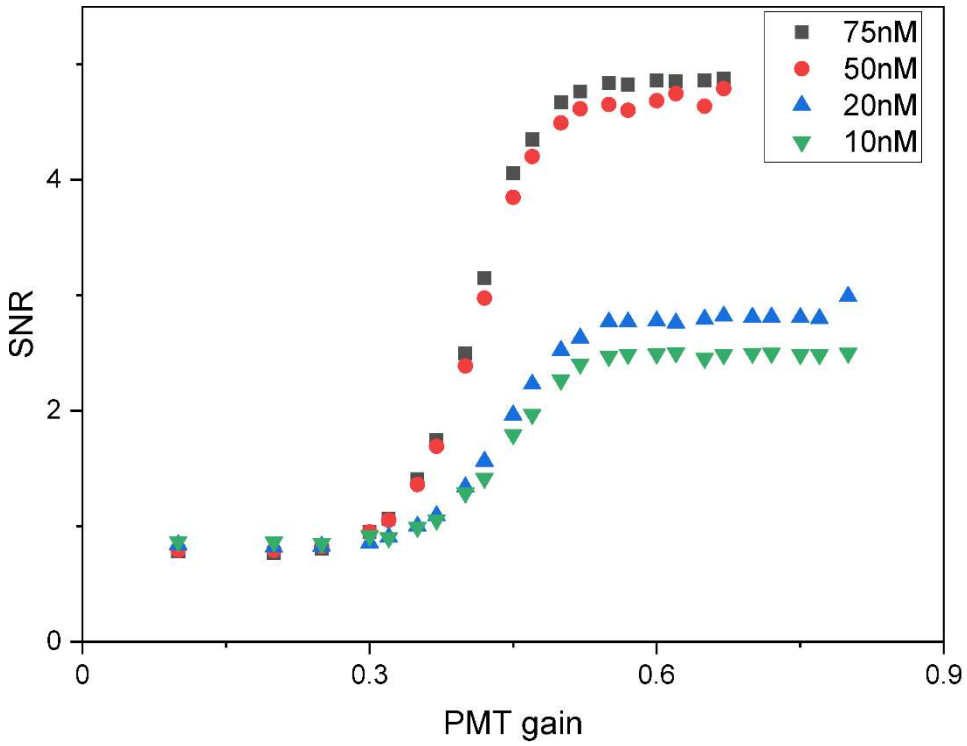

Figure A6: PMT signal to noise as a function of PMT gain. To operate the PMT in the linear range, it is best to optimise the detect signal between 0.3 and 0.6 gain for both lower (< 50nM) as well as higher concentration (> 50nM) as determined using fluorescein solution.

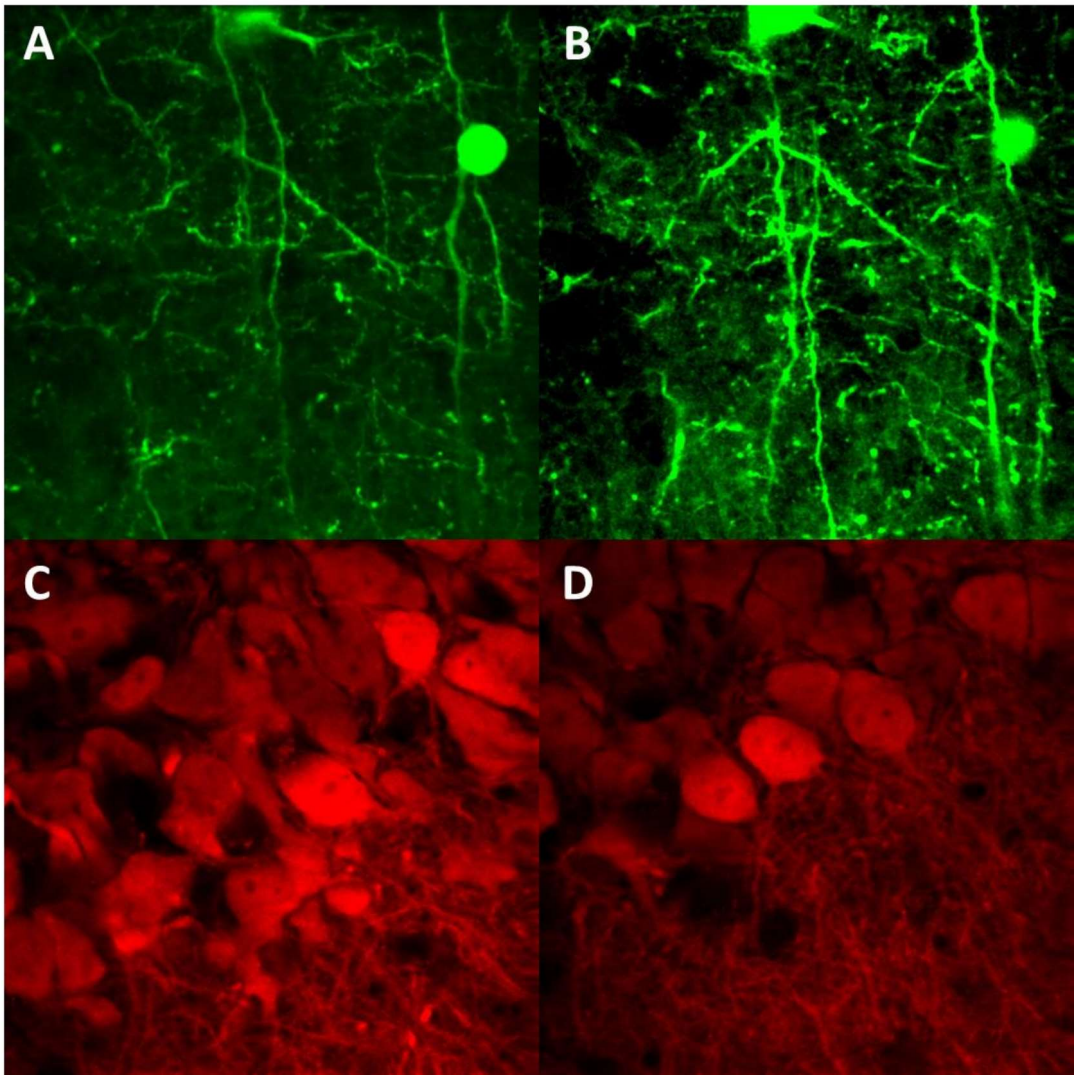

Figure A7: Two-photon imaging of 40µ brain sections.

(A) and (B) show two optical sections of a 40µm cortical brain section of Thy1-GFP mouse. (A) shows a distinct cell body near the top right corner. (B) shows clearly visible spines across the entire length of the dendrite.

(C) and (D) show two optical sections of a 40µm hippocampal brain section of mouse infused with tdTomato virus. Due to the high titre of the virus injected, many hippocampal cells are labelled, making it difficult to see the spines present in the dendrite of these neurons.

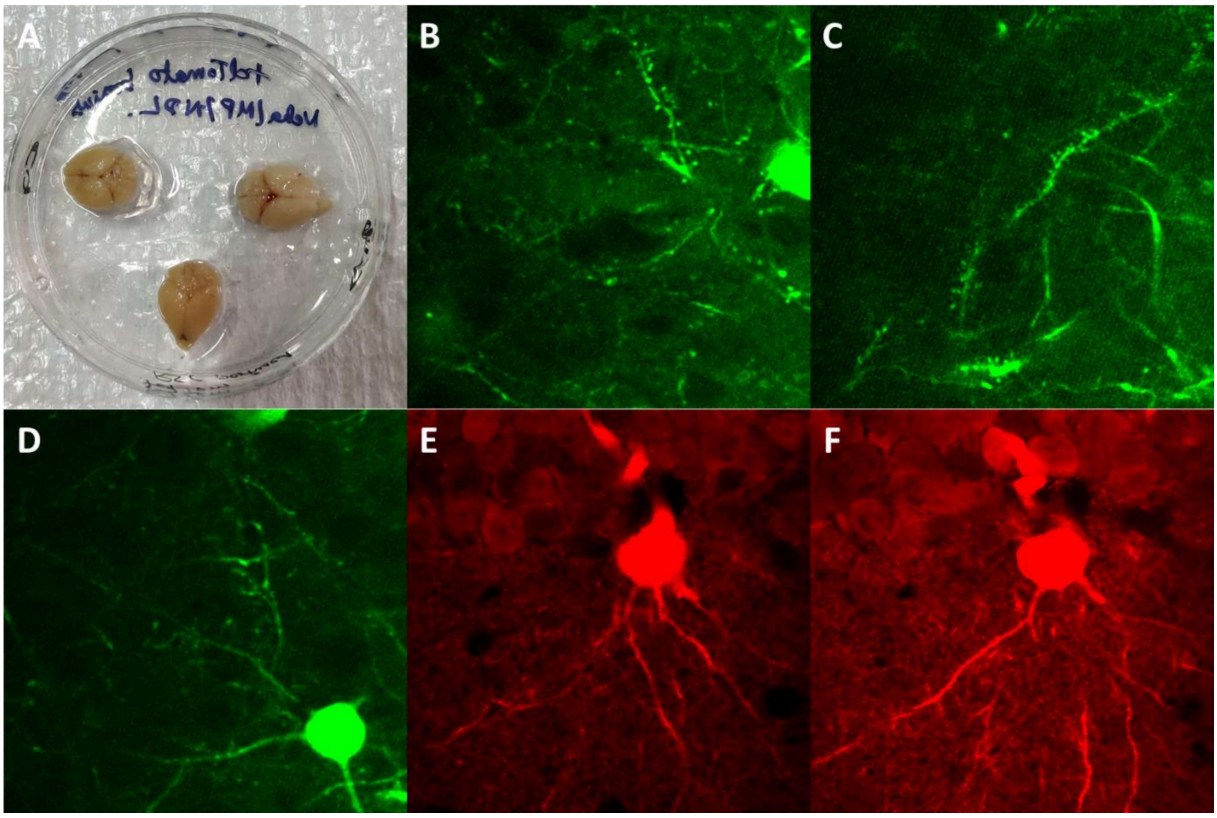

Figure A8: Two-photon imaging of ex-vivo brain.

(A) An image showing the ex vivo brain embedded in petri plate filled with 2% agar. (B), (C) and (D) show optical sections from a Thy1-GFP ex vivo brain. (B) and (C) show a dendrite with spine distinctly visible. (D) shows the presence of a cell body near the bottom right corner.

(E) and (F) show optical sections from an ex vivo brain infused with virus expressing tdTomato fluorophore. Both optical sections show dendrites with spines arising from the same labelled neuron.

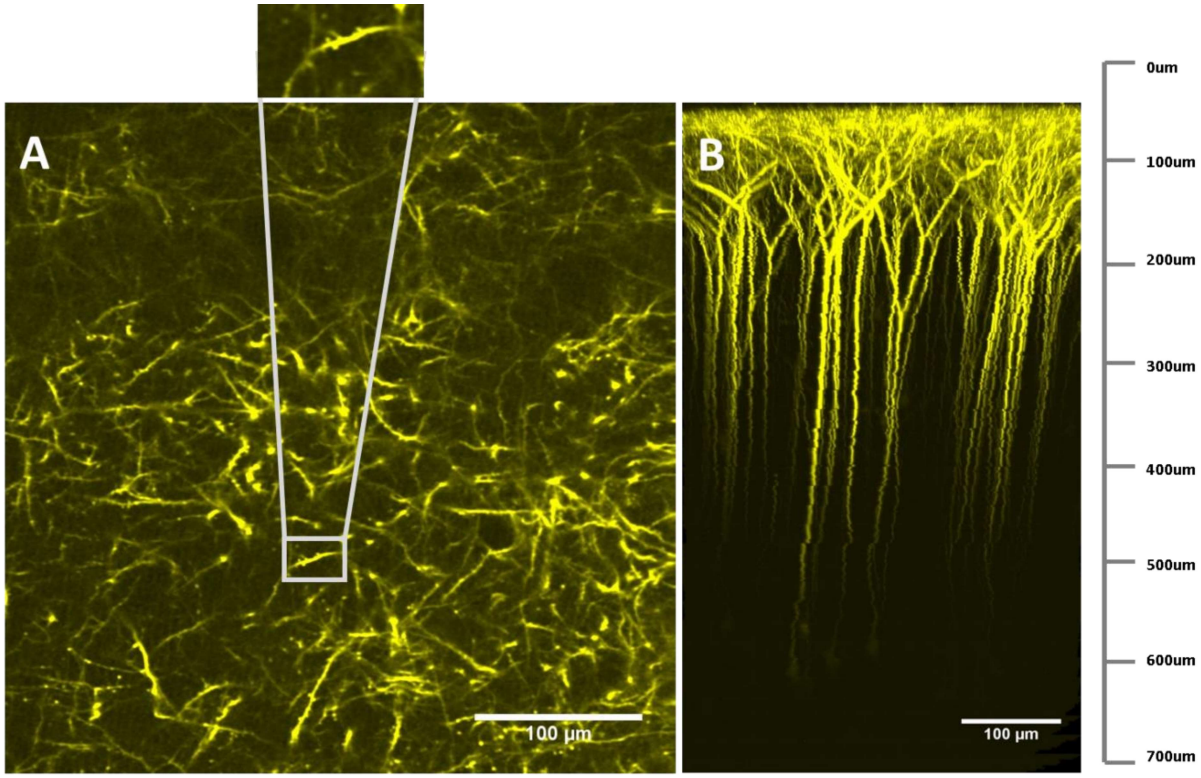

Figure A9: Two-photon in vivo image of the retrosplenial cortex of Thy1-eYFP transgenic mouse.

(a) An axial optical section showing dendrites visualised through YFP fluorescence of stochastically labelled neurons. Grey box shows a magnified region of dendrite with small protrusions called spines (synapses).

(b) A transverse image of the imaged volume showing the length of the neuron from dendrites at the top, through the axon, to the cell body at the bottom. We can image to a depth of 600µm of the retrosplenial cortex in Thy1-eYFP transgenic mice.

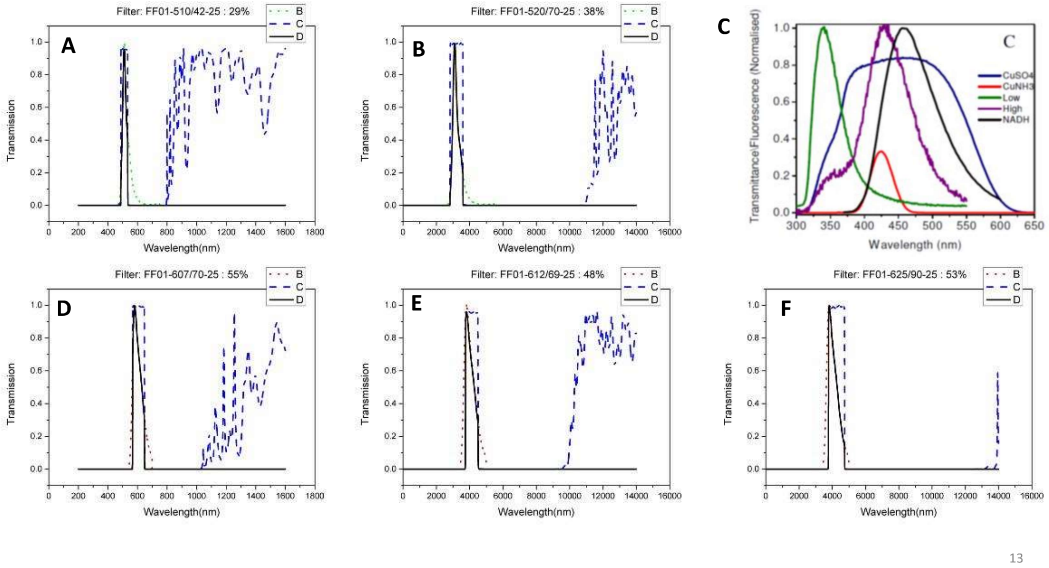

13

Figure A10: Efficiency of bandpass emission filters used for two-photon imaging of GFP and tdTomato. Dotted green or red lines represent the fluorophore emission spectra for GFP ((A),(B)) and tdTomato ((D)-(F)) respectively. Dashed blue line represents the bandpass filter transmission. Solid black line represents the overlap between the filter transmission and fluorophore emission spectra. Area under the solid black line represents the filter efficiency for the fluorophore (reported in %). Dark blue line in (C) represents the transmittance for Copper sulphate solution, which is used to filter out infrared excitation light (Subpanel (C) adapted from Balaji ().

A.7 Tables

Source	Wavelength (nm)	Lateral resolution (nm)	Depth resolution (nm)
Excitation light	780	453.1428571	1881.904762
Excitation light	800	464.7619048	1930.15873
Excitation light	900	522.8571429	2171.428571
Yellow-Green Beads	515	299.1904762	1242.539683
Red Beads	607	352.6380952	1464.507937
Fluorescein	517	300.352381	1247.365079
Rhodamine B	583	338.6952381	1406.603175
GFP	510	296.2857143	1230.47619
tdTomato	580	336.952381	1399.365079

Table A1: Rayleigh criterion for different wavelength of light.

Sr.	Issue	Possible cause	Possible solution
1	Graded fluorescence in space.	Non-uniform illumination of sample.	Check input beam alignment (Input, galvo mirror, scan lens, tube lens, mirror, objective backfocal, sample).
2	Graded fluorescence in space.	Emitted fluorescence is incompletely captured.	Check emission path alignment (Sample, dichroic, collection lens, detector).
3	Bright spots appearing in a periodic way.	Systematic noise from stray light.	Check that detector is appropriately shielded from light of electronics (Computer screen, torch light, LCD/LED lights)

4	Image appears blurry. Fluorescence at a pixel appears as streaks.	Fluorescence of a pixel is spilling over to the next causing streaks.	Modify dwell time to match the DAQ digitisation time, e.g., increase dwell time.
5	Histogram of fluorescence values is right skewed. OR Fluorescence values are saturated.	Electronic saturation.	Modify PMT gain to reduce signal amplification. OR Modify SRS settings to increase the number of signal bins.

Table A2: Troubleshooting for improving acquired image quality.

A.8 References

J. Balaji, 2004, '*Probing biological systems with localized excitation'*, PhD thesis, Tata Institute of Fundamental Research, Mumbai.

Appendix B

Molecular probes to visualise neuronal structure and activity.

B.1 Introduction

The molecular probes and viral vectors developed over the course of my PhD tenure to aid the visualisation of neuronal structure and activity is described in this chapter.

B.2 Generation of plasmid constructs for in vivo imaging

We designed constructs required for visualising neuron structure as well as exciting neurons and imaging the resulting calcium activity. These constructs were cloned into AAV backbone vector and have been packaged into a virus.

The constructs pAAV-CaMKII-GCaMP6f-2A-C1V1 and pAAV-CaMKII-tdTomato using Addgene plasmid # 51087 (pAAV-CaMKIIGCaMP6-2A-nls-dTomato) and the gene of interest (GOI), i.e., GCaMP6f-2A-C1V1 or tdTomato. The outline of the cloning strategy is given in fig. B1. The backbone pAAV-CaMKII plasmid was obtained by restriction digestion of Addgene plasmid # 51087 (pAAV-CaMKII-GCaMP6-2A-nls-dTomato) with BamHI and HindIII. The size of the pAAV-CaMKII backbone is 5049bp.

The GCaMP6f-2A-C1V1 insert of size 2499bp was generated by amplified using polymerase chain reaction (PCR) using the forward and reverse primers containing BamHI and HindIII. After setting a ligation mix of the digested insert and backbone, the mixture was transformed into DH5 competent cells. The transformed colonies were screened by colony PCR using the primers specific for the insert GCaMP6f-2A-C1V1. Colonies that showed a positive band in colony PCR was grown in LB media and used for plasmid extraction. The isolated plasmid was validated by

digestion with BamHI and HindIII restriction enzymes for insert release. Fig. B2 (A) shows the release of the insert of size 2499bp in lane 4.

The tdTomato insert of size 1499bp was generated by PCR amplification from CMV-tdTomato plasmid using the forward and reverse primers containing BamHI and HindIII. This insert was digested with restriction enzyme BamHI and HindIII overnight and purified by gel extraction. The gel purified tdTomato insert and pAAV-CaMKII backbone was kept for ligation overnight, transformed into DH5 competent cells and plated on LB agar plates containing ampicillin antibiotic. The colonies were screened using primers for tdTomato gene. The screen colonies were validated by digesting the plasmid with BamHI and HindIII restriction enzymes (Fig. B2 (B)). The clones were also validated by PCR.

B.3 Virus production of cloned constructs

The expression of the constructs was validated by transfecting the plasmid of interest into N2a cell line via Lipofectamine transfection. The cells were imaged after 48 hours to see the expression of the fluorophore. CMV-GFP and CaMKII-GCaMP6f-2A-dTomato plasmids was used as a control for transfection. For virus production, the plasmid of interest was co-transfected into HEK293T cell line via Calcium phosphate transfection with AAV packaging plasmids, pHelper and DJ8. The cells were imaged after 48 hours to see the expression of the fluorophore. After 60 hours, the cells were harvested and processed further for virus extraction. During virus extraction, the cells were harvested and lysed by subjecting the cell suspension to 5 rounds of freeze/thaw cycles by alternating the tubes between the dry ice-ethanol bath and the 37°C water bath. The supernatant containing the AAV viral particles was collected. 40µl of the supernatant was used for viral transfection into N2a cell line using polybrene. The rest of the supernatant was made into aliquots and stored at -80°C. Expression of CMV-GFP, CaMKII-tdTomato and CaMKIIGCaMP6f- 2A-nls-dTomato was seen three days from viral transfection (Fig. B3 (A)).

B.4 Virus expression in hippocampus and Retrosplenial cortex

Next, the expression of the virus in mouse brain was validated by injecting 2µl of the viral supernatant into the hippocampus and the retrosplenial cortex. Fluorophore expression was checked by sacrificing the mouse after 21 days, extracting and sectioning the brain, and imaging for tdTomato or GFP fluorescence. Figure B3 (B) and (C) show the expression of the fluorophores delivered via AAV in the hippocampus and retrosplenial cortex respectively.

B.5 Figures

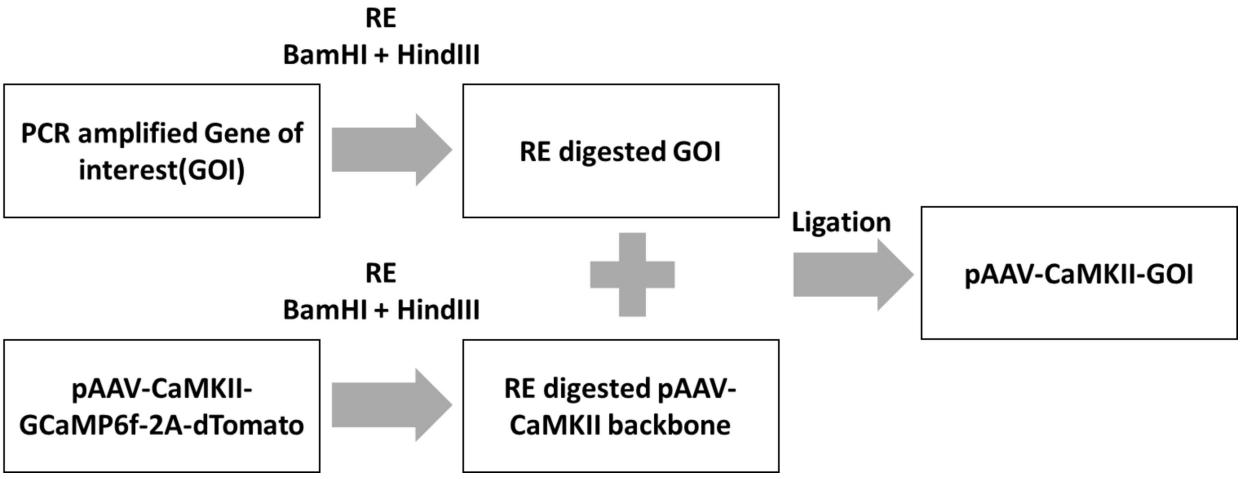

Figure B1: Schematic of cloning strategy used to clone pAAV-CaMKII-GCaMP6f-2A-C1V1 and pAAV-CaMKII-tdTomato. Paav-CaMKII-GCaMP6f-2A-dTomato was digested with BamHI and HindIII to create a Pavv-CaMKII backbone. The gene of interest (GOI) was amplified via PCR using primer with BamHI and HindIII restriction sites. Both the backbone and GOI after digestion were mixed in a ligation mixture and transformed into competent cells to obtain plasmids where the GOI and backbone fused to form the desired construct: pAAV-CaMKII-GOI.

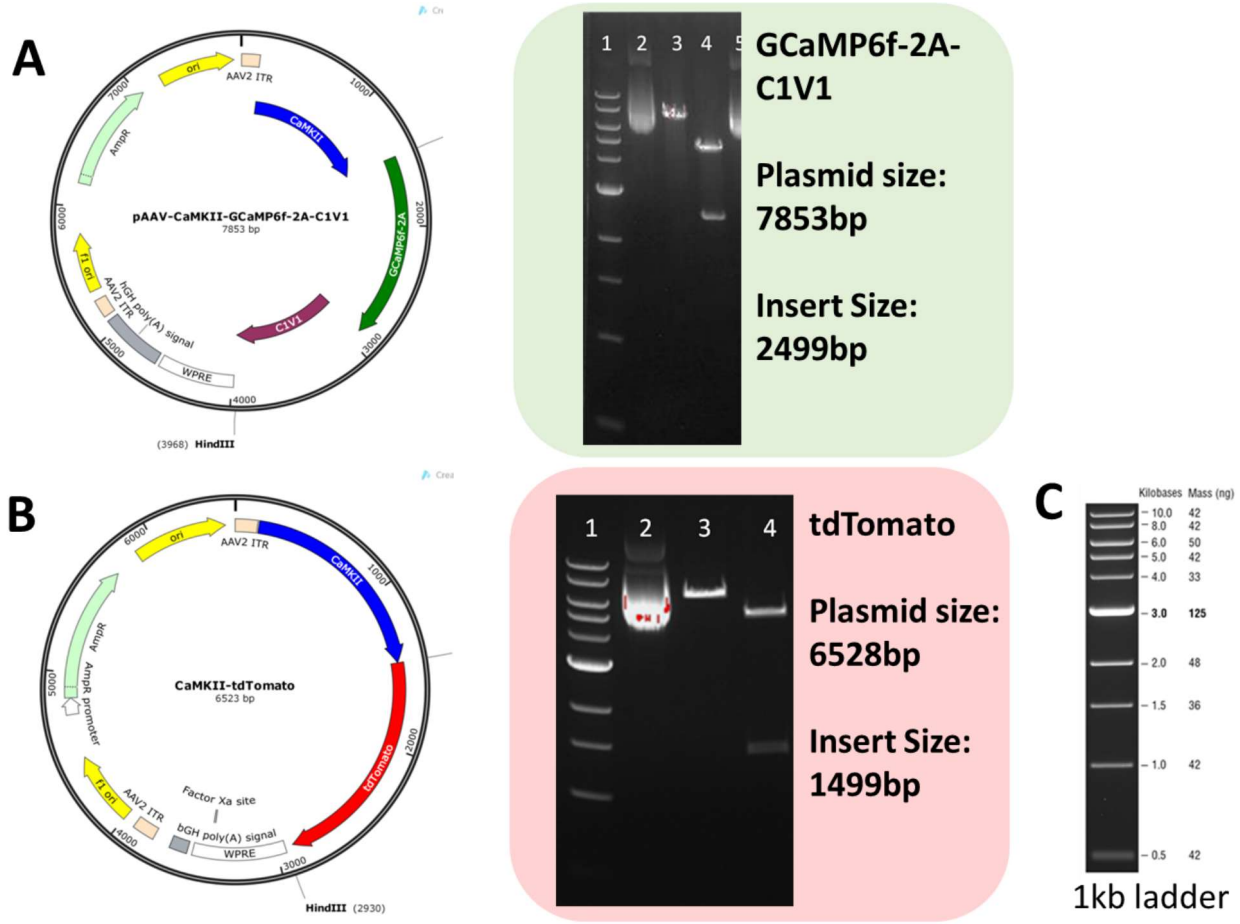

Figure B2: Restriction digestion confirmed the insertion of GOI in pAAV-CaMKII backbone.

(A) Left: Schematic representing the elements in pAAV-CaMKII-GCaMP6f-2A-C1V1. Right: Agarose gel image showing insert release to confirm presence of GOI in cloned plasmid. Lane 1: 1kb DNA ladder, lane 2: Undigested plasmid, lane 3: Linearised plasmid at 7853p, lane 4: Double digested (BamHI and HindIII) plasmid showing insert release at 2499bp.

(B) Left: Schematic representing the elements in pAAV-CaMKII-tdTomato. Right: Agarose gel image showing insert release to confirm presence of GOI in cloned plasmid. Lane 1: 1kb DNA ladder, lane 2: Undigested plasmid, lane 3: Linearised plasmid at 6528bp, lane 4: Double digested (BamHI and HindIII) plasmid showing insert release at 1499bp.

(C) 1kb DNA ladder (NEB) used as reference for DNA band size.

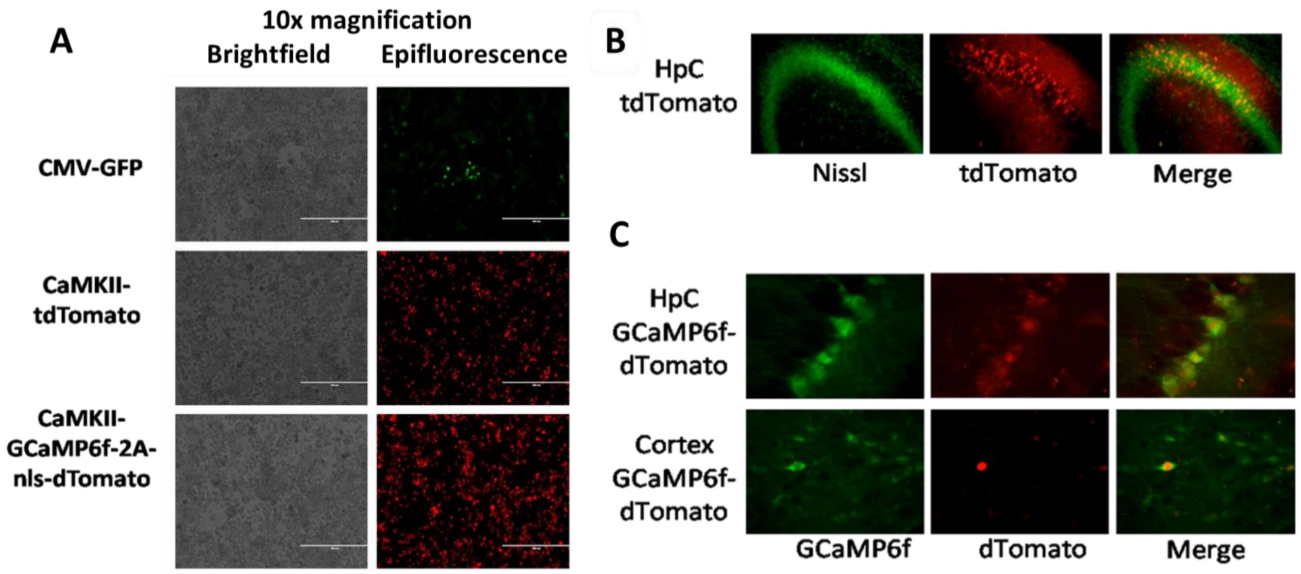

Figure B3: Expression of fluorophore delivered via AAV vectors.

(A) Viral infection in N2A cell line with three different fluorophores packaged into AAV vector.

(B) tdTomato fluorophore expression in a section of mouse hippocampus.

(C) GCaMP6f and dTomato fluorophore expression seen in a section of mouse hippocampus (top) and the retrosplenial cortex (bottom).

Appendix C

Instrumentation

C.1 Introduction

This chapter contains information on the mechanical, optical, and electronic instrumentation that were developed over the course of the PhD tenure for use in different projects related to this thesis as well as on-going projects in the lab.

C.2 Craniotomy for *in vivo* imaging of retrosplenial cortex in anesthetised head fixed mice

I carried out craniotomy of transgenic mice to facilitate in vivo imaging of fluorescently labelled neurons in the retrosplenial cortex in anesthetised, head fixed mice as previously described (Trachtenberg et al., 2002; Łukasiewicz et al., 2016). The process is described in detail below.

All surgical tools and glassware used for surgery were autoclaved before use. A glass bead sterilizer was used to maintain the sterility during and in between surgeries (30s-1min). The stereotaxic table was sterilized and wiped with 70% ethanol before the surgery. The mouse was then anaesthetised in an induction chamber using isoflurane before transferring it to the stereotaxic table with 1.5-2% isoflurane and 0.3 L/min oxygen (Fig. C1 (A)). A tail pinch response was tested to ensure that the mouse was fully sedated. Neosporin ophthalmic ointment was applied on the eyes to maintain the moisture in the cornea and to prevent contracting eye infection. The mouse was injected subcutaneously with Dexamethasone to prevent brain swelling. Hair was removed using a trimmer and the skin was cleaned with Betadine solution followed by 70% ethanol. The skin was cut using sterilized scissors with the help of forceps exposing the skull. Lidocaine ointment was used as a topical analgesic during surgery. Using a scalpel, the periosteum was removed, and the skull was cleaned. The skin was glued onto the

skull using a cyanoacrylate glue. A sterile 6mm coverglass was positioned over the skull between the bregma and lambda to mark the region of the cranial window (Fig. C1 (B)). It was centred at RSC coordinates: AP, bregma -2.8; ML, bregma 0. A high-speed pneumatic dental drill with a small diameter bur (Φx 0.6mm, cat # 14961, SS White) was used to outline the 6mm diameter circle. Using sterile saline dipped swabs and gelfoam, bone dust and occasional bleeding were cleaned. Once a thin layer of bone was remaining, the bone was carefully removed with fine forceps by lifting it in an upward direction. Gelfoam soaked in sterile saline was used to prevent any bleeding. Once the bleeding stopped a coverglass was placed on the top of the dura in the drilled hole. The edge of the coverglass was attached to the skull using epoxy glue. The rest of the surgical area was sealed with dental acrylic. An aluminium head bar to fix the head of the mouse to a tip toe tilt stage was glued in the front part of the skull (Fig. C1 (C-D)). Any exposed skull region was covered using dental acrylic. A small well was created around the cranial window to leave a cavity for holding water (as an immersion medium) for imaging with a water immersion objective. After the dental acrylic solidified, the mouse was removed from the stereotaxic table and transferred into a recovery cage. Anti-inflammatory, analgesics (Carprofen) and antibiotics (TMS) were given for post-operative care. Two weeks of recovery time was given before using the mice for an experiment. The implanted cranial window has been stable for up to 3 months.

The dosage of the operative drugs used are listed below.

1. Isoflurane - Inhalation anaesthesia administered during the surgery. 1.5-2%.
2. Neosporin - Topical eye ointment to prevent drying of the eyes.
3. Dexamethasone – Administered subcutaneously to reduce brain swelling. Concentration: 6mg/kg.
4. Lidocaine - Topical analgesic applied on the skull before drilling.
5. Carprofen –Anti-inflammatory administered subcutaneously post-surgery during recovery (2-3 days). Concentration: 5mg/kg.
6. Trimethoprimsulfamethoxazole (TMS) – Oral administration of antibiotic provided in drinking water post-surgery for a week. Concentration: 1mg/ml.

C.3 Alignment software for longitudinal in vivo imaging

To facilitate longitudinal *in vivo* imaging of the same volume of cortex over days, I designed a software to overlay a real-time video with a reference image. The software allows the user to compare the unique blood vasculature (seen through the cranial window on the mouse head) during an imaging session with a previous or reference image of the veins captured on imaging day 1, to locate the same area for repeated imaging across days.

The software was written in JAVA and utilises the following libraries:

1. ij.jar: ImageJ v51.
2. webcam-capture-0.3.12.jar
3. bridj-0.7.0.jar
4. slf4j-api-1.7.2.jar
5. JDK 1.8 (Default)

The software can be utilised on any operating system with JAVA JRE. Video acquisition can be carried out with a generic webcam compatible with the webcam capture package (Bartosz Firyn). A link to the software and the source code is given in Appendix D.

The usage of the software is briefly described as follows. On launching the GUI, the user must select a web camera from a drop-down menu and click 'Connect' button. On successful connection, the status changes to "Connected to camera". Next, the user must select the dimensions of the video capture and click 'Set' button. The GUI uploaded an appropriate reference image of a grid and the status changes to "Reference image uploaded". The user may upload a reference image of their choice using 'Load' button (Status changes to "Reference image uploaded" when image is successfully uploaded). The user starts the video display by clicking 'Start' button under live feed. The GUI displays the video, as well as the video overlayed on the reference image in the 'Overlay' section. The transparency of the reference image can be modified using the overlay scale bar with overlay set to zero showing the reference image, and the set to 100 showing the video. The user can capture a video frame by clicking the 'Capture' button. This prompts the user to select a directory to store the file. 'Capture' saves both the video frame as well as the overlay of the video frame with the reference image in the selected directory.

To stop the video display, click the ‘Stop’ button.

C.4 Optical setup on linear stage for measuring fluorescence lifetime

In Chapter 8, we developed a novel method to estimate the fluorescence lifetime from steady state measurements. We derived a theoretical expression to estimate the number of molecules in the ground state that is available for excitation when a pulse pair with inter-pulse duration of t_{sep} is incident on the sample. The expression relates the average fluorescence or steady state measurement from a fluorophore sample as a function of inter-pulse duration. To experimentally verify the analytical expression, we required a system that can deliver pulse pairs of excitation beams, vary the inter-pulse duration of these pulse pairs, and measure the steady state fluorescence emitted by the excited sample. The following subsections describes the components built to establish this system for performing the lifetime experiments with fluorophore solutions as samples.

Description of the optics setup:

The optical setup was designed (Fig. C3 (A)) such that the input pulsed excitation beam was split into two: a fixed (pump or reference) beam and a delay (probe or moveable) beam. The beam was split using a 50-50 beamsplitter creating a dual arm beam path. A fixed path arm and a delay line with varying path length. The distance travelled by the beam in varying path arm is controlled by optical delay line consisting of a travelling retroreflective mirror. Increasing the distance of the retroreflective mirror from the beamsplitter increased the amount of distance travelled by the delay beam, and thus increased the inter-pulse duration between fixed and delay beams. The distance of the retroreflective mirror was adjusted with the use of a linear stage powered by an Arduino microcontroller (described below, Fig. C3 (B).) The output arm at the beamsplitter, where the fixed and delay beam join, was sent through an objective to focus and excite a fluorophore solution in a cuvette. Alignment and spatial overlap of the two beams was assessed using physical targets at a point close to the beamsplitter and a point farther away (>2m). The emitted fluorescence was captured using an scMOS camera attached with

appropriate filters to block the background infrared light Fig. C3 (C).

Description of the electronics:

Arduino boards and their associated expansion shields are open-source microcontroller kits available for building electronic devices. I used an Arduino along with a L293D driver shield to control the stepper motor (Nema23 Stepper Motor Model: 57BYGH56) of the linear stage. A 5V SMPS powers the Arduino boards and the stepper motor to move the linear stage. The power supply with the Arduino boards was put together in a control box (Fig. C3 (D)). The control box has electronics required to control two stepper motors at a time.
The Arduino sketch uses the AFMotor.h library to communicate with the stepper motor. The user provides input of the distance to be moved through a Java-based GUI (see next section). Through serial communication interface (i.e., USB), the information is sent to the Arduino. The Arduino sketch converts the distance information to the number of steps of the stepper motor as follows:
Given that the step angle is 1.8 deg/step and that 1 turn is 360 deg/ revolution, we calculate the number of steps per turn as 360/1.8 = 200 steps per revolution. For a pitch of 5mm, 1cm linear distance correspond to 400 steps or 2 turns.

At the moment, the code facilitates the command for driving one stepper motor at a time. The code can be easily modified to incorporate a second stepper motor as per the requirement of the user. A link to the sketch is given in Appendix D.

Description of the GUI software:

The user operates the linear stage through a GUI written in JAVA (Fig. C3 (E)). The GUI software utilises jSerialComm-2.5.2.jar library to communicate with the Arduino through the COM port. The Arduino microcontroller contains the sketch or code that converts the user commands sent through the GUI to signals for the appropriate/required movement of the stepper motor to position the linear stage.

The software can be utilised on any operating system with JAVA JRE. A link to the software and the source code is given in Appendix D.

After the user has uploaded the Arduino sketch/code, as well as setup the GUI

software, the linear stage can be controlled as given in the following description. On launching the GUI, the user must connect to the Arduino by clicking ‘Connect’ button. The status changes to “Connected”. Once connected, the user must initialise the position of the stage using ‘Set zero’ button. This position of the stage is marked as the origin or reference point for the Arduino to calculate the movement of the stage. As a good practice, it is best to initialise the stage when it is at one end and mark that as the origin or reference position. Next, the user must enter the number corresponding to the desired distance of stage movement in centimetres and click ‘Go’ button to execute the command. At the end of the usage, it is good practice to return the stage to the reference position. Then, the user must click ‘Disconnect’ button.

C.5 Assembly of power supply Hamamatsu M13414 to operate Hamamatsu PMT H7422

We built a two PMT detection system to simultaneously image two fluorophores in our custom-built two photon microscope system. In the process, we assembled the power supply, Hamamatsu M13414, required to operate the PMT, Hamamatsu PMT H7422, as mentioned in the manual. A brief schematic highlighting the main connections are shown in Fig. C4 (A). Briefly, a 12V AC adapter powers the M13414 microcontroller board through connector 01. A parallel line with voltage reduced to 5V powers the different sections in connector 05. Connector 05:3 and 19 powers the peltier and PMT fan. A separate line connected via a switch, contains connectors 05:7 and 17. Connector 05: 7 powers the PMT, whereas connector 05: 17 powers external voltage control used to set the gain of the PMT. Alongside these connections, we added the connections for LED indicators (through L293D driver) to indicate the status of the PMT (not shown). The completed connections are shown in Fig. C4 (B), and the finished product is shown in Fig. C4 (C). Fig. C4 (D) shows the PMT in an operation state, where the LED lights indicate the following state of the power supply:

1. Green LED – Power supply on.
2. Yellow blinking LED – Peltier not ready.
3. Yellow LED – Peltier ready, PMT can be turned on.
4. Red LED – PMT overload. Switch off PMT, reduce gain.

5. LCD display – Current PMT gain.

C.6 Figures

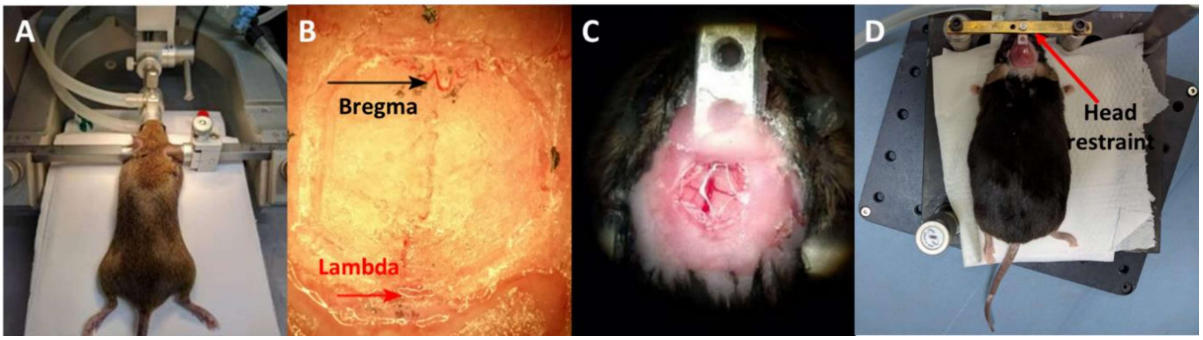

Figure C1: Craniotomy for in vivo imaging of retrosplenial cortex in anesthetised head fixed mice. (A) An anesthetised mouse placed on a stereotaxic apparatus for precise location of RSc coordinates.

(B) An image of the exposed skull showing the bregma (black arrow) and lambda (red arrow).

(C) An image of a mouse head with a cranial window implantation. Aluminium head bar attached using dental cement for restraining the head on the stage for in vivo imaging.

(D) An image showing an anesthetised mouse with the head restraint onto a tip toe tilt stage using the head bar prior to in vivo imaging.

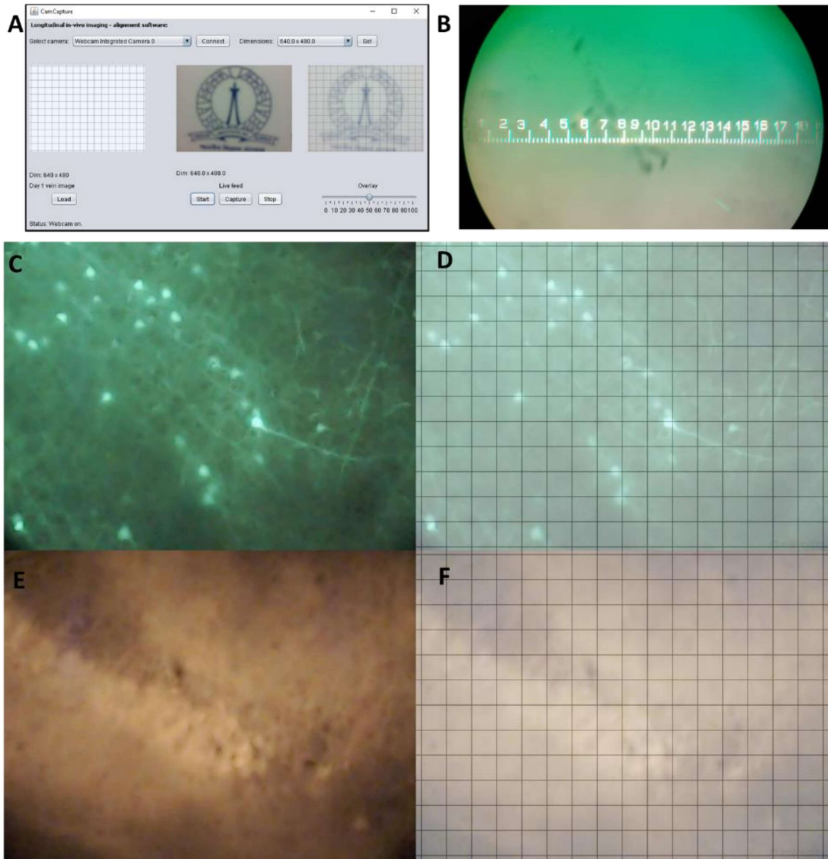

Figure C2: Alignment software for longitudinal in vivo imaging.

(A) A snapshot of the alignment software's GUI.

(B) A graticule measuring the field of view to be ~18mm.

(C – D) A section cortex of a Thy1-GFP transgenic mouse as visualised through the alignment software. (c) showing the GFP positive neurons with the cell body and dendrites. (D) shows the overlay of the imaged section's area with a reference grid for proper alignment.

(E – F) A section of hippocampus infused with AAV expressing CaMKII-tdTomato as visualised through the alignment software. (E) showing the neurons infected with AAV expressing the tdTomato fluorophore (cell bodies). (F) shows the overlay of the imaged section's area with a reference grid for proper alignment.

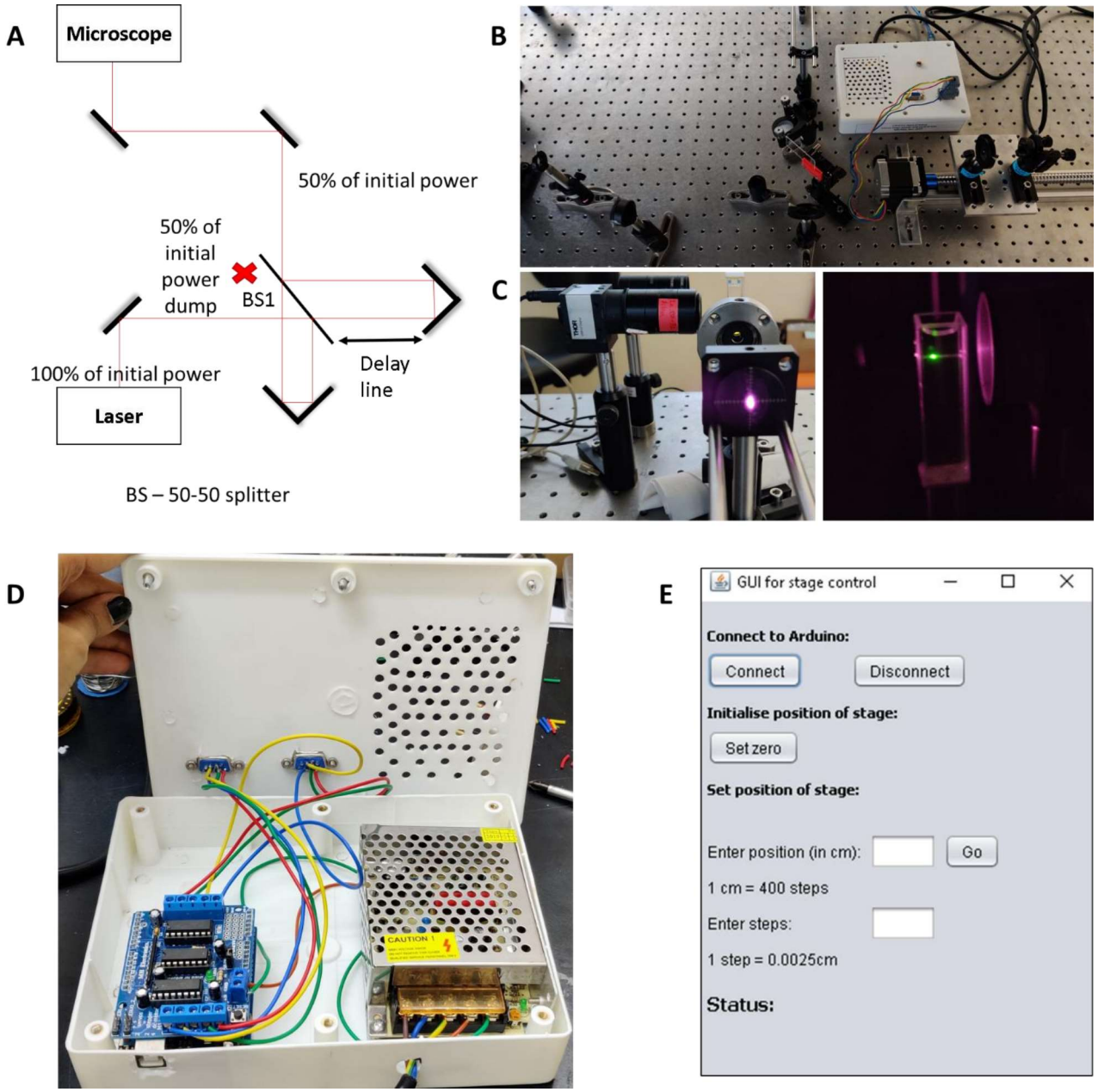

Figure C3: Optical setup on linear stage for measuring fluorescence lifetime.

(A) Schematic representation of the optical setup required for measuring fluorescence lifetime using

steady state fluorescence measurements.

(B) Image of the optical setup showing the beam splitter and delay line.

(C) Alignment of two beams at the back focal plane of the objective visualised on a marked/calibrated target to ensure the overlap of the pump and probe beams (left). Emitted fluorescence from fluorescein solution in a cuvette (right).

(D) Assembled microcontroller box consisting of an arduino, L293D driver arduino shield, and a 5V DC power supply to power, drive, and send commands to the stepper motor to control the linear stage.

(E) GUI written in JAVA swing for controlling the linear stage.

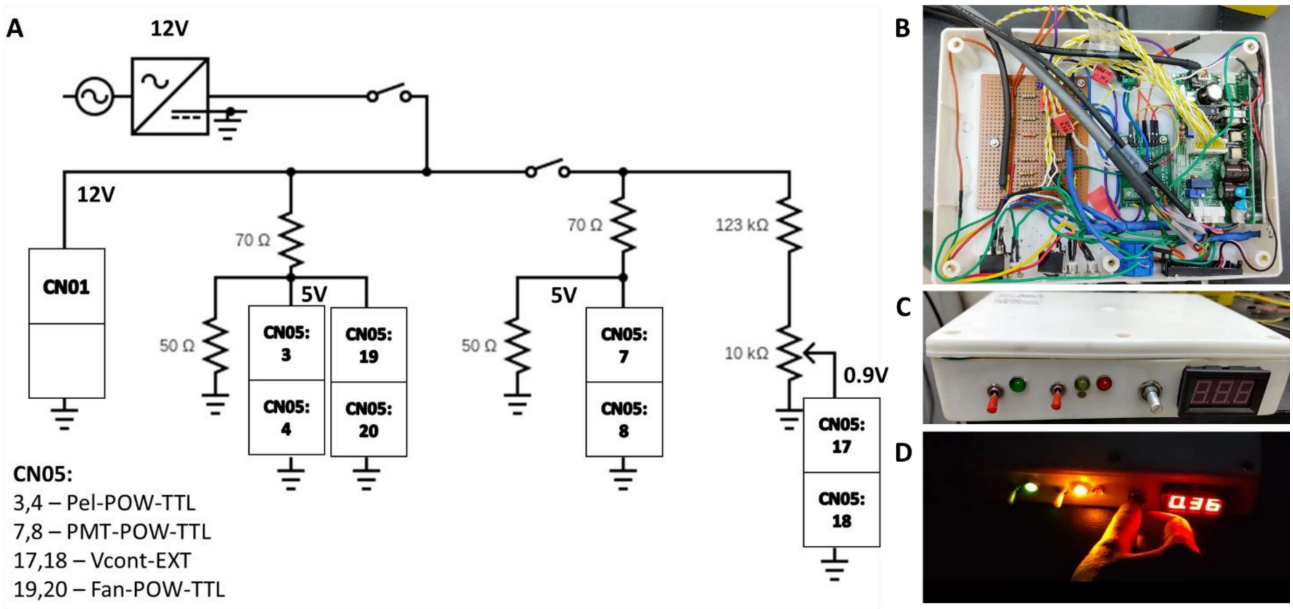

Figure C4: Assembly of power supply Hamamatsu M13414 to operate Hamamatsu PMT H7422.

(A) Schematic representation of the electronic connections required to power the microcontroller on M13414 module.

(B) Assembled power supply module with L293D driver for powering indicator LEDs, potentiometer to control gain (control voltage), and LED screen to indicate the gain (voltage)

(C) External body of the power supply box.

(D) Working PMT power supply showing power ON, peltier ON, and a gain of 0.36.

C.7 References

Bartosz Firyn. Webcam Capture API.

Łukasiewicz, K., M. Robacha, Ł. Bożycki, K. Radwanska, and R. Czajkowski. 2016. Simultaneous two-photon in vivo imaging of synaptic inputs and postsynaptic targets in the mouse retrosplenial cortex. *J. Vis. Exp.* 2016:e53528. doi:10.3791/53528.

Trachtenberg, J.T., B.E. Chen, G.W. Knott, G. Feng, J.R. Sanes, E. Welker, and K. Svoboda. 2002. Long-term in vivo imaging of experience-dependent synaptic plasticity in adult cortex. *Nature*. 420:788–794. doi:10.1038/nature01273.

Appendix D

Software and Code Book

The software and code book used for data extraction and analysis carried out in this thesis work is available on the lab Github page - https://github.com/neurodynamicslab.